THÈSE

Pour l'obtention du grade de
DOCTEUR DE L'UNIVERSITÉ DE POITIERS
UFR des sciences fondamentales et appliquées
XLIM
(Diplôme National - Arrêté du 25 mai 2016)

École doctorale : Sciences et ingénierie pour l'information, mathématiques - S2IM (Poitiers)
Secteur de recherche : Electronique, Microélectronique, Nanoélectronique et Micro-ondes

Présentée par :
Manuel Milla Peinado

Modélisation et validation expérimentale du canal de transmission radio sol-projectile pour la conception d'un transceiver numérique

Directeur(s) de Thèse :
Rodolphe Vauzelle

Soutenue le 19 décembre 2018 devant le jury

Jury :

Président	**Michel Hassenforder**	Professeur, ENSISA, Mulhouse
Rapporteur	**Ghaïs El Zein**	Professeur, INSA, Rennes
Rapporteur	**Guillaume Villemaud**	Maître de conférences, CITI, INSA, Lyon
Membre	**Rodolphe Vauzelle**	Professeur, XLIM, Université de Poitiers
Membre	**Herve Boeglen**	Maître de conférences, XLIM, Université de Poitiers
Membre	**Jean-François Diouris**	Professeur, IETR, Université de Nantes
Membre	**Dirk Schmoltzi**	Docteur, Institut de recherche franco-allemand, Saint Louis
Membre	**Loic Bernard**	Docteur, Institut de recherche franco-allemand, Saint Louis

Pour citer cette thèse :
Manuel Milla Peinado. *Modélisation et validation expérimentale du canal de transmission radio sol-projectile pour la conception d'un transceiver numérique* [En ligne]. Thèse Electronique, Microélectronique, Nanoélectronique et Micro-ondes. Poitiers : Université de Poitiers, 2018. Disponible sur Internet <http://theses.univ-poitiers.fr>

THESE

Pour l'obtention du Grade de

DOCTEUR DE L'UNIVERSITE DE POITIERS

(Faculté des Sciences Fondamentales et Appliquées)
(Diplôme National - Arrêté du 25 mai 2016)

Ecole Doctorale : Sciences et Ingénierie pour l'Information, Mathématiques (S2IM)

Secteur de Recherche : Electronique, Microélectronique, Nanoélectronique et Micro-ondes

Présentée par :

Manuel Milla Peinado

****

MODELISATION ET VALIDATION EXPERIMENTALE DU CANAL DE TRANSMISSION RADIO SOL-PROJECTILE POUR LA CONCEPTION D'UN TRANSCEIVER NUMERIQUE

****

Directeur de Thèse : M. Rodolphe Vauzelle

****

Thèse soutenue le 19 Décembre 2018 devant le jury composé de :

****

JURY

M. Ghaïs El Zein, Professeur, INSA de Rennes	Rapporteur
M. Guillaume Villemaud, Maître de Conférences, HDR, INSA de Lyon	Rapporteur
M. Jean François Diouris, Professeur, Université de Nantes	Examinateur
M. Michel Hassenforder, Professeur, ENSISA Mulhouse	Examinateur
M. Rodolphe Vauzelle, Professeur, Université de Poitiers	Directeur de Thèse
M. Hervé Boeglen, Maître de Conférences, Université de Poitiers	Examinateur
M. Loïc Bernard, Chargé de Recherches, HDR, ISL	Examinateur
M. Dirk Schmoltzi, Chargé de Recherches, ISL	Examinateur

MODELING AND EXPERIMENTAL VALIDATION OF A BASE - PROJECTILE CHANNEL MODEL FOR THE CONCEPTION OF A DIGITAL TRANSCEIVER.

A Thesis Presented To
The University of Poitiers

In Collaboration with
The French - German Research Institute of Saint Louis

Directed by
Professor M. Rodolphe Vauzelle

Supervised by
Associated Professor M. Hervé Boeglen
Research Scientist. M. Loïc Bernard
Research Scientist. M. Dirk Schmoltzi

Written by
Manuel Milla Peinado

In Partial Fulfillment
of the Requirements for the Degree
Doctor of Philosophy in the
University of Poitiers

University of Poitiers
December 2018

MODELING AND EXPERIMENTAL VALIDATION OF A BASE - PROJECTILE CHANNEL MODEL FOR THE CONCEPTION OF A DIGITAL TRANSCEIVER.

Date Approved: 19 December 2018

To my parents and sister

ACKNOWLEDGEMENTS

First of all, I would like to express my profound gratitude to my thesis supervisors, M. Hervé Boeglen, M. Loïc Bernard, M. Dirk Schmoltzi and my thesis director M. Rodolphe Vauzelle for their support, guidance and patience. Thank you very much for your valuable suggestions, time and encouragement throughout the three years of thesis.

This work has been possible thanks to the financial support of the DGA and ISL. I will be always grateful to both institutions for having shown confidence in me. At the same time, I would like to thank XLIM staff for their assistance during my PhD.

I would like to thank the members my reviewers, M. Ghaîs El Zein, M. Guillaume Villemaud, M. Jean François Diouris, M. Michel Hassenforder and M. Philippe Pouliguen for having accepted to evaluate my work.

Finally, words will never be enough to express my gratitude to my parents M. Manuel Milla Valdivia, Ms. Sacramento Peinado Martínez and my sister Mrs. Irene Milla Peinado for having always been with me during the last three years. I owe you everything.

TABLE OF CONTENTS

LIST OF TABLES

LIST OF FIGURES

SUMMARY

This thesis summarizes three years of work in the field of wideband characterization of the radio channel in projectile applications. The popularization of the miniaturized electronics has allowed the instrumentation of projectiles. The information gathered by the onboard sensors needs to be sent from the projectile to the base station as efficiently as possible by means of bi-directional communication links. In order to fulfill this requirement, it is fundamental to optimize every element in the communication chain. The channel, which is the medium where the radio wave propagation takes place, is one of the elements to be modeled. With the purpose of characterizing the radio channel in projectile applications, this thesis has been structured in five chapters: in chapter one and two, the general context of the thesis is presented, introducing the reader to this topic and giving the necessary elements to understand the rest of the manuscript. In chapter three, we address the problem of developing the necessary elements in order to characterize the propagation channel. The first contribution of this thesis is found here in the form of a set of procedures to perform channel modeling. In chapter four and five, we present our results. While in chapter four a preliminary study of the channel is performed, a complete characterization is given in chapter five. This chapter ends with the presentation of the second contribution of this thesis, i.e. a channel model to be used in simulations in order to improve the projectile-base station communication link. In a last stage, the conclusions and open questions are detailed.

Cette thèse résume trois années de travail dans le domaine de la caractérisation large bande du canal radio pour des applications projectiles. L'instrumentation des projectiles évolue avec la miniaturisation de l'électronique et l'accroissement constant de ses performances. L'échange de données par liaison sans fil bi-directionnelle entre le projectile et la station de base doit s'effectuer aussi efficacement que possible. Afin de répondre à cette exigence, il est fondamental d'optimiser chaque élément de la chaîne de communication. Le canal, qui est le support où la propagation des ondes radio prend place, est l'un des éléments à modéliser. Dans le but de caractériser le canal radio pour ces applications, cette thèse a été structurée en cinq chapitres: dans les premier et deuxième chapitres, le contexte général de la thèse est présenté et donne les éléments nécessaires pour comprendre le reste du manuscrit. Au chapitre trois, nous abordons le problème du développement des briques nécessaires pour caractériser le canal de propagation. Une des contributions de cette thèse est la définition d'un ensemble de procédures pour effectuer une modélisation de canal. Dans les chapitres quatre et cinq, nous présentons nos résultats. Alors qu'au chapitre quatre une étude préliminaire du canal est effectuée, une caractérisation complète est donnée au chapitre cinq. Les chapitres se terminent par la présentation d'un modèle de canal dédié aux simulations de communications numériques afin d'améliorer la liaison avec le projectile. Dans une dernière étape, les conclusions et les questions ouvertes sont détaillées.

CHAPTER I

INTRODUCTION

The use of electromagnetic waves for the transmission of information propitiated the advent of wireless communications at the beginning of the 20^{th} century [64]. This milestone was one of the major technological breakthroughs in the history of humanity. However, the technical limitations at that time restricted their use to governments and private companies with enough economic power to cover the associated deployment and exploitation costs. At that age, institutions like the famous British Broadcasting Corporation and equivalents in other countries started to be created. The access to this technology for the general public has been slowly growing from the early 40s to the explosion of mobile wireless capable devices in the early 90s [43]. During these years, we have moved from the primitive 'over-and-out' systems popularized after the World War II to the current so-called smart phones. Nowadays, the number of applications which take advantage of the mobile wireless technology are almost impossible to enumerate. Certainly, its use has been widespread in almost every technological application.

In the frame of applications for defense and security, the wireless communication with projectiles or ballistic missiles has been an active area of interest from the late 50s to nowadays [87]. One of the related research areas is the development of instrumented projectiles. These kinds of projectiles are generally accoutered with a non explosive payload. Instead, a range of sensors are carried with the purpose of monitoring some variables of interest (temperature, attitude, position, etc). Generally speaking, a projectile is much smaller than a ballistic missile, the available space for the payload being an issue. As a result of this limitation, the development of instrumented projectiles has been gaining importance with the embeddability of the digital electronics available on the market.

Nevertheless, instrumenting a projectile is still a demanding task which requires to face several constraints. We could arrange them in two groups: electronic survivability and

telemetry constraints. Effectively, one of the major challenges is to protect the payload from the g-shock at the moment of the firing. In real firings, g-forces higher than 30 kG can be expected, these tremendous forces can destroy the embedded electronics without the proper g-hardening mechanism [62]. However, once we can assure the operation of the carried electronics, we can focus our attention on the telemetry constraints. It is the objective of every telemetry system to send the data gathered by the sensors to the receiving station as efficiently as possible. Usually in this context, the flight time of a projectile is in the range of a few minutes. For that reason, it is mandatory the use of high throughput transmitters [73]. The recent advances in electronic miniaturization in conjunction with the availability of high performance radio chips nowadays allow the implementation of bi-directional communication links between the projectile and the ground station.

In the context of wireless mobile communications there is a variety of elements which can affect the performance of the communication system. The performance being the capability of delivering reliable information between the transceivers. One of these elements is the channel, which is the medium where the wave propagation takes place. When an electromagnetic wave propagates through the channel, it will interact with the matter present in the propagation scenario. As a matter of fact, it is possible to establish a relation between the radiated waves and the received ones. The precise characterization of this relation is called channel modeling, i.e. an abstraction of the propagation scenario is presented in terms of a mathematical model. In the literature, one can find channel models for a large range of mobile wireless applications like those already used in telephony [85, 86] or vehicle-to-vehicle (V2V) communications [5]. However, the conditions in this thesis will be slightly different from those usually assumed in civil applications. Some of the key parameters usually taken into account for their conception are several orders of magnitude away from the ones concerned by this thesis. For instance, the speed between the transceivers which can be up to 3 times the speed of sound. This value is far away from the usual few tens of kilometers per hour in V2V applications. As we will see, some of the parameters in the channel model will depend on the relative speed between the transceivers.

One of the main objectives of this thesis is to optimize the communication performance in

the field of instrumented projectiles. For that reason, a great part of the work performed will be devoted to the study of the propagation conditions and the conception of a channel model for its use in future experiments. The literature in the frame of instrumented projectiles is limited because of security and publishing policy restrictions. In this thesis, we will have to define a set of data analysis procedures in the channel modeling field after having taken into account this limitation. For this reason, some of the usual algorithms employed in the communication chain have to be modified. In a last stage, the basics for the designing of a digital transceiver can be proposed once the channel is known and a communication strategy has been defined.

Taking into account the previous exposed context, the contributions of this thesis can be summarized as follows:

- Developing of the necessary instruments and algorithms: the novelty of this work lead to the introduction of a different approach to the supersonic channel modeling.
- Conception of a channel model for super-sonic instrumented projectiles: knowing the propagation channel is crucial in the optimization of a telemetry system, we need to model the channel in order to minimize its impact on the radio link performance.

All of these contributions require from the expertise of several institutions to be successfully achieved. In our case, this thesis has been supported by the following three institutions: the XLIM laboratory, the The French - German Research Institute of Saint-Louis (ISL) and the *Direction Générale de l'Armement* (DGA).

Each one contributed differently in the accomplishment of our objectives: the role of XLIM and ISL has been the scientific supervision of the project. The financial support has been provided by both ISL and DGA. The three institutions provided testing facilities and technical support.

- XLIM: this institution is a multidisciplinary research institute located on several geographical sites, being the XLIM section from the University of Poitiers the one involved

in this thesis. XLIM incorporates more than 440 people among professors, CNRS researchers, engineers, technicians, post-doctoral researchers, PhD students and administrative staff. This research institution has been structured around three centers of activity: electronics, photonics and mathematics - computers science and image. The branch involved in this thesis belong to the XLIM Smart System and Network section.

- ISL: The French-German Research Institute of Saint-Louis is a bi-national research institute established by the Federal Republic of Germany and the French Republic on the basis of a treaty signed in 1958. The main research facility is located in Saint - Louis, while experiments requiring the use of explosives or projectiles are tested at Baldersheim facility. Both sites are located in Alsace, France. The core mission of ISL the Research, scientific studies and basic predevelopment in the field of defense and security. ISL has reinforced its activities on issues of civil security and countermeasures against terrorism encountered both at home and during overseas military operations. This thesis was carried out in the Sensors, Telemetry and Communications (STC) group from Division II.

- DGA: this institution depends on the French Ministry of Armed Forces. Its mission is to manage the equipment of the French army, technologically prepare its capacities and promote the exportation of French manufactured armament. For these tasks, a budget around 25 euro billions was assigned in 2016. This institution provides financial support for approximately 130 PhD programs every year.

The rest of this document is organized as follows: in chapter 2 we will present the main channel concepts and terminology required to understand this manuscript. Additionally, we will introduce some of the techniques used in the conception of a channel model (channel sounding) and why it is necessary to adapt the channel sounding process to our domain. The chapter will end by showing the specific constraints and requirements which motivated a new approach in the channel modeling for projectile applications.

In chapter 3 we will first present all the instruments and equipment available at the beginning of the thesis. Later, with the use of these elements we will show how we develop a

channel sounding method adapted for the requirements and constraints explained in chapter 2. The hardware and algorithms used will be detailed in order to allow the reproduction of our methods by other research groups with the aim of improving the proposed methodology. The chapter will end by showing the conceived prototype for channel sounding.

The first results will be shown in chapter 4 by performing a preliminary study of the environment to model. We will have to pay attention to several phenomena related to the flight dynamics which may affect the flight of the projectile. Concretely, two effects will be studied (spinning and nutation) in order to evaluate their impact in the communication performance. This chapter will set the basis for a wideband channel characterization in chapter 5.

The construction of a channel model for projectile applications will be finally detailed in chapter 5. In this chapter, the data recovered from experiments at low speed and real firings (supersonic speed) will be analyzed and used to develop a channel model. The concepts presented in chapter 2 concerning the definition of a channel model will be applied here. In addition, we will show the full use of the methodology and prototype conceived in chapter 3. The chapter will end with the presentation of the channel model and a discussion about the future of transceivers developed at ISL.

Finally, the conclusions and future work will be detailed.

CHAPTER II

WIRELESS CHANNEL & CHANNEL SOUNDING

In this chapter we will introduce the main subject of study of this thesis, which is the wireless propagation channel. As it is shown in Fig. 1, the channel can be seen as an abstraction of everything which happens to a wave from the radiation to the reception.

As we will introduce later, several phenomena are implied in wave propagation. However, from the point of view of the receiver, the channel can be seen as an element which has the property of modifying the transmitted information. The characterization of how the channel affects the transmitted signals is called channel modeling. In this chapter, we will present the main elements to be taken into account in this discipline.

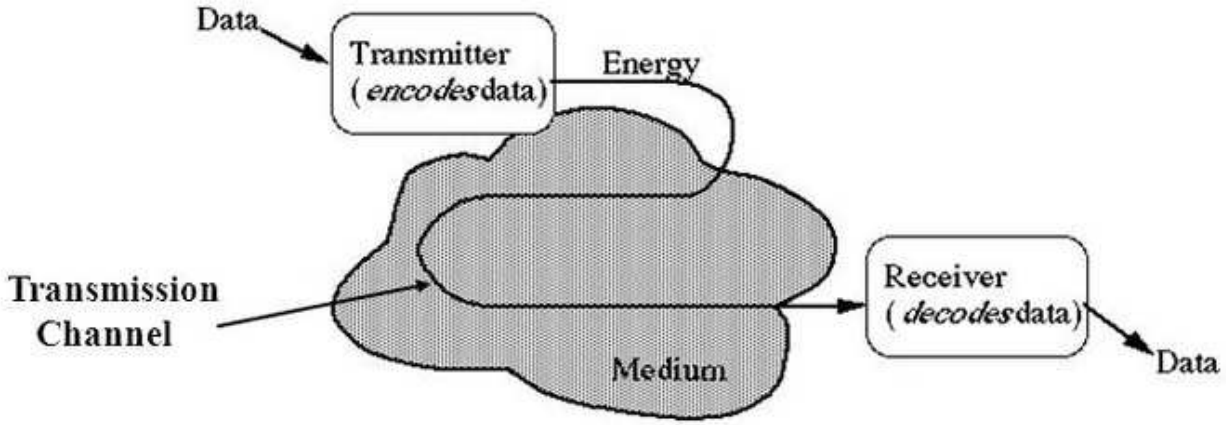

Figure 1: Simplification of a Transmission System.

This chapter has been structured as it follows: in section 2.1, the channel will be treated from the point of view of the physical effects involved in wave propagation. We will start with the simplest propagation scenario. Subsequently, the rest of the elements involved will be introduced step by step.

In section 2.2, we will change our manner to approach the propagation channel. Instead of focusing on the physics behind wave propagation phenomenon, we will approach its modeling from the point of view of the signal processing. We will see how the channel can be seen

as a linear system characterized by its Impulse Response, i.e. Channel Impulse Response (CIR). Additionally, the convenience of considering the channel as a stochastic process will be discussed.

In practical situations, we need a method to obtain the CIR. Some of these methods require to *sound* the channel in order to extract the CIR. This process is called channel sounding and consists of the studying of how the channel modifies a known test signal. A revision of the most popular channel sounding techniques will be presented in section 2.3. In spite of their popularity and efficacy, the classical channel sounders cannot be employed to achieve the objectives of this thesis. Their weight, size and power consumption prevent us to embed these kind of sounders in projectile applications. As we will see in chapter 3, this constraint will lead to the proposition of a channel sounder which can be utilized in the optimization of the radio link performance in projectile applications.

2.1 Wireless Channel Concepts

In this thesis, the channel characterization problem has been treated from the engineering point of view. This is, we are more concerned about how the channel modifies the received signal rather than the physics behind the propagation channel. However, it is important to introduce the involved phenomena in order to follow the rest of the manuscript. With this objective, we will introduce three channel related concepts in this section: path loss, multipath and Doppler effect. They are respectively treated in sections 2.1.1, 2.1.2 and 2.1.3. Additionally, we introduce the expected power profile measured at the receiving station in section 2.1.4.

2.1.1 Path Loss

One of the effects present in almost every propagation channel is the wave attenuation, i.e. the loss of wave energy as it propagates through the medium. In the following, this concept will be called path loss. In order to include this effect as one of the parameters to be modeled, we can start by considering the simplest radio link possible. This is a Line - of - Sight (LOS) situation in vacuum (free space) like the one sketched in Fig. 2.

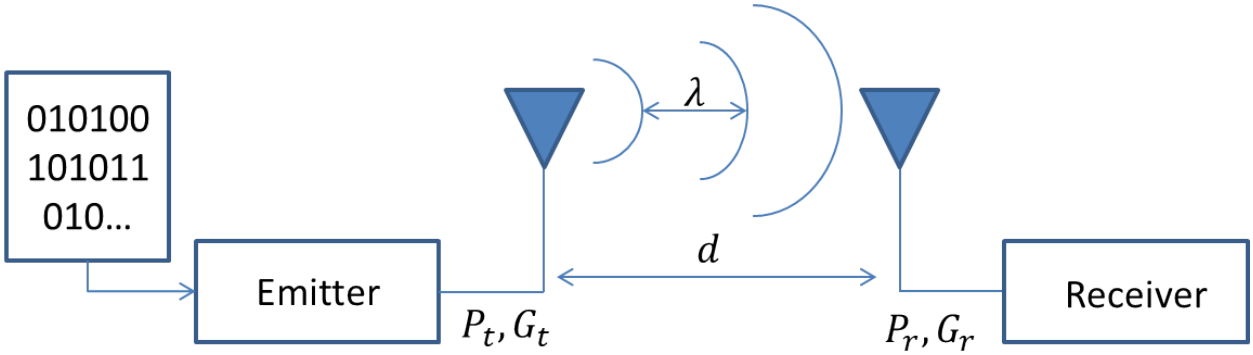

Figure 2: Free Space Radio Link.

In this scenario, two transceivers are separated by a certain distance d. The information generated by the emitter is being transmitted in the form of spherical waves with a certain wavelength λ. In a basic theoretical case, these spherical waves would have to be radiated by an isotropic antenna, i.e. an antenna capable of radiating the same amount of energy in all directions.

Assuming a spherical wavefront in the situation described by Fig. 2, the power density S_1 per area unit at a distance d_1 can be obtained by dividing the total radiated power P_t by the sphere surface. We can obtain then $S_1 = P_t/4\pi d_1^2$. After a time, the wave will have traveled a distance $d_2 > d_1$. As a consequence, now the same radiated power P_t is equally distributed over a greater surface, being the new power density $S_2 = P_t/4\pi d_2^2 < S_1$.

It is outside of the scope of this manuscript to give an exhaustive treatment of the antenna theory. For this purpose, we can refer to [12]. However, it is necessary to introduce some antenna related concepts before continuing. Concretely, we will introduce:

- Antenna Gain ($G(\theta, \phi)$): an isotropic antenna is an ideal device which is not possible to implement in real applications. Instead, antennas do not radiate the same amount of energy in every direction. They have *privileged* directions called *antenna lobes* (See Fig. 3). Accounting for these privileged directions, G is the parameter which measures how well an antenna converts the input power into electromagnetic waves in a specific direction. The radiation/reception direction is usually expressed in terms of the elevation (θ) and azimuth (ϕ) angles as we can see in Fig. 3.

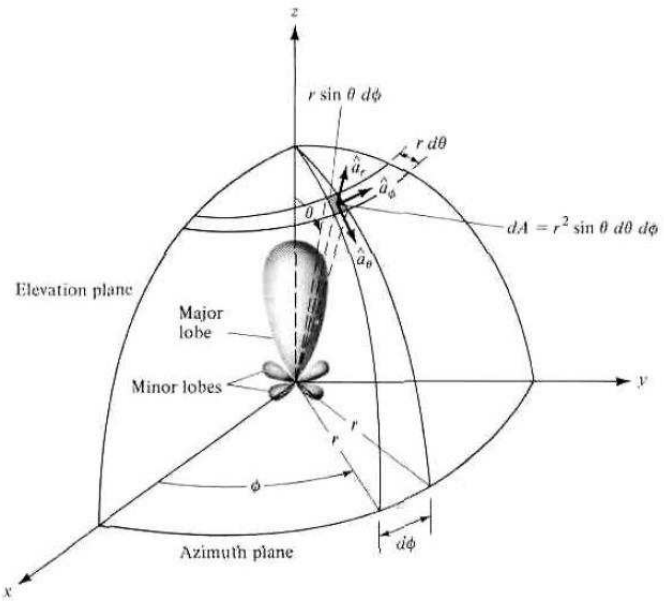

Figure 3: Antenna Lobes and Frame Definition. Image from [12].

- Antenna Effective Area ($A_{eff}(\theta, \phi)$): the parameter $A_{eff}(\theta, \phi)$ accounts for the effective area of the receiver antenna in a given direction. This parameter is related with the antenna gain $G(\theta, \phi)$ and the wavelength λ in the form: $A_{eff}(\theta, \phi) = (\lambda^2/4\pi)G(\theta, \phi)$.

- Antenna Polarization: this property makes reference to the polarization of the emitted waves by the antenna. The polarization of a wave is the figure described by the wave's electric field observed from the direction normal to the wave propagation. Depending on the figure described, the wave is said to be linearly, circularly or elliptically polarized (See Fig. 4[1]). In the case of an elliptically polarized wave, the Axial Ratio (AR) is a dimensionless parameter defined as the ratio of the major axis (OA) to the minor axis (OB), i.e. AR = OA/OB. The polarization of a wave (antenna) is given by its polarization vector $\hat{\rho}$. For further information about the implications of the wave polarization and how the polarization status is found, please refer to [12].

With these two new elements, we can define the measured power at a distance d as $P_r = [P_t/(4\pi d^2)]\, G_t(\theta, \phi) A_{eff}(\theta, \phi)$. Where $G_t(\theta, \phi)$ is the gain of the emitting antenna and $A_{eff}(\theta, \phi)$ is the effective area of the receiving one. The previous expression can be

[1]Image from: http://hyperphysics.phy-astr.gsu.edu/hbase/phyopt/polclas.html

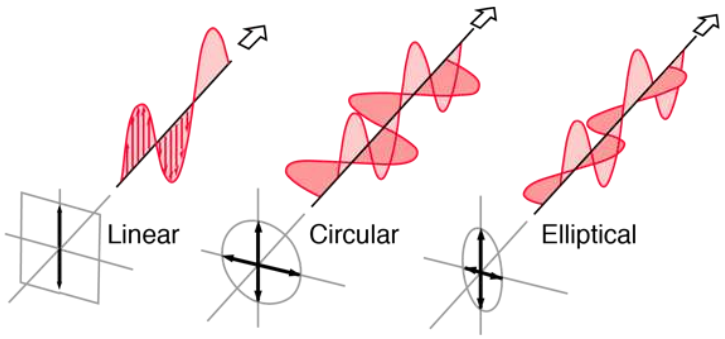

Figure 4: Wave Polarization Cases.

rearranged in order to obtain the Friis' equation [40].

$$P_r = P_t G_t(\theta,\phi) G_r(\theta,\phi) \left(\frac{\lambda}{4\pi d}\right)^2 \tag{1}$$

This equation was derived by Harald T. Friis from the Bell telephone laboratories in 1946 when he was developing a broadband microwave system for telephony. In order to obtain this expression, one can follow the previous reasoning or derive this formula from Fresnel optics, Gaussian beam or mode analysis as it is shown in [48]. Some additional variables like circuit mismatching and antenna polarization can be added to this equation in order to account for them in the free space scenario. In this case, the form of the Friis' equation will be [12]:

$$P_r = P_t \overbrace{(1-|\Gamma_t|^2)(1-|\Gamma_r|^2)}^{\text{Circuit Mismatching}} G_t(\theta,\phi) G_r(\theta,\phi) \left(\frac{\lambda}{4\pi d}\right)^2 \underbrace{|\hat{\rho}_r \cdot \hat{\rho}_t|^2}_{\text{Polarization Mismatching}} \tag{2}$$

where the parameter $\Gamma_{t,r}$ represents the reflection coefficient between the antenna and the rest of the electronic elements (circuit mismatching) and $\rho_{r,t}$ represents the antenna polarization, i.e. the operation $|\hat{\rho}_r \cdot \hat{\rho}_t|^2$ defines the polarization mismatching between the antennas. When dealing with expressions like the Friis' equation, one may prefer to use a different representation of Eq. 2 as it appears in [99]:

$$
\begin{aligned}
10log_{10}(P_r) &= 10log_{10}(P_t) \\
&\quad - 10\alpha log_{10}(d) \\
&\quad + 20log_{10}\left(\frac{\lambda}{4\pi}\right) \\
&\quad + 10log_{10}(G_t(\theta,\phi)G_r(\theta,\phi)(1-|\Gamma_t|^2)(1-|\Gamma_r|^2)\,|\hat{\rho}_r\cdot\hat{\rho}_t|^2) \\
P_r(dBW) &= P_t(dBW) - 10\alpha log_{10}(d) + C
\end{aligned}
\tag{3}
$$

In Eq. 3, α is known as the path loss exponent. This parameter generalizes Eq. 1 for other scenarios rather than restricting its use to the free space case treated in the Friis' formula. As we can see, the C parameter accounts for antenna gain, circuit mismatching, antenna polarization and the working frequency.

The value of the path loss exponent may vary from less than 2 in indoor environments where the wave can be guided, to 3 or higher in high-loss propagation scenarios. In Tab. 18, we show typical empirically obtained values for α in different propagation scenarios [83]. In practical cases, it is common to use empirically obtained path loss models like the ones appearing in [91, 81]. By utilizing them, the radio engineer in charge of the deploying a radio link will have an estimation for the expected path loss behavior in some common propagation scenarios.

Table 1: Common Path Loss Exponent Values.

Environment	**Path Loss Exponent**
Free Space	2
In building LOS	1.6 - 1.8
NLOS factories	2 - 3
NLOS buildings	4 - 6
Urban area	2.7 - 3.5
Shadowed urban area	3 - 5

Depending on the emission/reception frequency, the atmosphere can affect the path loss component in long range radio links. In fact, some molecules in the atmosphere can resonate in the same range of frequencies of the telecommunication system. This creates energy absorption peaks which severely affects the power level at the receiver side [88].

The attenuation due to gases, rain, etc., is a concern for long range radio links where

emitting frequencies higher than 20 GHz are employed. This value is away from the frequency range concerned by this thesis which is 2.3 GHz. Additionally, the distances between transceivers in this thesis will be in the order of a few hundreds of meters. As a result, the effect of the attenuation caused by atmospheric gases will not be taken into account.

In a channel where only the path loss phenomenon is present, we know the measured signal at the receiving station must be an attenuated delayed replica of the emitted one. We can suppose a path loss attenuation A. In this situation, the received signal $y(t)$ can be expressed as $y(t) = Ax(t - \tau)$, where τ is the propagation delay $\tau = d/v$, and v is the propagation speed of the wave in the medium.

2.1.2 Multipath

The vacuum propagation scenario in Fig. 2 is an ideal situation which is not valid in most of the cases. In a non ideal propagation scenario, an electromagnetic wave will encounter a multiplicity of obstacles on its way. In this section, we present the three most common wave interaction phenomena. These are: refraction (and reflection), diffraction and scattering. As we can see in Fig. 5, the three phenomena are related with the wavelength of the signal (λ) and the size of the object (A).

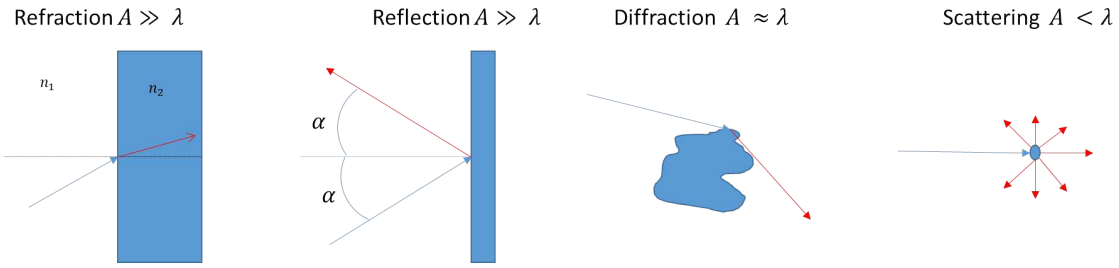

Figure 5: Refraction, Diffraction and Scattering.

- Refraction: this phenomenon is the change in the direction of propagation of a wave when it traverses from one medium to another with different refractive indexes. The refractive index n is defined as the ratio between the speed of light in the vacuum c and the speed of light in the medium v so that $n = c/v$, where $c = 3 \times 10^8$ m/s. In a reflection, the incident wave return to the medium instead of penetrating through the

new one.

- Diffraction: this phenomenon will occur when a wave encounters an obstacle, an aperture or a slit. It was one of the first indicators of the wave nature of the light. Diffraction can be explained through the Huygens - Fresnel principle, which is applicable when a wave encounters an obstacle whose size is in the order of its wavelength. Depending on the geometric characteristics of the obstacle, the diffracted wave will interfere with itself creating a distinctive diffraction pattern. One of the first empirical experiments on this topic was the Young's experiment carried out in 1801 [53].

- Scattering: when an electromagnetic wave propagates through the medium, it usually encounters particles or inhomogeneities on its path. The incident wave will make the local charge of the particle to oscillate, these oscillations will occur mostly in the same frequency of the incident wave. Consequently, the particle will re-radiate a part of the energy of the incident wave while another part will be absorbed. This process is called scattering. In general, scattering occurs when a wave encounters an obstacle whose size is lower than its wavelength.

As a result of the interaction of the electromagnetic waves with the medium, several copies of the original emitted wave will be received at different instants. This is the so called multipath effect, which is sketched in Fig. 6[2]. In the following, each one of the these copies will be a multipath component (MPC). In radio communications, the multipath effect is mostly responsible for making the communication possible in Non Light-of-sight (NLOS) links [7]. In the rest of this thesis, the term *scattered* will make reference to a signal or wave which has been either reflected, diffracted or scattered. In the same way, a *scatterer* will be an element capable of producing a MPC.

In a multipath propagation scenario, each one of the scattered signals will travel a different distance. Moreover, in addition to the path loss experienced, the signal will be also attenuated as a result of the interaction with the matter. Let us to assume some of the

[2]Image from: `http://docwiki.cisco.com/wiki/Wireless_Technologies`

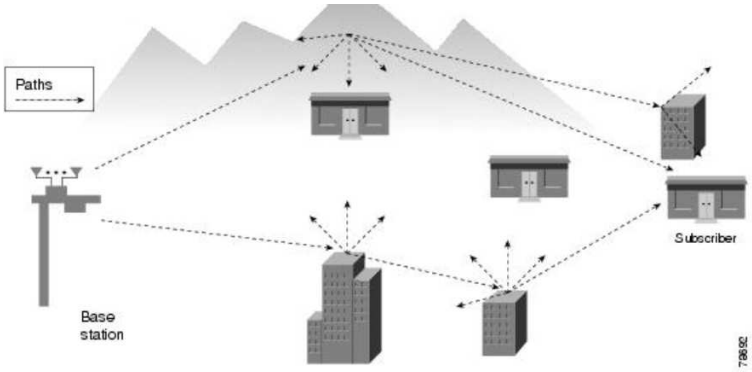

Figure 6: Multipath Propagation Scenario.

MPCs cannot be detected by the receiver, i.e the noise floor of the reception system will mask them. In this situation, the received signal can be expressed in terms of N MPCs as it appears in Eq. 4, where A_i and τ_i respectively represent the global attenuation and propagation delay of the i-th MPC.

$$y(t) = \sum_{i=1}^{N} A_i x(t - \tau_i) \tag{4}$$

2.1.3 The Doppler Effect

So far, we have assumed static transceivers and scatterers. When either the transceivers or the scatterers change their relative position with respect to each other, they will introduce an additional element to be taken into account in the received signal. This new parameter is the Doppler effect.

The Doppler effect is the change of the measured frequency for an observer in relative movement with respect to the source. In order to illustrate this statement, we can consider the harmonic plane wave represented by Eq. 5:

$$A\left(t, \vec{r}\right) = cos\left(\omega t \pm \vec{k}\vec{r}\right) \tag{5}$$

where $\vec{k}$ is the wave vector, i.e the vector which points in the wave propagation direction, and $\vec{r}$ is the position vector between the transceivers. We introduce the change in their relative position by making $\vec{r}$ dependent of time. In that case, we transform Eq. 5 into:

$$\begin{aligned} A\left(t,\vec{r}\right) &= cos\left(\omega t \pm \vec{k}\vec{r}\right) \\ &= cos\left(\omega t \pm \frac{2\pi}{\lambda}\left|\left|r(\vec{t})\right|\right| cos(\alpha(t))\right) \end{aligned} \tag{6}$$

We know the frequency of the wave is the derivative of its phase with respect to the time variable. If we assume the angle between $\vec{k}$ and $\vec{r}$ to change slowly enough so we can make $\alpha(t)$ independent of the time variable as $cos(\alpha(t)) = cos(\alpha)$, we can obtain the frequency ω_f of the received wave as:

$$\omega_f = \frac{\left[\omega t \pm \frac{2\pi}{\lambda}\left|\left|r(\vec{t})\right|\right| cos(\alpha)\right]}{dt} = \omega \pm \frac{2\pi}{\lambda}\frac{\left|\left|r(\vec{t})\right|\right| cos(\alpha)}{dt} \tag{7}$$

As we can see, the wave with angular frequency ω as been transformed into a wave with angular frequency ω_f just taking into account the relative movement between the electromagnetic sources. The second term in Eq. 7 is the so called Doppler frequency. If we are in the case of non accelerated sources, the instantaneous Doppler frequency ω_D can be obtained as:

$$\omega_D = \pm\frac{2\pi}{\lambda}\left|\left|\vec{v}\right|\right| cos(\alpha) \tag{8}$$

If we apply this reasoning to each one of the scattered signals, our received signal will be a completion of delayed attenuated Doppler shifted replicas. For that reason, $y(t)$ in Eq. 4 can be modified as it is shown in Eq. 9, where we account for the Doppler effect.

$$y(t) = \sum_{i=1}^{N} A_i(t)x(t-\tau_i)e^{j\omega_{Di}t} \tag{9}$$

2.1.4 Large, Medium and Small Scale Fading

So far, we have introduced the three most common physical effects involved in wave propagation. As we are about to show, it is possible to establish a relation between them and the measured power profile at the receiving side in a mobile wireless scenario.

As we can see, it is possible to split the measured power profile (Fig. 7) into three phenomena: large, medium and small scale fading.

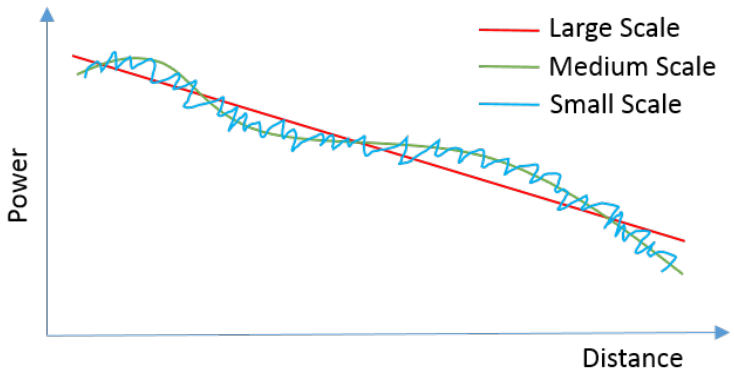

Figure 7: Large, Medium and Small Scale Fading.

- Large scale fading: this phenomenon accounts for the attenuation of the signal because of the distance between the transceivers. In the previous sections, it has been introduced as path loss.

- Medium scale fading: also known as slow fading, this phenomenon is the result of the wave interaction with large objects (buildings, mountains, etc). The diffraction phenomenon is mostly responsible for the behavior of this kind of fading.

- Small scale fading: this is the result of the wave interaction with scatterers (multipath) in mobile environments (Doppler effect). As we will see in section 2.2.4.1, this kind of fading is highly influenced by the Doppler characteristics of the channel.

As we can see, in the last sections we have implicitly introduced these concepts. In the rest of this thesis, we will search for a characterization of the mobile supersonic channel at ISL's testing facility. For this purpose, it will be necessary to find the large, medium and small characteristics of the channel.

2.2 The Channel as a Filter

In the previous section, we have presented the three main phenomena involved in wave propagation in the context of wireless communications, i.e. path loss (attenuation), multipath and Doppler effect.

In the next sections, we will change the way we approach the channel characterization. We will not seek for giving an analytical expression for the channel behavior. Instead, firstly

we will treat the channel as a filter, i.e. an element which acts on the emitted signal (input) and modifies the way it is received (output). In signal processing, a filter is defined in function of its Channel Impulse Response (CIR), concept which will be introduced in section 2.2.1. When working with filters, sometimes it is convenient to work in the frequency domain rather than in the time domain. For this purpose, the Bello's equation will be presented in section 2.2.2. Finally, we will introduce how the channel can be seen as a stochastic process in section 2.2.3.

2.2.1 The Linear Time-Variant Channel

This section will help us to introduce some useful operations which will be later used in the rest of the thesis. We need to define the concept of *linear system*. We have previously mentioned the channel affects the transmitted signal, we can then imagine our channel as an operator L which works on two (or more) functions (real or complex) $x_1(t)$ and $x_2(t)$. The operator L is said to be linear if and only if:

$$L\left[ax_1(t) + bx_2(t)\right] = aL\left[x_1(t)\right] + bL\left[x_2(t)\right] \tag{10}$$

The concept of linearity yields to the principle of superposition, i.e. the output $y(t)$ of a linear system is a linear combination of the inputs:

$$y(t) = L\left[ax_1(t) + bx_2(t)\right] = aL\left[x_1(t)\right] + bL\left[x_2(t)\right] \tag{11}$$

If the variables a and b (which can be either real or complex) are independent of time, we are in the case of a Linear Time Invariant (LTI) system. On the other hand, if these coefficients are time dependent, what we have is a Linear Time-Variant (LTV) system.

It is time to introduce the concept of causality and non-causality. A system is said to be causal if the output at t does not depend on future values of the input. Otherwise the system is non-causal. This property is important because only causal systems are realizable, i.e. they can be implemented in real applications. On the other hand, causal systems show less attracting behavior than the non-causal ones. In other words, a realizable application will approximate the ideal properties of its non-causal equivalent, which only have mathematical

meaning. Remarkably, if a linear causal system is relaxed, i.e. no previously excited, the output is 0 until an input is applied at t_o.

$$y(t) = 0, t < t_o$$

After having presented the linearity and causality concepts, we are in conditions to introduce the Channel Impulse Response (CIR) $h(t, \tau)$.

The impulse response $h(t, \tau)$ is the output of a relaxed linear system after having been excited with the input signal $\delta(t)$. If the channel properties do not change within the period $[t_0 - \alpha/2, t_0 + \alpha/2]$, the CIR can be expressed as $h(\tau)$ in this period of time. We will introduce now the function $\delta(t)$, which is the impulse function also known as Dirac's delta. It presents the following properties:

$$\delta(t) = 0, t \neq 0$$

$$\delta(t) \to \infty, t = 0$$

$$\int_{-\infty}^{\infty} \delta(t)dt = 1$$

The same properties are invariant to a translation in the time axis, which yields to $\delta(t - \tau) = 0$, $t \neq \tau$ and $\delta(t - \tau) \to \infty, t = \tau$. The integral with respect to the t variable is 1 independently of the translation. An interesting result derived from these properties of the impulse function is the possibility of expressing any function in terms of a linear combination of $\delta(t)$ functions.

The product property state: $x(t)\delta(t - \alpha) = x(\alpha)\delta(t - \alpha)$. At the same time, we can define the shifting property as:

$$x(\alpha) = \int_{-\infty}^{\infty} x(t)\delta(t - \alpha)dt$$

Combining the product property and the shifting property we can obtain:

$$x(t) = \int_{-\infty}^{\infty} x(\alpha)\delta(t - \alpha)d\alpha, \alpha \in t$$

We can assume now $x(t)$ is the input of the system L, the output $y(t)$ is then defined:

$$y(t) = L\left[x(t)\right] = L\left[\int_{-\infty}^{\infty} x(\alpha)\delta(t-\alpha)d\alpha\right] = L\left[\int_{-\infty}^{\infty} x(t-\alpha)\delta(\alpha)d\alpha\right] \tag{12}$$

If we impose the extended linearity condition, the order of the system function and the integral operation can be interchanged:

$$y(t) = L\left[x(t)\right] = L\left[\int_{-\infty}^{\infty} x(t-\alpha)\delta(t)d\alpha\right] = \int_{-\infty}^{\infty} x(t-\alpha)L\left[\delta(t)\right]d\alpha$$

For simplicity, the operation $L\left[\delta(t)\right] = h(t,\tau)$ is the already mentioned *impulse response of the channel*, CIR. Additionally, we define the convolution between two functions as the operation:

$$\begin{aligned}(f*g)(t) &= \int_{-\infty}^{\infty} f(t-\alpha)g(\alpha)d\alpha \\ y(t) &= \int_{-\infty}^{\infty} x(t-\alpha)h(\alpha)d\alpha\end{aligned} \tag{13}$$

We conclude the output of the system is the convolution between the input signal and its CIR. We have shown how the CIR completely determines the properties of the channel. Quite often, it is preferable to work in the frequency domain rather than in the time domain. It is possible to demonstrate that Eq. 13 can be turned into Eq. 14:

$$Y(f,t) = H(f,t)X(f,t) \tag{14}$$

where $Y(f,t)$, $H(f,t)$ and $X(f,t)$ are respectively the frequency representation of $y(t)$, $h(t,\tau)$ and $x(t)$. As we can see, the convolution operation has been transformed into a multiplication in the frequency domain. The rigorous analysis of linear systems can be object of a quite large document, for a complete understanding of these systems and their implications in the signal processing, please refer to [6].

As we can notice, in the last section we implicitly assumed the principle of superposition, i.e. we presented separately the path loss, the multipath and Doppler effect. At the end of section 2.1, we obtained an expression for the received signal in function of these phenomena.

In this section, we have shown how if the channel is treated as a filter, all these effects are contained in the CIR. In some case, we also mentioned the convenience of working in the frequency domain rather than in time domain. In the next section, we will clarify this question by presenting the Bello's functions. The channel then will be no longer treated in function of the implied physical phenomena but treated as a filter where the CIR is required to be characterized.

2.2.2 The Bello's Functions

This set of functions are used to describe a linear time-variant channel in both time and frequency domains. They were firstly introduced by P. Bello in 1963 [14]. They are four: the time-variant impulse response $h(t, \tau)$, the Doppler-variant impulse response $s(\tau, f')$, the time-variant fransfer function $H(f, t)$ and the Doppler variant transfer function $T(f, f')$.

2.2.2.1 The time-variant impulse response

We have seen in the previous sections how the channel affects the received signal. What we obtain at the receiver side is a linear combination of attenuated Doppler shifted replicas of the emitted signal $x(t)$. As we discussed in the previous section, we can express the output signal $y(t)$ as the result of filtering the input $x(t)$.

An interesting manner of representing the CIR is fixing the time variable at a determined instant t_0 in order to obtain a representation of the power contribution of each MPC (multipath component), $|h(t_0, \tau)|^2 = |h(\tau)|^2$. In other words, we can represent the power of each one of the N MPCs in terms of its delay at a fixed time instant t_0. This way of representing the multipath effect is called the Power Delay Profile (PDP).

The PDP is one of the first elements to be defined in every channel model as it gives a clear representation of how the received power is distributed over the delay. It is clear then the PDP is a function of τ, which is defined as the time difference between the emitted signal and the received one as we defined in Eq. 4. An hypothetical PDP ($P(\tau)$) is shown in Fig. 8. This element gives information of some important channel properties as they are the mean Excess Delay (τ_e), RMS delay spread (τ_{RMS}), Maximum Excess Delay (τ_m). They

are respectively defined below:

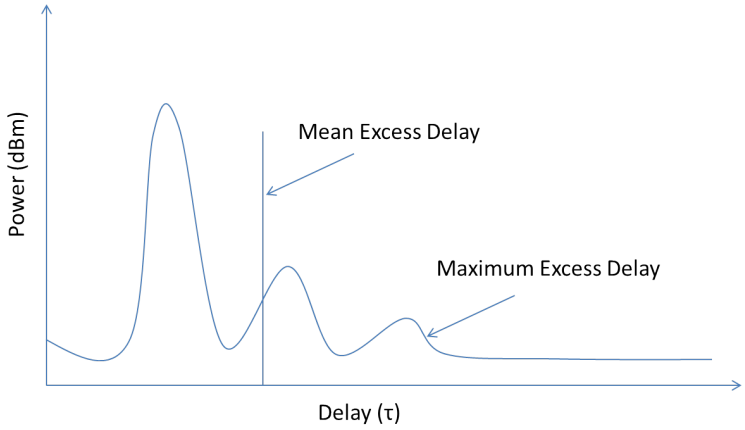

Figure 8: Power Delay Profile.

- Mean Excess Delay τ_e

  Formally, this parameter is the first moment of the PDP (Eq 15). It can be seen as the center of mass of the graph.

$$\tau_e = \int \tau PDP(\tau) d\tau \tag{15}$$

- RMS Delay τ_{RMS}

  Defined as the root of the second central moment of the PDP (Eq. 16), this parameter accounts for the standard deviation about the mean excess delay and gives an outlook of the importance of the multipath effect. The parameter τ_{RMS} is intrinsically linked to the coherence bandwidth as we will show in Sec. 2.2.4. This parameter also related to the Inter-Symbol-Interference (ISI).

$$\tau_{RMS} = \left[\int (\tau - \tau_e)^2 PDP(\tau) d\tau \right]^{\frac{1}{2}} \tag{16}$$

- Maximum Excess Delay

  This is the delay of the most delayed detectable path.

If we consider the channel as a filter, we can simplify its construction by considering only a discrete number of MPCs. Following this reasoning, the channel can be seen as a Tapped Delay Line (TDL) structure found in Fig. 11. In this construction, the taps are used in order to model the multipath and Doppler properties of the propagation channel. Let us to assume this filter is densely constructed. The word *densely* means we can place as many scatterers (channel taps) as we want. In this case, the delay (τ) is not a discrete variable but a continuous one in the interval $\tau \in [t, t+\epsilon]$. Following this reasoning, we can express the output $y(t)$ of this filter as:

$$y(t) = \int_{-\infty}^{t} x(t_0)h(t_0, t)dt_0 \tag{17}$$

The propagation delay can be expressed as τ as $\tau = t - t_0$, i.e. the time difference between the instant t_0 at when we excite the channel and the current time t. In this case Eq. 17 operation becomes:

$$y(t) = \int_{0}^{\infty} x(t-\tau)h(\tau, t)d\tau \tag{18}$$

The lower limit of the integral comes from the causality property of the channel, $h(t, \tau) = 0$ for $\tau < 0$. The upper limit means ideally we can receive attenuated copies coming from very long distances. In practical cases these will be undetectable because of the noise floor of the reception system. For that reason the upper limit can be also τ_m as previously defined.

2.2.2.2 Time-variant transfer function

The convolution operation represented in Eq. 18 is equivalent to a multiplication in the frequency domain. Using this property, $y(t)$ can be expressed through an inverse Fourier transform. The time-variant transfer function $H(f, t)$, is the Fourier transform of the time-variant impulse response with respect to the delay variable. It is used as it appears in Eq. 19 in order to obtain $y(t)$. In this case, $X(f)$ also represents the Fourier transform of the emitted signal $x(t)$.

$$y(t) = \int_{-\infty}^{\infty} Y(f)e^{j2\pi ft}df = \int_{-\infty}^{\infty} X(f)H(f,t)e^{j2\pi ft}df \tag{19}$$

2.2.2.3 Doppler-variant impulse response

Neither the function $h(t,\tau)$ nor $H(f,t)$ can directly describe the channel in function of its Doppler properties. For this purpose, we can define the Doppler-variant impulse response $s(\tau, f')$ as it appears in Eq. 20, where f' is the Doppler frequency variable. As we can see, the Fourier transform of $h(\tau,t)$ with respect to the t variable allows us to relate each delayed component with its Doppler shift.

$$s(\tau, f') = \int_{-\infty}^{\infty} h(\tau,t)e^{-j2\pi f't}dt \tag{20}$$

It is possible to express $y(t)$ in terms of $s(\tau, f')$

$$y(t) = \int_{0}^{\infty} x(t-\tau)h(\tau,t)d\tau = \int_{0}^{\infty} x(t-\tau)\left[\int_{-\infty}^{\infty} s(\tau,f')e^{j2\pi f't}df'\right]d\tau \tag{21}$$

$$y(t) = \int_{0}^{\infty}\int_{-\infty}^{\infty} x(t-\tau)s(\tau,f')e^{-j2\pi f't}df'd\tau \tag{22}$$

The previous equations describe explicitly the dispersive nature of the channel as they include both τ and f' variables.

Following the same reasoning as in section 2.2.2.1, it is possible to represent the power of each multipath component in function of its Doppler behavior. Such representation is called Doppler Spectrum, $S(f') = |s(\tau_0, f')|^2$. For instance, depending on the configuration of the propagation scenario, it is possible to obtain an analytical expression for the Doppler spectrum in some specific propagation scenarios. This is the case for Rayleigh [32] channel models and the Gaussian shaped Doppler spectrum usually found in satellite communications [15, 75]. In some other practical situations, the Doppler spectrum can be constructed through a superposition of classical Doppler spectra [4]. In Fig. 9, we show the typical Doppler spectrum for a Rayleigh channel.

We can define some parameters associated with the Doppler spectrum $S_{hh}(f)$. For Example, the mean Doppler Shift (f_e), the RMS Doppler Spread (f_{RMS}) and the maximum

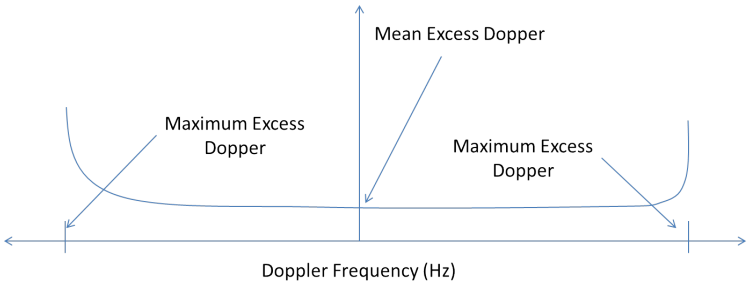

Figure 9: Doppler Spectrum.

excess Doppler (f_m):

- Mean Doppler Shift f_e

  This parameter is the analogous to τ_e defined in Eq. 15 and represents the first moment of the Doppler Spectrum $S(f')$.

$$f_e = \int f' S(f') df' \tag{23}$$

- RMS Doppler Spread f_{RMS}

  Defined as the root of the second central moment of the Doppler Spectrum (Eq. 24), this parameter accounts for the standard deviation about the mean Doppler shift and gives an outlook of the importance of the Doppler effect. The parameter f_{RMS} is intrinsically linked to the coherence time as we will show in Sec. 2.2.4. This parameter also related to the Inter-Carrier-Interference (ICI).

$$f_{RMS} = \left[\int (f' - f_e)^2 S(f') df' \right]^{\frac{1}{2}} \tag{24}$$

- Maximum Excess Doppler f_m

  The maximum measurable Doppler shift.

2.2.2.4 Doppler-variant transfer function

This function $T(f, f')$ is used to relate the spectra of both output and input signals. It is defined as the two dimensional Fourier transform of $h(\tau, t)$.

$$T(f, f') = \int_{-\infty}^{\infty} \int_{0}^{\infty} h(\tau, t) e^{-j2\pi(f't + f\tau)} d\tau dt \tag{25}$$

We can graphically represent the Bello's functions as it appears in Fig. 10. This figure is useful in order to rapidly relate through the Fourier transform a function with its pair.

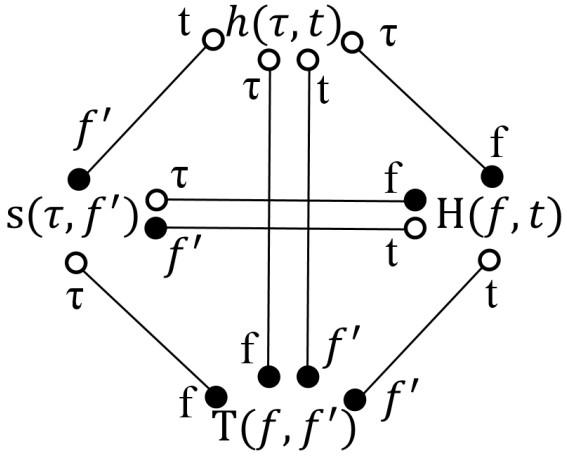

Figure 10: Bello's functions.

2.2.3 The channel as a stochastic process

In a real scenario, the random nature of the channel makes the Bello's functions to become stochastic processes. A stochastic process $\mu(t, s)$ is a function of t (time) and s, a random variable. They have the following properties according to the treatment given to the variables involved [82]:

- If t is a real variable and s is a random variable, then $\mu(t) = \mu(t, s)$ represents a family of sample functions.
- If t is a variable and $s = s_0$ (a constant), then $\mu(t) = \mu(t, s_0)$ is a realization, i.e. a sample function of the stochastic process.
- If $t = t_0$ and s is a random variable, then $\mu(t_0)$ is also random variable.
- If $t = t_0$ and $s = s_0$, then $\mu(t_0)$ is a number, real or complex.

It is out of the scope of this thesis to give a rigorous treatment of stochastic processes (for this purpose, see [13]). However, it will be useful to give some intuitive guidelines to

understand them. We can introduce how the channel behaves as a stochastic process with the help of the time-variant impulse response $h(t, \tau)$. Even though we can extend the following reasoning to any of the Bello's functions. Because the random nature of the channel, τ will be treated as the random variable as it accounts for the propagation delay, which is not determined as we will be assuming a certain relative movement between the transceivers and scatterers.

If we continue by examining the channel response $h(t, \tau)$ at $\tau = \tau_0$, what we obtain is the channel behavior $h(t) = h(t, \tau_0)$ only for the delayed attenuated Doppler shifted replicas whose propagation delay is $\tau = \tau_0$. In other words, we are only examining one of the sample functions possible.

If we decide to examine the channel at $t = t_0$, the value of $h(t_0)$ will depend on the random variable τ. It is reasonable to assume the channel response at t_0 to be also a random variable, i.e. we neither know a the a priory propagation delay τ nor the channel response at τ. Finally, if we are interested in examining the channel at instant t_0 for the multipath components arriving at τ_0, what we will obtain is a numeric value of the sample function $h(t, \tau_0)$ at t_0.

In the following, we will use two operations usually employed when working with stochastic processes. The first one is the expected value operation $E\{\dot{}\}$, it can be defined as:

$$E\{\mu(t_1)\} = \int \mu_1 p_\mu(\mu_1)\, d\mu_1 \tag{26}$$

where μ_1 is the random variable assigned to a stochastic process at instant t_1 with density probability function $p_\mu(\mu_1)$. The second operation we need to define for the next sections is the autocorrelation of two random variables $r_{\mu\mu}(t_1, t_2)$, which is defined as:

$$r_{\mu\mu}(t_1, t_2) = E\{\mu^*(t_1)\mu(t_2)\} = \int\int \mu_1 \mu_2 p_{\mu_1\mu_2}(\mu_1, \mu_2) d\mu_1 d\mu_2 \tag{27}$$

where the asterisk represents the conjugate of the random variable and $p_{\mu_1\mu_2}(\mu_1, \mu_2)$ is the joint probability function of the random variables μ_1, μ_2.

2.2.3.1 Wide Sense Stationary Uncorrelated Scattering Processes

A stochastic process is said to be Wide Sense Stationary (WSS) if it fulfills the following two conditions:

$$E\{\mu(t)\} = m_\mu \tag{28}$$

where m_μ is a constant. The other condition to be fulfilled is:

$$r(t_1, t_2) = r(t_2 - t_1) = r(\tau) \tag{29}$$

which means the autocorrelation of the process depends only on the time difference $t_2 - t_1$. Treating the CIR as a stochastic process, the channel will be WSS if it respects:

$$r_{hh}(\tau_1, \tau_2; t, t + \tau) = r_{hh}(\tau_1, \tau_2; \tau) \tag{30}$$

This property accounts for the statistical independence of the different scattered Doppler shifted replicas at the receiver. On the other hand, the Uncorrelated Scattering (US) property accounts for the statistical independence of the scattered replicas with respect to its propagation delay. For an US channel, we will obtain the following autocorrelation function:

$$\begin{aligned} r_{hh}(\tau_1, \tau_2; t_1, t_2) &= E\{h^*(\tau_1, t_1)h(\tau_2, t_2)\} \\ &= \delta(\tau_1 - \tau_2)S_{hh}(\tau_1; t_1, t_2) \end{aligned} \tag{31}$$

The WSSUS channel model will have to account for both Eq. 30 - 31, leading to:

$$r_{hh}(\tau_1, \tau_2; t, t + \tau) = \delta(\tau_2 - \tau_1)S_{hh}(\tau_1, \tau) \tag{32}$$

Nowadays, the WSSUS assumption is the one adopted for almost every channel model in mobile applications we can find. Usually, these models are presented in the form of Tapped Delay Line (TDL) models where the time-variant gain coefficients are now uncorrelated. Additionally, these parameters are modeled as colored Gaussian processes. We can find examples of TDL based models in [23, 104, 55]. The general form of a TDL model is shown in Fig. 11.

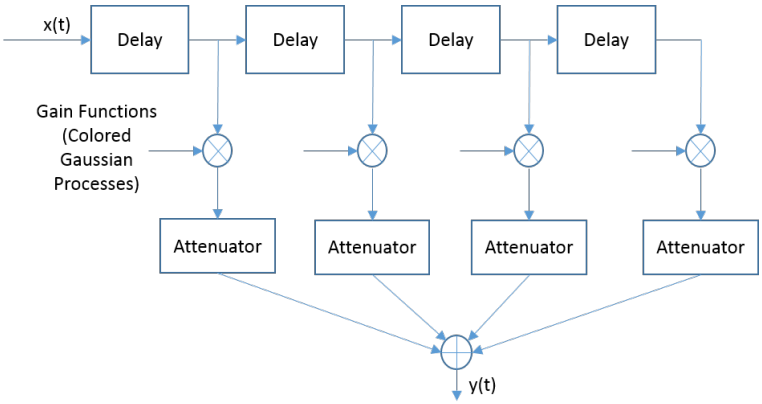

Figure 11: Tapped Delay Line Wideband Channel Model.

2.2.4 Time & Frequency Selectivity

In previous sections we have shown how the multipath and Doppler effects have an impact in the channel properties. In this section, we will classify the channel in function of its behavior in time and frequency by linking the channel properties with the multipath and Doppler effect.

2.2.4.1 Frequency Selectivity

The frequency selectivity of a channel is related with its coherence bandwidth (B_c). This parameter is defined in function of the multipath properties of the channel. In general, B_c is approximated as $B_c \approx 1/\tau_{RMS}$.

In digital mobile radio systems, the information is transmitted in modulated symbols. These symbols are time limited over a period (T_{sym}). When the symbol rate $f_{sym} = 1/T_{sym}$ is much smaller than B_c, the channel is said to be *frequency non-selective*. This result is valid as long as τ_{RMS} does not exceed 10 percent to 20 percent of the symbol interval. When these conditions are not fulfilled, the channel is said to be *frequency selective*. Signals transmitted over frequency-selective channels suffer from ISI, i.e. a received symbol is affected by the previously transmitted ones.

We can define a classification of the emitted signals in function of the coherence bandwidth concept. On the one hand we have narrowband signals, these are signals whose bandwidth W is smaller than the coherence bandwidth of the channel in which they are

transmitted. If this condition is fulfilled, we say the signal has been transmitted over a flat fading channel. On the other hand, a signal is said to be wideband if its bandwidth is larger than the channel coherence bandwidth. In this case, the signal is said to be transmitted over a fading channel. These concepts are graphically shown in Fig. 12.

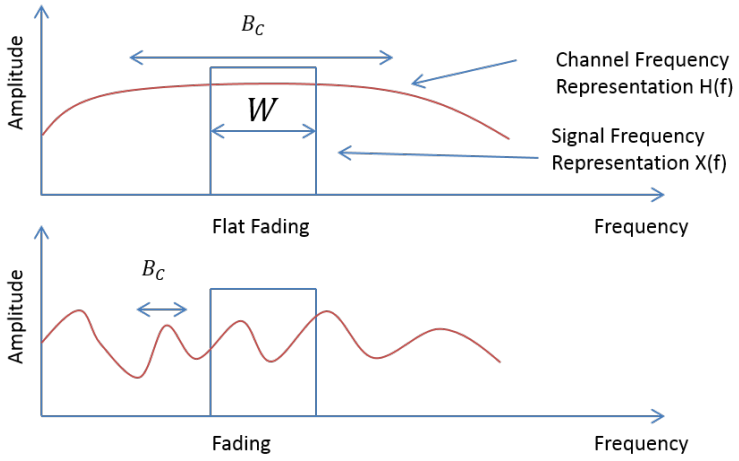

Figure 12: Frequency selectivity.

An equalizer is an element of the transmission chain in charge reconstructing the spectrum of the received signal. Generally speaking, this element will be easier to implement in flat-fading channels than in fading channels. This concept will be exploited in chapter 3 when defining a channel modeling strategy. A summary of the flat fading conditions can be found below:

- $f_{sym} << B_c$, alternatively we can establish $0.1 < \tau_{RMS}/T_{sym} < 0.2$
- no ISI
- simple equalizer

2.2.4.2 Time Selectivity

The time selectivity of a channel is related to the coherence time (T_c). This variable relates the Doppler effect with the time we can consider a channel to be stationary. It is obtained as $T_c = 1/f_{RMS}$. When the symbol period is much smaller than the coherence time ($T_{sym} << T_c$) the signal is said to be transmitted over a slow fading channel. In such situation, the

frequency of the channel envelope's oscillations is small compared to the symbol period. The slow fading is more related to shadowing (large obstacle obstruction) rather than a high Doppler spread because of the relative speed between transceivers and the interference caused by scatterers. In conclusion, in a slow fading situation we find:

- Low Doppler Spread ($T_{sym} << T_c$).
- The oscillations of the channel's envelope amplitude can be considered to be constant during the symbol transmission.

On the contrary, the coherence time can be much smaller than the symbol period ($T_{sym} >> T_c$). In this case, the oscillations of the channel's envelope amplitude will be high compared to the symbol period so the channel cannot be considered constant over the symbol transmission. The fast fading situation is more related to the speed of the transceivers and the multipath components. In a fast fading situation we find:

- High Doppler Spread ($T_{sym} >> T_c$).
- The oscillations of the channel's envelope amplitude cannot be considered to be constant during the symbol transmission.

The slow and fast fading channels are respectively also respectively known as time non-selective or time selective channels.

2.3 The Need for Channel Sounding

In the last sections, we have treated the channel either from the point of view of the physics or from the signal processing approach. In this section, we will present an empirical method to characterize the channel.

Channel sounding is an empirical method for characterizing the channel. In channel sounding, the channel is excited with a receiver-known test signal. The changes on this signal after having propagated through the channel are analyzed at the receiver side with the objective of extracting the channel properties, i.e. the CIR.

Generally speaking, we can classify channel sounders in two categories: narrowband channel sounders and wideband channel sounders. The first ones make use of a narrowband exciting signal which propagates through a flat fading channel. The channel parameters usually obtained are the path loss exponent, the propagation delay, signal angle of arrival (AoA) and the Doppler shift. On the contrary, wideband channel sounders excite the channel with a wideband signal which propagates through a fading channel. This kind of approach allows to characterize all the previous channel properties plus the multipath and Doppler properties of the MPCs. This technique permits a better insight into the channel behavior.

In sections 2.3.1 - 2.3.2, we will present the basic elements a channel sounder presents. Additionally, some popular channel sounding techniques in conjunction with already developed channel sounders can be found here.

2.3.1 Narrowband sounding techniques

With this kind of sounding techniques, the multipath properties of the channel are not studied being the path loss, the Doppler shift and the propagation delay of the LOS component the principal parameters to study. Depending on the antenna configuration, for example, by the use high directive antennas, the AoA of the test signal can be also studied. As we have shown in section 2.2.4.2, when the channel coherence bandwidth is much greater than the signal bandwidth, the condition of narrowband communication is fulfilled. In practice, in most of the cases this condition is achieved if the channel is excited with a single tone [80].

In narrowband channel sounding, the emitter excites the channel with a single tone $s(t) = A_0 cos(\omega t + \phi_0)$. At the receiver, the signal $y(t) = K A_0 cos((\omega - \omega_D)t + \phi_r(t))$ can be used for channel characterization, being K the attenuation, ω_D is the Doppler shift due to the relative movement of the transceivers and $\phi_r(t)$ is the time-varying signal phase.

Even though this technique may appear limited with respect to the channel parameters which can be analyzed, with a proper equipment it can be used in a wide range of applications. For example, the transcontinental radio link can be studied. An example of this kind of narrowband channel sounding is presented in [46], where a characterization of the ionospheric channel between the Antarctica and Spain is performed. In this study, the transmitter

system consists on a monopole antenna transmitting equally spaces tones from 2 to 30 MHz in intervals of 500 kHz. Each tone was transmitted during 10 s being 20 W the transmission power of the system. Because of the unavailability of path resolving of this kind of sounder, the Signal-to-Noise Ratio (SNR) at the receiver side was the main studied parameter. The scheme of the the transmitter for this experiment is shown in Fig. 13.

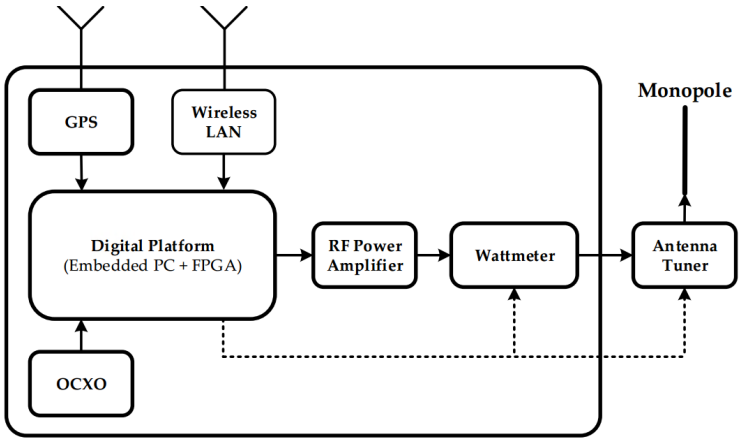

Figure 13: Scheme of the Ionospheric Channel Sounder [46].

2.3.2 Wideband Channel Sounding Techniques

In situations where the narrowband condition is not fulfilled, i.e. the coherence bandwidth of the channel is smaller than the bandwidth of the transmitted signal, a wideband channel sounding is required. We can group the channel sounders of this category with respect to the kind of testing signal they employ [80]. The most popular are: periodic pulses, pulse compression sounders, convolution matched-filter sounders and swept time-delay crosscorrelation (STDCC) sounders.

2.3.2.1 Periodic Pulse Sounding Method

A sounder which uses this method tries to emulate the mathematical reasoning presented in section 2.2. In practice, an impulse $\delta(t)$ cannot be generated. Instead, what we can do is to transmit a short duration pulse as exciting signal. In such a case, the measured signal at the receiver approximates the convolution operation of the CIR with the impulse signal. The time-varying channel behavior is then also approximated by transmitting a series of equally spaced short duration pulses. The period T_s between two consecutive pulses has to be short

enough to allow the tracking of each individual propagation path with a certain precision, which is defined by the user requirements. Additionally, this period has to be larger enough to ensure the complete decaying of all MPCs. This is due to the necessity of analyzing an ISI free signal. In these sounders, the Doppler characterization is achieved by coherent demodulation of the received signal. The concept is illustrated in Fig. 14.

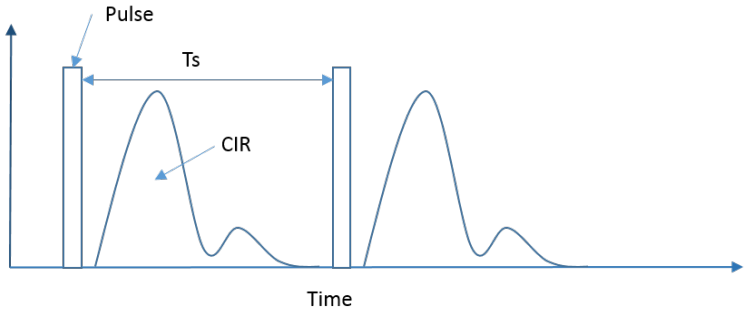

Figure 14: Periodic Pulse Sounding Process.

In [84] we can find an example of a sounder using this technique in an industrial environment. Pulses of 10 ns were transmitted being $T_s = 500$ ns. The output power was 14 dBm at 300 MHz. An additional example of this technique can be found in [21].

2.3.2.2 Pulse Compression Techniques

Pulse compression techniques are based on the spectral properties of white Gaussian noise (WGN). The theoretical two sided WGN power spectral density as well as its correlation function is shown in Fig. 15.

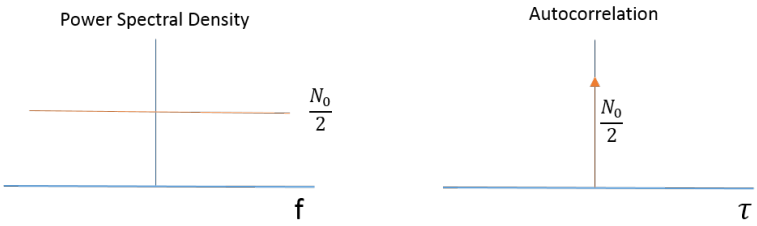

Figure 15: WGN Spectral Density and Autocorrelation Function.

Using the LTV channel properties we introduced in section 2.2.1 and the expected value operation defined in section 2.2.3, it is possible to establish a relation between the WGN spectral density and the CIR. Starting from:

$$E\left[n(t)n^*(t-\tau)\right] = R_n(\tau) = \frac{N_0}{2}\delta(\tau) \tag{33}$$

We can obtain the crosscorrelation between the channel response to the WGN signal ($w(t)$) and the WGN signal itself as shown in Eq. 34

$$E\left[w(t)n^*(t-\tau)\right] = E\left[\int h(\zeta)n(t-\zeta)n^*(t-\tau)d\zeta\right] \tag{34}$$

The extended linearity condition can be applied allowing the interchange of the $E\{\}$ and the integral operators:

$$E\left[\int h(\zeta)n(t-\zeta)n^*(t-\tau)d\zeta\right] = \int h(\zeta)E\left[n(t-\zeta)n^*(t-\tau)\right]d\zeta \tag{35}$$

$$= \int \frac{N}{2}\delta(\tau)h(\zeta)d\zeta = \frac{N_0}{2}h(\tau) \tag{36}$$

As we have seen, the crosscorrelation operation in Eq. 35 will be the CIR scaled by the power spectral density of the WGN test signal. In practice, it is not possible to generate a pure WGN signal. One of the solution is to use signals which approximate the properties of the WGN in a certain frequency band. One of the signals that fulfill this condition are the so called maximal-length pseudo-random binary sequences. They are known in the literature as m-sequences or alternatively PN sequences [74].

An example of a channel sounder using this technique can be found in [54]. The PN sequences were generated using feedback shift registers. The carrier frequency of the system was 2.154 GHz according to the UMTS range of frequencies. In this case, the chip rate of the m-sequences could vary between 2.5 MHz and 60 MHz. With the objective of allowing Doppler characterization, the period t_{IR} between the emission of one PN sequence and another was chosen to respect:

$$f_{Dmax} = \frac{1}{2t_{IR}} \tag{37}$$

where f_{Dmax} is the maximum expected Doppler shift.

2.3.2.3 Convolution Matched-Filter Techniques

This kind of sounders implement the sounding process introduced in section 2.3.2.2 with the help of matched filters to the test signal (CMF). We know the signal at the receiver $y(t)$ is a superposition of attenuated Doppler shifted delayed replicas of the PN transmitted m-sequence $s(t-\tau)$. We can consider only the N relevant replicas in terms of power. In this case, the received signal $y(t)$ can be expressed as

$$y(t) = \sum_{i=0}^{N} a_i e^{j\theta_i} s(t-\tau_i) \tag{38}$$

The impulse response of the CMF is given by $h_{CMF}(\tau) = s(-\tau)$. The crosscorrelation output in Eq. 34 is then modified as it follows

$$\begin{aligned} E\left[y(\zeta)h_{CMF}(t-\zeta)\right] &= \int \sum_{i=0}^{N} a_i e^{j\theta_i} s(\zeta-\tau_i)s(\zeta-t)d\zeta \\ &= \sum_{i=0}^{N} a_i e^{j\theta_i} \int s(\zeta-\tau_i)s(\zeta-t)d\zeta \\ &= \sum_{i=0}^{N} a_i e^{j\theta_i} R_s(t-\tau_i) \end{aligned} \tag{39}$$

What we obtain is a superposition of N attenuated, Doppler Shifted and delayed replicas of the autocorrelation function $R_s(\tau)$. For this reason, the minimum resolvable path is determined by the width of the autocorrelation peak, which is twice the chip period T_c for a PN sequence constructed with rectangular chips.

An interesting real implementation of this sounding procedure at 2.4 GHz can be found in [58]. In this article, the authors implement a channel sounder by using GNU Radio software and URSP devices. These elements will be described in Chapter 3.

2.3.2.4 Swept time-delay Crosscorrelation Method

The first use of STDCC sounders can be found in [34]. In this technique, the channel sensing signal is also a binary m sequence as in the previous methods. However, at the receiver the incoming signal will be correlated with a lower frequency replica. For that reason, the autocorrelation output in Eq. 35 will be scaled in time. In order to illustrate this concept, we

can define the following test signal $s(t)$ (Eq. 40) as the m-sequence $m(t)$ BPSK modulated. In this situation, $m(t)$ can switch between 0 and 1. The bit rate of m(t) will be called f_e.

$$s(t) = m(t)cos(2\pi F_c t) \tag{40}$$

Because of the influence of the channel, the received signal $s'(t)$ can be assumed to adopt the form in Eq. 41:

$$s'(t) = \sum_{i=0}^{N} a_i m(t-\tau_i)cos(2\pi F_c t + \phi_i) \tag{41}$$

The $s'(t)$ signal can be down-converted to f_c and their in-phase I and quadrature Q obtained by splitting the analysis process in two parts: one for the $I(t)$ signal (I component) and the other one for a 90^o phased replica (Q component):

$$\begin{aligned} I(t) &= \sum_{i=0}^{N} a_i m(t-\tau_i)cos(2\pi f_c t + \phi_i) \\ Q(t) &= \sum_{i=0}^{N} a_i m(t-\tau_i)sin(2\pi f_c t + \phi_i) \end{aligned} \tag{42}$$

The I and Q components can be mixed with a down-clocked and modulated version of $s(t)$ as $g(t) = m`(t)cos(2\pi f_c t + \phi_i)$ where the bit rate for $m`(t)$ will be f_r. The k factor in this kind of sounding is defined as:

$$k = \frac{f_e}{f_e - f_r} \tag{43}$$

Finally, they are also filtered in order to remove the f_c component:

$$\begin{aligned} RI(t) &= \sum_{i=0}^{N} a_i m(t-\tau_i)m`(t)cos(2\pi f_c t + \phi_i)cos(2\pi f_c t) \\ &= \sum_{i=0}^{N} a_i m(t-\tau_i)m`(t)cos(\phi_i) \\ RQ(t) &= \sum_{i=0}^{N} a_i m(t-\tau_i)m`(t)sin(2\pi f_c t + \phi_i)cos(2\pi f_c t) \\ &= \sum_{i=0}^{N} a_i m(t-\tau_i)m`(t)sin(\phi_i) \end{aligned} \tag{44}$$

The output signals are found by integrating both RI and RQ signals.

$$\begin{aligned} OI(t) &= \sum_{i=0}^{N} a_i \left[\int_{t-T}^{t} m(t-\tau_i) m^{`}(t) dt \right] cos(\phi_i) \\ &= \sum_{i=0}^{N} a_i R(\frac{t}{k} - \tau_i) cos(\phi_i) \\ OQ(t) &= \sum_{i=0}^{N} a_i \left[ \int_{t-T}^{t} m(t-\tau_i) m^{`}(t) dt \right] sin(\phi_i) \\ &= \sum_{i=0}^{N} a_i R(\frac{t}{k} - \tau_i) sin(\phi_i) \end{aligned} \tag{45}$$

2.3.3 Discussion on Channel Sounding Techniques

The necessity for high throughput transceivers in the field of instrumented projectiles is causing the abandon of the single carrier modulation techniques. Thanks to the miniaturized electronics currently available, applications like video transmission from projectiles is being possible [42]. As a result, the general trend is to migrate the single carrier communication scheme to multicarrier systems. This is due to their robustness in frequency selective channels [100, 63]. Generally speaking, a multicarrier system will imply the use of a wideband channel model. For that reason, in this thesis we need to perform a wideband channel characterization. In the previous section, we have presented a set of popular channel sounding strategies. It is time to clarify why we need to propose an alternative channel sounding technique.

In [84, 21] two channel sounders based on the periodic pulse method are presented. This sounding method is the simplest one: only a short duration sensing signal is transmitted in equally spaced time intervals. The duration of this time interval has to be greater than the maximum delay spread of the channel. The simplicity of this technique is attractive. However, as we can see in [90], commonly several responses need to be averaged in order to improve the quality of the noisy received signal. Additionally, the generation of high-power short pulses can introduce undesired components (non-linearities in the power amplifiers) which can be confused with non-existent multipath components.

The autocorrelation properties of the m-sequences make these kind of sounders quite

popular. Apart from the already cited paper [54], we can find a good example of how these sounders work in [29]. In this paper, the authors showed how they managed to perform Ultra Wideband (UWB) channel sounding in the frequency range from 3.6 GHz to 6 GHz in an indoor scenario. However, the bulky complex hardware involved in these sounders make them more suitable for propagation scenarios where both emitter and receiver are static in their positions. A situation which is not fulfilled in our case.

The convolution matched filter technique was also utilized by Bajwa in [11]. A mobile radio channel sounding in the city of Birmingham was carried out in the band of 436 MHz. The delay resolution of the system was 0.1 μs. Even though this technique has proven to be useful in the channel characterization, it presents a disadvantage to us: the presence of the matched filter which have to be implemented either by software or hardware. Effectively, we are already constrained by other elements (size, power, space, etc.). With the objective of keeping our channel sounder methodology as simple as possible, it is not convenient the inclusion of a new element in the sounding process.

The use of STDCC channel sounders is widely spread. We can find applications from outdoor static scenarios [30], artificially created multipath scenarios [56] to satellite applications [51]. As far as we are concerned, they present the same disadvantages of the previous described sounding methods: the non-embbedability of the hardware used in projectile applications.

As a conclusion, the presented channel sounding techniques cannot be employed in the context of this thesis. What we need, is a technique permitting to sound the channel fast enough to characterize its Doppler behavior, a requirement set by the supersonic flying speed of an instrumented projectile. Additionally, it should be a wideband channel sounding. Effectively, multicarrier transmission techniques will be used in the future at ISL. Finally, with the objective of keeping the budged under control, the proposed sounding technique will have to be implemented with commercial off-the-self embeddable hardware.

2.4 Conclusion: Special Requirements and Constraints of this Thesis

The wireless channel and the elements defining its properties have been introduced in this chapter from section 2.1 to section 2.2. Firstly, we started by describing the most common physical effects in radio propagation. Secondly, we showed how the channel modeling can be approached from the point of view of the signal processing. Subsequently, we introduced the importance of treating the channel as a stochastic process, a condition determined by the random nature of the wireless mobile propagation scenario.

In section 2.3, an empirical method to perform channel modeling was presented, i.e. channel sounding. Several channel sounding techniques were presented. Unfortunately, the channel sounders implementing these techniques cannot be used in this thesis with the objective of characterizing the propagation channel in projectile applications. For that reason, the first one of the objectives of this thesis is the development of a channel sounding technique to be used the field of projectile communications. Our particular requirements:

- Speed: the channel sounder should be able to produce enough CIRs estimations in order to characterize a Doppler shift of several kHz.
- Embeddability: the channel sounder should be small enough for its testing in real conditions, i.e. fired within a projectile.
- Reliability: the channel sounder should be able to survive the high acceleration in the barrel of the cannon.
- Flexibility: the channel sounder should be able to be employed in a multiplicity of environments.

In the next chapter 3, we will present the instruments we had at our disposition at the beginning of the thesis and how they will contribute to the achievements of our objectives. The proposed channel sounding methodology will also be presented along with its hardware implementation. In the next chapters, the developed prototype will be employed to construct

a channel model for the propagation scenario where the firing tests are carried out at ISL. This channel model represents the second objective of the thesis.

CHAPTER III

INSTRUMENTS & FACILITIES. DEVELOPMENT OF AN EMBEDDED CHANNEL SOUNDER

We finished chapter 2 after having detailed the requirements and constraints we have to face in channel modeling. In order to be able to characterize the channel for projectile applications at ISL, first we have to make an inventory of the already available resources (instruments, facilities, etc) we can use for achieving this objective. As in any other engineering problem, this is an important step to be done before making a realistic proposition for the missing instruments. This chapter was structured in four sections:

In section 3.1, we will detail the material resources available. From software to hardware tools, the main characteristics for each one of the items will be mentioned.

As we mentioned in section 2.4, in order to experimentally characterize the wireless channel we need to make use of a channel sounder. Having in mind the lack of channel sounders suitable for our application, we need to develop our own channel sounding technique. For this reason, section 3.2 is dedicated to this task. The proposed channel sounding technique will be presented as follows: in section 3.2.1, its key elements are given. Not only its advantages but also the weak points will be detailed. After having presented the main elements of our channel sounding technique, we continue by detailing our channel sounding methodology in section 3.2.2.

In section 3.3, the conceived channel sounder prototype is presented. This instrument will allow us to characterize the channel in real conditions.

Finally, the required steps before testing our channel sounder will be given in section 3.4.

3.1 Laboratory Tools & Facilities

Before starting the development of any project, it is necessary to know the available tools in order to approach the task in a realistic manner. Concerning the objectives of the thesis exposed in the introductory chapter, a determined set of tools is required in order to study the propagation channel. In this section, we will enumerate all the tools and facilities we could use at the beginning of the thesis. Additionally, a minimum of knowledge about its operation will be given.

In a first approach in channel modeling, it is common to use software propagation simulators as we can see in [61, 44, 59]. In our case, we can use a the XLIM developed software presented in 3.1.1. However, some elements which can affect the wave propagation phenomenon cannot be easily simulated with this software. For example, this is the case of the spinning of the projectile, subject which will be treated in chapter 4. If we want to reproduce the spinning of a projectile at the laboratory, we will have to use the instrument presented in section 3.1.2.

When passing from simulation to real testing, we needed a flexible equipment in order to test different techniques as easily and quickly as possible. Designing a radio system from scratch is not the objective of this thesis. For that reason, we needed to make use of some radio equipment already available on the market. The solution for this problem was to use the programmable hardware presented in section 3.1.3 in conjunction with the antenna equipment in section 3.1.4. Additionally, in projectile applications it is common to use custom designed antennas. The best procedure in order to parametrize them as accurately as possible is to measure their parameters in an anechoic chamber. Ours is presented in section 3.1.5. Another useful instrument in antenna characterization and channel modeling is a Vector Network Analyzer (VNA), the one we used can be found in section 3.1.6.

Finally, some of our channel modeling procedures will require the use of already designed instrumented projectiles. The one we utilized can be found in section 3.1.7. In this case, its geometrical properties and communication system unit is presented.

3.1.1 The RaPSor Ray Tracing Simulator

RaPSor is a ray propagation simulator used in research and education which was developed at XLIM laboratory. It is coded in the JAVA language and works over the Netbeans platform, this makes it an open and extensible tool as it was released under CDDL license. In RaPSor, the input is a propagation scene written in XML. The propagation scene shall describe the geometry of the scenario along with its electrical properties. The software allows to select the type of antennas for emission and reception as well as the simulation level of detail. This level of detail is expressed in terms of the wave interaction phenomena (reflection, diffraction and scattering) and accounts for the number of interactions which should be taken into account. The higher the level of detail, the longer it takes to complete a simulation. In practice, we should find a compromise between the accuracy of the simulation and the execution time.

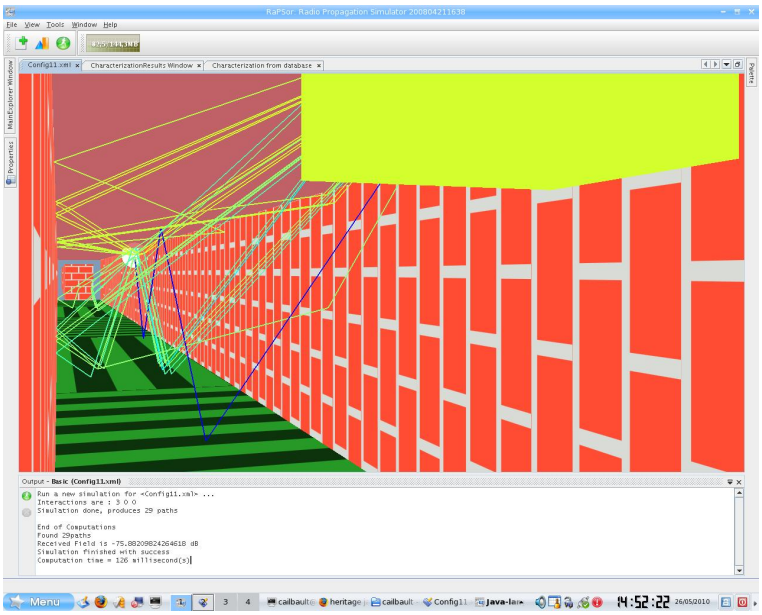

Figure 16: RaPSor Graphical Interface.

The simulation output is given both graphically and in the form of Comma Separated Files (CSV) files. An example of the RaPSor graphical output is shown in Fig. 16. In the CSV files, useful information to obtain the CIR can be found. For example, the power of each multipath component, its angle of arrival and the phenomenon which caused it.

3.1.2 Spinning Bench

As we will see later in chapter 4, some projectiles spin while flying for stabilization purposes. In a spin-stabilized projectile, the embedded antenna will spin along with the projectile. Hence, in order to study the spinning effect on the received signal we will need to reproduce this situation at our laboratory. For this purpose, we can use the spinning bench shown in Fig. 17. This instrument is composed of two modules: an electronic control module, which controls the spinning frequency, and an emitting module. With this instrument, the spinning condition for patch antennas commonly utilized in projectiles can be tested at a maximum spinning rate of 60 Hz.

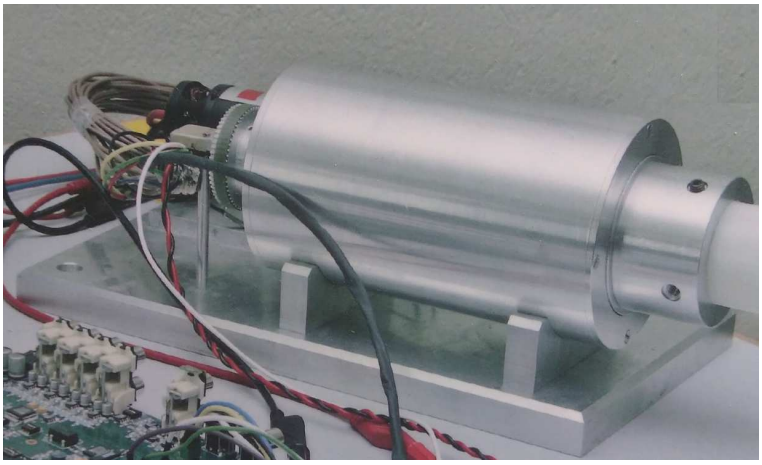

Figure 17: Spinning Simulator Module.

3.1.3 Software Defined Radios

A Software Defined Radio (SDR) is a hardware device which can be programmed to operate as a radio. In general, they consist on a Field Programmable Gate Array (FPGA), a radio front end and a timing block in order to keep both subsystems synchronized. Of course, they include all the needed interfaces to allow user interaction. A complete state of the art of these devices can be found in [35]. The property of being programmable make them incredibly flexible as they can be used to implement almost every radio application possible. Usually, the only restrictions are the maximum emission/reception frequency, which is in the order of a few GHz and the maximum sampling frequency, up to a few hundreds of MHz.

In order to describe the hardware behavior of our radio systems by software, GNU Radio

was employed in the context of this thesis [1]. This free & open software provides signal processing blocks to implement SDR in a friendly graphical environment. Additionally, the user can define its own processing blocks. When working with SDRs, this software is one of the most popular ones.

The SDR equipment available in our laboratory to be used in conjunction with GNU Radio was: several units of Universal Software Radio Peripheral (USRP) equipment from Ettus Research [52] and the PicoZed SDR 2x2 SOM from Avnet [9].

3.1.3.1 Ettus Research USRP

Ettus Research is an American brand from National Instruments since 2010. They are specialized in the development of SDR, being their most famous product the already mentioned USRP equipment. The USRPs we could use were the X310 and the B200 models (Fig. 18). Their features are specified in Tab. 2.

(a) USRP X310.

(b) USRP B200.

Figure 18: USRP Available Models.

Table 2: USRP X310/B200 Comparison.

	X310	B200
Frequency Range	DC - 6 GHz	70 MHz - 6 GHz
Internal Reference Accuracy	2.5 ppm	2 ppm
Maximum Baseband Bandwidth	120 MHz	56 MHz
Maximum ADC / DAC Sample Rate	200 / 800 MS/s	61.44 / 61.44 MS/s
ADC / DAC Resolution	14 / 16 bits	12 / 12 bits
Output Power	10 dBm	10 dBm
Dimensions	27.7 x 21.8 x 3.9 cm	9.7 x 15.5 x 1.5 cm
Weight	1.7 kg	0.350 kg

Table 3: PicoZed SDR 2x2 SOM Features.

Frequency Range	70 MHz - 6 GHz
Internal Reference Accuracy	-
Maximum Baseband Bandwidth	56 MHz
Maximun ADC/DAC Sample Rate	-
ADC / DAC Resolution	12 / 12 bits
Output Power	7.5 dBm
Dimensions	100 x 62 mm
Weight	-

3.1.3.2 Avnet PicoZed SDR 2x2 SOM

The PicoZed SDR 2x2 SOM is a Software Defined Radio (SDR) which integrates the AD9361 transceiver from Analog Devices (Fig. 19). Its principal characteristics can be found in Tab. 3.

Figure 19: PicoZed SDR 2x2 SOM.

Table 4: Antenna Properties Comparison

	NE5023	VERT2450
Typical Frequency of Operation	2400 MHz	Dual Band 2400/5000 MHz
Polarization	Circular	Vertical Linear
Radiation Pattern	Directional 23°	Omnidirectional
Gain	17.5 dBi	2 dBi

3.1.4 Antennas

The antennas used in our experiments were the NE5023 from Hyptra and the VERT2450 from Ettus Research (see Fig. 20). Their characteristics are shown in Tab. 4.

(a) Deployed Hyptra NE5023 Antenna.

(b) Ettus VERT2450.

Figure 20: Antennas Used in Experimentation.

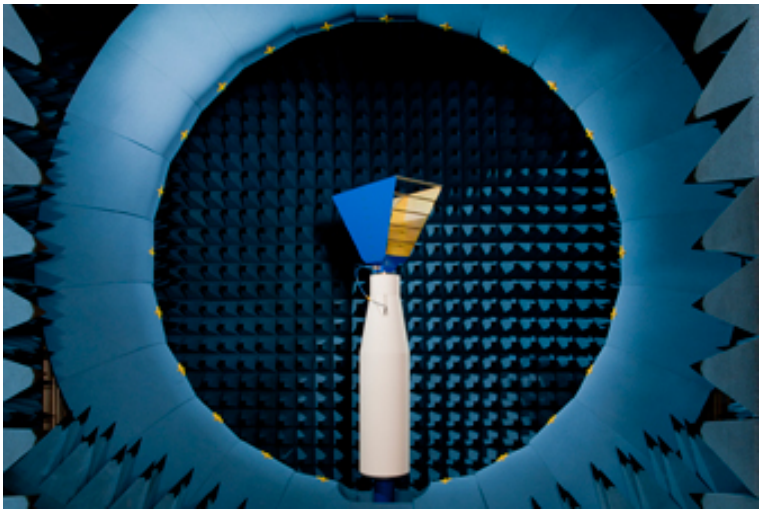

Figure 21: ISL Multi-Probe Near-Field Antenna Measurement System.

3.1.5 Anechoic Chamber

An interesting testing facility at ISL is the near-field antenna measurement system (Fig. 21). This anechoic chamber allow us to obtain the far field radiation pattern of an antenna through near-field measurements.

3.1.6 Vector Network Analyzer

The Vector Network Analyzer (VNA) we utilized was the ZVA40 model from Rohde & Schwarz. It is a high class 4 ports VNA which can operate in a wide range of frequencies, from 10 MHz to 40 GHz. During this thesis, it was used mainly to study the S parameters of the elements employed in order to assure a good matching between them. Adittionaly, indoor Channel sounding can be also performed. It was also employed for the first test of our channel sounder which will be described in section 3.2.

3.1.7 The Basic Finner

The basic finner (BF) is a well-known reference projectile, i.e. a projectile with defined dimensions and fully determined aerodynamic characteristics. It consists of a 20° nose cone in a cylindrical body with 4 rectangular fins [36]. The BF is defined according with its l/d ratio, this is, the ratio between its length and its diameter. In the BF definition, d makes reference to the caliber of the projectile, which was 28 mm for the experiments already

performed at ISL [36, 18]. In Fig. 22(a), we can see the standard dimensions of a BF. The ISL's implementation used in our experiments can be seen in Fig. 22(b).

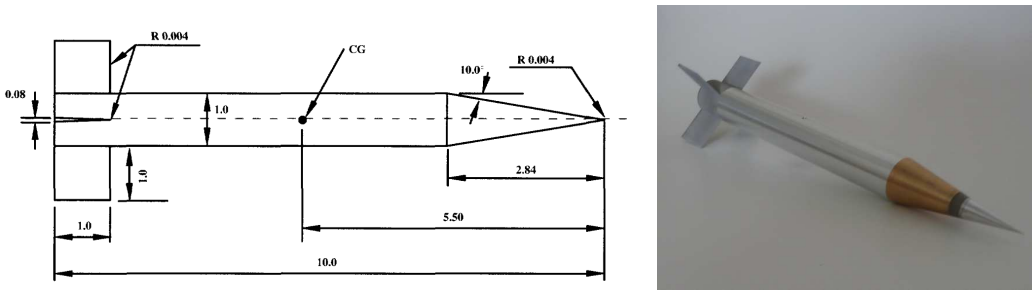

(a) BF Dimensions. (b) ISL Basic Finner.

Figure 22: BF Concept and Implementation.

The embedded IRIG106 [2] compatible telemetry system consists of a S-band miniaturized digital transceiver and a specially designed monopole antenna. This antenna is placed at the nose of the projectile and is connected to the Printed Circuit Board (PCB) through a coaxial line. The same configuration as the one appearing here was successfully tested in another ISL study on aeroballistics [16].

The ISL telemetry system is assembled on two circular PCBs with a diameter of 20mm. This configuration was chosen in order to allow its embedding in the BF as it is only 12 mm long. The transmitter was a programmable low cost commercial off-the-shelf device containing all the desired blocks for data transmission (PLL, VCO, digital filters, etc.). Different digital modulations are available (example: GFSK) with a maximum bit rate of 2 Mb/s. The output power is limited to 24 dBm in the frequency range from 2.26 to 2.40 GHz. An image of the transceiver can be seen in Fig. 24(a).

We achieved a bandwidth greater than 300 MHz with a maximum gain of 2.9 dBi. This configuration was chosen for its reliability after having being successfully tested in firings where accelerations up to 30.000 g were measured. The measured radiation pattern obtained with our anechoic chamber can be found in Fig. 24(b).

3.1.8 Firing Field at Baldersheim

The firing field at Baldersheim (Alsace, France) is the main outdoor testing facility at ISL. This is the propagation scenario where our experiments concerning instrumented projectiles

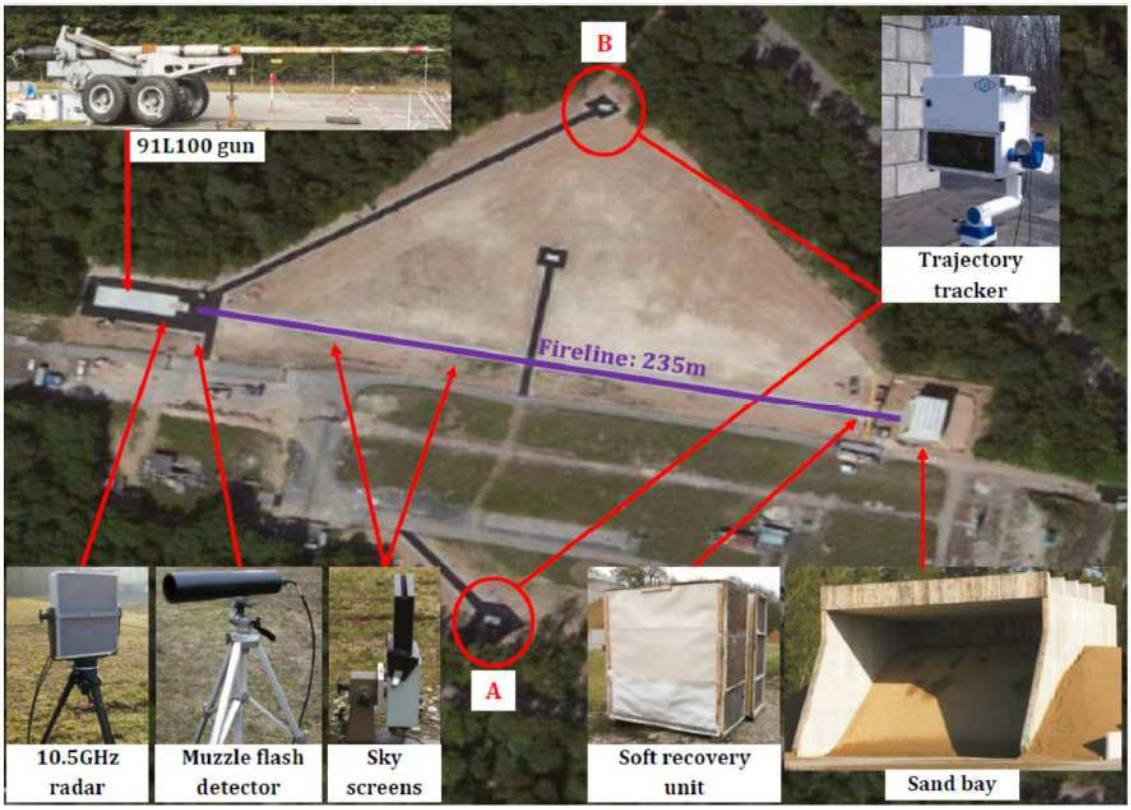

Figure 23: Baldersheim Testing Facility.

will be carried out. Indeed, the channel model will be obtained for this particular scenario.

The configuration of this facility is sketched in Fig. 23. As we can see, a 235 m fireline is available for projectile testing. Additionally, a 1000 m fireline is being rehabilitated while the redaction of this document. The following elements can be used for the testing of instrumented projectiles:

- Launcher: our launchers (guns or cannons) can fire projectiles from Mach 0.6 to Mach 5. The diameters can vary from 20 to 155 mm for spin stabilized projectiles and from 10 to 98 mm for fin stabilized ones.

- Muzzle flash detector: this device is in charge of detecting the flash at the muzzle of the launcher in order to trigger the trajectory tracker. Muzzle flash detection is not only used in research. Additionally, it has applications in the real battlefield as we can see in [68].

- Sky screens: these elements are employed for fine tuning of the trajectory tracker.

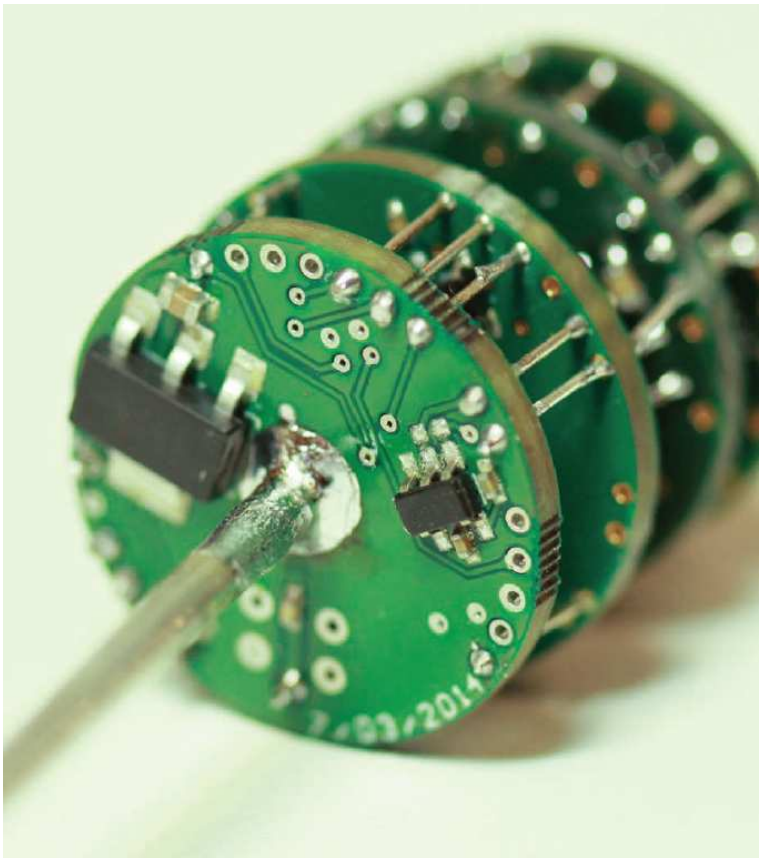

(a) BF S-Band Transmitter.

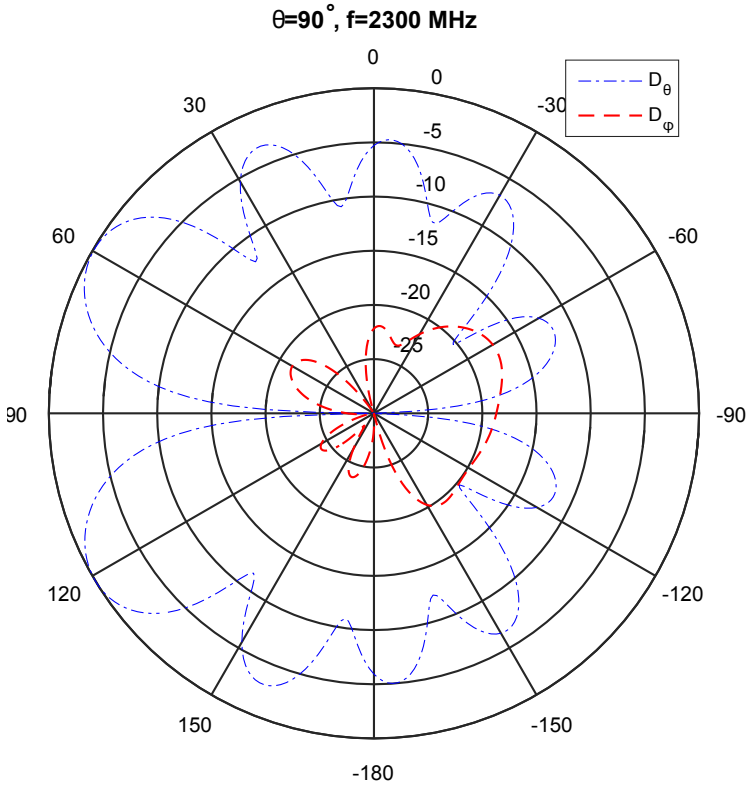

(b) BF Antenna Radiation Pattern.

Figure 24: BF Telemetry.

They detect the moment at when the projectile passes over them.

- Trajectory tracker: this element is in charge of video tracking the projectile for flight analysis purposes. It is really useful for performing failure analysis as it is able to take more than 6000 images per second.

- Soft recovery unit: the firing of an instrumented projectile is expensive. For that reason, it is convenient to recover the electronics of the projectile in most of the cases possible. Here, the objective of reuse them in future firings. The soft recovery unit is used in order to receive the projectile and save it from total destruction. The maximum speed for a safe recovery is less than 3.5 Mach [19] and depends on the projectile geometry and mass.

- Sand bay: a secured impact area.

3.2 OFDM Channel Sounding

Regarding the requirements and constraints already exposed in section 2.4, we decided to develop an adapted channel sounder for our necessities. As we specified, it shall be flexible enough to be used in a multiplicity of propagation scenarios and embeddable. Moreover, only the items already detailed in the last section 3.1 can be used in its implementation.

The introduction to our channel sounder has been structured in two parts: first, we will introduce the OFDM technique in section 3.2.1, which is the key concept behind our channel sounder. As we will see, OFDM is a multicarrier transmission technique intended for digital communications. If we want to base our channel sounding methodology on OFDM, it is necessary to implement a series of procedures. They will be exposed in section 3.2.2.

This whole section is focused on the definition of the channel sounding methodology. We have tried to separate the proposed sounding methodology as much as possible from its hardware implementation, which will be presented in section 3.3. Even though some of the features of our channel sounder will be limited by the hardware available, most of the channel sounding algorithms are hardware independent as they are heavily based on signal

processing. By defining the methodology in such way, we will be fulfilling the flexibility requirement.

3.2.1 Introduction to OFDM

Orthogonal Frequency-Division Multiplexing (OFDM) is a special case of multicarrier transmission where the spectrum of a carrier overlaps with those from the adjacent tones. This modulation scheme is very flexible and provides the transmission chain with some interesting advantages. For example, adaptive loading and transmitter - receiver diversity among others. Nowadays, this modulation scheme has been adopted in a wide range of wireless communication systems including digital radio broadcasting, terrestrial video broadcasting, satellite communications, etc.

The first patent using this transmission technique appears in 1970 with the U.S patent 3488445 issued by Chang and the Bell labs [25]. Previously to the publication of this patent, this communication scheme was also described by Chang in 1966 [24]. However, we have to wait until 1971 for the introduction of the OFDM technique as we use it today [105]. In this paper, Weinstein and Ebert introduced the use of the Fast Fourier Transform (FFT), guard intervals, and time limited transmission. In 1985, Cimini proposes the use of OFDM for mobile communications [31]. Being implemented by an increasing number of applications, OFDM became more and more popular with the years. In 1995, the first OFDM-based standard was published, it was addressed for Digital Audio Broadcasting (DAB) [38]. Later in the 2000s, OFDM was adopted for the IEEE 802.11 family protocols [50]. Nowadays, OFDM is one of the most used modulation techniques.

OFDM is based on two main concepts: Frequency Division Multiplexing (FDM) and orthogonality. FDM accounts for the simultaneous transmission of several tones while the second one implies the spectrum overlapping of these tones. In this thesis, we employ packet based OFDM. As a result, the OFDM transmission is time limited and organized in frames. At the same time, an OFDM frame is structured in symbols. The OFDM frame structure in this thesis follows the one proposed by the IEEE 802.11 protocol [76]. The symbols composing an OFDM frame are: synchronization, preamble and data symbols. The basic

OFDM frame structure is presented in Fig. 25.

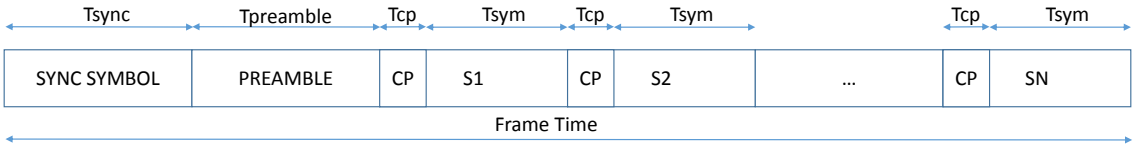

Figure 25: OFDM Basic Frame Structure.

- Synchronization Symbol: this section is used for time and frequency synchronization purposes.
- Preamble: the preamble symbol is used for channel estimation purposes. Some examples showing how the preamble symbol is used for channel estimation in real time OFDM transmission can be found in [102, 39, 112, 109].
- Cyclic Prefix (CP): usually placed before the l-th OFDM symbol; it is composed of its last L samples. This element is placed here to avoid ISI.
- Data Symbol: these sections are in charge of carrying the user data.

The synchronization symbol differs in its conception from the rest of the frame. This element is basically a periodic signal which can be easily identified at the receiver side. Its position at the beginning of the frame sets the time reference of the OFDM frame. Its applications in time and frequency synchronization will be detailed in section 3.2.2.2.

The CP is a really important part of the OFDM frame and needs to be introduced before explaining how the OFDM symbols are constructed. Moreover, the building of the preamble and data symbols requires the introduction of the orthogonality concept, which will be introduced in section 3.2.1.1. Being CP and orthogonality independent concepts, we can start by showing how the inclusion of the CP improves the performance of the OFDM transmission technique. A graphical representation of how the CP works can be found in Fig. 26.

We know the multipath effect will spread the transmitted information. In this case, a symbol with a duration of T_{sym} time units will be spread into a symbol of duration $T_{sym}+\tau_{max}$

where τ_{max} is the maximum excess delay of the CIR. From now on, we will be setting the delay reference $\tau = 0$ at the arriving instant of the LOS path.

In the situation sketched in Fig. 26, we can graphically see what happens when the CP is not used. In such case, the $(L+1)$th received symbol of duration $T_{sym} + \tau_{max}$ contains information of the previous Lth symbol. As a consequence, the OFDM frame will be demodulated in presence of ISI. In the figure, the red color indicates the section of the OFDM symbol affected by ISI.

The CP, which is the blue section in Fig. 26, contains a copy of the last section of the $(L+1)$th OFDM symbol (green section). As we can see in the figure, the transmitted information will still be affected by the multipath effect. However, if we include the CP, the $(L+1)$th symbol will be not affected by the information of the previous Lth symbol. With the inclusion of the CP, the information of the Lth symbol (red) will be contained in the CP section. This condition is true as long as a CP of duration higher than τ_{max} is employed. Nevertheless, the $(L+1)$th symbol will suffer from disturbances because of the multipath effect (yellow color). However, these disturbances come from the $(L+1)$th symbol itself, not being affected by the previous Lth symbol. As a result, ISI is avoided.

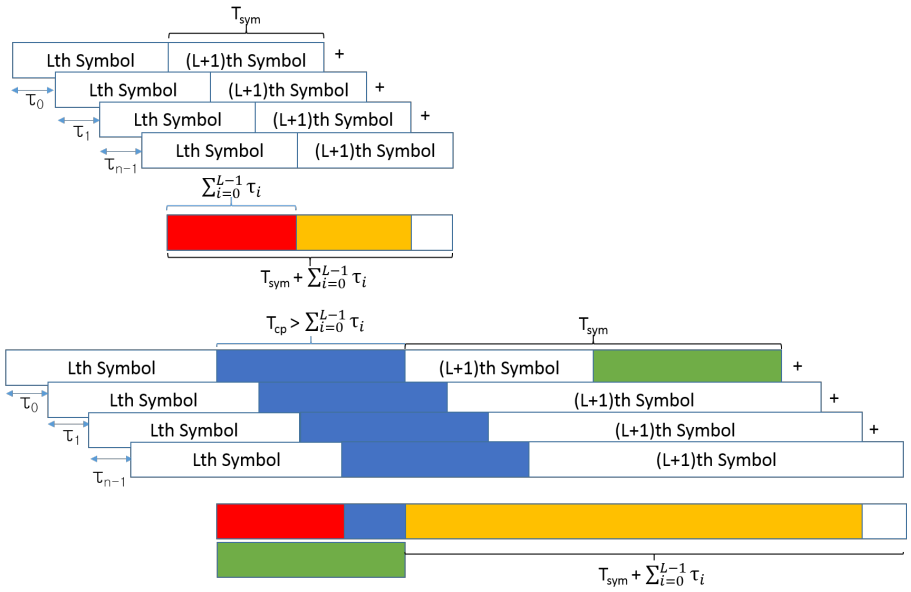

Figure 26: Cyclic Prefix Concept.

Before presenting the orthogonality principle, we can introduce the general scheme of the OFDM transmission chain, which can be found in Fig. 27.

As we can see, the process of generating an OFDM frame can be structured in several stages:

- In a first stage, the original bit stream is arranged in N groups of M bits. The modulator, which quite often follows a MPSK/MQAM scheme, is in charge of assigning a symbol to each one of the N groups according to a pre-defined constellation.
- The serial - parallel converter allocates these N symbols in N different carriers, which leads to the frequency representation of the transmitted signal.
- A N-length Inverse Fast Fourier Transform (IFFT) operation is performed in order to obtain the I-Q signals in the discrete time domain, we obtain here the discrete time representation of the transmitted signal.
- In the next stage, the CP is added according to the previous reasoning.
- The signal is then converted to the analog domain by a D/A converter.
- Finally, the signal is upconverted to the desired frequency f_c and radiated to the medium.

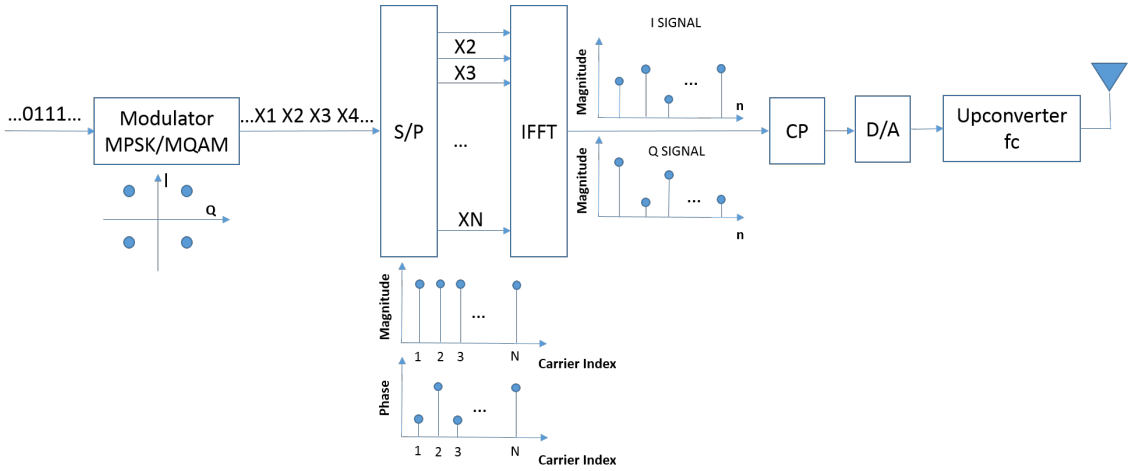

Figure 27: OFDM Transmission/Reception Chain.

3.2.1.1 Orthogonality

Orthogonality is probably the main concept behind the OFDM transmission technique as it allows spectrum overlapping, which could not be possible to achieve without the orthogonality principle. Mathematically, two signals $f(t)$, $g(t)$ are said to be orthogonal over a period T if they fulfill the condition:

$$\int_T f^*(t)g(t)dt = 0 \tag{46}$$

We can consider a set of N complex carriers defined by $\{e^{j2\pi f_k t}\}_{k=0}^{k=N-1}$. According to Eq. 46, they will be orthogonal if

$$\int_T f^*(t)g(t)dt = \int_T e^{j2\pi f_k t}e^{-j2\pi f_i t} = 0 \quad i \neq k \quad i,k = 0,1,...,N-1 \tag{47}$$

In order to fulfill the orthogonality criterion, OFDM technique spaces the N carriers as $f_k = \{k/T_{sym}\}_{k=0}^{N-1}$, where T_{sym} is the emission time of the OFDM symbol. If we apply this restriction to Eq. 47 we obtain:

$$\begin{aligned}\int_T e^{j2\pi f_k t}e^{-j2\pi f_i t} &= \int_{T_{sym}} e^{j2\pi \frac{k}{T_{sym}}t}e^{-j2\pi \frac{i}{T_{sym}}t} \\ &= \int_{T_{sym}} e^{j2\pi \frac{k-i}{T_{sym}}t} = 0 \quad \text{if } k \neq i\end{aligned} \tag{48}$$

Consequently, an OFDM signal will be composed of N subcarriers where the subcarrier spacing is $1/T_{sym}$ in order to fulfill the orthogonality principle.

3.2.1.2 The Convenience of OFDM for Channel Sounding

As we have seen in the previous section, the orthogonality principle allows to transmit a series of adjacent carriers with spectrum overlapping. There are several effects which can destroy the orthogonality of an OFDM signal as we will detail in the next sections.

If the orthogonality of the signal is preserved, what OFDM allows is to characterize a fading channel through a series of flat fading channels. Each one of these flat fading channels correspond to each one of the subcarriers composing the OFDM signal. This concept is illustrated in Fig. 28

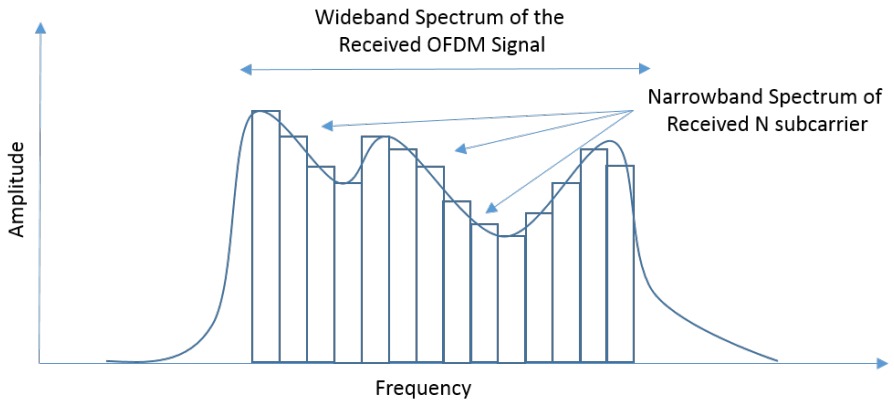

Figure 28: OFDM Channel Sounding Concept.

In our channel sounder methodology, it will be one of our major concerns to preserve the orthogonality of the OFDM signal employed for exciting the channel. If the orthogonality has been preserved, the relation between the frequency response of the channel and its impulse response is merely a Fourier Transform. According to the Bello's equations already presented in section 2.2.2, we can then characterize the channel behavior in the time domain through its behavior in the frequency domain. At the same time, the OFDM technique allows to simplify the study of the channel frequency behavior.

The OFDM transmission technique has been already proposed for channel sounding in a multiplicity of domains. One of these research fields is the characterization of (wireless or not) low mobility propagation scenarios. For example, in [77] the authors characterize a Power Line Communication (PLC) scenario. In a wired communication link as the one concerned by their study, the Doppler effect can be neglected. For that reason, they did not take this aspect into account and no Doppler estimation algorithm was proposed. In [49], an OFDM sounding procedure is well detailed and an IFFT based method for estimating the multipath influence is proposed. In this paper, the methodology was evaluated in a low speed mobility scenario up to 45 km/h. As a result, the authors do not specify a Doppler estimation algorithm as the expected Doppler shift in their study is 100 Hz. In [97], we found another interesting example of an OFDM channel sounder in a low mobility scenario. However, the complexity of their setup (fiber optics, rubidium clocks, etc.) make their solution impossible to implement for us.

OFDM sounders have been proposed for high speed propagation scenarios. In the recent years, the necessity of establishing reliable wireless communications links on High-Speed Railways (HSR) has been growing. In this field, the unique properties of the OFDM transmission technique are being employed in the modeling of the HSR channel. For example, a preliminary study from the point of view of a receiving antenna placed at the rooftop of a train moving at 300 km/h can be found in [108]. A much more complete OFDM based HSR sounding scheme is given in [113]. The properties of the sounding signal and the reception equipment are well described. However, there is not enough information about how to deal with the Doppler effect in HSR scenarios.

In military applications, there is an interest in modeling the Air-Ground (AG) channel by means of OFDM channel sounding. For example, in [93] an OFDM channel sounder is utilized to model the AG channel in the L-Band between an aircraft and a mobile base station. The multipath and Doppler channel statistics are obtained through Fourier Transforms. A similar measurement campaign is presented in [26]. However, in this case the results are given in function of the wireless link performance once the OFDM signal has been analyzed, for that reason, neither the multipath algorithm estimation nor the Doppler estimation method are given. An additional example of OFDM AG channel modeling can be found in [107]. Again, the authors are concerned of sounding the link performance and not necessarily in extracting the channel properties.

As a conclusion, it is fair to state we are not the first ones in using OFDM transmission technique for channel sounding. However, we have detected a lack of description of the multipath and Doppler estimation methods. In the following sections, we will detail how an OFDM signal is constructed in conjunction with the elements to be taken into account for proper channel sounding. An OFDM channel sounding methodology will be specified and the methods to extract the time and frequency properties of the propagation channel will be given with enough detail to be reproduced by other research groups. Additionally, we will justify the construction of the OFDM sensing signal as a function of the hardware available.

3.2.1.3 Modulation

Having presented the orthogonality principle, we are in conditions of introducing how the OFDM symbols are constructed. This process is performed after the mapper in Fig. 27. In OFDM, both data and preamble symbols are constructed following this scheme.

In order to construct an OFDM symbol $s(t)$, N mapped groups of M bits $(X(k)_{k=0}^{N-1})$ are assigned to each one of the N possible subcarriers as it is shown in Eq. 49.

$$s(t) = \sum_{k=0}^{N-1} X(k) e^{j2\pi f_k t} \quad 0 < T \leq T_{sym} \tag{49}$$

In order to respect the orthogonality principle exposed in section 3.2.1.1, we set $f_k = k/T_{sym}$. Being OFDM a digital transmission technique, it will be necessary to set an optimal sampling period T_s. If we set this variable to $T_s = T_{sym}/N$ we can obtain the discrete-time OFDM symbol as

$$s(n) = \sum_{k=0}^{N-1} X(k) e^{j2\pi \frac{k}{T_{sym}} n T_s} = \sum_{k=0}^{N-1} X(k) e^{j2\pi \frac{k}{N} n} \quad n = 0, 1, ..., N-1 \tag{50}$$

It is obvious that signal $s(n)$ is the discrete Inverse Fast Fourier Transform (IFFT) of the signal $\{X(k)\}_{k=0}^{k=N-1}$. As it is shown in Fig. 27, each $X(k)$ is a point of a MPSK/MQAM constellation allocated in a different subcarrier.

We can treat the case of an OFDM symbol which has been transmitted over a noiseless ICI-ISI free channel. If we assume perfect synchronization between the transceivers, the receiving station will sample the symbol after having downconverted it to its baseband representation. In order to demap the allocated M bits at the k-th subcarrier $X(k)$, a FFT operation is performed.

Before continuing, we will present the identity in Eq. 51 as it will be intensively used in the next sections.

$$\sum_{n=0}^{N-1} e^{j2\pi An} = e^{j\pi(N-1)A} \frac{sin(\pi NA)}{sin(\pi A)} \tag{51}$$

At the receiver side, the FFT operation is performed in order to obtain the content at the k-th subcarrier as it is shown in Eq. 52:

$$\begin{aligned} X(k) &= \frac{1}{N}\sum_{n=0}^{N-1} s(n)e^{-j2\pi kn/N} \\ &= \frac{1}{N}\sum_{n=0}^{N-1}\left[\sum_{i=0}^{N-1} X(i)e^{j2\pi\frac{i}{N}n}\right]e^{-j2\pi kn/N} \\ &= \frac{1}{N}\sum_{n=0}^{N-1}\sum_{i=0}^{N-1} X(i)e^{j2\pi\frac{i-k}{N}n} \\ &= \frac{1}{N}\sum_{i=0}^{N-1} X(i)\sum_{n=0}^{N-1} e^{j2\pi\frac{i-k}{N}n} \end{aligned} \tag{52}$$

If we consider the identity Eq. 51, we can transform Eq. 52 into Eq. 53 just taking into account that $A = (i-k)/N$.

$$X(k) = \frac{1}{N}\sum_{i=0}^{N-1} X(i)e^{j\frac{N-1}{N}(i-k)}\frac{sin(\pi(i-k))}{sin(\pi(i-k)/N)} = \begin{cases} X(k) & \text{if } i-k=0 \\ 0 & \text{otherwise} \end{cases} \tag{53}$$

3.2.1.4 Time Synchronization

As we have seen, OFDM systems make use of the discrete time IFFT/FFT operations for modulation/demodulation. If we assume the transmitter perfectly modulates the OFDM signal, we still require to know the first sample of the OFDM symbol in order to avoid causing ICI or ISI at the receiver side. We can assume a certain OFDM frame detection algorithm is employed at the receiver side. This algorithm will be providing an estimation for the best sampling instant with a certain error δ. This error in the sampling instant is known as Sample Time Offset (STO). We can distinguish between four cases as we sketch in Fig. 29 [28].

- Case 1: no STO at all, the right sampling instant has been given by the algorithm. No undesired effects are present and the orthogonality of the OFDM symbol has been preserved.

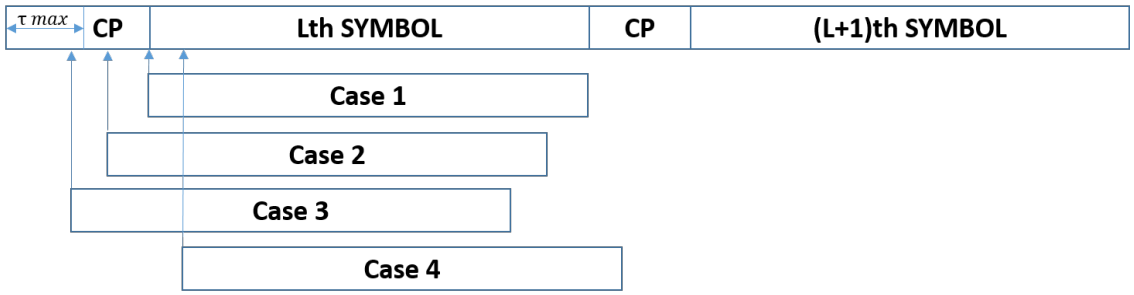

Figure 29: STO Possible Cases.

- Case 2: in this case, the algorithm has estimated a sampling instant δ time units before the right instant. The Lth sampled symbol will not overlap with the $(L+1)$th and no information of the $(L-1)$th symbol is present. In such situation ISI is avoided. We can express the demodulated OFDM received symbol at the k-th subcarrier $Y_l(k)$ as follows:

$$\begin{aligned} Y_l(k) &= \frac{1}{N}\sum_{n=0}^{N-1} x_l(n+\delta)e^{-j2\pi nk/N} \\ &= \frac{1}{N}\sum_{n=0}^{N-1}\left[\sum_{i=0}^{N-1} X_l(i)e^{-j2\pi(n+\delta)i/N}\right]e^{-j2\pi nk/N} \\ &= X_l(k)e^{-j2\pi k\delta/N} \end{aligned} \tag{54}$$

  As we can deduce from Eq. 54, the demodulated constellation of the OFDM symbol will be a rotated copy of the original one. In this case, each point will be rotated $2\pi\delta/N$ radians from its original position. The situation is sketched in Fig. 30, where a value of $\delta = 1$ was assumed for an OFDM symbol of 32 subcarriers and a QPSK constellation.

  This situation is easy to handle at the receiver side, i.e. only a 1-tap equalizer is required to rotate the received constellation back to its original position.

- Case 3: the maximum excess delay τ_{max} of the CIR is assumed to be less than the total duration of the cyclic prefix $\tau_{max} < T_{CP}$. When the sampling instant Si is such that it fulfills the condition $Si < \tau_{max}$, it means the Lth sampled symbol contains information of the $(L-1)$th one, i.e. ISI occurs. As we will show, at the same time ICI is also

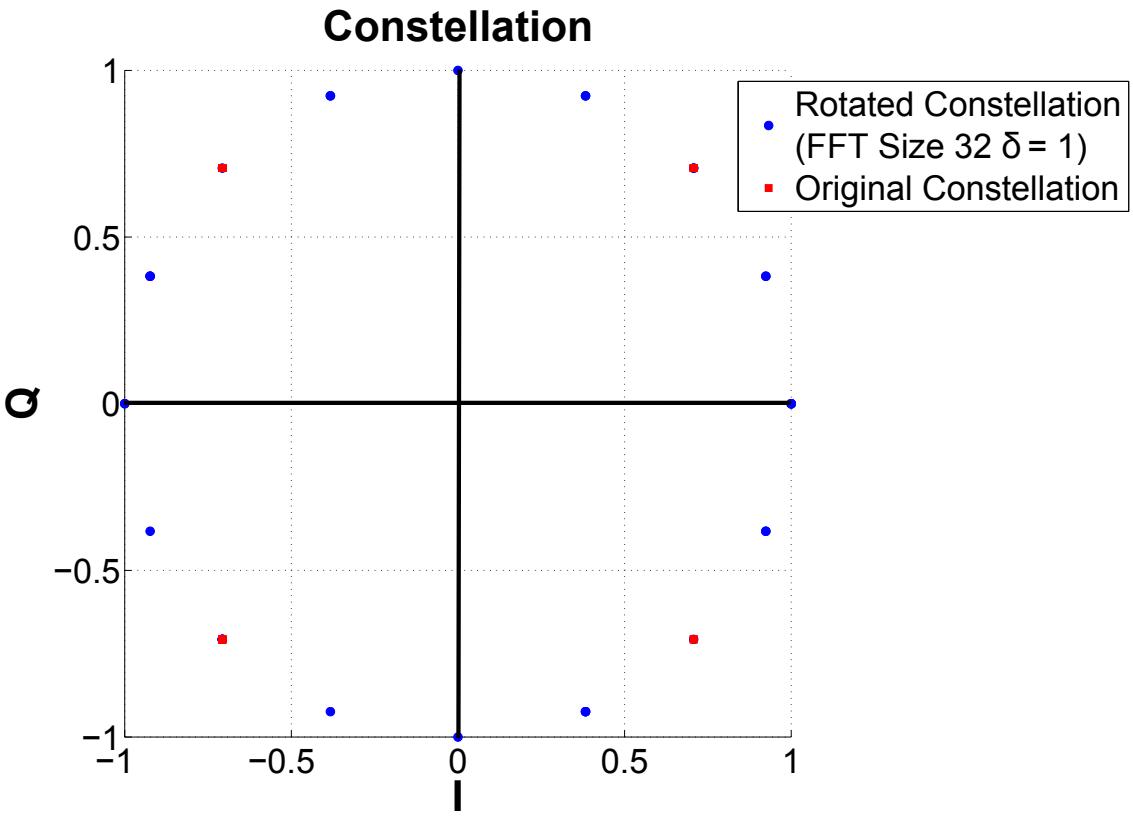

Figure 30: Constellation in STO Case II with $\delta = 1$.

present.

- Case 4: this case is equivalent to case 3, except now ISI comes from the $(L+1)$th symbol. Equivalently, ICI is also present. We will show mathematically how this happens. The demodulated symbol $Y_l(k)$ in case 4 (the same reasoning is valid for case 3) can be expressed as follows:

$$Y_l(k) = \sum_{n=0}^{N-1-\delta} x_l(n+\delta)e^{-j2\pi nk/N} + \sum_{n=N-\delta}^{N-1} x_{l+1}(n-N_g+\delta)e^{-j2\pi nk/N} \tag{55}$$

For clarification purposes, an example of this situation can be found in Fig. 31. Where we suppose a $\delta = 2$ situation for 8 samples long OFDM symbol with a 4 samples long CP (N_g).

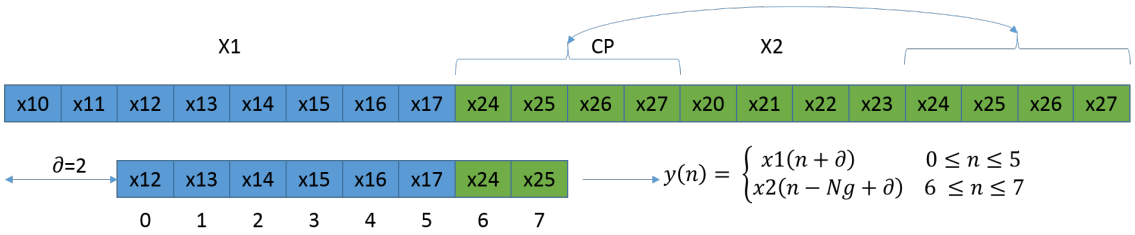

Figure 31: Sampled Received Symbol in STO Case 4.

If we substitute $x_l(n+\delta)$ and $x_{l+1}(n-N_g+\delta)$ by their construction through the FFT we can obtain:

$$Y_l(k) = \sum_{n=0}^{N-1-\delta} \left[\frac{1}{N} \sum_{i=0}^{N-1} X_l(i) e^{j2\pi(n+\delta)i/N} \right] e^{-j2\pi nk/N} + \sum_{n=N-\delta}^{N-1} \left[\sum_{i=0}^{N-1} X_{l+1}(i) e^{j2\pi(n-N_g+\delta)i/N} \right] e^{-j2\pi nk/N} \tag{56}$$

If we develop Eq. 56:

$$Y_l(k) = \frac{1}{N} \sum_{i=0}^{N-1} X_l(i) e^{j2\pi\delta i/N} \sum_{n=0}^{N-\delta-1} e^{j2\pi(i-k)n/N} + \frac{1}{N} \sum_{i=0}^{N-1} X_{l+1}(i) e^{j2\pi(\delta-N_g)i/N} \sum_{n=N-\delta}^{N-1} e^{j2\pi(i-k)n/N} \tag{57}$$

Again, after the application of the identity given by Eq. 51 on the first term of Eq. 57, we have:

$$Y_l(k) = \overbrace{\frac{N-\delta}{N} X_l(i) e^{j2\pi i\delta/N}}^{Rotation} + \overbrace{\sum_{i=0, i\neq k}^{N-1} X_l(i) e^{j2\pi i\delta/N} \sum_{n=0}^{N-1-\delta} e^{j2\pi(i-k)n/N} + \underbrace{\frac{1}{N} \sum_{i=0}^{N-1} X_{l+1}(i) e^{j2\pi(\delta-N_g)i/N} \sum_{n=N-\delta}^{N-1} e^{j2\pi(i-k)n/N}}_{ISI}}^{ICI} \tag{58}$$

As we can see, this effect is quite destructive and should be avoided. The first term of the equation is similar to the one in case 2 plus an amplitude modulation. The second term in Eq. 58 indicates that the demodulation of the content allocated at the k-th carrier depends on the information from the other carriers, i.e. the symbol is demapped

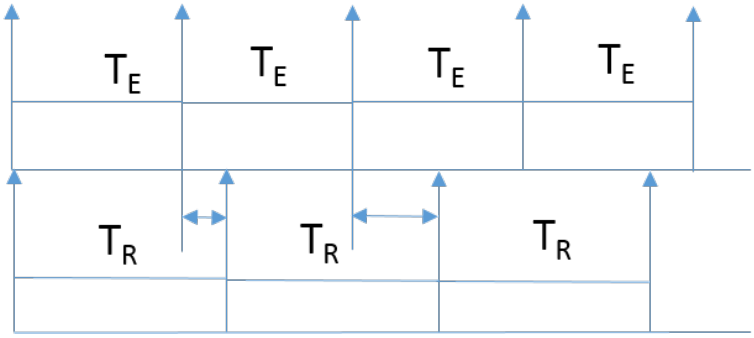

(a) Sampling Frequency Offset.

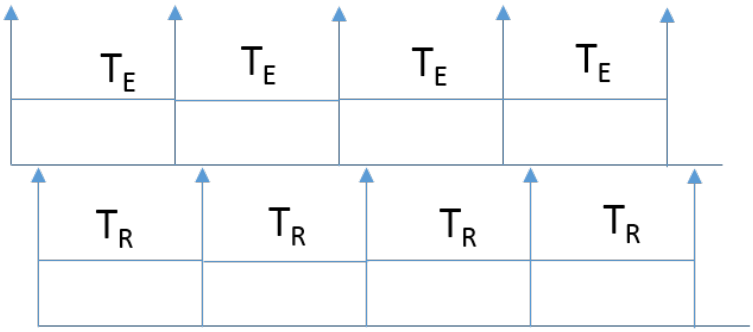

(b) Clock Phase Offset.

Figure 32: Clock Synchronization Undesired Effects.

in presence of ICI. Finally, the third term in Eq. 58 indicates the demodulation of the symbol l depends on symbol $l+1$, i.e. ISI is also present.

We have introduced the importance of estimating the sample instant of the OFDM symbol in order to avoid destroying the orthogonality. In real digital systems, we have to consider two additional undesired effects: the Sampling Frequency Clock Offset (SFO) between the emitter and the receiver. Additionally, even if no SFO exists, an offset in the sampling instant is likely to be present. Let us to present each phenomenon separately.

- Sampling Frequency Offset (SFO): the situation is sketched in Fig. 32(a). We assume the sampling rate of the receiver can be expressed as $T_R = (1+\beta)T_E$, being T_E the emitter's sampling rate. The β parameter is often measured in ppm and can be expressed as $\beta = (T_R - T_E)/T_R$.

  As usual, the received OFDM symbol is demodulated through a FFT operation:

$$
\begin{aligned}
Y(k) &= \sum_{n=0}^{N-1} x(n')e^{j2\pi kn/N} = \sum_{n=0}^{N-1}\left[\frac{1}{N}\sum_{i=0}^{N-1} X(i)e^{j2\pi(1+\beta)in/N}\right]e^{-j2\pi kn/N} \\
&= \sum_{i=0}^{N-1} X(i)\frac{1}{N}\sum_{n=0}^{n-1} e^{j2\pi n(i(1+\beta)-k)/N} \\
&= \sum_{i=0}^{N-1} X(i)\frac{1}{N}e^{j\pi(i(1+\beta)-k)(N-1)/N}\frac{sin(\pi(i(1+\beta)-k))}{sin(\pi(i(1+\beta)-k)/N)}
\end{aligned} \tag{59}
$$

In modern digital systems, it seems to be fair to assume $\beta << 1$. In that case, we can simplify Eq. 59 into:

$$
Y_r(k) = Y(k)\ \underbrace{sinc(k\beta)e^{j2\pi k\beta(N-1)/N}}_{\text{Amplitude and Phase Distortion}} + \overbrace{Z(k)}^{ICI} \tag{60}
$$

where $sinc(k\beta) = sin(\pi k\beta)/(\pi k\beta)$ and

$$
Z(k) = \sum_{k\neq i}^{N-1} X(i)\frac{1}{N}e^{j\pi(i(1+\beta)-k)(N-1)/N}\frac{sin(\pi(i(1+\beta)-k))}{sin(\pi(i(1+\beta)-k)/N)} \tag{61}
$$

As we deduce from Eq. 60, SFO causes both amplitude and phase distortion plus ICI at the received symbol $Y_r(k)$. The $Z(k)$ parameter can be modeled as noise. Its implications will be treated in the next section 3.2.1.5.

- Clock Phase Offset: in this case, the clocks of the involved transceiver do not differ in their sampling frequencies. However, an offset in the sampling instant may still be present. This offset will cause a rotation in the constellation as we have already shown when studying the sampling instants.

3.2.1.5 Frequency Synchronization

We know from chapter 2 the emitted signal will be frequency shifted because of the Doppler effect when mobile transceivers are implied. Let us to assume an OFDM symbol transmitted by a mobile transceiver. In this situation, we can assume a Doppler shift ϵ at the receiver side. The parameter ϵ is the Doppler shift normalized to the subcarrier spacing. Working on the received symbol, the demodulated constellation will be obtained as:

$$
\begin{aligned}
Y(k) &= \sum_{n=0}^{N-1}\left[\frac{1}{N}\sum_{i=0}^{N-1}X(i)^{2\pi in/N}\right]e^{-j2\pi(k+\epsilon)n/N} \\
&= \sum_{i=0}^{N-1}X(i)\frac{1}{N}\sum_{n=0}^{N-1}e^{j2\pi(i-k-\epsilon)n/N} \\
&= X(k)\underbrace{e^{-j\pi\frac{N-1}{N}\epsilon}\frac{sin(\pi\epsilon)}{Nsin(\pi\epsilon/N)}}_{\text{Amplitude and Phase Distortion}} + \underbrace{\sum_{k\neq i}^{N-1}X(i)\frac{1}{N}\sum_{n=0}^{N-1}e^{j2\pi(i-k-\epsilon)n/N}}_{ISI}
\end{aligned}
\tag{62}
$$

We can see how this effect has exactly the same form as the SFO effect already presented. For this reason, SFO can be considered as an additional Doppler shift. In Fig. 33, we can observe the QPSK constellation of a 64 subcarriers OFDM symbol for different ϵ values.

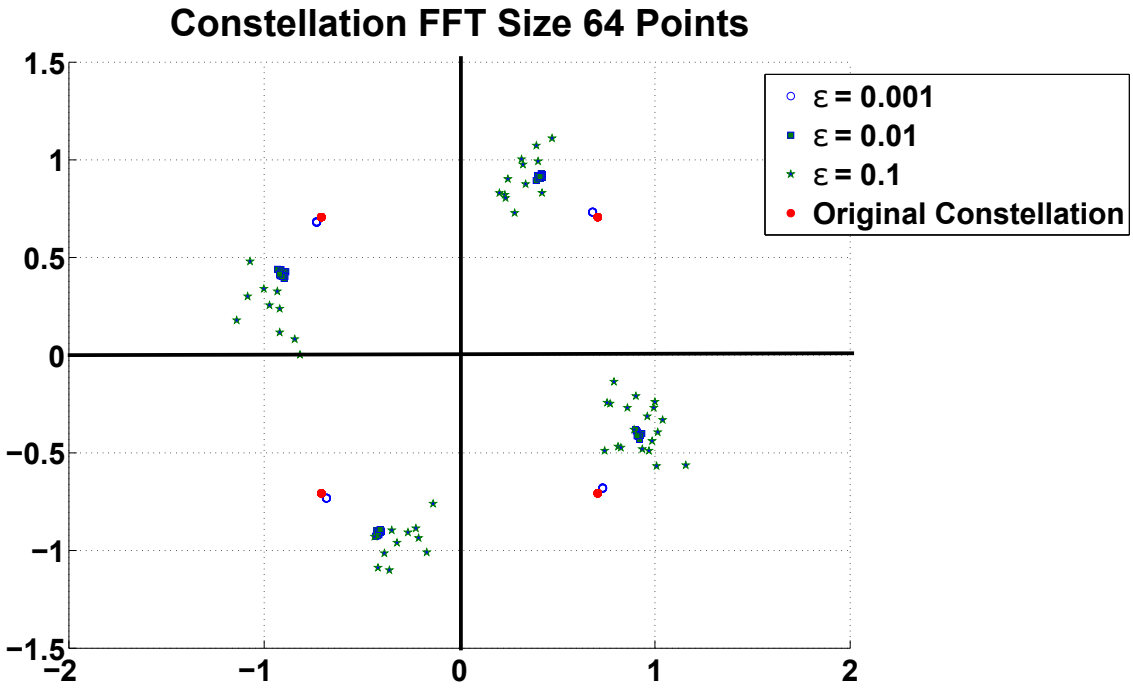

Figure 33: Effect of the Doppler Shift in the Received Constellation.

As we can see, for small values of ϵ only the phase rotation can be appreciated. However, as the value of ϵ raises, a highly noisy-rotated constellation is obtained at the receiver side. It is possible to obtain an analytical expression for the noise contribution of SFO and CFO. In [106, 94], the power of the ICI caused by SFO in Eq. 60 is obtained as:

$$
VAR\left[Z(k)\right] \approx \frac{(\pi k\beta)^2}{2} \tag{63}
$$

After some calculus, it is possible to obtain the expression in Eq. 64 in order to also account for the Doppler shift.

$$VAR\left[Z(k)\right] \approx \frac{(\pi(k\beta+\epsilon))^2}{3} \tag{64}$$

It is easy to see how this expression converges to Eq. 63 when $\epsilon \to 0$. Remarkably, the power of the interference does not depend on the emission power. Having a fixed value for ϵ means a constant contribution for a given emission power. As a consequence, CFO will rule the error behavior of the system if it is not properly compensated. In presence of CFO, the OFDM received symbol $Y(k)$ will adopt the form:

$$Y(k) = \frac{1}{N}\sum_{k=0}^{N-1} X(k)H(k)e^{j2\pi(k+\epsilon)n/N} + Z(k) \tag{65}$$

where $H(k)$ is the Channel Frequency Response (CFR) at the k-th subcarrier and $Z(k)$ is white Gaussian noise as usual. If we operate Eq. 65 as we have been doing in this section, it is possible to obtain:

$$\begin{aligned} Y(k) &= \frac{sin(\pi\epsilon)}{Nsin(\pi\epsilon/N)}e^{j\pi\epsilon(N-1)/N}X(k)H(K) + \overbrace{I(k)}^{ISI} + \overbrace{Z(k)}^{Noise} \\ I(k) &= e^{j\pi\epsilon(N-1)/N}\sum_{i\neq k}^{N-1}\frac{sin(\pi(i-k-\epsilon))}{Nsin(\pi(i-k-\epsilon)/N)}X(k)H(k)e^{j\pi(i-k)(N-1)/N} \end{aligned} \tag{66}$$

In Eq. 66 it is clearly shown how if CFO is not compensated, $I(k) >> Z(k)$ and an effective communication is not possible even for high SNR values.

3.2.2 Channel Sounding Methodology

Once we know the main sources of errors an OFDM system can experience, we can start the definition of our sounding method, more precisely, the OFDM sounding signal.

Three parameters will be considered at this point: the sampling rate Ts, symbol emission time $Tsym$ and the number of carriers N. Considering these elements and the usual OFDM frame structure showed in Fig. 25, it will be possible to define the frame emission time T_f.

The general concept of the proposed channel sounder is sketched in Fig. 34. On the emitter side, the mobile unit will be equipped with a telemetry system able to continuously

emitting an OFDM frame of duration T_f. The base station (receiver side) will be composed of a SDR sampling the channel at T_s in the user defined band. These samples will be sent to a computer for processing. For security reasons, the computer will be storing the raw measurement on its hard disk. This will allow post-processing in case of a failure of any of the systems involved.

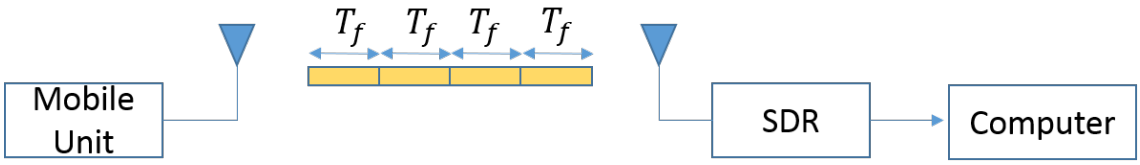

Figure 34: Basic Scheme of the Proposed Channel Sounder.

3.2.2.1 The sounding signal

We will start by defining an optimal sampling rate. If we have a look on Tab. 2 and Tab. 3, the maximum allowed sampling rate will be around 100 MS/s. In practice, we experienced problems with sampling rates higher than 40 MS/s. This comes from the difficulty of saving these samples in the laptop employed at the receiver side. In fact, if the sampling rate is too high, some of the samples will be lost as a result of the synchronization mismatch between the SDR and the hard disk in the laptop used at the receiving station. For security reasons, a sampling frequency of 20 MS/s was set, i.e. under this condition: $T_s = 50$ ns.

As we already know, an OFDM frame is composed of a synchronization symbol and some OFDM data symbols. At the receiver side, this frame has to be known in advance in order to perform channel sounding as it was specified in section 2.3. The easiest solution in order to reduce the complexity of the sounder is to emit always the same ODFM frame.

Two possible options arise: the first one is to build the OFDM frame at the emitter side by following the process in Fig. 27. Specifically, this solution implies to perform the IFFT operation for each one of the OFDM symbols composing the frame, the inclusion of the CP for each symbol, the addition of the synchronization symbol, the D/A conversion and finally the emission. The second solution for this issue is to pre-generate the OFDM frame and storing it at the emitter side. This was the chosen solution. In this case the only emitter

task is to perform the D/A conversion and radiating the frame.

In our sounder, the selected SDR for emitting was the Avnet's Picozed while the USRP X310/B210 from Ettus were used at the receiver side. This solution was based on the size and weight of these SDRs. As we can see, the only one which can be embedded in a projectile of a few tens of millimeters of diameter is the Avnet SDR. The Avnet SDR has an internal memory of 500 RAM blocks. Each one of them have 1024 addresses of 36 bits. In our sounder, we used just one to store the 1024 I - Q values of our OFDM frame. Using a single blockram makes routing and timing in the FPGA fabric very easy.

Taking into account the already defined value for Ts, the maximum frame duration is found to be $T_{fmax} = 1024 \times 50$ ns $= 51200$ ns. Assuming the worst case possible, i.e. just one channel estimation can be obtained per received frame, the channel sounding frequency F_{IR} will be $F_{IR} = 1/T_{fmax} = 20.53$ kHz. According to Eq. 37, our worst case F_{IR} will be enough to characterize the Doppler spectrum of the channel. In this extreme case, a maximum Doppler shift up to 7.82 kHz ($f_c = 2.3$ GHz) is expected for a projectile flying at Mach 3.

Having set Ts and T_{fmax}, it is time to determine the length of the CP. As it was stated in section 3.2.1, the CP is composed of some of the last samples of the OFDM symbol. At the same time, we showed how its length is related to the maximum expected excess delay. In the construction of the CP, we will consider the multipath distance resolution MP_{res}. This parameter is determined by the light's speed and T_s as we show in Eq. 67:

$$MP_{res} = T_s c = \frac{3E8ms^{-}1}{20E - 6s^{-1}} = 15 \text{ m} \tag{67}$$

If we look at Fig. 23, we can consider the following case: an instrumented projectile arriving at the sandbay and a receiving station placed just where the cannon is. In order to set the length of the CP, we can use the ellipse model for TDL channel models presented by Parsons and Bajwa in [79]. This model places both emitter and receiver in the focal points of a series of ellipses. Each ellipse represents a region where a scatter produces a MPC with a delay smaller than a multiple of MP_{res}. On the other hand, a scatter in the ellipse border

will produce a MPC component with a propagation delay equal to a multiple of MP_{res}.

Considering a multipath resolution of 15 m, the ellipses concerning the previous situation can be found in Fig. 35(a). Having set d_0 to 235 m, i.e. the fireline length at Baldersheim. The gray ellipse accounts for the scatterers producing MPCs where the propagation delay τ_0 is between $d_0/c \leq \tau_0 \leq d_0/c+50$ ns. Alternatively, the distance d traveled by these scattered rays will be in the range of $235 \leq d \leq 250$ m. Following this method, the red ellipse has been computed for the scattered rays with a maximum delay of 15 times the multipath resolution. This corresponds to a maximum distance of 460 m.

The maximum emission power for the Avnet's SDR is 9 dBm (-21 dBW). We can use this parameter to study what happens in the best case propagation scenario possible. In other words, when the whole power is radiated from the emitter to the receiver in a free space situation. In such ideal case, we will take into account distance between the transceivers, the emission power and the noise floor at the receiving station. The power received from the scatterers placed at the edge of the ellipses in Fig. 38 is computed assuming no circuit mismatching, no polarization mismatching, no energy absorption by the scatter and the whole signal reradiated in the receiver's direction. Applying this conditions to Eq. 1 we obtain Fig. 36. As we can deduce, a CP of 16 samples (16×50 ns $= 800$ ns) will be enough for our purposes as the maximum power level from the scatterers at the edge of the red ellipse ($d = 460$ m) is under the typical noise floor of -100 dBW. Quite often in OFDM systems, the CP represents 25 % of the symbol period. That would imply a symbol of 64 samples and 64 subcarriers, we obtain then $T_{sym} = 3200$ ns (64×50 ns $= 3200$ ns). Moreover, the subcarrier spacing will be $\Delta f = 1/T_{sym} = 312.5$ kHz. In a Mach 3 flight, $\epsilon = f_{Dmax}/\Delta f = 0.025$, where $f_{Dmax} = 7.82$ kHz for an instrumented projectile emitting in the 2.3 GHz band.

In practice, the 64 subcarriers are not used, i.e. they are not modulated. This is performed in order to introduce a guard band in the OFDM symbol spectrum. In our case, the 52 central subcarriers were modulated having 2×6 non modulated subcarriers as in the 802.11g protocol. This reduced the sounding bandwidth from 20 MHz (64×312.500 kHz) to approximately 16 MHz (52×312.500 kHz).

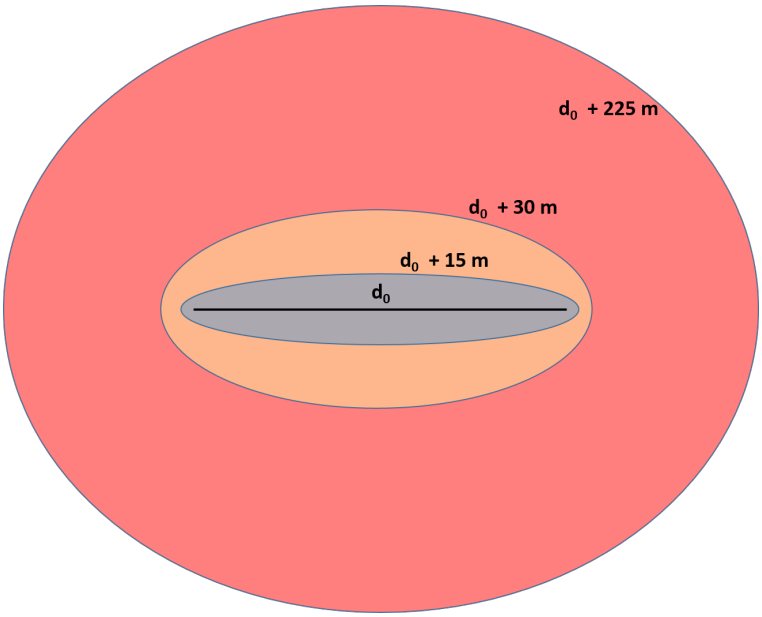

(a) Ellipse Model.

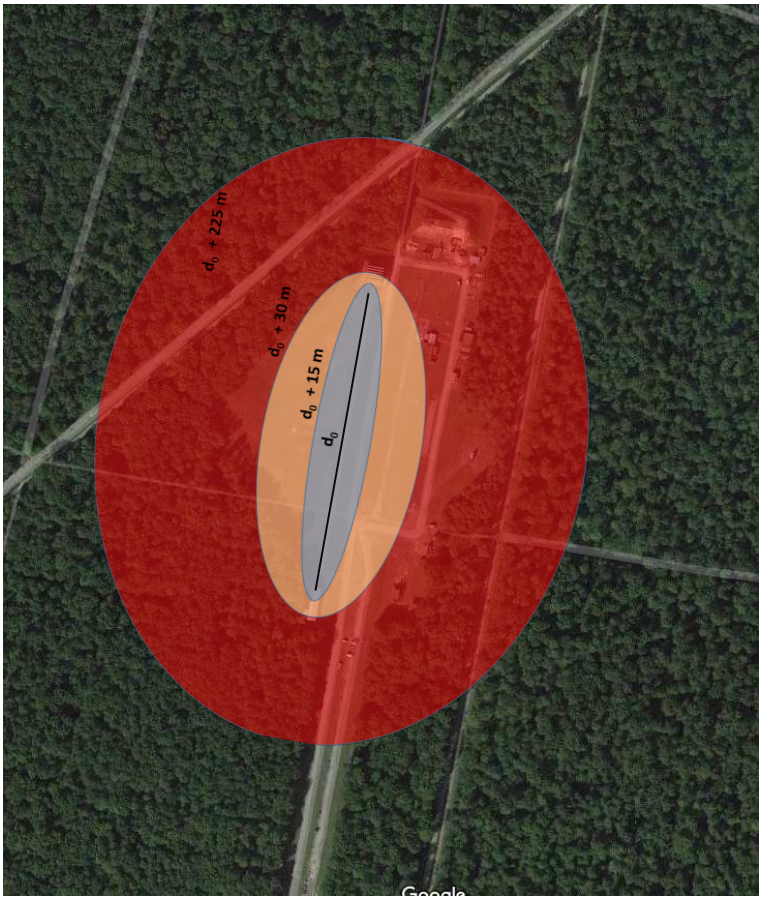

(b) Ellipse Model in Baldersheim.

Figure 35: Ellipse Model by Parsons and Bajwa.

$$P_r(dBW) = -21dBW + 10log10\left[\left(\frac{\lambda}{4\pi d}\right)^2\right] \tag{68}$$

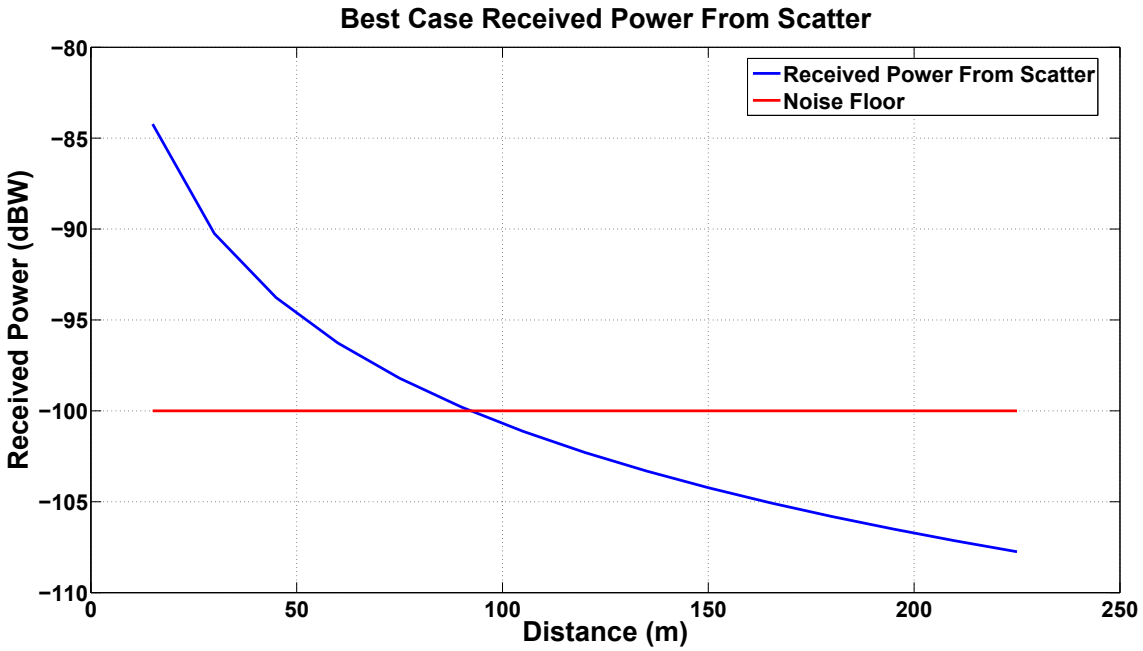

Figure 36: Best Case Received Power from Scatterers according to Parsons & Bajwa Model.

We already have all the elements needed for defining the OFDM sounding signal and the expected sounder performance. Knowing the available space from 1024 samples at the emitting side, they were structured as follows: 2×32 silent samples, 160 samples for synchronization symbol, 800 samples for OFDM data symbols. The next Tab. 5 summarizes the sounder performance and the structure of the OFDM testing signal.

Finally, the OFDM channel sounding method we propose is sketched in Fig. 37. In this sounding scheme the difficulty is mainly at the receiver side. On the contrary, the emitter operation is limited to continuously emitting an OFDM frame of duration 51200 ns. In Fig. 37, the black period corresponds to the silent samples. We will describe the receiver side operation in the next following sections. As a brief introduction, its stages are sketched here:

- IQ: in this stage the IQ components of the OFDM signal are obtained through a sampling process at $T_s = 50$ ns.

Table 5: Performance of the Proposed OFDM Channel Sounder.

OFDM Channel Sounder	51200 ns 1024 samples		
Frame structure	1600 ns of silence 32 samples	8000 ns synchronization symbol 160 samples	40000 ns OFDM symbols 800 samples 80 samples/symbol 16 CP + 64 samples 10 OFDM symbols
Sampling Frequency	50 ns		
Multipath Resolution	15 m		
Carriers	64		
Carrier Spacing	312.500 kHz		
Bandwidth	20 MHz (Total) / 16.25 MHz (Effective)		
Minimum Channel Sampling Frequency	20.53 kHz		

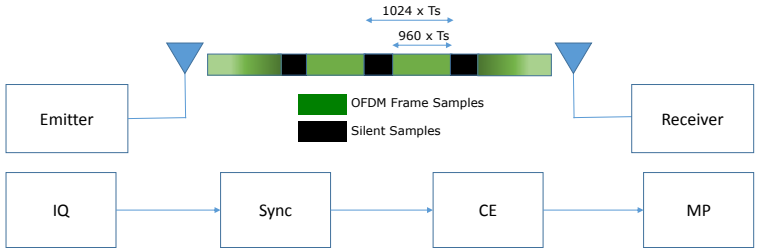

Figure 37: Proposed OFDM Channel Sounding Method.

- Sync: frequency and time synchronization is performed here in order to avoid ISI and ICI.
- CE: the CFR of the channel is found in this stage.
- MP: the CIR is obtained from the CFR in this stage.

3.2.2.2 Sampling and Frequency - Time Synchronization

This stage is in charge of obtaining the I-Q components of the OFDM frame and performing time and frequency synchronization in order to avoid the undesired effects explained in the last sections. The I-Q samples are obtained after having down-converted the emitted signal back to its baseband representation. As we have discussed, we have to deal with STO, SFO and CFO. In modern digital systems, SFO is usually not taken into account as its impact at the receiver side is considered to be negligible [106, 94]. For this reason, we will focus our attention on STO and CFO.

Once the I - Q samples are available, it is time to determine when an OFDM frame has been received, i.e. time synchronization. Moreover, this frame is likely affected by CFO as we know from section 3.2.1.5. For such reason, an estimation for both STO and CFO is required. The problem of OFDM synchronization is a widely studied subject where the authors have approached the problem mainly from three different points of view: either by assuming perfect time synchronization [71], either by assuming perfect frequency synchronization [69, 78] or by assuming both parameters have to be obtained [69, 92, 103, 70, 22]. In general, algorithms searching form both parameters at the same time use the autocorrelation method, which is sketched in Fig. 38(a).

One of our constraints is the expected flight time of the projectile. In this situation, the synchronization algorithm shall provide a great efficiency in terms of time. From the last cited algorithms, the most suitable for our application was the method proposed by Canet in [22]. It provides the best sampling instant (time synchronization) and a CFO estimation (frequency synchronization) at the same time by filtering the OFDM frame with the digital filter graphically defined in Fig. 38(b).

As it is shown in Fig. 38(c), this filter produces a signal y with the following characteristics:

- The n-th sample which maximizes $||y(n)||$ indicates the last sample of the synchronization frame. This sample is used as a time reference to obtain the position of the OFDM symbols.

- The CFO is obtained as $CFO = angle\left(y(max)\right)/2\pi 16T_s$

As any other digital transmission system, the reliability of the channel sounder is highly limited by the noise conditions in which the reception is being performed. For that reason, it is important to have a SNR estimation method, permitting us to have an idea of the accuracy we can expect. In order to estimate the SNR, we first obtain the noise power by computing the standard deviation σ of the samples taken between one frame and another (the silent samples). The obtained noise floor is assumed to remain constant during the packet

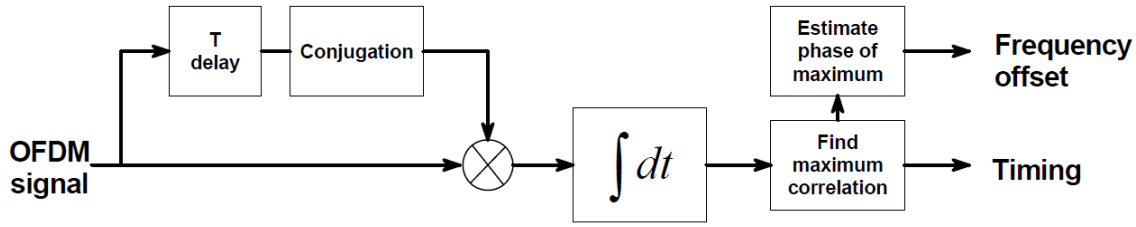

(a) General Synchronization Process.

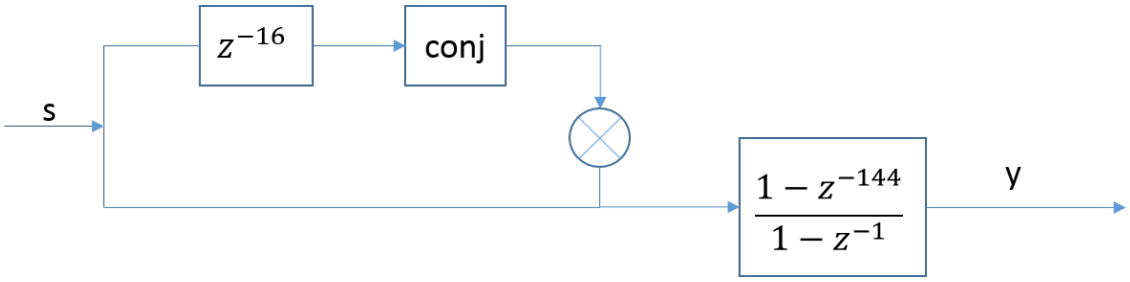

(b) Synchronization Filter by Canet.

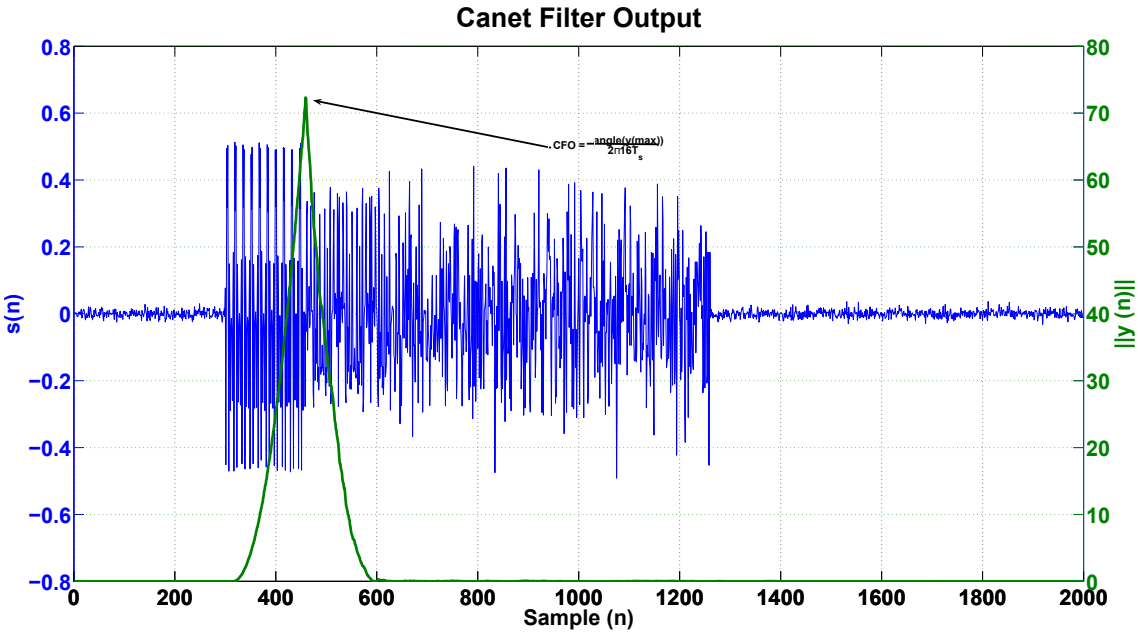

(c) Typical Filter Output.

Figure 38: OFDM Time & Frequency Synchronization Process.

reception. According to Fig. 37, time intervals of $64 \times T_s$ seconds are used for this purpose. Once the packet has been isolated by the synchronization algorithm, the auto-correlation r_i is obtained for each i-th symbol. As we know, the initial sample of the autocorrelation signal has a value of $r_i(0) = p_i + \hat{\sigma_i}^2$, being respectively: p_i the estimated frame power and $\hat{\sigma_i}^2$ the noise power. We have to assume then $\sigma^2 \approx \hat{\sigma_i}^2$. Finally, the SNR is obtained as it appears in Eq. 69, where N is the number of OFDM symbols.

$$SNR = 10log_{10}\left[\frac{1}{N\sigma^2}\left(\sum_{i=1}^{N} r_i(0) - \sigma^2\right)\right] \tag{69}$$

3.2.2.3 Channel Frequency Estimation

After having synchronized the OFDM frame, it is time to obtain the CFR. In our channel sounder, we use the OFDM CFR estimator proposed in [49]. In this sounding scheme, the emitted OFDM frame is known in advance by the receiver. As a consequence, we can treat each one of the data symbols as pilot symbols. The process of obtaining the CFR estimation can be expressed as it appears in Eq. 70, i.e. we average the least squares (LS) estimation [102] of each of the S_i symbols of the OFDM frame. The N parameter (number of OFDM symbols) can be defined by the user in function of the channel coherence time as well as on the power noise level.

$$\hat{H} = \frac{1}{N}\sum_{i=1}^{N} LS(S_i) \tag{70}$$

We can compare the performance of this proposed CFR estimator in terms of its MSE error in the presence of WGN. The results can be found in Fig. 39. In this simulation we took into account our OFDM frame (8 data symbols with 64 subcarriers). Each point of the graph represents the MSE error for a determined SNR value. Assuming the error behavior can be modeled as a Gaussian random variable, the error bars in the graph are the computed standard deviation at each SNR value.

Based on this algorithm, we can also define a method to evaluate the validity of a CFR

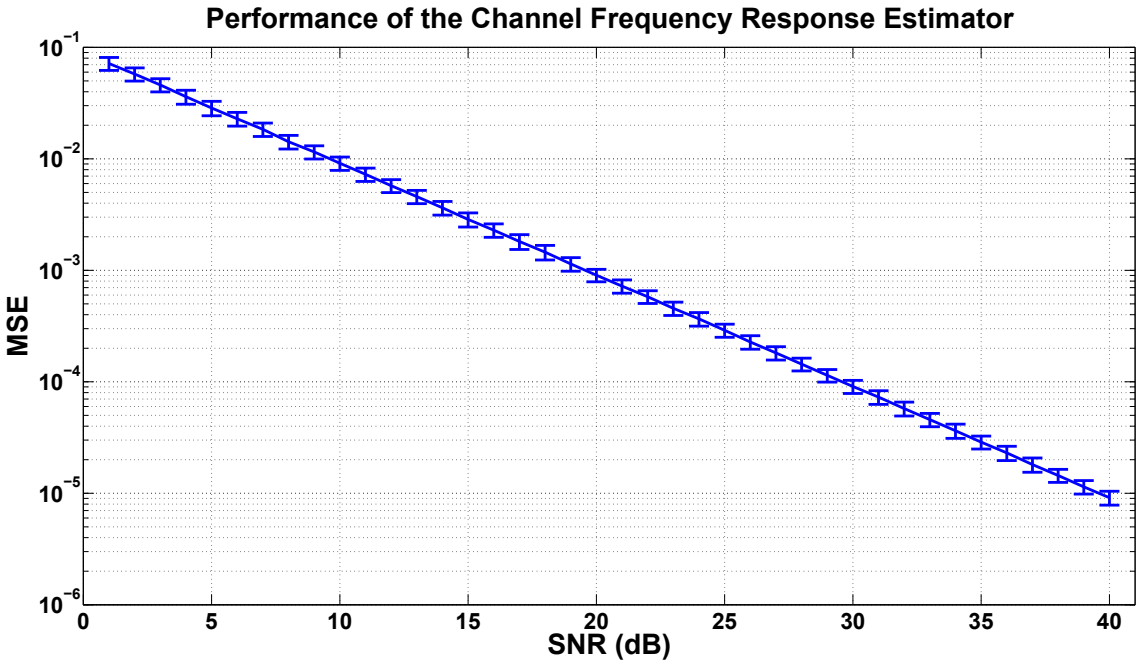

Figure 39: Performance of the CFR Estimator in Presence of WGN.

estimation for channel sounding purposes. According to Eq. 70, the CFR estimation performed over an OFDM frame is an average of N classical LS estimations [102]. In the following, a CFR estimation will be considered valid if the N OFDM symbols composing the frame can be equalized employing the CFR without errors under the hard-decision criterion. The equalized QPSK symbols at the k-th subcarrier from the i-th OFDM symbol ($X^i_{eq}(k)$) are obtained at the receiver side as it shown in Eq. 71. This method ensures that the channel properties remain constant over the OFDM frame duration, i.e. the channel coherence time is at least 51200 ns in our case. The hard-decision criterion is represented graphically in Fig. 40.

$$X^i_{eq}(k) = Y^i(k)/\hat{H}(k) \tag{71}$$

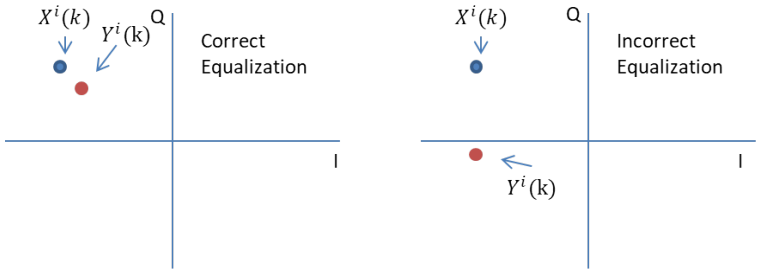

Figure 40: Hard Decision Method.

3.2.2.4 Multipath Estimation

The signal model we will use can be described as it appears in Eq. 72. In this situation $x(n)$ is the sampled OFDM symbol, L is the maximum resolvable path, which is determined by the length of the cyclic prefix (CP), K_i is the path's gain and v is white Gaussian noise. We will assume CFO and STO are perfectly estimated before applying this method.

$$s(n) = \sum_{i=0}^{L-1} K_i x(n-i) + v(n) \tag{72}$$

Assuming the SNR is high enough, each point of the 64-point CFR estimation $\hat{H}$ obtained in Sec. 5.5.2 can be approximated as we show in Eq. 73.

$$\begin{aligned} \hat{H}(k) &= \frac{S(k) + V(k)}{X(k)} \\ &= \frac{\sum_{i=0}^{L-1} K_i X(\omega_k) e^{-j2\pi ki}}{X(k)} + N(k) \\ &= \sum_{i=0}^{L-1} K_i e^{-j2\pi ki} + N(k) \quad k = 0, \cdots, 63 \end{aligned} \tag{73}$$

The problem of finding the CIR has been reduced to find the K_i values which minimize the classical Least Squares Error problem described by Eq. 74.

$$\underset{K_i}{\operatorname{argmin}} \sum_{k=0}^{64} \left|\left| \hat{H}(k) - \sum_{i=0}^{L-1} K_i e^{-j2\pi ki} \right|\right|^2 \tag{74}$$

The K_i values are found through Eq. 75, where $K = [k_0 \quad k_1 \quad \cdots \quad K_{15}]^T$, $\hat{H} = \left[\hat{H}(0) \quad \hat{H}(1) \cdots \hat{H}(63)\right]$ and M is the matrix

$$M = \begin{bmatrix} 1 & e^{-j2\pi i_1 \times 1/64} & e^{-j2\pi i_2 \times 1/64} & \dots & e^{-j2\pi i_{15} \times 1/64} \\ 1 & e^{-j2\pi i_1 \times 2/64} & e^{-j2\pi i_2 \times 2/64} & \dots & e^{-j2\pi i_{15} \times 2/64} \\ \vdots & \vdots & \vdots & \vdots & \vdots \\ 1 & e^{-j2\pi i_1 \times 63/64} & e^{-j2\pi i_2 \times 63/64} & \dots & e^{-j2\pi i_{15} \times 63/64} \end{bmatrix}$$

As we can see, the $(M'M)^{-1}M'$ product is a fixed N × M matrix where M is the number of OFDM subcarriers and N is the length of the CP. Such a matrix can be stored in the system memory in order to save resources for real time channel estimation.

$$K = (M'M)^{-1} M'\hat{H} \tag{75}$$

3.2.2.5 Example of Use

In this section, we show how our sounder is capable to characterize a 2 - path channel in both frequency and time domain with Vector Network Analyzer (VNA) like performance in the 2.3 GHz frequency band. The experiment setup is shown in Fig. 41.

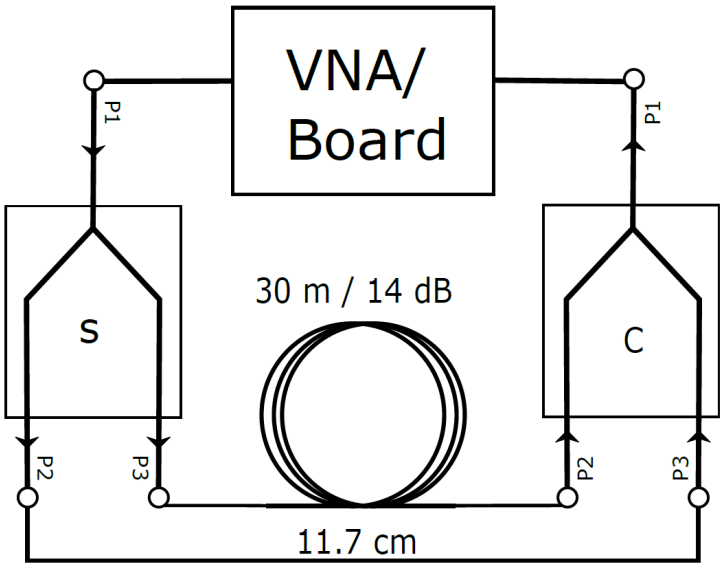

Figure 41: 2-Path Laboratory Setup.

The 2-path situation is achieved by using two power dividers/combiners (S and C respectively) and 30 meters of RG213/U 50 Ω cable. The signal at the input port of the power

divider S ($S_{P1}(t)$) is divided in two different signals, respectively called $D(t)$ and $L(t)$. These signals are combined by C after having propagated by different paths. The signal $C_{P1}(t)$ at the C output port can be written as $CP1(t) = D(t) + L(t) = D(t) + De^{-\alpha l}(t - l/c_0)$, where α is the attenuation factor of the cable measured in dB/m, l is the length of the cable (30 m in our case) and c_0 is the light propagation velocity in the cable, 0.66c according to the datasheet. We did not measure α. Instead, the total attenuation of the cable was obtained, giving a value of 14 dB. No other parasite effect of the cable was taken into account. Under these assumptions, $L(t)$ signal must be a 14 dB attenuated 151.51 ns delayed replica of D(t).

The VNA used is the ZVA40 model from Rohde Schwarz R equipped with the ZVAX-TRM40 extension unit already mentioned in section 3.1.6. The OFDM channel sounder consists of the Avnet's PicoZed SDR 2x2 SOM which integrates the Xilinx Z7035 Zynq R -7000 All Programmable SoC with the Analog Devices AD9361 integrated RF Agile Transceiver. In this case, this board was used at the same time for emitting and receiving tasks.

The frequency behavior of the channel can be obtained by exploiting the S-parameters of the 2 port network with the help of the VNA. In that case, the transfer function of the network (CFR) is then obtained as the S_{21} parameter. Later, we transmit a series of OFDM frames over the network by using 2 ports of the Avnet board. One for emitting the OFDM frames at the input port of S and the other one connected to C output port in order to receive the packets. In Fig. 42, we show both amplitude normalized frequency spectra obtained through the S_{21} parameter and the amplitude of the CFR obtained with the method exposed in section 3.2.2.3. Both curves show a great agreement with theoretical two-wave interference spectrum, which is given by Eq. 76 and derived from the experiment's setup. In Eq. 76, L is the loop length 30 m and d is the length of the shorter path, i.e 11.7 cm. As we normalize the spectrum amplitude, the a value representing the amplitude of the signal arriving through the shorter path can be arbitrarily chosen. The b amplitude is then determined as $b = a10^{14/20}$.

$$A = \left[a^2 + b^2 + 2abcos\left(\frac{2\pi f}{c'}(L - d)\right)\right]^{\frac{1}{2}} \tag{76}$$

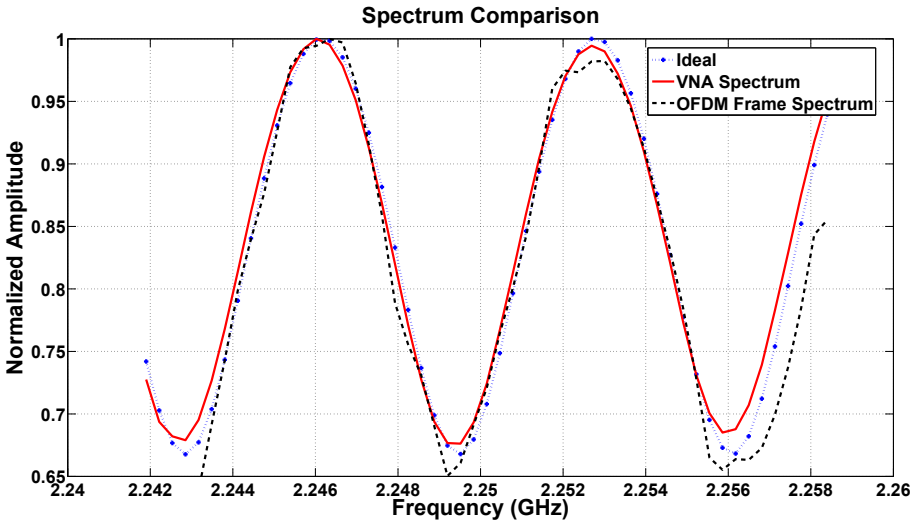

Figure 42: 2-Path CFR Comparison.

In order to obtain the CIR, we apply the method in section 3.2.2.4 to both CFRs, the one obtained with the VNA and the ones from the OFDM frames. The result can be found in Fig. 43, where we show the power contribution of each one of the K_i variables in Eq. 72. This representation is equivalent to the PDP of the 2-path network. Having normalized the power contribution to K_0, we see how the power contribution of K_4 (i.e the $\approx$ 150 ns replica) is -14.89 dB in the case of the CIR obtained for the VNA CFR and -12.19 dB for the CIR obtained through OFDM sounding. A quite convenient result taking into account the cost of both equipments.

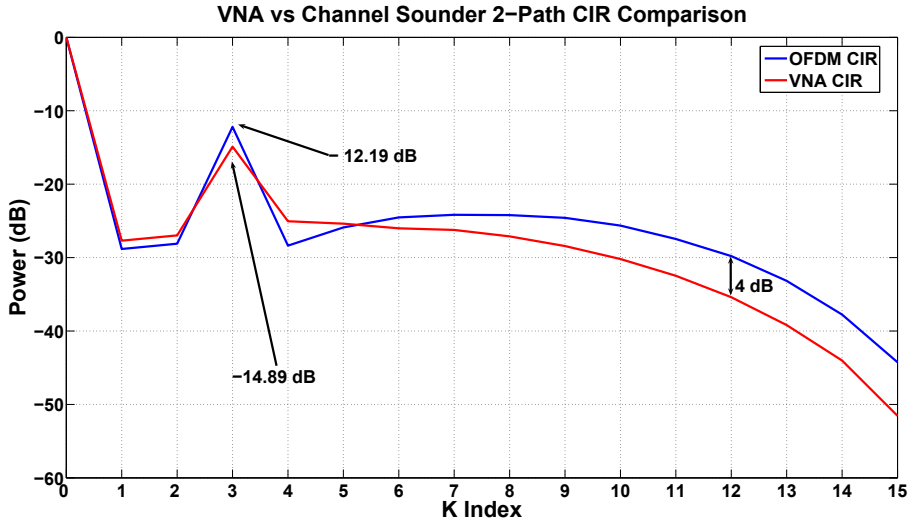

Figure 43: 2-Path CIR Comparison.

3.3 Flight Prototype

The final prototype of the embedded OFDM channel sounder based on the Avnet's Picozed board can be seen in Fig. 44. In the figure, we find the main elements necessary for its operation: these are the power supply system, which uses two Li-ion batteries, a specially designed circular patch antenna, the Avnet's Picozed board, and the projectile itself. All these elements are mounted on a support structure (in black) in order to integrate the electronics in the projectile. Once the projectile is equipped with the channel sounder, the integrated electronics are molded inside the projectile with an epoxy resin. This epoxy keeps the electronics safe in both blast and impact conditions. Finally, the white conical element at the rear of the projectile acts as an aerodynamic stabilizer. Additionally, it serves also as a protection for the antenna surface against the hot gases inside the firing chamber of the cannon.

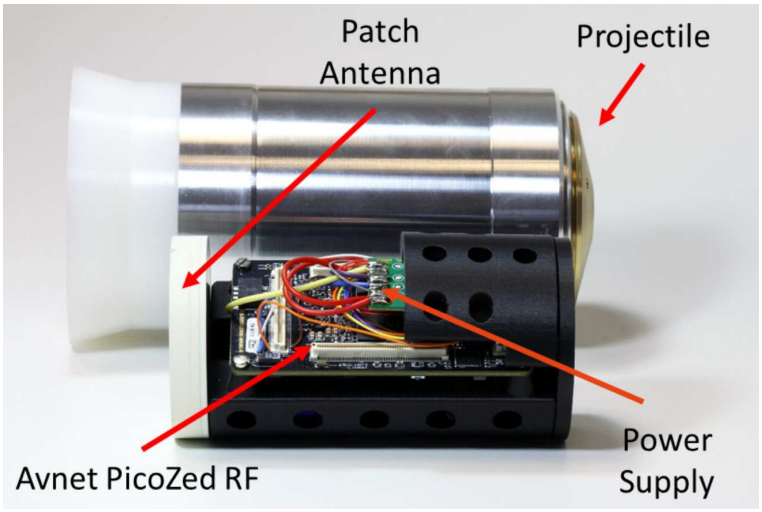

Figure 44: OFDM Channel Sounder Prototype

The engineering model of the prototype can be found in Fig. 45[1]. We can better appreciate in this drawing the space constraints we have to face in instrumented projectiles. As we can see, the projectile can be seen as a 192.2 mm length cylinder with a diameter of 91 mm.

[1]Prototype conceived by Andreas Zeiner from the ABX group at ISL

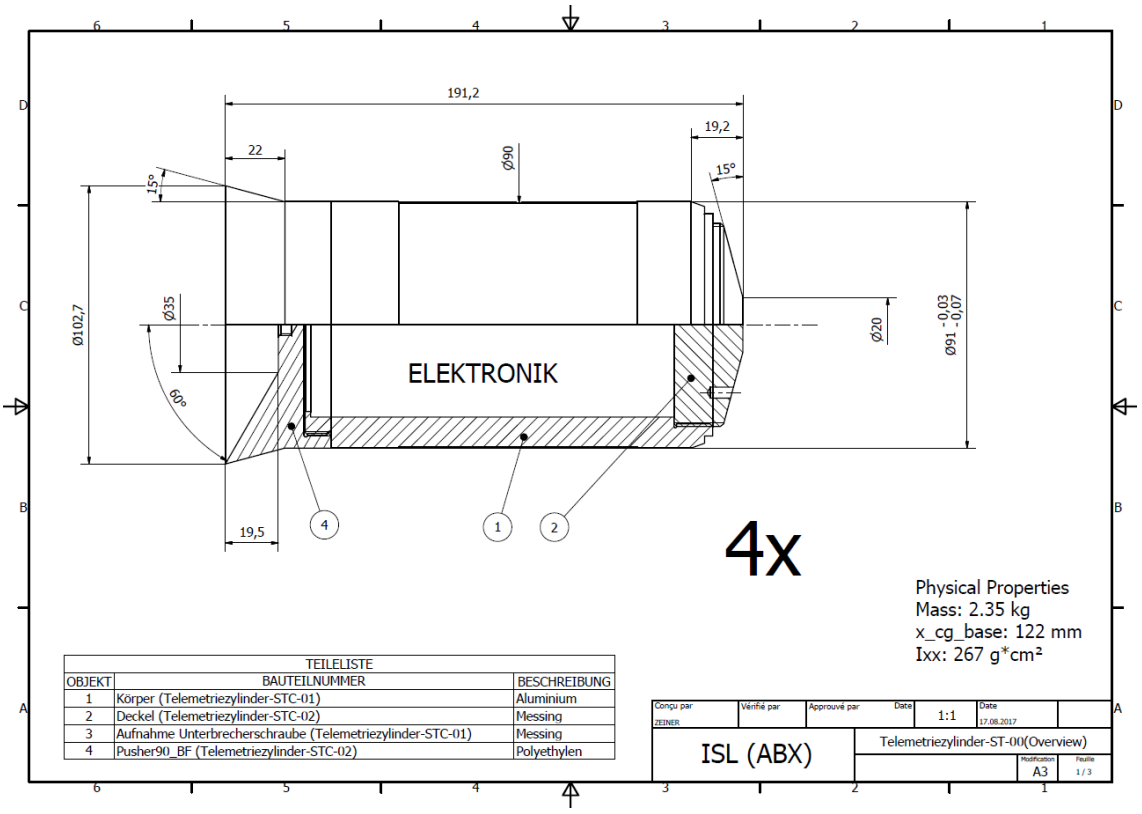

(a) Channel Sounder Prototype: Technical Drawing.

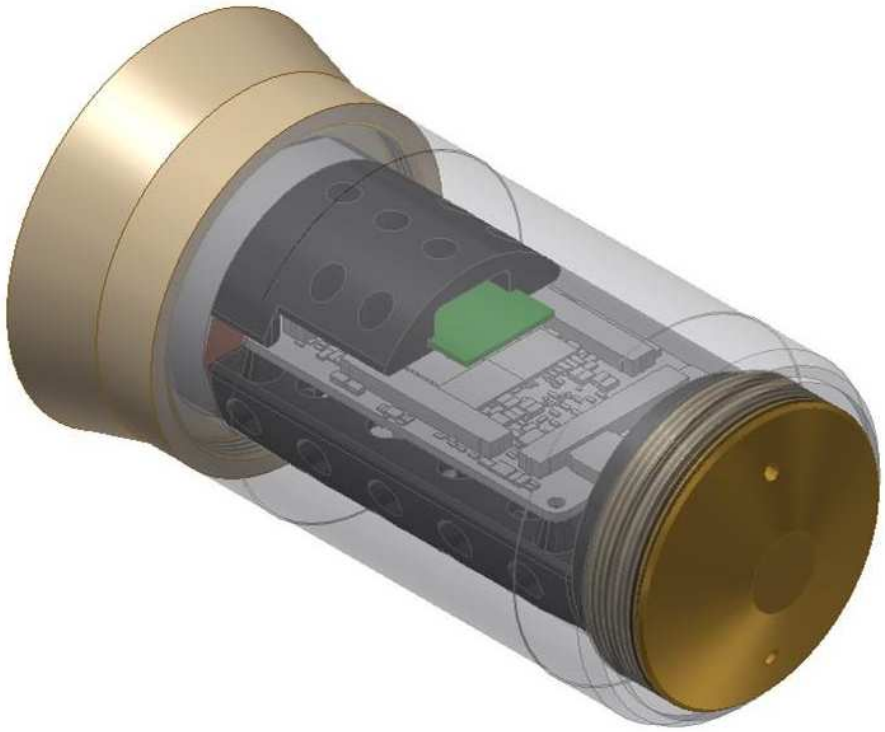

(b) Channel Sounder Prototype: 3D - Model.

Figure 45: Engineering Model of the Embedded OFDM Channel Sounder.

3.4 Conclusions: Deploying the Channel Sounder

In this chapter we have presented the problem of conceiving a channel sounder with a limited amount of resources. We started in section 3.1 by enumerating the instruments, tools and facilities available at the beginning of this thesis. This is a really important step to do as it allows to set the limits of what we can do according to our resources.

We proposed in section 3.2 a channel sounding method based on the OFDM technique and SDR devices. In order to introduce our channel sounding procedure, it was necessary to familiarize the reader with the OFDM transmission technique. After that, the basics of its capabilities for channel sounding can be understood. Additionally, the elements which can affect its performance were studied in order to account for them in the final solution. We continued in a second stage with the proposition of a channel sounding methodology. The main elements considered for its conception were the environment of where the channel sounder is going to be operated and the limitations set by our radio equipment. The important aspects in OFDM like frame duration, sampling rate, number of subcarriers, etc., were defined. The proposed sounding methodology allows to obtain both frequency and time properties at the same time by taking advantage of the OFDM transmission. Finally, the prototype of the instrumented projectile carrying the channel sounder was presented in section 3.3.

At this point, we are ready to perform a channel sounding campaign at the Baldersheim firing site. However, it was necessary to perform a preliminary study of the firing conditions. Effectively, a firing campaign is costly regarding the equipment used and staff involved. We have to consider the possibility of completely destroying the prototype and not being able to reuse it. For that reason, we performed a series of studies in order to have a rough idea of what we can expect in the firing campaign in chapter 4.

CHAPTER IV

PRELIMINARY STUDY OF THE PROPAGATION CHANNEL

The conception of a digital transceiver for projectile applications requires from a precise characterization of the wireless radio channel. As it was introduced in chapter 2, the radio engineer has two different strategies for approaching this problem: either by means of simulations or by performing channel sounding.

In projectile applications, the flight mechanics of the projectile have to be taken into account in the modeling of the propagation channel. However, the study of their implications in the communication link is a demanding task from the operational point of view. Certainly, firing campaigns are expensive and they depend on a multiplicity of factors, i.e. pyrotechnical staff, availability of the firing field, delays in the development of the projectile prototype, etc. For these reasons, it is useful to have instruments allowing us to reproduce the flight behavior of the projectile in laboratory. In this thesis, two flight mechanics will be considered: spinning and nutation, both of them presented in section 4.1.

We will continue by studying their implications in channel modeling in section 4.2. Nutation will be studied by means of simulations while the impact of the spinning on the received signal will be experimentally treated.

The results out of these simulations and experiments will lead to an analysis of the Doppler shift observed in real firings in section 4.3. As a result, we will knowledge about what to expect when performing channel sounding with our OFDM embedded channel sounder.

Finally in section 4.4, we will set the basis for a full wideband characterization of the propagation channel at ISL's firing range facility.

4.1 *The Projectile's Attitude and the Implications on the Doppler Shift*

In this section, we introduce some aspects related to the projectile's attitude. In aeronautics, the word *attitude* makes reference to the orientation of a body with respect to a given reference frame. As it is shown in Fig. 46(a) for the case of an aircraft[1], the attitude of the body can be given in function of three angles. They are, respectively, the yaw pitch and roll angles.

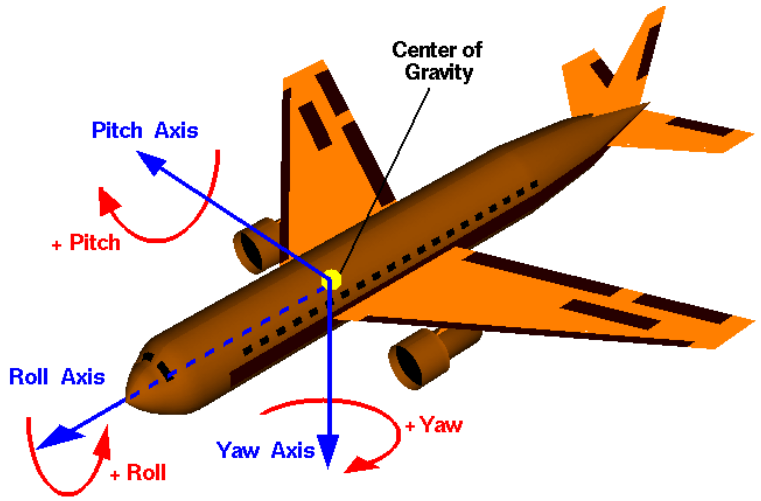

(a) Attitude angles.

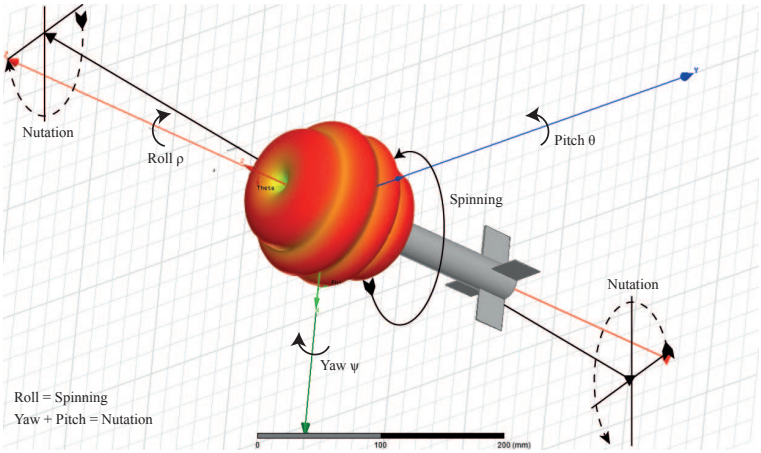

(b) Nutation and Spinning in a Projectile.

Figure 46: Attitude Considerations.

In Fig. 46(a), the yaw angle is defined in the plane containing the wings and the nose of the aircraft. The movement from side to side of the aircraft's nose over this plane is

[1]Image available at https://www.grc.nasa.gov/www/k-12/airplane/rotations.html

called yaw movement. The pitch movement is the up-down movement of the aircraft's nose in the plane which contains the nose and the perpendicular vector to both wings and nose. Finally, the roll angle is the up-down movement of the wings. In the case of a projectile, the definition of the attitude angles is equivalent as we can see in Fig. 46(b). In the following sections 4.1.1 - 4.1.2, we will present two aerodynamic effects: nutation and spinning. As we will see, they can be modeled in terms of the three attitude angles.

Before continuing with the next sections, it is necessary to define the projectile's reference frame. As shown in Fig. 47, it will be defined in function of the classic euclidean axes and the three mentioned attitude angles: ψ (yaw), θ (pitch) and ϕ (roll).

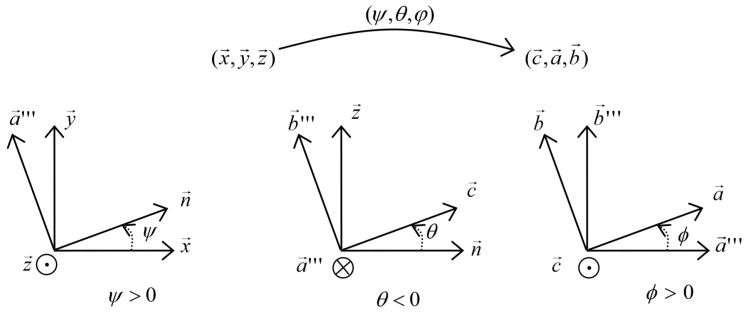

Figure 47: Projectile's Attitude Reference Frame

In this frame, z-axis points towards the center of the earth and the x-axis is aligned with the projectile's longitudinal axis. Additionally, the y-axis points according to the left hand rule. Hence, the attitude matrix A is a composition of three rotation matrices as we show in Eq. 77, where each one of the matrices B, C and D respectively correspond to the rotation matrices of the yaw, pitch and roll angles.

$$\mathbf{A} = \mathbf{BCD} \tag{77}$$

$$\mathbf{B} = \begin{bmatrix} cos(\psi) & sin(\psi) & 0 \\ -sin(\psi) & cos(\psi) & 0 \\ 0 & 0 & 1 \end{bmatrix} \tag{78}$$

$$\mathbf{C} = \begin{bmatrix} cos(\theta) & 0 & -sin(\theta) \\ 0 & 1 & 0 \\ sin(\theta) & 0 & cos(\theta) \end{bmatrix} \tag{79}$$

$$\mathbf{D} = \begin{bmatrix} 1 & 0 & 0 \\ 0 & cos(\phi) & sin(\phi) \\ 0 & -sin(\phi) & cos(\phi) \end{bmatrix} \tag{80}$$

4.1.1 Spinning

Spin stabilization is a technique used in ballistics in order to keep the projectile pointed to the right direction in an efficient flight. Depending on the payload and the projectile's propulsion system, a spin-stabilized projectile will suffer from some undesired effects. This is an issue in the case of missiles. In these applications, where liquid propellant is commonly employed in the propulsion system, this stabilization method can make the fuel to spin along with the object. As a consequence, additional forces will appear acting on the projectile's body and the flight can prematurely terminate. In [33], a trajectory prediction model for liquid-payload projectiles is presented. Such trajectory predictions require the development of non-linear models with 6 degrees of freedom where the Newton's equations of motion, the payload, the influence of the earth's rotation, the Magnus effect, the atmospheric wind and the air density should be taken into account [37].

A characterization of the projectile's flight is not the objective of this section. For that reason, we will assume a simplified case. In our assumption, we will always consider a gun fired projectile (no liquid propellant) flying on a straight trajectory. In this situation, the spin movement can be simplified and described in terms of the D matrix (Eq. 80). Taking advantage of this simplification, we can focus on characterizing the impact from spinning at the receiving station.

As we will show, the spinning of an electromagnetic source shifts the carrier frequency. From the point of view of the receiver, this frequency shift can be confused with the traditional Doppler shift. If the source of electromagnetic waves is a spin-stabilized instrumented

projectile, this shift is caused due to the changing aspect at which the antenna phase pattern is viewed.

The effect of spin-stabilized emitting devices on the received signal has been studied from the beginning of satellite communications, where it was common to use circularly polarized signals emitted by turnstile antennas [65]. Contemporaneously, the same effect was observed in projectile communications where linearly or elliptically polarized radio waves were studied [60]. In GPS applications, this effect has been given the name of *phase wrap-up* and its implications have a major importance when ultra high accuracy is required if less than 4 GPS signals are available [98].

A rigorous explanation of the physics behind this phenomenon has been recently given by Mashhoon [66]. His treatment of the problem was considered as one of the possible explanations of the Pioneer anomaly [101]. This anomaly, which is a deviation between the predicted and the obtained data from the *Pioneer* 10/11 spacecrafts was considered to have its origin in the rotation of the spacecraft. Finally, this hypothesis was discarded as shown by Anderson in a paper written in conjunction with Mashhonn [8]. In this paper, they explain how the additional shift introduced by the rotation of the antennas was already compensated at the beginning of the mission by the communications team.

Let us consider the case of a source of circularly polarized planar waves, the electric field of this wave can be expressed as $\vec{E}(t) = cos(\omega_c t)\hat{x}' \pm sin(\omega_c t)\hat{y}'$ in a determined point in the space. The $\pm$ symbol accounts for both wave polarization cases: LHCP (Left Hand Circular Polarization) and RHCP (Right Hand Circular Polarization). In the figure, the $\hat{x}' - \hat{y}'$ frame is attached to the emitting source and $\omega_c = 2\pi f_c$ is the carrier frequency.

If the source of electromagnetic waves rotates at a constant angular velocity $\omega_r = 2\pi fr$, it is possible to express the measured electric field for a non-accelerated observer in the $\hat{x} - \hat{y}$ frame. The situation is illustrated in Fig. 48.

The components of the measured electric field can be obtained through the corresponding rotation matrix in Eq. 81, where each field component can be obtained as it follows:

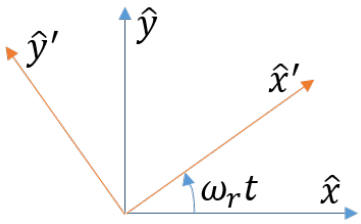

Figure 48: Spinning Electric Field.

$$\begin{bmatrix} E_x \\ E_y \end{bmatrix} = \begin{bmatrix} cos(\omega_r t) & -sin(-\omega_r t) \\ sin(\omega_r t) & cos(\omega_r t) \end{bmatrix} \begin{bmatrix} cos(\omega_c t) \\ \pm sin(\omega_c t) \end{bmatrix} \tag{81}$$

$$\begin{aligned} E_x &= cos(\omega_c t)cos(\omega_r t) \mp sin(\omega_c t)sin(\omega_r t) \\ &= \frac{1}{2}\{cos((\omega_c + \omega_r)t) + cos((\omega_c - \omega_r)t) \mp cos((\omega_c - \omega_r)t) \pm cos((\omega_c + \omega_r)t)\} \\ &= cos((\omega_c \pm \omega_r)t) \end{aligned} \tag{82}$$

$$\begin{aligned} E_y &= cos(\omega_c t)cos(\omega_r t) \pm sin(\omega_c t)cos(\omega_r t) \\ &= \frac{1}{2}\{sin((\omega_c + \omega_r)t) - sin((\omega_c - \omega_r)t) \pm sin((\omega_c + \omega_r)t \pm sin((\omega_c - \omega_r)t)\} \\ &= \pm sin((\omega_c - \omega_r)t) \end{aligned} \tag{83}$$

We have derived the expression for the frequency shift introduced by the spinning of the electromagnetic source in the case of circularly polarized (CP) waves. The generalization for elliptically polarized electromagnetic sources can be found in [60]. According to Mashhoon, the angle of incidence of the impinging wave with respect to the observer will also modify this shift as it appears in Eq. 84, where α is the angle of incidence.

$$f_D = \pm f_r cos(\alpha) \tag{84}$$

4.1.2 Nutation

In our case, nutation is an undesired effect which should be kept to the minimum in order to not affect the projectile's trajectory. In nutation movement, both center of air pressure and center of mass are implied [67]. In flight, the center of pressure is slightly ahead of the

center of mass. The combination of this situation along with the projectile's spinning will produce a small rotation at the projectile's tip.

Nutation can be modeled as a composite movement of the yaw and pitch angles. In order to obtain the N matrix which describes this movement, we can set to zero the roll angle in Eq. 77.

$$\mathbf{N} = \begin{bmatrix} cos(\psi)cos(\theta) & sin(\psi)cos(\theta) & -sin(\theta) \\ -sin(\psi) & cos(\psi) & 0 \\ cos(\psi)sin(\theta) & sin(\psi)sin(\theta) & cos(\theta) \end{bmatrix} \tag{85}$$

In the following, we will assume an harmonic behavior for both ψ and θ angles as it appears in Eq. 86 - 87.

$$\psi = \psi_{max} cos(2\pi f_{\psi} t + \alpha_{\psi}) \tag{86}$$

$$\theta = \theta_{max} cos(2\pi f_{\theta} t + \alpha_{\theta}) \tag{87}$$

We will consider the same maximum angle of excursion for both angles $\psi_{max} = \theta_{max}$, the same rate of change $f_{\psi} = f_{\theta} = f_p$ and a 90° phase difference between them, i.e. $\alpha_{\theta} = \alpha_{\psi} \pm \pi/2$. The ISL attitude studies on this subject have set a maximum excursion angle for both yaw and pitch of 4°, while f_p can vary from 0 to 100 Hz. The characteristic movement of a nutating projectile under these conditions is shown in Fig. 49 for $\psi_{max} = 4^o$ and $f_p = 50$ Hz. The evolution of yaw and pitch angles can be found in Fig. 49(a) for a period of 100 ms. The projectile's tip position with respect to the Y-Z plane can be found in Fig. 49(b). Here, we can see how the radius of the circumference is approximately 3.5 cm for a 1 m projectile. Finally, the whole sketch is shown in Fig. 49(c) where $\omega_p = 2\pi f_p$ and $\omega_r = 0$ (no spinning).

In the instrumented projectiles developed at ISL, the antenna is either placed at the projectile's tip or at the tail. As we have shown in Fig. 49, the nutation movement will make the antenna to draw a spiral-like movement over its path, this will introduce an additional component in the Doppler shift which will be characterized through simulations.

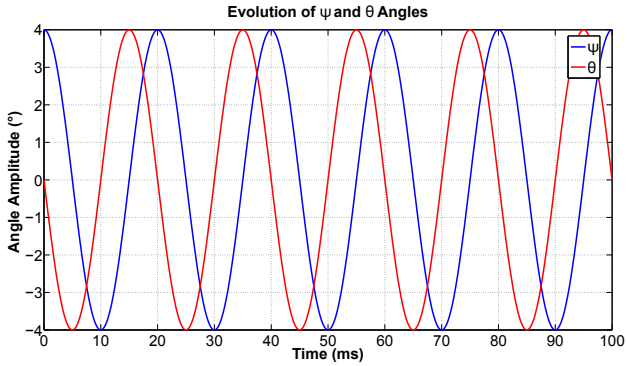

(a) Evolution of Pitch and Yaw Angles.

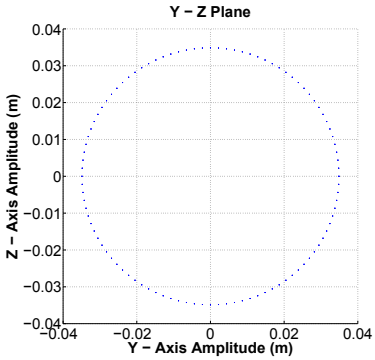

(b) Projectile's Tip Movement in the Y-Z Plane.

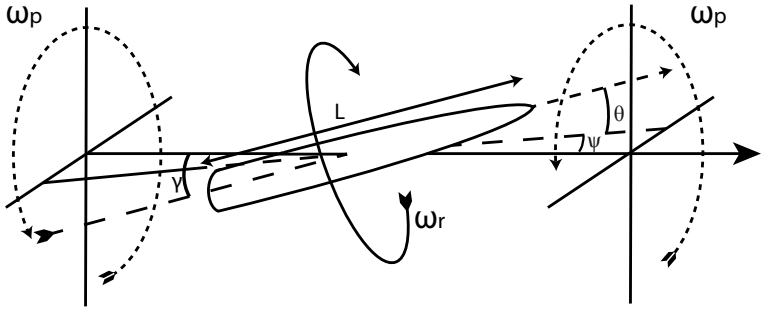

(c) Nutation Effect on the Projectile's flight.

Figure 49: Nutation Movement.

4.2 Nutation & Spinning: Laboratory Testing.

The objective of this section is to study these two effects in laboratory. Before performing a firing campaign, we need to know in advance which effects will have an impact on the received signals and which ones can be excluded in the channel characterization process. Later in the real firing campaign, we will focus our attention on the right channel parameters to model. Secondly, it is not possible to perform a firing campaign every time a channel property needs to be studied. For that reason, a simulation software is a powerful tool in order to keep both time and budged under control.

In this section, we will detail the testing performed in laboratory with the objective of finding the main properties of the channel in real conditions. Firstly, we performed a set of simulations with the RapSor software in section 4.2.1. By means of these simulations, the impact of the nutation on the received signal will be obtained. Additionally, the capabilities of this simulation software will be exploited in order to have a first insight into the channel

Doppler characteristics. The evolution of the Doppler shift for the LOS component and the influence of the multipath effect in the Doppler spectrum will be estimated.

In a second stage, we will focus our attention on the characterization of the spinning effect in the radio channel. For this purpose, section 4.2.2 has been divided in two subsections: we present in section 4.2.2.1 the experimental setup we built in conjunction with the testing conditions. The data analysis and the results concerning this question will be presented in 4.2.2.2.

The analysis performed in this section will allow us to gain knowledge about the channel properties. In order to verify the results obtained from our simulations and laboratory experiments, the telemetry data from a previous projectile firing campaign will be treated in section 4.3. We will show how we are able to reuse the recorded data for channel estimation purposes even when it was not initially intended for this purpose. This analysis will help us to accept or not the results out of our laboratory testing.

4.2.1 Simulations: Nutation & Multipath Effect

We will start this section with the simulations corresponding to the study of the implications of the projectile's nutation on the Doppler shift. For this purpose, we will utilize a simplification of the ISL's experimental field in Baldersheim. A sketch of the scene utilized in the simulation is shown in Fig. 50.

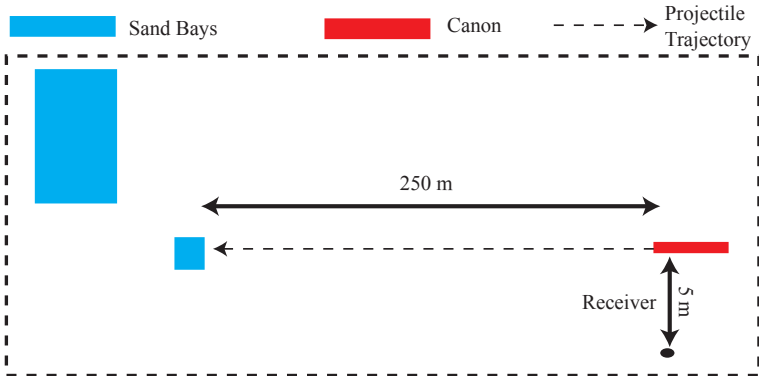

Figure 50: Baldersheim Simplification

The main environmental elements taken into account were the ground (in our case it could be modeled by asphalt) and the receiving blocks. The electromagnetic properties required to

launch the simulation were obtained in [57] and they can be found in Tab. 6. The position of the cannon is also indicated in the figure for illustrative purposes.

Table 6: Material Electrical Properties

	Electrical Conductivity σ(S/m)	**Relative Electrical Permittivity ϵ_r (No Units)**
Asphalt	2E-3	6
Sand Bays	1E-1	9

In order to study the impact of the nutation on the Doppler shift, we assumed a projectile flying along a straight path (no parabolic flight) during the first 31 ms of flight. The result of the simulation is shown in Fig. 51. The blue line corresponds to the computed Doppler shift because of the flying speed of the projectile. In the simulation, this speed was considered to be 680 m/s. Up to this point, only the LOS path was considered with the following nutation conditions for the projectile: $f_\psi = f_\theta = 100$ Hz and $\psi_{max} = \theta_{max} = 4°$. The red line corresponds to a simulation along the same path for a non-nutating projectile. In both cases, the frequency of the single carrier emitted by the antenna was set to 2.3 GHz. This frequency band is the most common one for the embedded telemetry systems utilized at ISL, which are designed to be compliant with the IRIG106 standard [41].

Neither the frequency nor the deviation angle were chosen arbitrarily for the simulation. They correspond to empirically measured values during several firing campaigns at ISL. It was determined that the typical range of the nutation angular frequency is 30 -100 Hz. The deviation angle has a maximum value of 4^o for the tested projectiles. Indeed, the simulation was carried out in order to account for the worst case possible.

Regarding the simulation results, we can conclude the nutation effect will not have a significant impact at the receiver. If we look more precisely at the Doppler frequency values caused by nutation, we can observe they are around 10 Hz (zoomed part in Fig. 51). This is negligible compared with the expected high Doppler shift values in the order of several kHz due to the projectile's supersonic speed. For that reason, the nutation effect will be excluded from the channel modeling.

Taking advantage of the RaPSor software capabilities, we can analyze at the same time

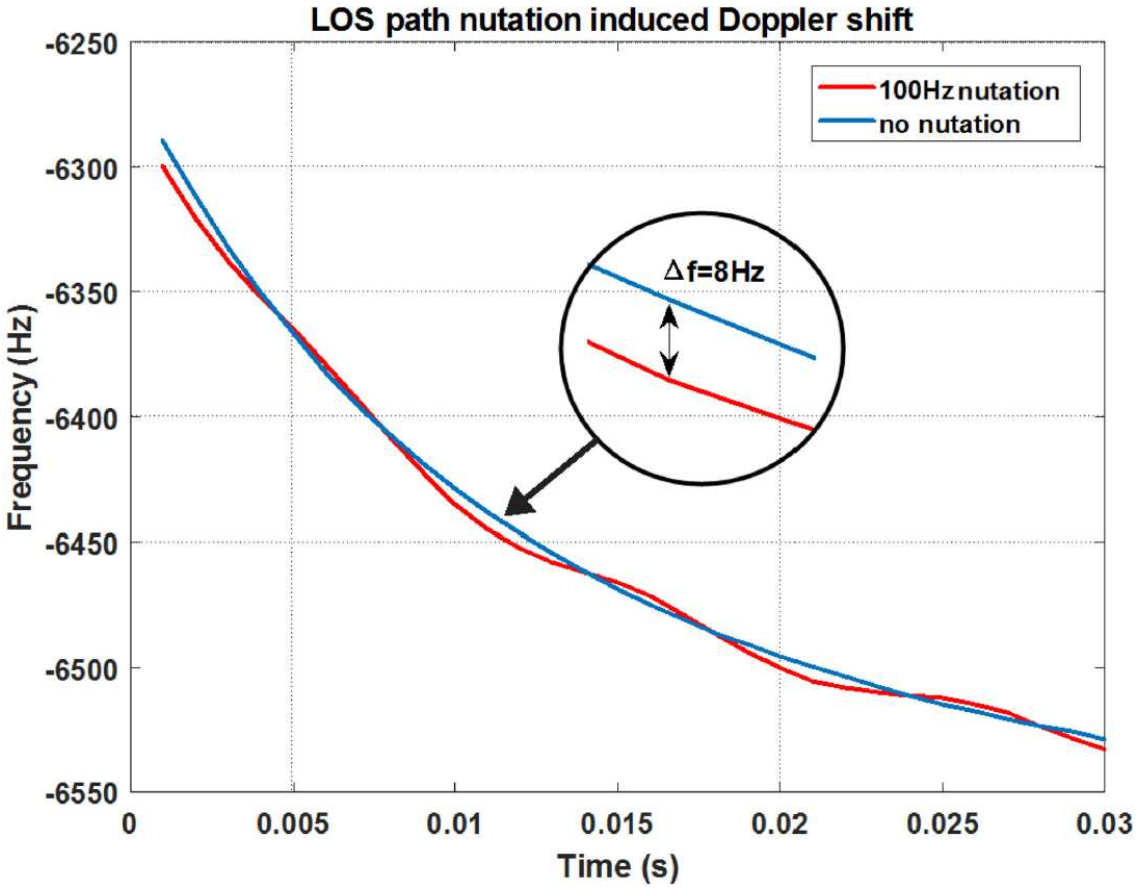

Figure 51: Nutation Impact on the Doppler Shift.

the impact of the multipath effect in this propagation environment. For this purpose, a much more complete propagation scenario was simulated in RaPSor. In fact, we took into account most of the buildings present at the Baldersheim testing field.

An example of the graphical RaPSor output for this situation can be found in Fig. 52. As we can see, the 3D view gives visual information about the propagation paths found by RaPSor.

As we notice in Fig. 23, Baldersheim testing facility is a quite isolate area in the middle of a forest. In RaPSor, it is easy to model buildings. However, the inclusion of foliage is an issue as it was initially designed for indoor environments. In a first approach, we have considered that the diffuse Multipath Components (MPCs) due to the foliage were not as powerful as the specular MPCs. Consequently, we did not take them into account in the simulation.

The simulation results for an omnidirectional receiving antenna located as in Fig. 50

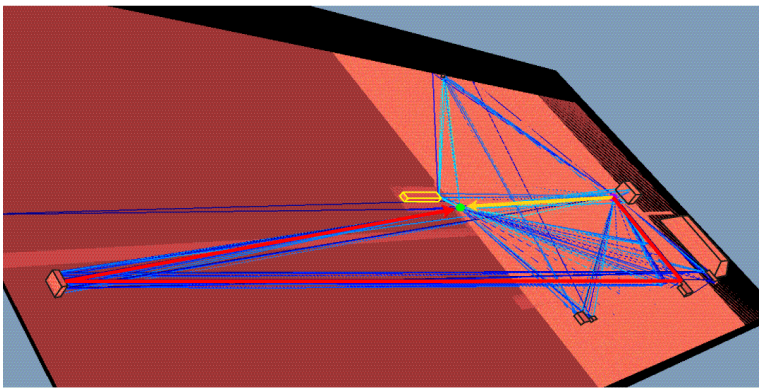

Figure 52: Baldersheim Propagation Scenario.

are shown in Fig. 53. As we can see, it shows two power dominant paths which are always present during the flight, one of them being the LOS path. We can see how the software finds a destructive interference 0.01 s after the firing instant causing the LOS path the only one contributing to the received power. Fig. 53 shows the power evolution of these two paths (blue and orange curves). On the same figure, we have also represented the evolution of the power of the remaining MPCs (red curve) and the Rice K factor (i.e. the ratio of the LOS power over the scattered power).

RaPSor also allows to have a first insight into the Doppler spectrum. In a propagation scenario as the one we are concerned, the LOS path is obviously a determinant part in the resultant Doppler shift. This can be clearly seen in Fig. 54, which shows the Doppler shift evolution during the flight for the LOS path (red curve). In the same figure, the Doppler shift when the totality of the MPCs have been taken into account (black curve) is also showed.

The hundreds of Hz of difference between the red curve (LOS Doppler Shift) and the black curve (Doppler Shift taking into account all the MPCs components) can be explained by the fact that some significant (i.e. in power and angle) MPCs appear or disappear because of the interactions with the environment. This behavior will be later studied by experimentation in section 4.3. As it will be shown, the observed variations in the simulation and the ones corresponding to the measurements do not appear at the same time instants. This is because of the configuration of the receiving station. In the experimentation case, it was equipped

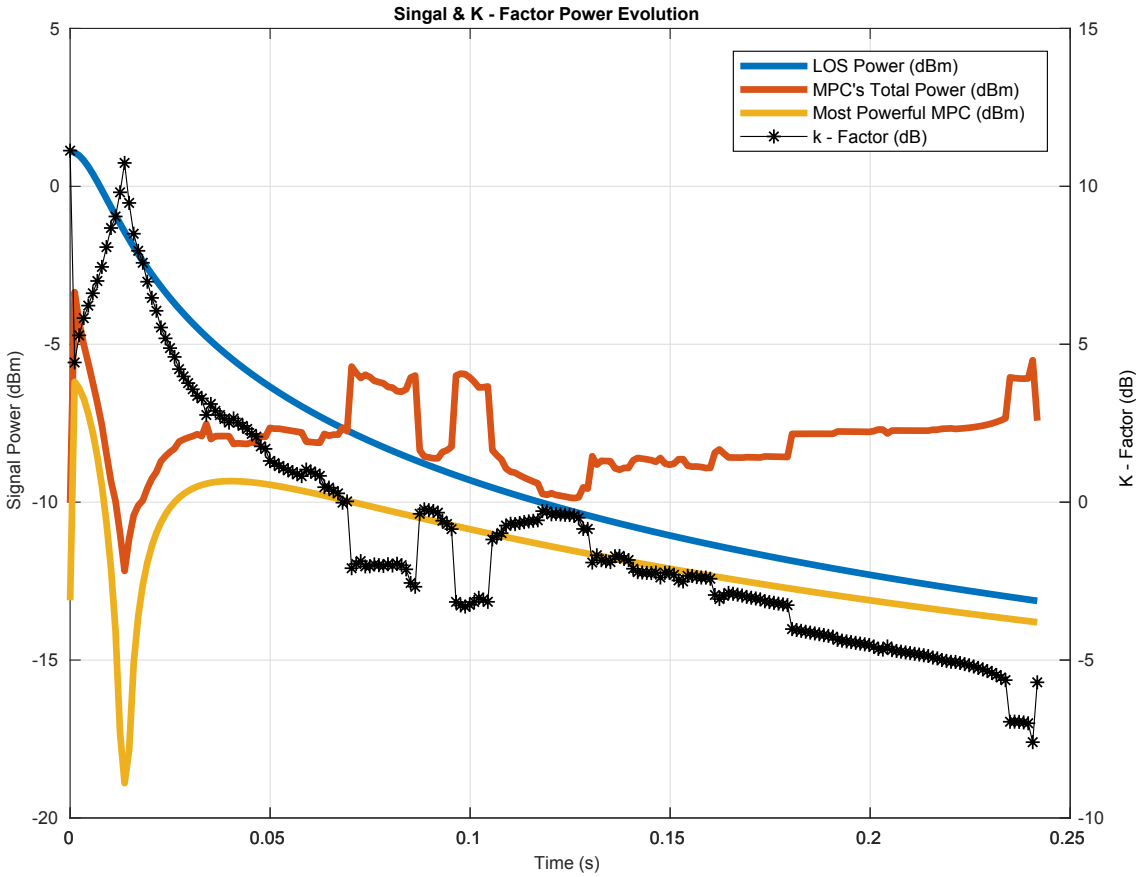

Figure 53: Propagation Simulation Results in Baldersheim with RaPSor.

with a directional antenna (i.e. it 'sees' fewer MPCs). Moreover, the ISL scene model suffers from a lack of accuracy as we have mentioned. More specifically, we have not been able to take into account the diffuse MPCs.

Finally, an estimation of the typical Doppler spectrum at the impact instant can be found in Fig. 55. It clearly shows a dominance of the LOS ray in the range of the -6.5 kHz as predicted by Eq. 8, where $\lambda = 0.13$ m, the projectile's speed $||\vec{v}|| = 680$ m/s and the angle between the LOS $\vec{k}$ vector and the speed vector is 180°. However, this result has to be considered as an approximation to be confirmed by our analysis in section 4.3 and later in chapter 5. In fact, RaPSor does not take into account our limitations in the multipath resolution we exposed in section 3.2.2.1. The different testing conditions in addition the difficulty to model a complex propagation scenario in RaPSor requires the Doppler Spectrum in Fig. 55 to be considered as an approximation.

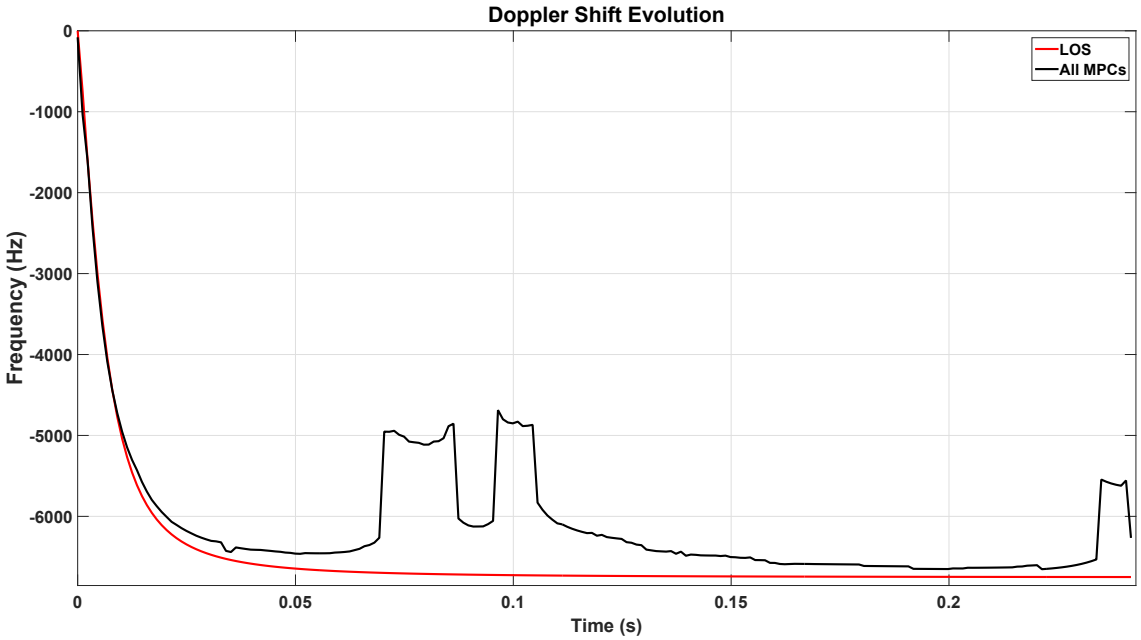

Figure 54: RaPSor Simulation: Evolution of the LOS Doppler Shift.

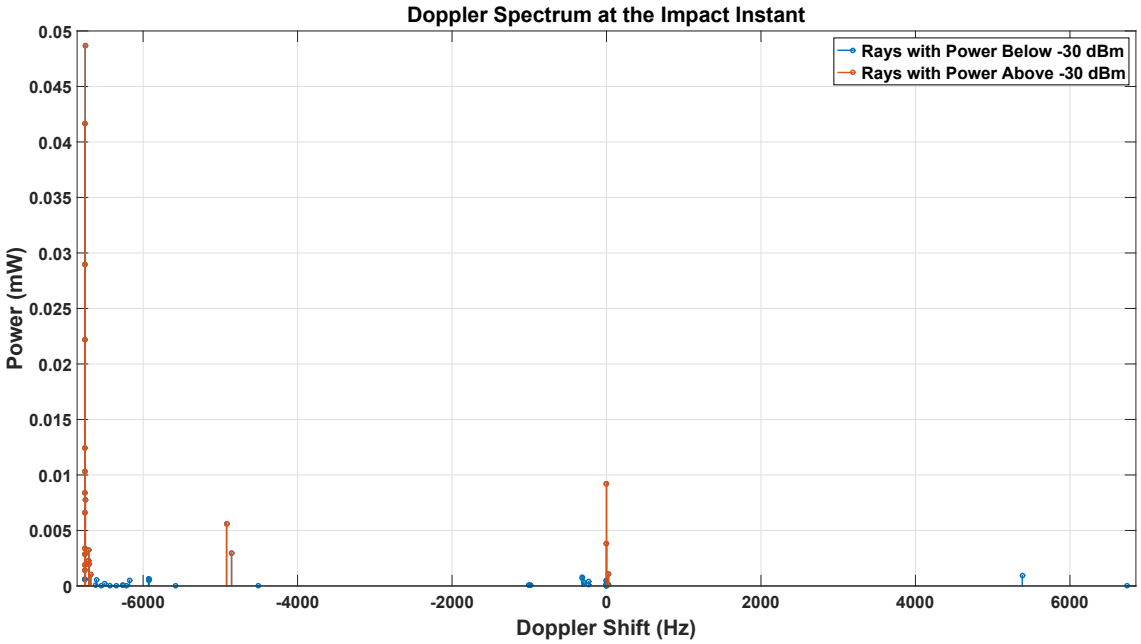

Figure 55: Doppler Spectrum at the Impact Instant for an Omnidirectional Station.

4.2.2 Evaluating the Impact of the Projectile's Spinning

4.2.2.1 Spinning Experiment Setup

A sketch of the experiment setup designed to analyze the Doppler shift because of the spinning of the projectile's antenna is shown in Fig. 56(a). Additionally, the real setup can

be found in Fig. 56(b). The spinning condition of the projectile is achieved by placing the projectile's antenna on spinning bench already presented in Sec. 3.1.2. This spinning module can be either controlled by PWM driver or a DC motor, both of them allow a maximum spinning frequency around 60 Hz. Initially in this experiment, the emitting antenna was a 32 mm diameter circularly polarized (CP) patch antenna associated to a programmable electronic driver providing a single tone in the 2.2- 2.4 GHz range. The reception equipment consist on a $\lambda/2$ dipole at 2.4 GHz and the digital signal oscilloscope 91604A from Agilent Technologies.

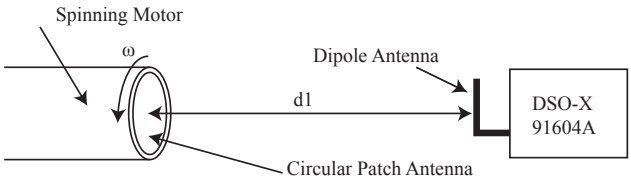

(a) Spinning Doppler Setup Sketch.

(b) Spinning Doppler Characterization Equipment.

Figure 56: Experimental Setup for Spinning Doppler Characterization.

The distance d_1 in Fig. 56(a) was set to 0.5 m. This allows both the emitter and receiver antennas to operate in the far field region according to Eq. 88. Where D is the maximum dimension of the antenna and λ is the wavelength.

$$d_1 \geq \frac{2D^2}{\lambda} \tag{88}$$

The CP antenna is similar to the one appearing in [17]. Its Axial Ratio (AR) was measured in an anechoic chamber at ISL facilities and its evolution with the frequency is given in Fig 57(a). This experimental setup was used four times, each one at a different frequency. The objective was to observe how the spinning frequency shifts the emitted waves for 4 different polarization status. The selected frequencies and the AR associated can be found in Tab. 7.

When performing the experiment, we had to account for the emitting frequency and the sampling frequency of the digital oscilloscope. At the time when the experiment was

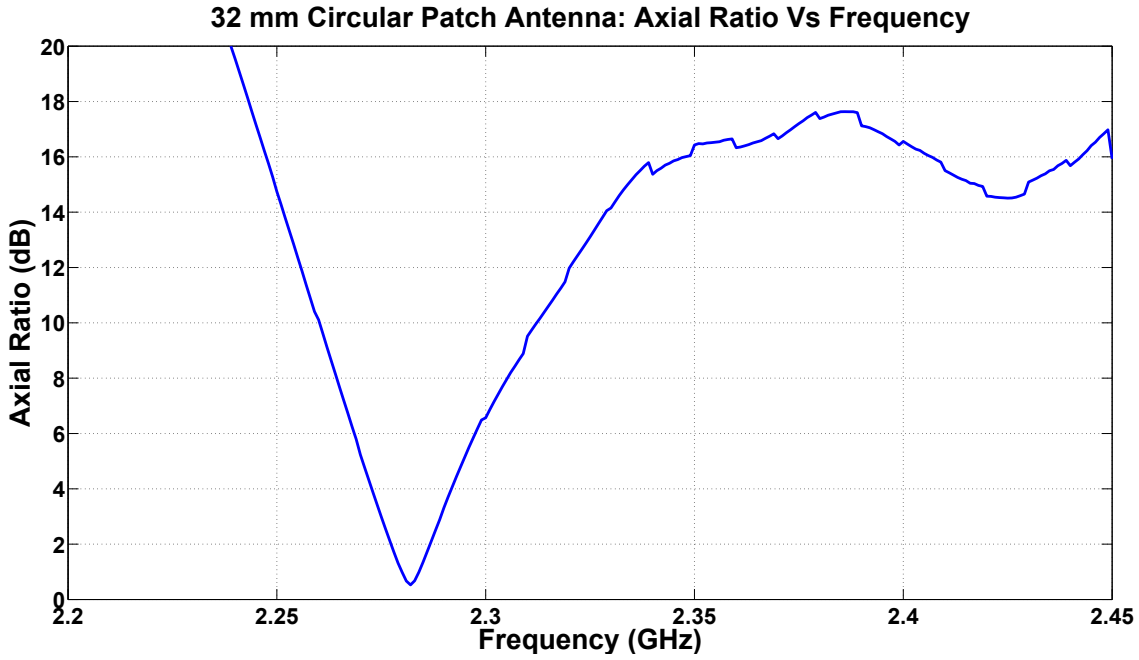

(a) 32 mm Antenna Axial Ratio Characterization.

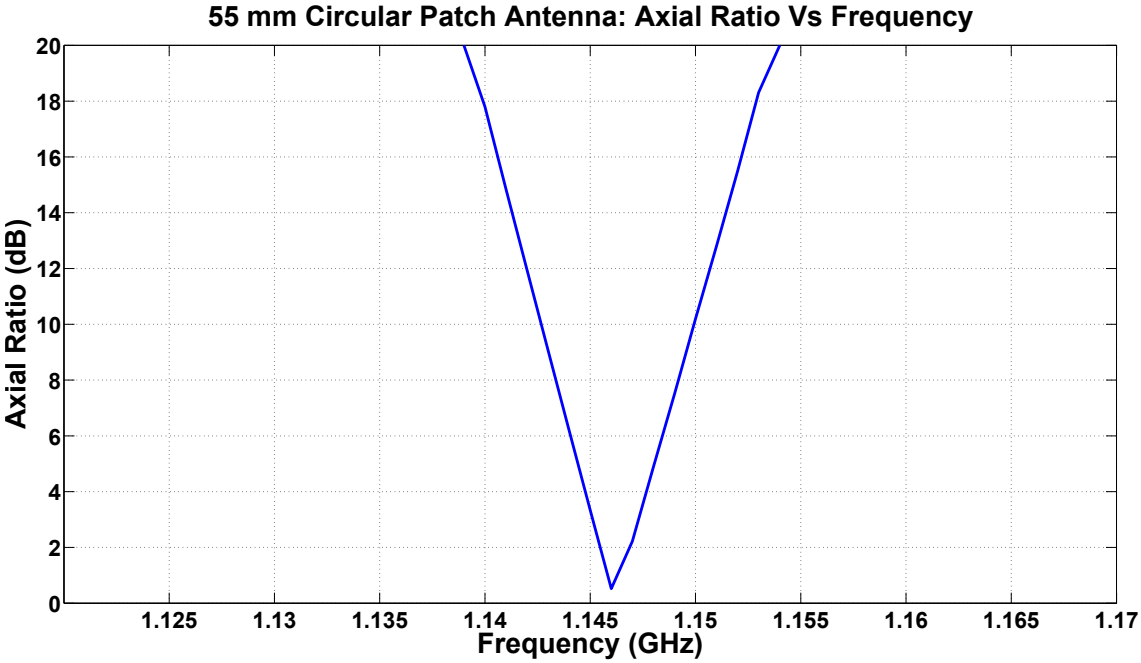

(b) 55 mm Antenna Axial Ratio Characterization.

Figure 57: Circular Polarized Projectile's Antennas: Axial Ratio - Frequency Characterization.

Table 7: Selected ARs and Frequencies

Axial Ratio (dB)	Frequency (MHz)
0.5	2282
3	2290
6	2299
9.7	2311

performed, the SDR equipment was not ready. This implied the emitted wave had to be sampled at 5 GHz and later demodulated by software in order to observe the frequency shift. Being the memory of this oscilloscope a limited resource, only measurements of 0.02 s long could be stored. This value barely represents one period of the spinning frequency at 50 Hz. With the objective of being able of recording at least two periods at 50 Hz, we decided to lower the emitting frequency. A new 55 mm antenna equipped with a transmitter[2] configured at 1.150 GHz was employed. Lowering the emitting frequency allowed us to set the sampling frequency of the oscilloscope to 2.5 GHz. As we can deduce from Eq. 84, the Doppler shift induced by the antenna's spinning is independent from the emitting frequency. For such reason, the result out of the experiment originally thought to be performed in the 2.3 GHz band should be the equivalent to the new one in the 1.115 GHz band. The measured AR for this new antenna can be found in Fig. 57(b).

4.2.2.2 Data Analysis

A direct measurement of the spinning induced frequency shift implies the use of very stable frequency references in both emitter and receiver sides. Other experiments realized on this topic have employed rotating GPS antennas in conjunction with atomic clocks to reach this stability [20].

We cannot use such stable clock references. Instead, we developed a method to detect the frequency shift by means of measurements and signal processing. A graphical representation of the followed process can be found in Fig. 58. Each one of its stages will be discussed below.

[2]The author is grateful to L. Mura from UHA and H. Boeglen from XLIM for the conception of the transmitter

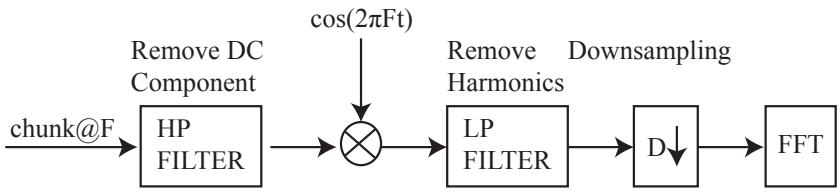

Figure 58: Spinning Data Flow Analysis.

- Signal's Division: the signal is divided in sections in order to facilitate the subsequent signal processing.

- HP Filter: the signal is filtered using a high-pass filter with a 2 GHz cut-off frequency. The aim of this stage is to decrement the total noise power in the analyzed signal as well as removing undesired harmonics.

- Signal Demodulation: the signal's section is demodulated at the theoretical programmed frequency in oder to prepare it for the next stages.

- LP Filter: we filter the signal by applying a low-pass filter in order to remove the remaining harmonics that appear in the demodulation stage.

- Downsampling: the expected signal at the input of this stage is in the range of a few kHz because of the difference in the programmed frequency of the emitter and the real single tone emitted. In this situation, we downsample the analyzed signal in order to avoid the computing of large time consuming FFTs.

- FFT: finally, this stage allows us to compute the frequency shift experienced by the carrier frequency due to the rotation of the emitting antenna. Because of the use of a non-ideal transmitter, the frequency of the signal at the output of this stage will be $f_r = f_k \pm f_s$, where f_k is the difference between the programmed frequency value and the real one emitted while f_s is the spinning frequency of the module. The f_k value is obtained in a two step measuring process, i.e. firstly we measure in the static case and secondly we allow the bench to spin.

The results out of this experiment can be seen in Tab. 20. In general, we found a

great agreement between the expected spinning frequency shift and the measured one if we consider the Mashhoon expression for CP waves. However, we cannot extract conclusions about the impact of the AR in the measured shift. In [60], the author gives the accumulated phase shift for several cycles. As in our case we only were able to analyze one cycle, the conditions could not be reproduced.

Table 8: Spinning: Measured Frequency Shift

Frequency (MHz)	Spinning Rate (Hz)	f_r (Hz)	$f_r - f_k$ (Hz)	Theoretical Shift (Hz)
1147 AR = 2.2 dB	0	340	0	0
	25	320	20	25
	50	313	27	50
1148 AR = 4.8 dB	0	348	0	0
	25	325.2	22.8	25
	50	298.4	49.6	50
1149 AR = 7.5 dB	0	305.4	0	0
	25	316.5	11.1	25
	50	347.1	41.6	50

The first column in Fig. 20 represents the spinning rate of the module, in this experiment it was set to spin at the regime of 0, 25 and 50 Hz. The second column represents the f_r values for each tested frequency and spinning regime. Finally in the third column, we find the experimental frequency shift induced by the spinning of the bench.

According to Eq. 84, if the angle α between the wave front and the receiving antenna is zero, frequency shifts of 0, 25 and 50 Hz are expected for the tested spinning frequencies. Similar values to those expected in theory were measured in most of the cases. Taking into account a maximum spinning of 60 Hz, we conclude this induced shift can be neglected if we compare its value with the typical Doppler shift measured in a super sonic flight, which is in the order of several kHz.

4.2.3 Conclusion on Nutation, Spinning and Multipath

In section 4.2.1, we studied the influence of the nutation in the Doppler shift at the receiver station by means of simulations. At the same time, RaPSor software allowed us to have a first insight into the multipath and Doppler properties of the channel. As we showed, the nutation induced Doppler shift can be neglected due its low value (in the order of a few Hz) compared to the one the Doppler shift caused by the LOS component.

The same reasoning can be applied to the results out of our spinning experiment in section 4.2.2. The spinning induced Doppler shift value is still in the range of a few tens of Hz, much lower value than the one produced by the multipath effect according to our simulations. Moreover, as well as in the previous case, it can be neglected if we take into account the LOS Doppler shift. Additionally, in a projectile firing it would be almost impossible to establish the origin of such a small frequency shift. As a conclusion, in the further analysis, the spinning of the projectile will be also excluded from the channel modeling.

In section 4.3, we will study the Doppler shift measured at the receiver station by analyzing the telemetry flight data from a previous firing campaign. As we will see, the discarding of nutation and spinning from the channel analysis will be experimentally justified.

4.3 Firing Tests

At the end of July 2015, the STC group organized a firing campaign to validate the design of a miniaturized low rate digital transmitter employed in projectile attitude measurements. These measurements were recovered at the beginning of this thesis for Doppler characterization of the radio channel. Although the transmitter used in the shots was a low rate system (2 Msps), we were able to use it for channel sounding and particularly to extract Doppler information from the linear phase digitally modulated data. The experiment took place at Baldersheim experimentation field. This time, four shots were performed with the previously presented BF in section 3.1.7. The configuration of the embedded telemetry system is shown in Tab. 9.

Table 9: BF Telemetry System Specifications

Carrier Frequency	2.3 GHz
Transmission Power	24 dBm
Modulation	MSK
Data Rate	2 Mbps

The 2.3 GHz MSK transmitted signal is captured by two software defined radios (SDRs) like the ones we presented in section 3.1.3. The first receiver, located near the gun, is connected to the Hyptra antenna presented in section 3.1.4. It was configured to point at the end of the projectile's trajectory. The second receiving station is located further down the trajectory to the right and is fitted with an omnidirectional antenna. The sampling rate of the first SDR was 25 Msps, having a sampling frequency of 16.7 Msps at the omnidirectional station. These two sample rates have been determined by the capabilities of the laptops GbE interfaces connected to the SDRs. A sketch of this measurement setup can be found in Fig. 59. In the figure, receiver 1 accounts for the position of the directional station being receiver 2 the position of the omnidirectional station.

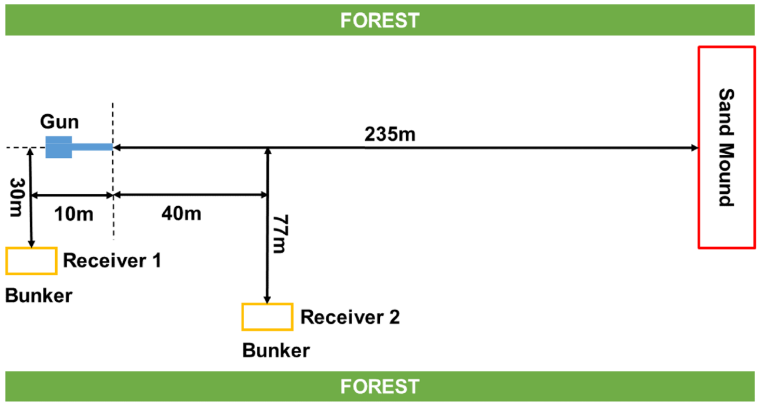

Figure 59: BF Firing Setup.

The Doppler estimation algorithm we have applied is based on the traditional MSK demodulation algorithm [95]. In the experiment, the MSK data is organized in frames of 320 bits, each frame starting with a synchronization word of 40 bits (abbreviated sync word

in the following). Our algorithm tracks the phase of the MSK transmitted sync words. Since our sync word has an equal number of 1 and 0 bits, the total phase evolution from the beginning to the end of the sync word should be zero if the carrier frequencies are well aligned. If the carrier frequency is Doppler shifted, an accumulated phase rotation in the analyzed sync word has to be present.

The following table Tab. 10 summarizes the maximum expected Doppler shift values (according to Eq. 8) for each one of the 4 firings at the directional station. The position of the receiver antenna was not changed in the firings.

Table 10: BF Firing Conditions

	Firing #1	**Firing #2**	**Firing #3**	**Firing #4**
Speed m/s (Firing / Impact)	430/346	877/767	860/760	930/833
Expected Doppler Shift (Hz)	-3433/-2762	-7001/-6123	-6866/-6067	-7425/-6650
Flight Time (s)	0.615	0.292	0.302	0.274

The results after having applied the Doppler shift estimation algorithm for the second firing are shown in Fig. 60. The first element to notice the maximum Doppler shift for Receiver 1 follows the predictions in Tab. 10 as well as the simulation value in Fig. 54, i.e. maximum values around -6.5 kHz. As expected, the Receiver 2 curve presents a sign change in the Doppler shift: when the projectile moves towards Receiver 2, the Doppler shift is positive, whereas when it moves away from it, the Doppler shift is negative.

This sign change happens at about one-sixth of the flight time, which corresponds to roughly 40 m from the gun. It can also be noticed that the Doppler shift for Receiver 2 shows a slow decay with slightly more fluctuations than for Receiver 1. Both receivers are equipped with the same RF daughter boards so the only difference lies in the antennas and sampling rates. Following the reasoning concerning the SFO, we considered the sampling rate did not have an influence in the measured Doppler shift.

Hence, receiver 1 'sounds' the channel with a directional antenna having an HPBW of 23°. We postulate this means that receiver 1 will not see as many MPCs as receiver 2, which is equipped with an omnidirectional antenna. We can also notice that both curves show the same trend after 0.21 s. We can clearly distinguish a positive step of about 1 kHz, with the Doppler shift remaining constant up to the end of the flight. RaPSor simulations linked this discrete steps in the Doppler shift to the presence of strong multipath components. This assumption will have to be verified with our channel sounder. Because of the narrowband properties of the MSK sounding signal, a multipath characterization of the channel is not possible at this stage.

Since the measured Doppler shift values are in accordance with the theoretical values expected, we can validate our Doppler shift estimation procedure.

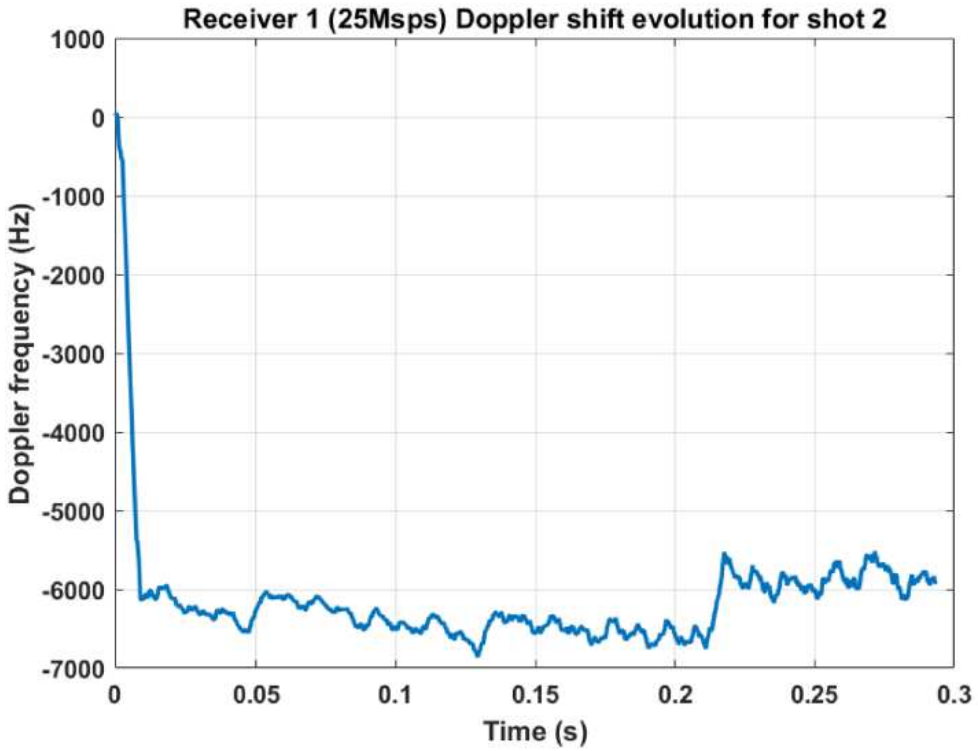

(a) Directional Station.

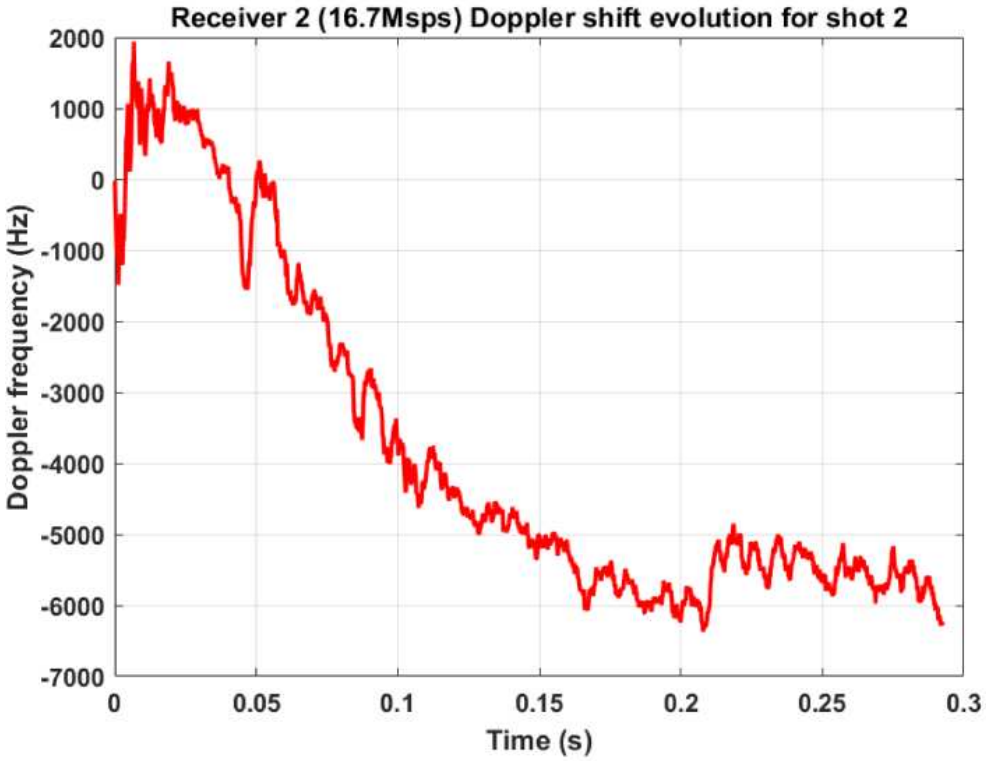

(b) Omnidirectional Station.

Figure 60: Doppler Shift Evolution for BF Firing 2.

4.4 Conclusions: Towards a Wideband Characterization of the Propagation Channel

We started this chapter by introducing two flight mechanics: the spinning and the nutation of the projectile. Before starting the channel characterization, it was necessary to know if they would have an impact on the received signal. It was determined that both of them could be neglected for channel modeling purposes.

However, the simulations performed with RaPSor allowed us to have a first insight into the Doppler behavior of the channel. Values in the range of -6.5 kHz were found taking into account a projectile flying at 680 m/s. This result was found by means of simulations and through the analysis of the data from previous experiments at ISL. It was also determined that the multipath effect can modify the LOS Doppler shift. Finally, a first estimation of the Doppler spectrum was obtained.

The analysis carried out in this chapter has served as a preliminary study of the channel behavior at Baldersheim. Some of the key properties of the channel were outlined. Concretely, the Doppler shift and the multipath effect. However, the channel was not completely characterized as the CIR was not obtained. The narrowband properties of the MSK signal used in the experiments prevented us from performing a wideband characterization of the channel in section 4.3. In the following chapter, we will employ our channel sounding prototype in order to perform a full wideband characterization.

CHAPTER V

WIDEBAND CHARACTERIZATION OF THE RADIO CHANNEL. CONCEPTION OF A CHANNEL MODEL AND CHANNEL SOUNDER VALIDATION

This chapter will be devoted to the modeling of the radio channel for the instrumented projectiles designed at ISL. In chapter 3, we studied the OFDM transmission technique and how it can be used for channel sounding purposes. Based on this technique, an OFDM based channel sounder was proposed. Before testing this device, a preliminary study of the propagation channel was carried out in chapter 4. As a result, we gained knowledge about the multipath and Doppler properties of the propagation channel at Baldersheim firing range. At the same time, elements like the spinning and the nutation of the projectile were excluded for the future channel model.

Before describing the experiments we carried out, we will recall the main reasons for performing a wideband characterization of the propagation channel in section 5.1. For this purpose, a revision of the telemetry systems previously utilized at ISL for instrumenting projectiles will be given.

The setup for the experiments performed will be detailed in section 5.2. Concretely, two sets of experiments were carried out: the first ones correspond to training experiments where we tested the capabilities of our channel sounder methodology at low speed. In the second set of experiments, the channel sounder prototype is tested in real firings (high speed) with the objective of characterizing the channel at Baldersheim testing facility.

With the aim of describing how the results are obtained in the following sections, the data analysis process for both low and high speed experiments is presented in section 5.3.

In section 5.4, we apply the data analysis process to obtain the first results with respect to the low speed experiments. Concretely, the path loss behavior of the channel will be

obtained. As we defined in chapter 3, in our channel sounder methodology the CIR of the channel is obtained after having obtained an estimation of the CFR. For this reason, special attention will be given to the performance of the CFR estimator in real conditions.

The definition of the channel model required by ISL starts in section 5.5. In order to sound the channel with the OFDM-embedded channel sounder, a firing campaign was performed in September 2017 where two base stations were deployed. We will detail the problems we encountered during these firings before presenting how the channel was characterized. As we will show, the recovered data at the base stations required a failure analysis. In spite of the problems we faced, the measurements could be used for channel modeling.

After having analyzed the measurements from the firing campaign, the TDL filter which models the channel will be specified in section 5.6. As we will show, it is based on the time and frequency characteristics we observed. This model represents the final outcome from the analysis of the firing campaign. Lastly, the implications in the conception of the future digital transceivers at ISL will be introduced in section 5.7.

Finally, the conclusions of this study are detailed in section 5.8.

5.1 The Need for Wideband Characterization

Telemetry and communications systems of instrumented projectiles developed at ISL have been evolving according to the evolution of the commercial off-the-shelf electronics. We can classify them in three different generations:

- First generation: this generation covers from the middle 80s until 2004. During this period of time, only completely analog devices were embedded in instrumented projectiles. These analog transceivers made use of single carrier transmission techniques with a maximum possible bitrate up to 1 Mbit/s. Since no error correction was implemented and signals had to be transmitted over a long range, the PCM-FM modulation scheme was used because of its robustness.

- Second generation: from 2004 to 2013, the STC group from the second ISL's division initiated the transition from analog to digital transceivers. These new telemetry and

communication systems increased the throughput up to 2 Mbit/s with a GFSK modulation and up to 4 Mbit/s with an OQPSK modulation. The selected chips would also have worked with more complex modulation schemes with higher date rates, although they were never used under these conditions for long rang telemetry tests. Moreover, they continued making use of single carrier modulation techniques. Depending on the application, the power consumption of the digital transceivers was higher than the one required to operate an analog one. This issue motivated their coexistence during this period of time.

- Third generation: from 2013 until today, the analog transceivers were completely abandoned. At the same time, an increasing demand for high-throughput applications has been detected. For example, instrumented projectiles requiring video transmission and real time attitude estimation have been designed. These new demanding applications motivated the transition from single carrier telemetry systems to more spectrum efficient multicarrier ones. However, before deploying a multicarrier transmission system, a wideband characterization of the channel is required.

5.2 Description of the Experiments

The validation of our channel sounding methodology as well as the testing of our hardware was organized in two measurement campaigns. The first one consist of a series of experiments performed at low speed by employing SDR equipment. The objective was to determine the performance of our channel sounding methodology. At the same time, we sought to anticipate as much as possible the weak points of our methodology. Certainly, a real firing campaign is expensive in terms of equipment cost and staff involved. For that reason, it was necessary to carry out these previous campaigns at low speed conditions before an instrumented projectile shooting. In September 2017, the second measurement campaign was carried out with our embedded channel sounder prototype.

In section 5.2.1, we will present the setup for the low speed experiments. At the moment we performed these experiments, the embedded sounder prototype was not ready. However,

the channel sounding methodology could be tested as it was designed to be hardware independent. During these experiments, USRP equipment in conjunction with omnidirectional antennas like the one appearing in section 3.1.4 were used at the emitter/receiver side.

The setup for the firing campaign at Baldersheim will be shown in section 5.2.2. This time, the channel sounder prototype was fully operational and four firings were performed. In this experiment, two base stations were deployed with the antenna equipment presented in section 3.1.4. Because of the expected impact of the high speed in the channel behavior, special attention will be given to the flight speed profile we observed during this campaign.

5.2.1 Low Speed Experiments

This measurement campaign was structured in two experiments. Unless otherwise specified, they will be respectively named experiment I and experiment II.

The first set of measurements was taken at the vicinity of the SP2MI faculty of the University of Poitiers (See Fig. 61). The emitter equipment was mounted inside a car and 4 round trips were performed from A to B and from B to A. In this situation, the receiver antenna was kept fixed at the position R. This area was mainly chosen for security reasons as we could safely drive the car at the maximum allowed speed (50 km/h) at its passage in front of the receiving antenna.

The second set of measurements were taken at the *Cité de l'Automobile* museum (Mulhouse, France, Fig. 62). This time, both stations (transmitting and receiving) were placed in two cars in order to perform 4 round trips from A to B and B to A. The cars were driven in opposite directions, both of them at a maximum speed around 30 km/h. The antennas were placed as sketched in Fig. 62(b).

The Doppler shift is not expected to have a great impact on the channel properties because of the low relative speed of the transceivers involved. This speed can be as high as 60 km/h for experiment II. According to Eq. 8, a maximum Doppler shift of 128.2 Hz is expected for the 2.3 GHz band, which is the frequency band in which these measurements were taken. Such small value compared to the subcarrier spacing of 312.5 kHz will produce a negligible impact on the received signal with respect to the noise level, as it was demonstrated

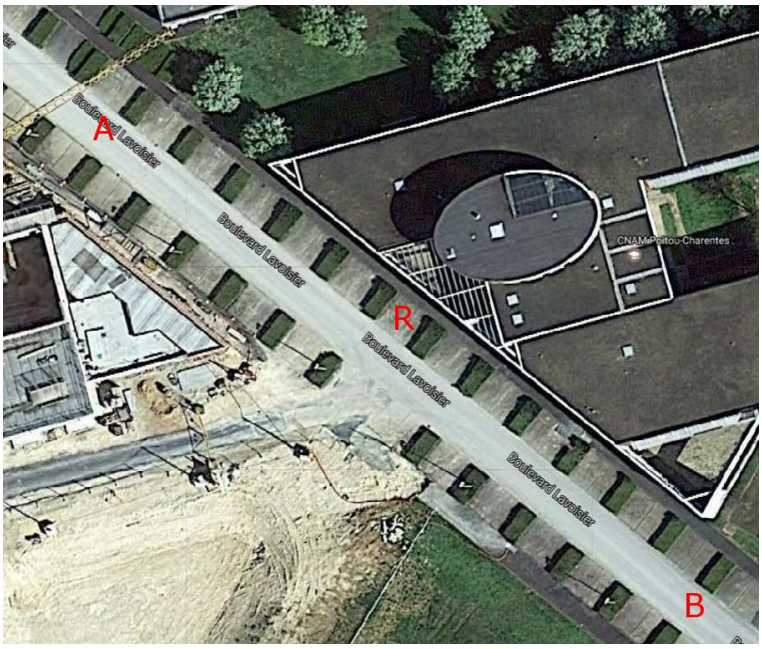

(a) SP2MI Experiment Environment.

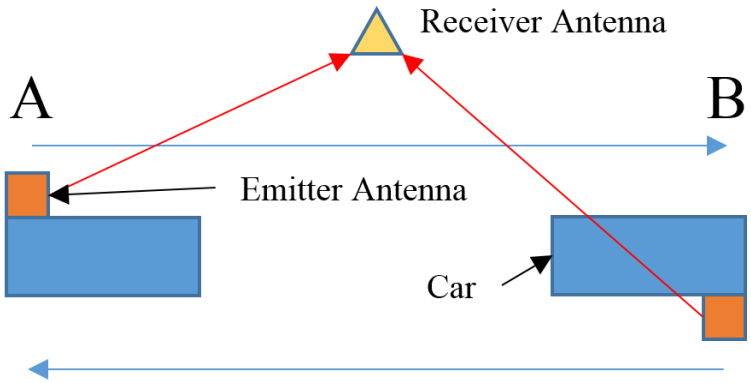

(b) SP2MI Experiment Sketch.

Figure 61: Low Speed Experiment. Experiment I.

through Eq. 66.

Nevertheless, it will be possible to observe a decreasing in the received power at the when the transceivers move away from each other. Indeed, the path loss of the channel in these experiments can be obtained.

At the same time, the increasing distance between the transceivers will imply a decrease in the SNR value. For that reason, it will be possible to obtain the performance of the CFR estimator proposed in section 3.2.2.3 with respect to the SNR.

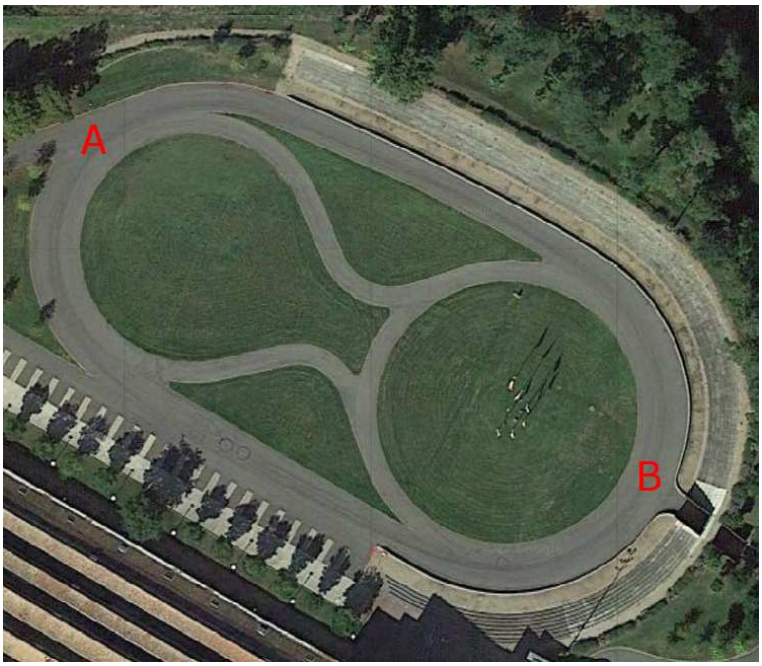

(a) CA Experiment Environment.

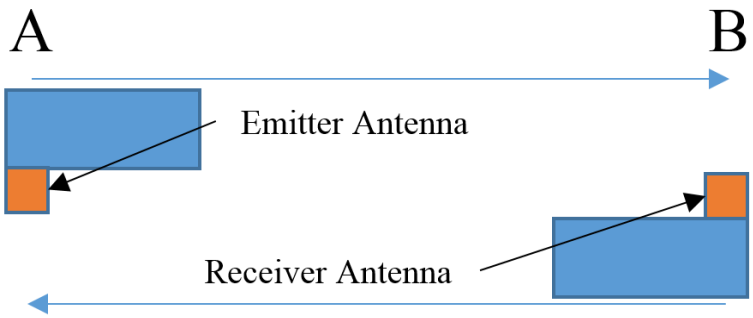

(b) CA Experiment Sketch.

Figure 62: Low Speed Experiment. Experiment II.

5.2.2 High Speed Experiment

The firing campaign described in this section was carried out in September 2017. During two days, four channel sounder prototypes like the one appearing in section 3.3 were tested. Two of the firings were performed with fully operational prototypes while the two other firings were performed with non-instrumented prototypes. As it was the first time this prototype was going to be fired, the interest in performing these non-instrumented firings was to test the flight behavior of the prototype as well as to heat the cannon in order to improve its accuracy.

Additionally, the configuration of the transmission system was different in the two instrumented firings: one prototype was prepared to emit in the 2205 MHz band while the other one was set to the 2250 MHz band. These two different bands were selected in order to assure at least 40 MHz bandwidth for each one of the embedded antennas. The optimal frequency band for each one of the prototypes was previously obtained in the ISL's anechoic chamber.

A summary of the firing configuration can be found in Tab. 11.

Table 11: Firing Configuration

	Electronically Instrumented	**Frequency Band (MHz)**
Firing #1	no	-
Firing #2	yes	2205
Firing #3	no	-
Firing #4	yes	2250

A drawing of the ISL firing field showing the experiment configuration can be found in Fig. 63. As it is shown, two receiving stations were deployed: one employing the parabolic circularly polarized Hyptra NE5023 antenna while in the other one we used the omnidirectional vertically polarized antenna VERT2450 from Ettus. In both of the cases, the data acquisition was carried out by two X310 SDR devices driven by a laptop.

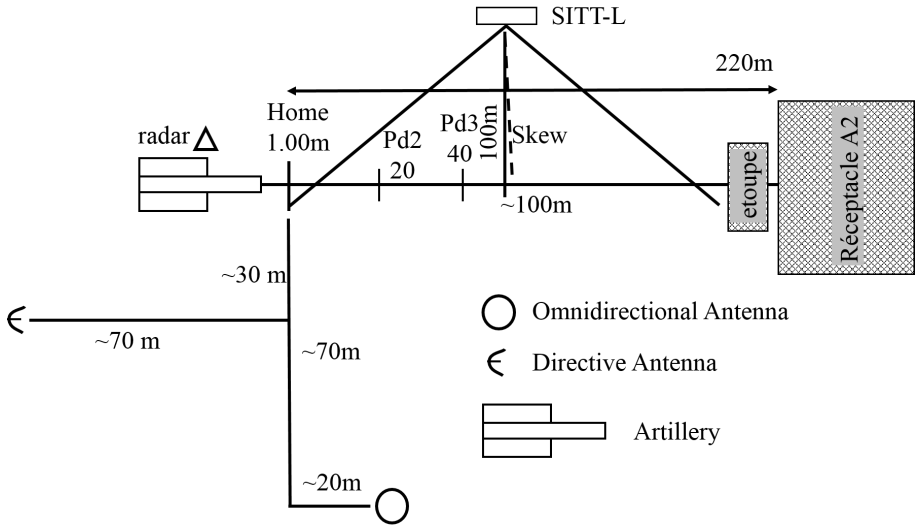

Figure 63: High Speed Experiment Setup.

The position of each receiving station was chosen in function of two criteria: on the one hand, we wanted to assure the LOS condition between the projectile and each one of the base stations. On the other hand, the position of the receiving stations during previous firings was taken into account. Concretely, the position of the omnidirectional station was the same as in the BF campaign in chapter 4.

The equipment used at the firing facility during the firings was:

- A cannon similar to the one appearing in section 3.1.8.
- Two receiving stations: one equipped with an omnidirectional antenna while the second receiving station was equipped with the high gain antenna presented in section 3.1.8. The position of these receiving stations is shown in Fig. 63.
- The ISL's radar equipment for accurate speed tracking of the projectile.
- The ISL's video equipment, this helps for both failure and flight behavior analysis. In the figure, it is identified with the SITL-L label.

5.2.2.1 Flight Profile

The Doppler effect is a key parameter to be taken into account in our channel model because of the flying speed of the projectile. Considering a maximum flying speed of Mach 3, Doppler frequencies in the range of 7.5 kHz can be expected. For that reason, this parameter cannot be neglected as it represents approximately the 2.4% of the subcarrier spacing. However, the staff in charge of configuring the firings considered Mach 3 an unsafe testing speed for this prototype.

Certainly, it was the first time this projectile was tested. This implies the flight behavior of the prototype is unknown. At the same time, the development cost of the prototype is in the order of several thousands of euros. It is clear then that a try and error testing is not possible. For that reason and always following their advice, the firing speed was set to Mach 2, i.e. approximately 680 m/s.

In Fig. 64, we show the speed profile for each one of the firings performed with our prototype. The initial flight speed at the moment of the firing is near 650 m/s. As a consequence of the air breaking, it descends to a value of approximately 400 m/s at the impact instant with the soft recovery unit. The average duration of the flight is in the order of 400 ms for the selected initial speed. As we can observe, the speed profile for each fired projectile follows a quite similar shape in all the firings. For this reason, an expression for the speed (v) as a function of the time (t) where just the initial speed v_0 is required can be found by polynomial fitting the experimental radar data obtained by the SITT-L equipment. The expression found in Eq. 89 is useful in order to reproduce the experiment results by means of simulations as well as in the definition of the channel model.

$$v = -5.84 \times 10^{-7} t^3 + 9.65 \times 10^{-4} t^2 - 8.44 \times 10^{-1} t + v_0 \tag{89}$$

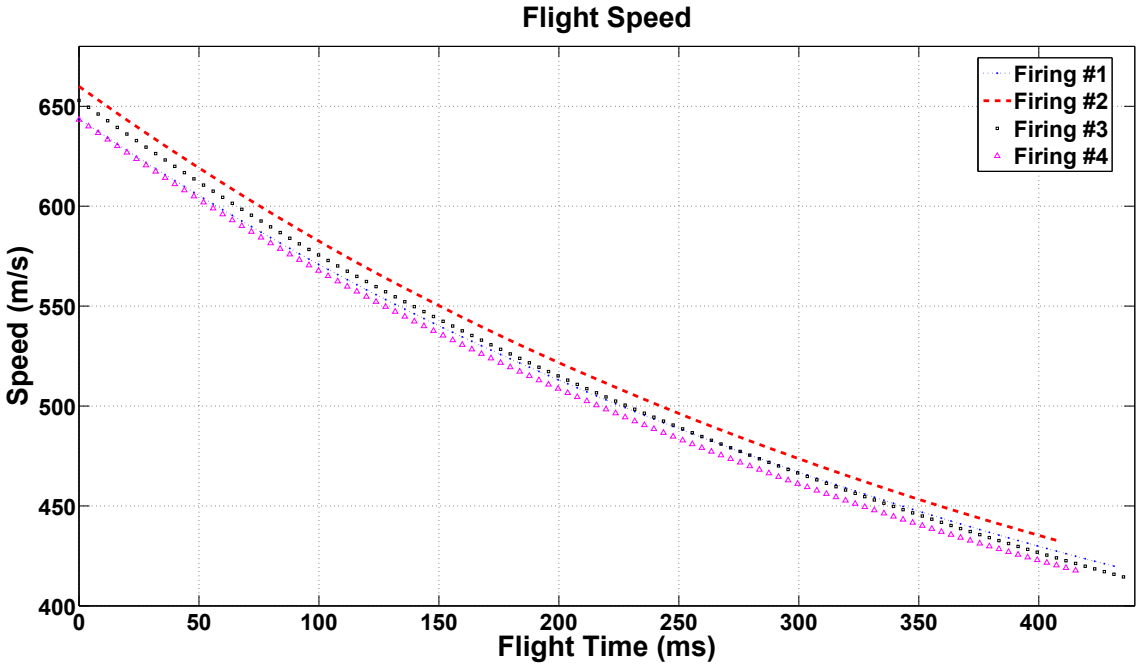

Figure 64: Projectile's Speed Profile

5.3 Experimental Data Analysis

In this section, we will present the data analysis process we followed in order to perform wideband channel characterization. Two different objectives are sought: in the case of the low speed experiments we test the capabilities of our methodology to work in the frequency domain, i.e. a multipath characterization of the channel will not be performed and only the performance of the CFR estimator will be evaluated. In contrast, the main objective in the high speed experiment is to find a channel model to be used in simulations, i.e. a tapped delay line channel model. For that reason, the multipath characterization will be performed as well.

The process is shown graphically in Fig. 65. Additionally, an explanation for each one of these stages can be found below:

- First task to do is to isolate each one of the received OFDM frames. This allows us to obtain an estimation of the SNR by analyzing the silent intervals between one frame and another. The SNR estimation algorithm in section 3.2.2.2 will be employed as well. In the rest of this chapter, every time we give a power value, it will be calculated through the digital signal sampled by the SDR. This is, it should be taken as a relative

value with respect to the real one which remains unknown.

- The second step is to characterize the path loss behavior between the emitting device and the receiving station. As we will see, this task is performed thanks to the path loss exponent determination algorithm presented in section 5.4. The large scale fading properties are then found here.

- The third step is to apply the CFR estimator. At this stage, we will evaluate its performance in function of the SNR value. The validity of the received OFDM frames will be evaluated for channel estimation purposes. Additionally, it is possible to obtain the Doppler behavior for the LOS component of the received signal by applying the algorithm defined in section 3.2.2.2.

- After having obtained the CFR and only in the case of the firing experiment, we will perform the characterization of the CIR. At this point, the channel is completely characterized. It is possible to model it as a TDL filter where the properties of each one of the taps have been determined through measurements. In channel modeling, the statistical behavior of each one of the taps of this filter is determined as a function of a stochastic process as we introduced in section 2.2.3.1. These stochastic processes represent the medium and small fading properties of the channel.

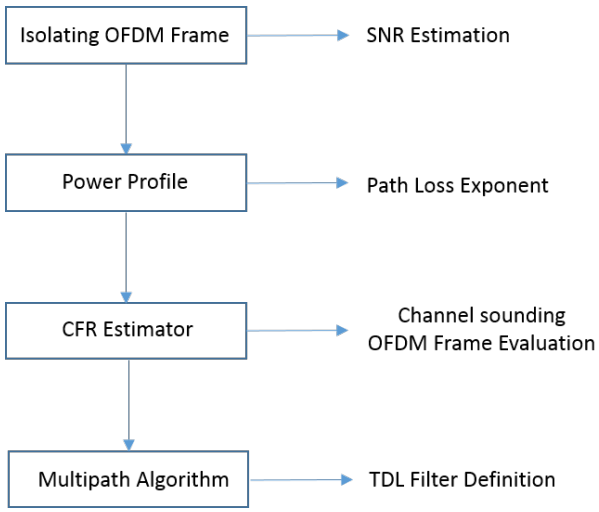

Figure 65: Channel Characterization Experimental Data Analysis

5.4 Testing the Channel Sounder At Low Speed

In this section we will present the results from the low speed campaign. Additionally, we will also define here the algorithm we employ in order to characterize the path loss behavior of the channel. The following algorithm was used in both low and high speed experiments.

As we showed in Tab. 18, the path loss exponent depends on the propagation environment. For that reason, we expect slightly different values for each one of the experiments performed. The problem to solve is to find the α value in Eq. 3. We will focus our attention on Eq. 90.

The distance d between the emitter and the receiver will be obtained by analysis of the propagation scenario in the low speed experiment. In the case of the high speed experiments, it can be obtained from the radar data and the position of the receiving stations. The C parameter is a different constant for each one of the measurements as we introduced in section 2.1.1. Our experiments covered a few hundreds of meters in all propagation scenarios. For that reason, we consider C as a constant which can be removed from the analysis in each one of the measurements. All the previous assumptions allow us to propose an algorithm to estimate the path loss exponent.

$$10log_{10}\left(\frac{P_r}{P_e}\right) = L = 10\alpha log_{10}(d) + C \tag{90}$$

The algorithm we propose is sketched below (named Algorithm 1). The basics behind its behavior are:

- From a starting point in the measured power profile, it performs a linear regression in the logarithmic axis with the objective of finding the path loss exponent. The slope of this regression the provisional path loss exponent. The goodness (R^2) of the regression will be utilized in the next steps.

- If the goodness of the regression is not good enough according to a previously defined threshold, a new regression is performed by including a higher number of power estimations i.e. OFDM frames.

- When the goodness of the regression is good enough, the path loss exponent for the section is stored and the process starts again.

Data: Power Evolution

Result: Deterministic Path Loss by Sections

i = InitialPoint;

f = InitialPoint + N;

while $f \leq MeasureLength$ **do**

  $[R, a, b] = linearRegression\,(measure, i, f)$;

  $Rold = R$;

  while $R \geq TH$ **do**

    $f = f + d$;

    $[R, a, b] = linearRegression\,(measure, i, f)$;

    if $R \geq TH$ **then**

      $Rold = R$;

    end

  end

  $store(a, b, Rold, i, f - d)$;

  $i = f - d + 1$;

  $f = f + N$;

end

Algorithm 1: Path Loss Determination Algorithm

As we have previously mentioned, in the next sections the given power values have to be considered as relatives quantities with respect to the absolute received power. The reception chain of the SDR front-end was configured to sample the received signal in the $[-1, 1]$ interval. These samples will be considered dimensionless in this chapter. Of course, they represent electric field values of the impinging waves. However, as a consequence of considering dimensionless the sampled signal, instead of expressing the received power profile in dBW it will be expressed in dB.

5.4.1 Path Loss

The estimated path loss exponent in the low speed experiments as well as the received power profile for each situation can be found from Fig. 66 to Fig. 68. Regarding the physical environment where the first experiment was carried out, we can see in Fig. 66 a good agreement between the expected value for the path loss exponent and the obtained one. As we showed in Tab. 18, the path loss exponent for an urban area can vary from 2.7 to 3.5 [91, 81]. In this case, the obtained value obtained was 2.45. The goodness of the linear fitting (R^2 parameter) was considered good enough for our purposes. If the path loss of the channel shows a linear behavior, it can be easily compensated. As a consequence, the path loss compensated power profile for this experiment can be found in in Fig. 66(b). As it was expected, the amplitude of the power oscillations increase with the time as the car moves away from the receiver station. This effect is related with the Doppler effect as it was presented in section 2.1.3.

In Fig. 67(a), we analyze what happened when the transmitted signal was obstructed by the car in the B - A round trip. In this situation, the maximum level of power we received was 12 dB lower than the value found in the A - B round trip. Apart from this phenomenon, the received power shows a much noisier behavior than the one observed in Fig. 66. For that reason and with the objective of finding a feasible region to analyze for the next steps, we had to operate our path loss estimation algorithm with an inferior goodness threshold value. It was set to 0.7 instead of the usual 0.8. If we consider the found value good enough according with this new goodness threshold, a path loss exponent of 2.27 was estimated. The compensated path loss received profile for this situation be found in 67(b). Again, we can see how the received power is centered around 0 dB, i.e. the path loss effect has been correctly compensated.

We can find in Fig. 68 one of the results corresponding to the set of measurements taken in *Cité de l'Automobile* museum. The first element to notice is the much softer power profile behavior. This phenomenon was expected as there were not close buildings which could produce strong reflections. In this case, the path loss algorithm could work on two regions.

In such situation, a similar path loss exponent was found, 2.11 and 2.15 for both of the regions analyzed by the algorithm.

This value is smaller than the one obtained in the previous experiments. A situation which is in accordance with the propagation scenario as this environment cannot be considered an urban area. The path loss estimation results can be seen in Fig. 68(a). As well as in the previous measurements, the path loss compensated power profile for the second area treated by the algorithm can be found in Fig. 68(b).

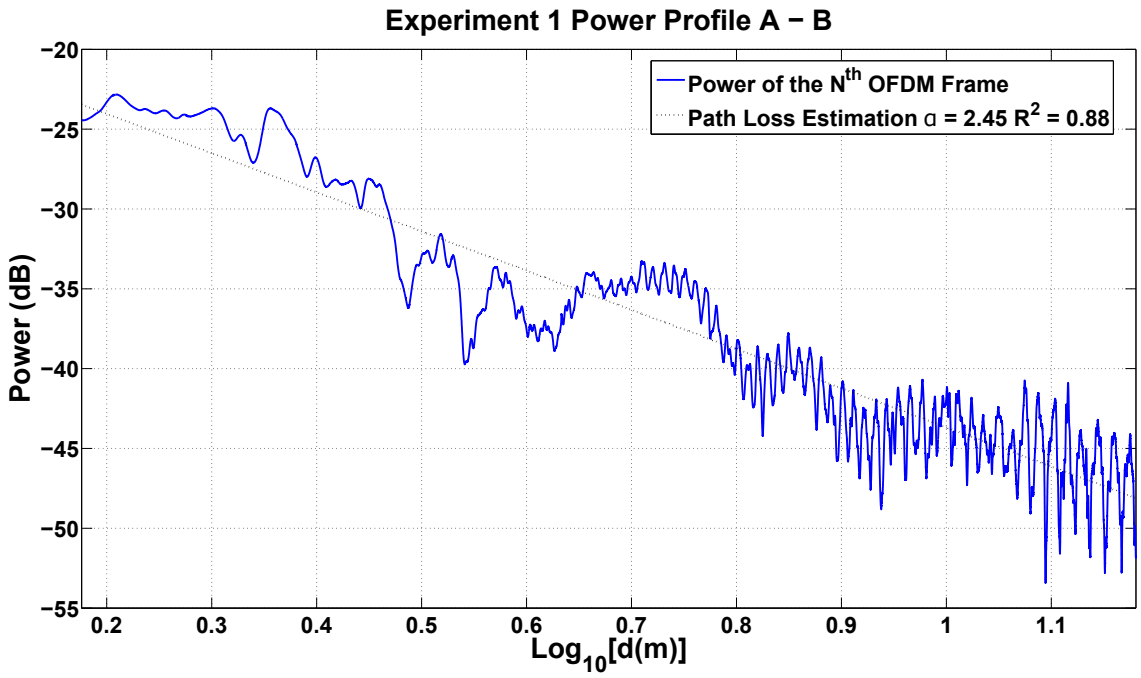

(a) Low Speed Experiment 1 A-B. Received Power Profile Log Scale.

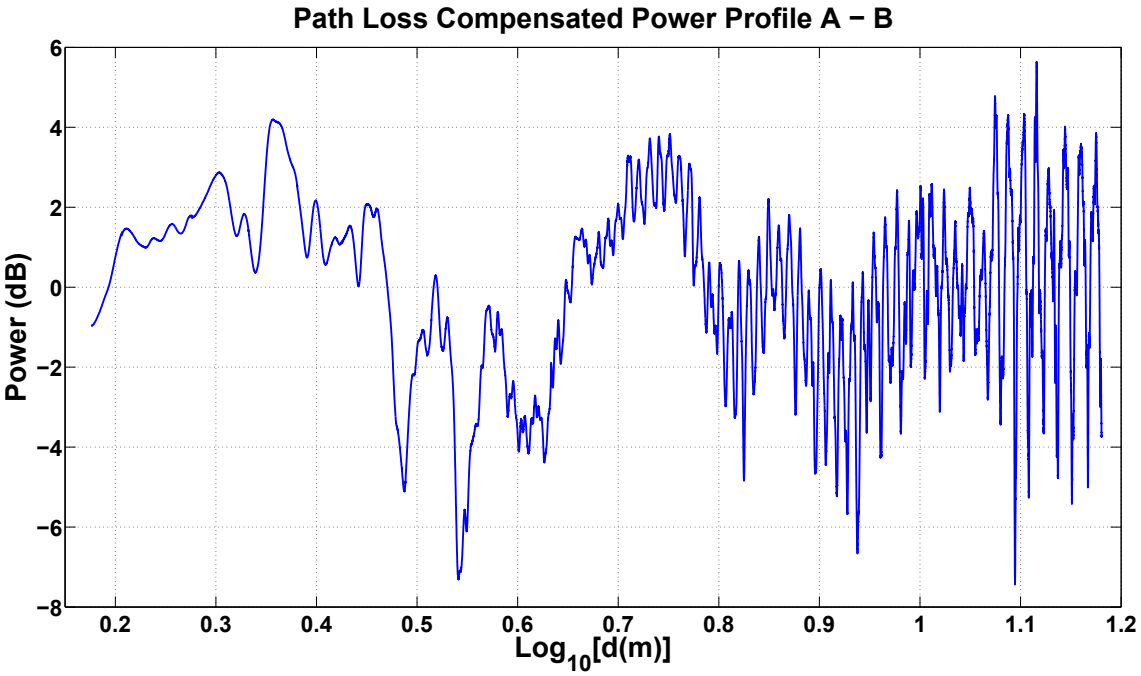

(b) Low Speed Experiment 1 A-B. Path Loss Compensated Power Profile.

Figure 66: Received Power Profile for Experiment 1 - Situation A - B.

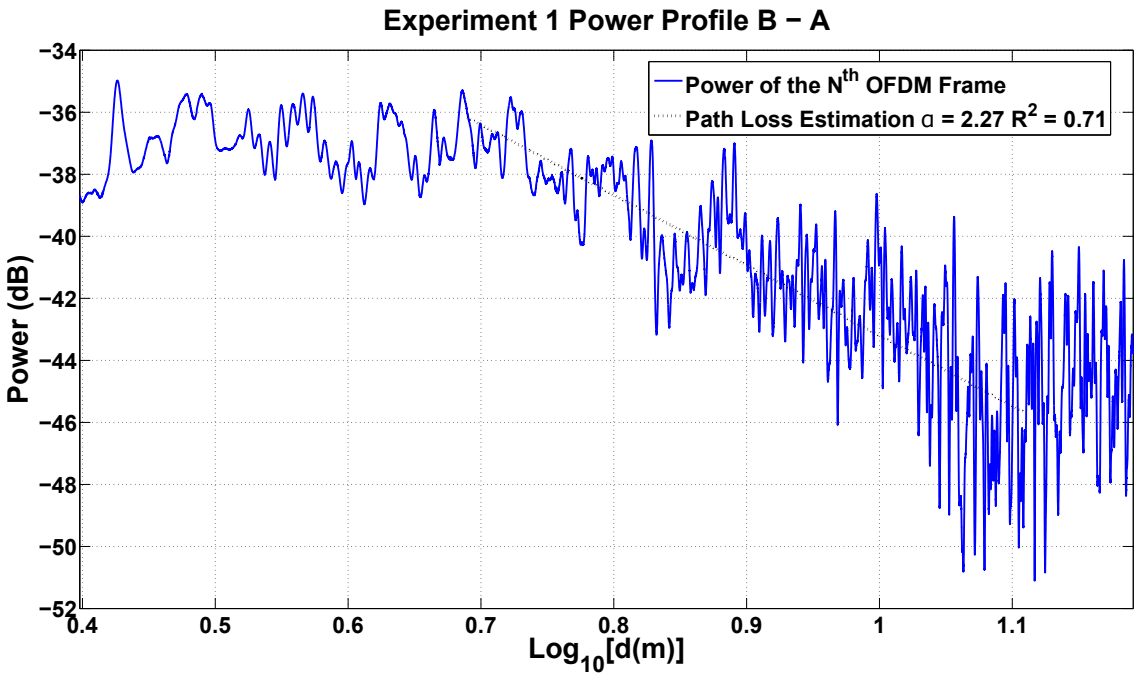

(a) Low Speed Experiment 1 B-A. Received Power Profile Log Scale.

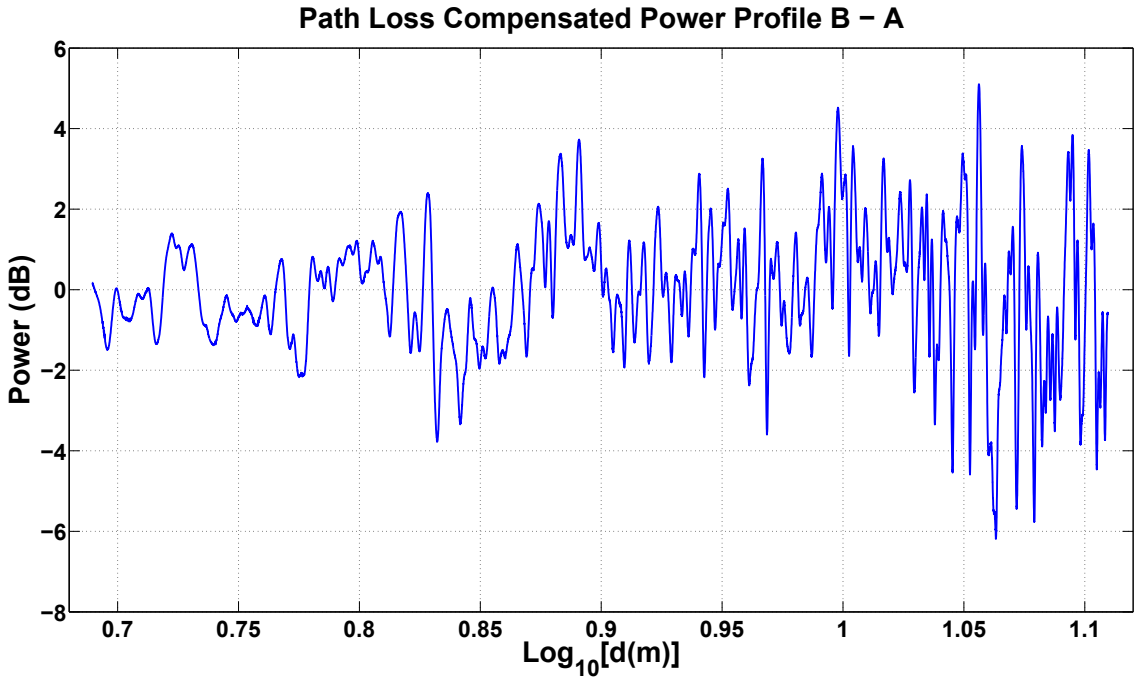

(b) Low Speed Experiment 1 B-A. Path Loss Compensated Power Profile.

Figure 67: Received Power Profile for Experiment 1 - Situation B - A.

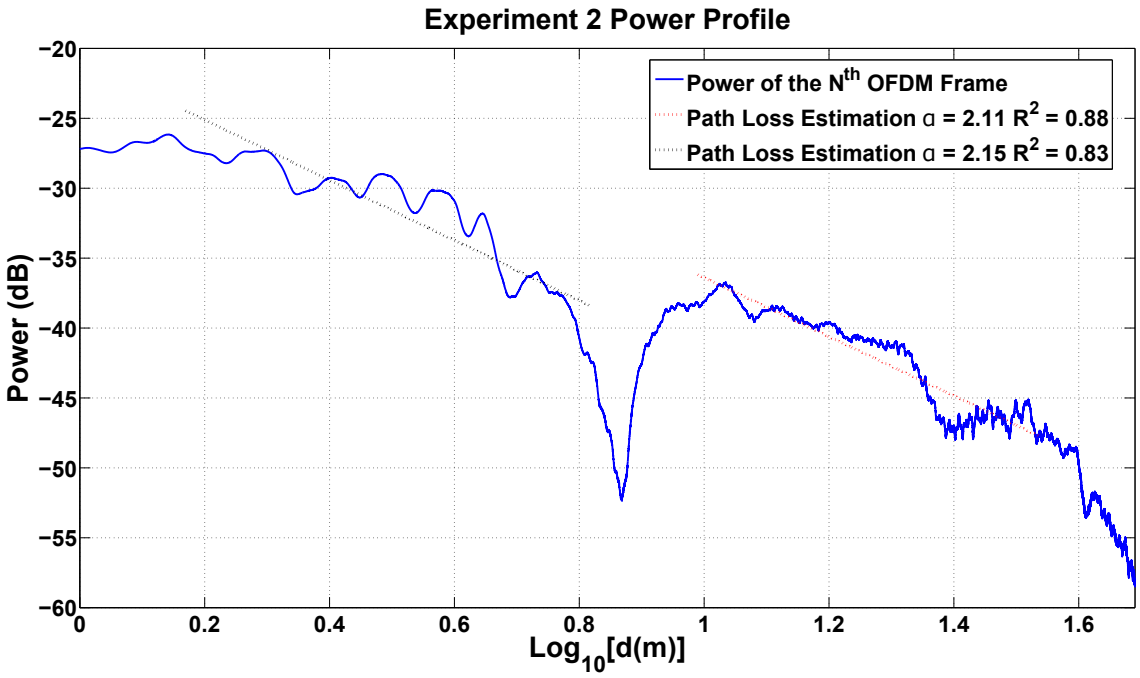

(a) Low Speed Experiment 2 Power Profile Log Scale.

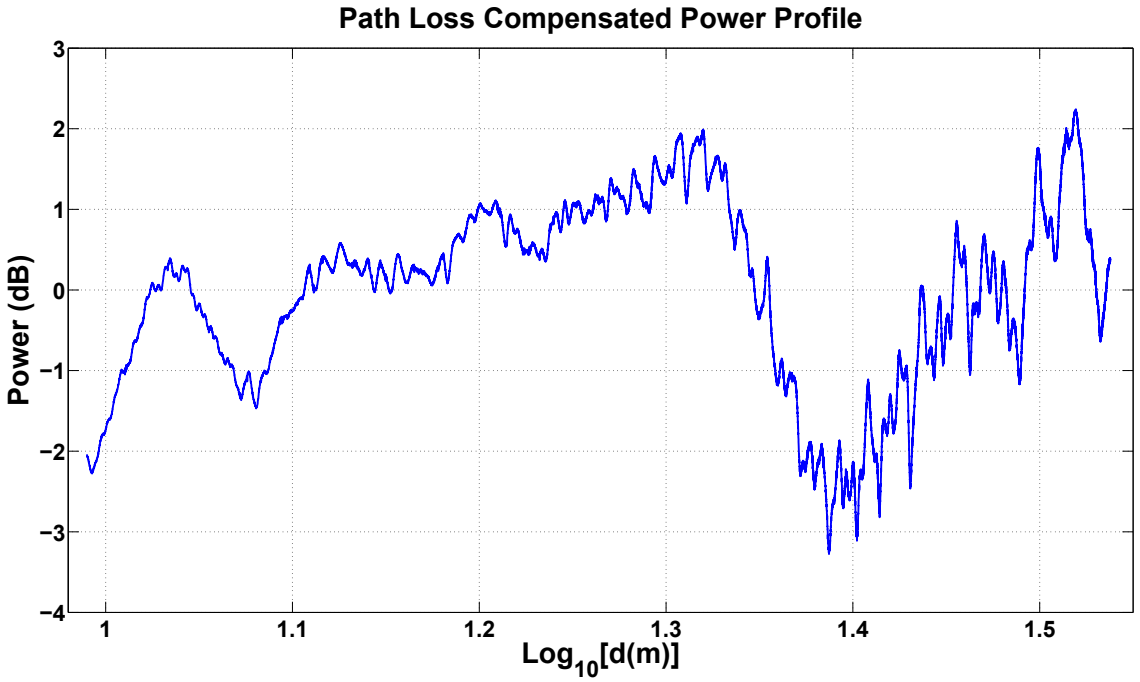

(b) Low Speed Experiment 2 Power Profile Lin Scale.

Figure 68: Received Power Profile for Experiment 2.

5.4.2 Channel Frequency Response Estimation: Low Speed Experiment

After having removed the path loss from the measurements, we can evaluate the performance of the proposed CFR estimation algorithm. The performance will be evaluated according to the error criterion set in section 3.2.2.3. The results for the experiment I can be found in Fig. 69. We have separated the two situations A - B (LOS) and B - A (obstructed LOS). In general, a good performance of the CFR estimator was found.

In the A - B situation (Fig. 69(a)), with a SNR range from 15 to 46 dB, only 689 out of 17126 OFDM received frames were found invalid for channel estimation purposes. None of the received frames with a SNR higher than 29 dB was found erroneous according to our criterion. The total packet error rate (PER) of this measurement is 4.02 %.

As it was expected, the B - A situation (Fig. 69(b)) is less favorable. In this case, OFDM frames in the SNR range from 18 to 34 dB were received. The position of the antenna in the car decreased the maximum received power by 12 dB. In this case, 842 out of 10000 OFDM frames where found invalid for channel estimation. This value represents 8.42 % of the global analyzed frames, this is twice the value found in the last experiment. In this situation, erroneous OFDM frames can still be found for SNR values up to approximately 31 dB because of the higher interference level in this obstructed LOS scenario.

A summary of the results for this experiment can be found in Tab. 12.

Table 12: Summary of the CFR Estimator Performance in Experiment I.

	Total OFDM Frames	**Invalid Frames**	**SNR Range (dB)**
Case A - B	17126	689 (4.02 %)	15 - 46
Case B - A	10000	842 (8.42 %)	18 - 34

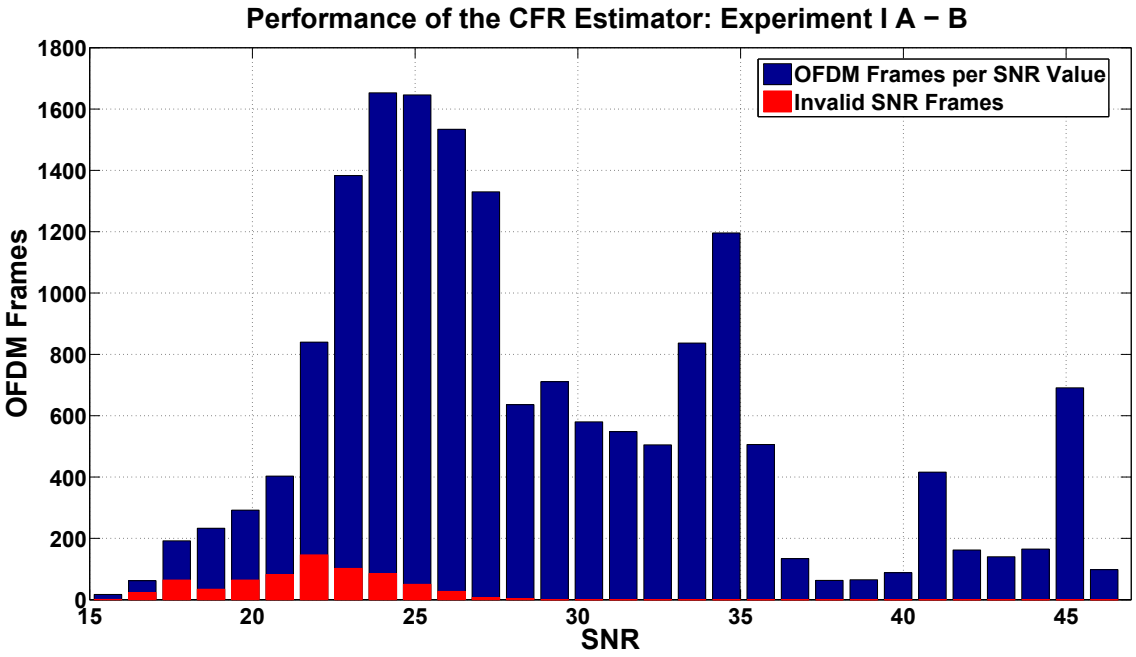

(a) A - B Situation.

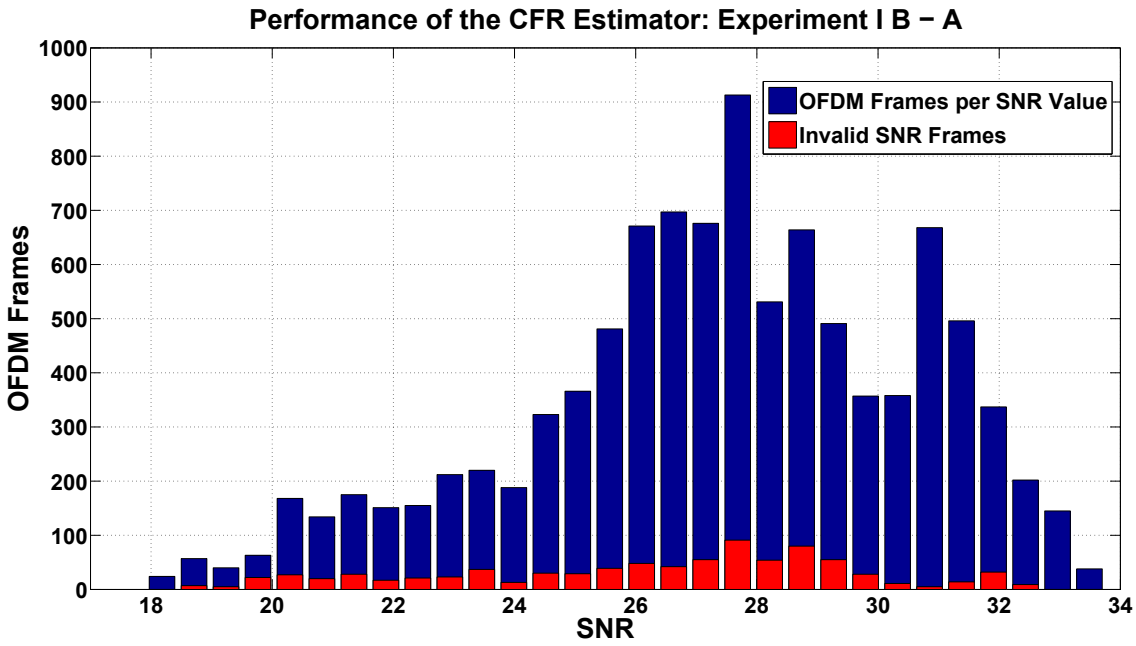

(b) B - A Situation.

Figure 69: Performance of the CFR Estimation in Experiment I.

We can find in Fig. 70 the performance of the CFR estimator in experiment II. In this case, no erroneous frames were found in the measurement region of interest. For that reason, all the frames would be suitable for channel estimation purposes. This time, 18702 OFDM frames were analyzed in a SNR range from 20 to 42 dB.

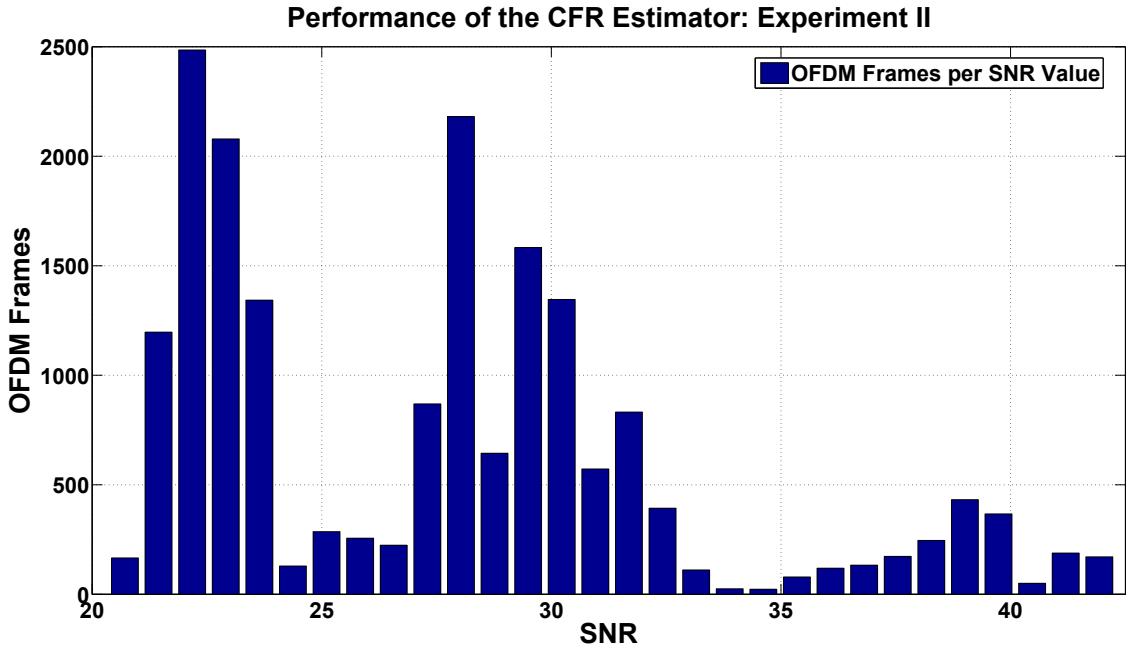

Figure 70: Performance of the CFR Estimation in Experiment II.

In general, the CFR estimator behaves properly. In Experiment I (case B-A), it was able to find approximately 93 % of the received OFDM frames valid for channel estimation purposes. Taking into account the obstructed LOS situation and the low gain of the omni-directional antenna, this result is satisfactory and allows us to continue with the validation of our channel sounder methodology.

5.5 Construction of the Channel Model

Up to this point, we have been showing the performance of the proposed channel characterization methodology in low speed scenarios. In this section, we will exploit our methodology for the characterization of the supersonic transmission channel at Baldersheim. In September 2017, a firing campaign was carried out with the objective of testing the channel sounder prototype described in section 3.3.

The channel construction model is sketched in Fig. 71. As we did in the case of the experiments performed at low speed, we will start with an analysis of the received power profile in section 5.5.1. Two elements will be treated: in a first stage, the objective is to find the path loss exponent (large scale channel behavior). In the second stage, a failure analysis had to be performed regarding the measured power profile from the flight of the projectile.

In spite of the detected anomalies, it was possible to continue with the characterization of the radio channel. In section 5.5.2, the channel behavior will be obtained. In this case, a Doppler shift characterization was performed because of the high speed of the projectile. The LOS Doppler properties are obtained here. After having studied this question, the performance of the channel frequency estimator will be evaluated.

Following our methodology, the multipath characterization of the channel is performed in section 5.5.3. The CIR in conjunction of the PDP of the channel is obtained here. It will be possible to obtain the small scale properties of the channel after having compensated the received power profile. In this section, the analysis of the PDP will allow us to define the channel model for this experiment.

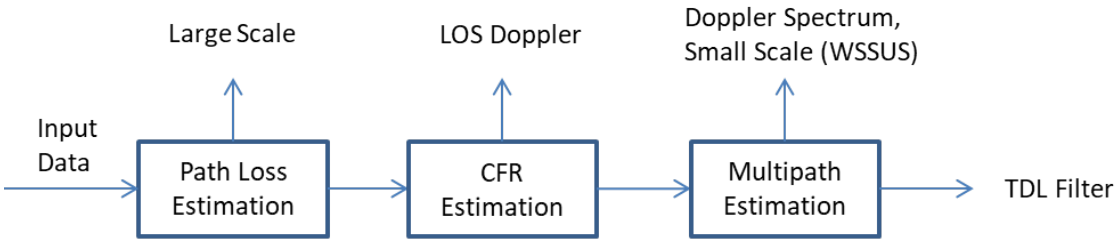

Figure 71: TDL Filter Definition.

The output of this process is a TDL filter constructed after having assumed the WSSUS channel conditions. Nowadays, TDL filters are used to model WSSUS wireless mobile radio channels in most of the situations. For example, some examples are given in [47, 96, 4, 111, 110]. As we mentioned in chapter 2, each one of the taps in the TDL filter represent a stochastic process accounting for the small scale properties of the channel, i.e. they do not account for the path loss, which is the reason why we proposed a path loss estimation algorithm.

5.5.1 Path Loss and Failure Analysis of the High Speed Experiments

We will start this section with a brief analysis of the data obtained from the firings. As it was the first time a prototype like the one we developed was tested, a certain grade of malfunction is expected. We can start our analysis by taking a look at the raw measurements we recorded. The following Fig. 72 shows the raw recording of the I component for the two instrumented prototypes at the directional station. It is clear something did not work properly with the instrumented projectile emitting at 2205 MHz as we can directly observe.

As we can see in the figure, the ADC of the X310 SDR at the receiving station was configured to store samples in the $[-1, 1]$ range with 14 bits precision. Such configuration was set in order to have a compromise between the maximum measured amplitude level and resolution. In this case, the X310 measured a maximum amplitude of 0.7 V for the prototype emitting in the 2250 MHz band while a value of 0.1 V was measured for the prototype in the 2205 MHz band. Taking into account the emission power was the same for both of the instrumented projectiles and the antenna position was not changed from one firing to another, we can conclude the difference of 0.6 V in the maximum amplitude value clearly comes from a prototype hardware failure.

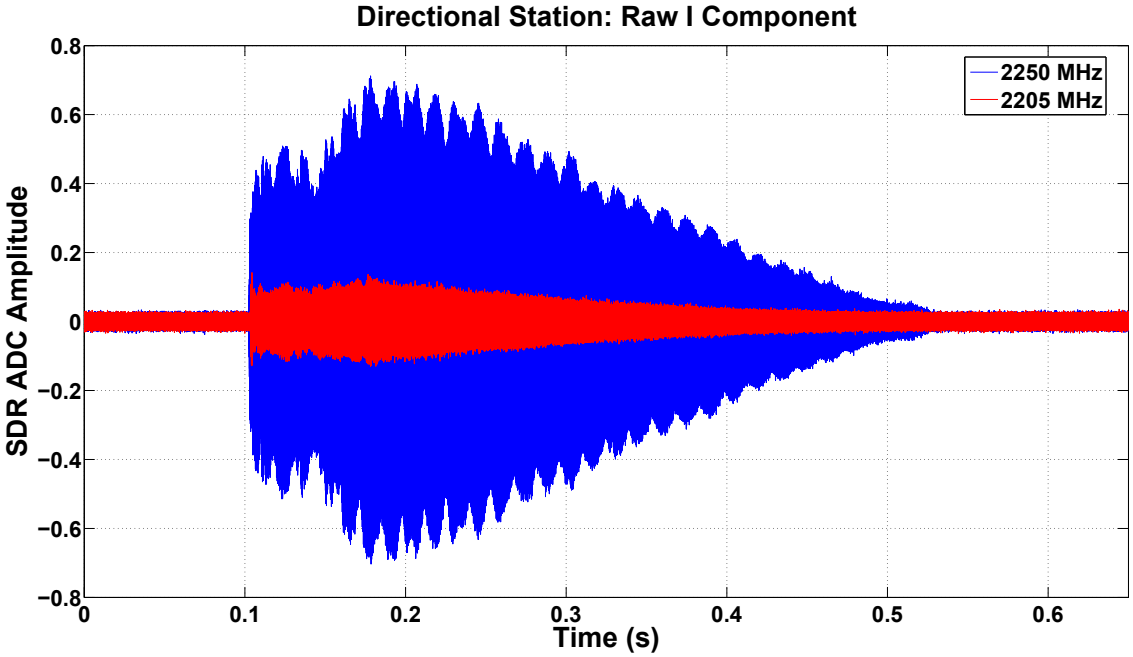

Figure 72: Raw Measurement at the Directional Hyptra Station.

In order to confirm the hardware failure assumption, we can take a look at the video recording equipment available at the firing site. This instrument is able of recording the whole flight of the projectile, from the firing to the impact with the sand bay. In the case of the 2205 MHz prototype, Fig. 73 shows an image taken 10 ms after the firing instant. We can see how the aerodynamic stabilizer at the rear of the prototype was separated from the projectile's body from the very beginning of the firing.

Figure 73: Video Recording 10 ms from the Firing Instant for the 2205 MHz Prototype.

This stabilizer does not only help to keep the projectile pointed in the right direction. In addition, it protects the antenna from the hot gasses in the firing chamber. After having seen how it is separated from the prototype's body just after a few milliseconds from the firing instant, we cannot assure it worked properly.

After a visual inspection, we detected a little hole at the bottom of the stabilizer produced during the fabrication process. This allowed the hot gasses to enter in the small cavity between the antenna and the stabilizer attachment so the high pressure of these gasses produce the separation of the stabilizer from the projectile's body. Additionally, the temperature of these gasses is assumed to be high enough to severely damage the patch antenna. Once the problem was detected, the stabilizers were replaced for the rest of the firings and this

problem was no longer observed.

The stabilizer problem previously described was not the sole anomaly we detected. The following Fig. 74 shows the power profile for the second instrumented prototype fired; the one which telemetry system was configured to emit in the 2250 MHz band. Once the received power has been estimated from each OFDM frame, we can observe an abrupt decreasing in the received power from -12 dB to -35 dB. This situation seems not being in accordance with what we should be observing.

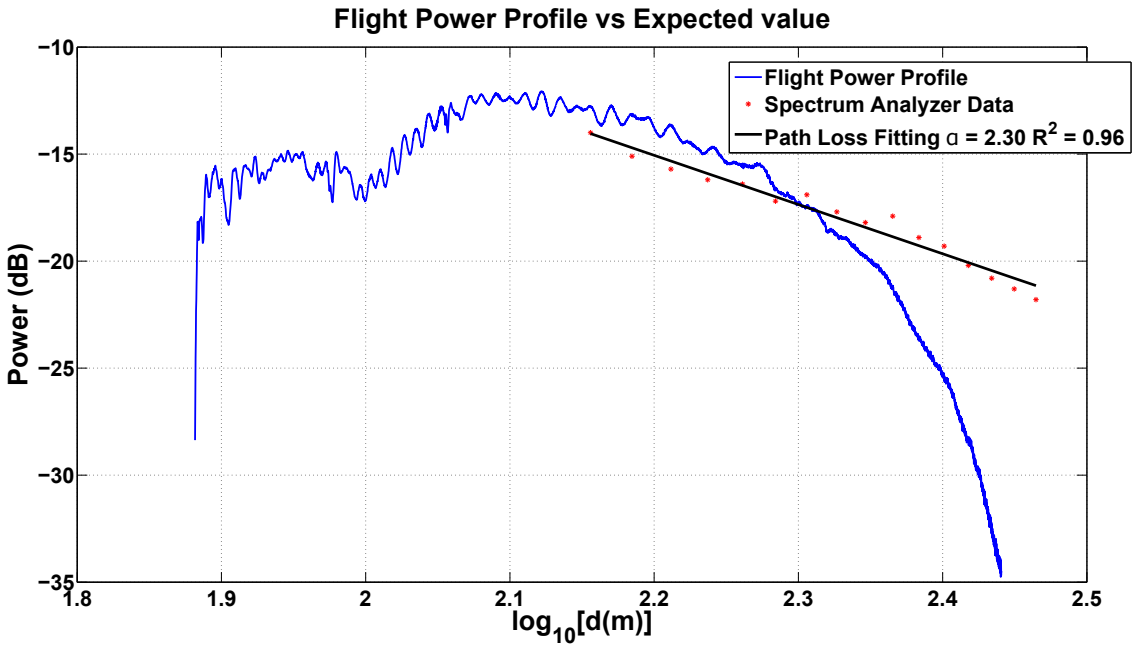

Figure 74: Power Profile Analysis for the 2250 MHz Prototype.

In order to clarify this, we performed an experiment consisting of emitting a single tone at 2250 MHz with a SDR equipment similar to the one accoutered in the prototype. Precisely, the same patch antenna as the one in the prototype was employed in conjunction with a B210 SDR at the emitting side. The received power was measured by connecting the directive Hyptra antenna to the portable spectrum analyzer PR100 from Rohde & Schwarz. In Fig. 74, the red points represent the measured power at intervals of 10 m while the black line represent the path loss fitting for these points.

The first element to notice is that the abrupt decreasing power we measured during the flight is no longer present. Secondly, the path loss exponent of 2.30 is a coherent value

according to the clear Baldersheim experimentation site. After having measured the expected power profile with the portable spectrum analyzer, we have to assume another power failure for the 2250 MHz prototype. One of the probable cases should be related to the stabilizer problem already observed in the 2205 MHz flight. Even when the attachment mechanism worked, probably the antenna was still damaged at the firing moment. The other possible hypothesis is a damage in the Avnet's Picozed power amplifier because of heat isolation problems.

Finally, the result of applying the proposed path loss estimation algorithm to the power profile at both receiving stations can be found in Fig. 75. The outcome confirms, in general, the anomaly in the received power because of the high values found for the path loss exponent. Let us to treat each case separately.

In Fig. 75(a), we can notice the three Regions of Interest (ROI) the algorithm treated. All of them show a great regression goodness, however, only the first one seems to be in accordance of what we should be obtaining as the path loss exponent found is 2.14. If we set the time reference at the firing instant, this region covers 100 ms of flight starting 86.4 ms after the firing instant. In terms of the distance traveled during this period of time, it covers 57.97 m of the firing line being the position of the first OFDM frame of this region 55.91 m from the cannon. The path loss exponent found for the other two regions is too high to be considered as correct. The summary of this measurement can be found in Tab. 13.

Table 13: Directional Station: Path Loss Characterization.

Directional Station Path Loss Characterization	**OFDM Frames**	**Path Loss Exponent**	**Distance Covered**	**Flight Time**	**Regression Goodness**
First ROI	2099	2.14	57.97 m	107.47 ms	0.91
Second ROI	1600	5.51	39.98 m	81.92 ms	0.98
Third ROI	999	11.84	23.43 m	51.15 ms	0.99

The received power evolution at the omnidirectional station can be found in Fig. 75(b).

Table 14: Omnidirectional Station: Path Loss Characterization.

Omnidirectional Station Path Loss Characterization	OFDM Frames	Path Loss Exponent	Distance Covered	Flight Time	Regression Goodness
First ROI	1500	5.179	57.97 m	107.47 ms	0.91
Second ROI	1600	15.17	39.98 m	81.92 ms	0.97

Here, we can notice the difference in the maximum received power with respect to the directional station. While a maximum received power of -12 dB was detected at the directional station, in this case we observe a maximum received power of -21 dB. As we will see later in section 5.5.2, this power difference will imply a higher number of invalid OFDM frames for channel estimation. Additionally, we observe a higher power variation with respect to the distance traveled, which is not surprising as the multipath influence in the received power is higher in the case of an omnidirectinal antenna.

This time, none of the ROI found applying our path loss estimation algorithm are good with respect to its value. The high regression goodness indicates right linear fitting, however, the path loss exponent is incoherent because of the power loss anomaly. A summary of the path loss characterization at the omnidirectional station can be found in Tab. 14.

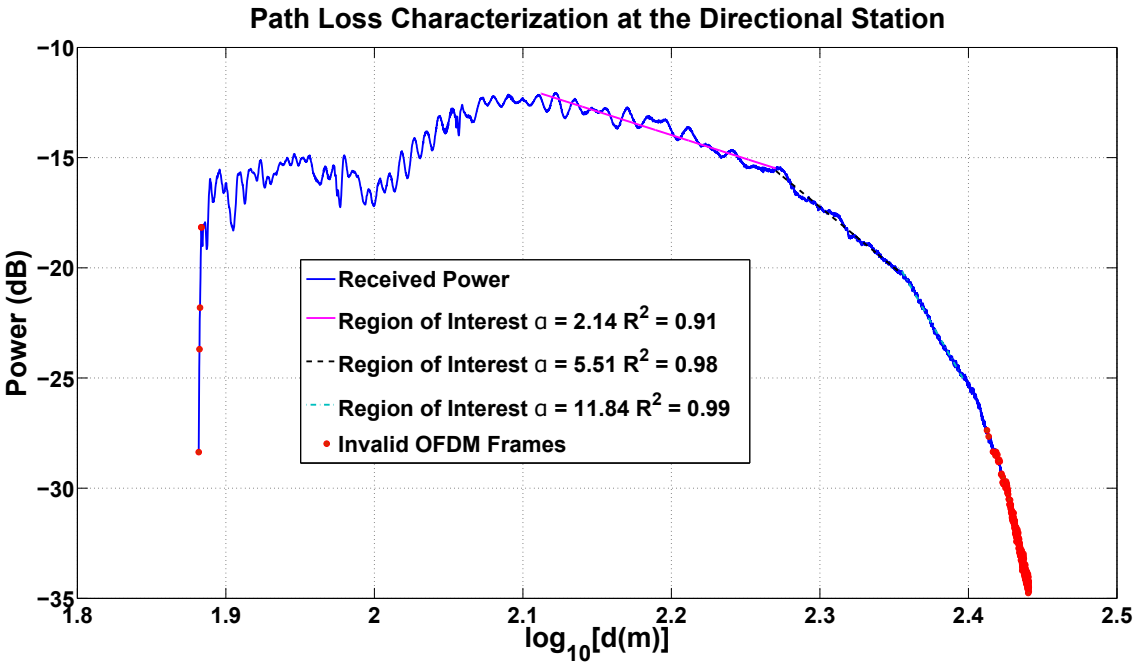

(a) Firing #4. Power Profile at Directional Station.

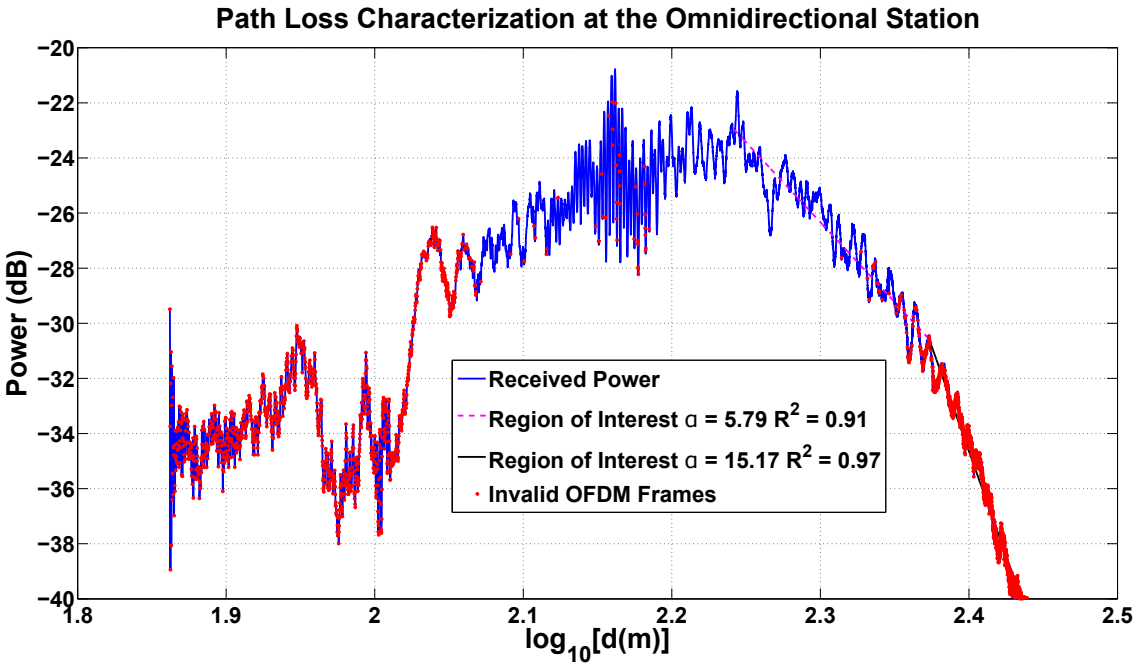

(b) Firing #4. Power Profile at Omnidirectional Station.

Figure 75: Received Power Profile for the 2250 MHz Measurement.

5.5.2 Channel Frequency Response Estimation

The results from the path loss characterization realized in the previous section 5.5.1 were not as good as we initially expected. In fact, they clearly induce us to think about a hardware failure in the prototype's transmission system. At this point, the question to answer is if the measurements can be used for channel characterization. In order to give an answer, we will continue applying the methodology defined in chapter 3 and the data flow analysis proposed in section 5.3. In other words, we will perform a frequency characterization of the channel assuming the data from the firings is exploitable.

We will start the frequency characterization of the channel by analyzing one of the elements discarded when we evaluate the performance of our channel frequency estimator in the low speed scenarios. As we exposed in section 5.4.2, the Doppler shift was considered negligible because of the relatively low expected value with respect to the subcarrier spacing. This assumption is no longer true considering the speed profile we faced in the case of a projectile firing. As we can see in Fig. 64, the prototypes were fired at an initial speed around 650 m/s. This initial value can produce a Doppler shift as high as 4.8 kHz depending on the antenna position for the emitting frequency of the prototype. This value is around 3 orders of magnitude away from the expected Doppler shift in the low speed scenarios and must be considered in our channel modeling process. This question will be treated in section 5.5.2.1.

We can also evaluate the performance of the proposed CFR estimator in our firing measurements in the same fashion as we did for the low speed experiment. This time, we will evaluate the number of OFDM frames which can be used for channel modeling. Additionally, we will perform a comparison between its performance in the high speed scenario with respect the low speed one. This analysis will be performed in section 5.5.2.2.

5.5.2.1 Carrier Frequency Offset Estimation

As we discussed in section 3.2.2.2, CFO has two components: the first one δf corresponds to the frequency difference between the local oscillators of the transceivers. The second one f_d is the Doppler shift component. As we already showed in section 2.1.3, the expected CFO value can be modeled as it appears in Eq. 91.

$$CFO = \delta f + f_d = \delta f + \frac{||\vec{v}||}{\lambda} cos(\alpha) \tag{91}$$

The situation at Baldersheim firing site is sketched in Fig. 76 where the position of the receiving stations (D and O) is given considering the cannon position as the origin of the coordinate system. If we consider the projectile is going to flight along the x axis, the angle α (station D) between the wave propagation vector $\vec{k}$ and the velocity vector $\vec{v}$ will vary between $\alpha_1 = 156.80°$ at the moment of the firing and $\alpha_2 = 173.75°$ at the impact instant. The angle β corresponding to the omnidirectional station, will vary from $\beta_1 = 74.05°$ to $\beta_2 = 160.71°$. In the case of the firing number four, the one corresponding to the prototype adjusted to emit at 2250 MHz, the initial speed was 643.23 m/s. According to radar measurements, the projectile decelerated to a speed of 424.55 m/s at the impact instant. Knowing the angles α and β, we can estimate the Doppler shift observed at each one of the receiving stations in both firing and impact instants. These theoretical estimations are summarized in Tab. 15.

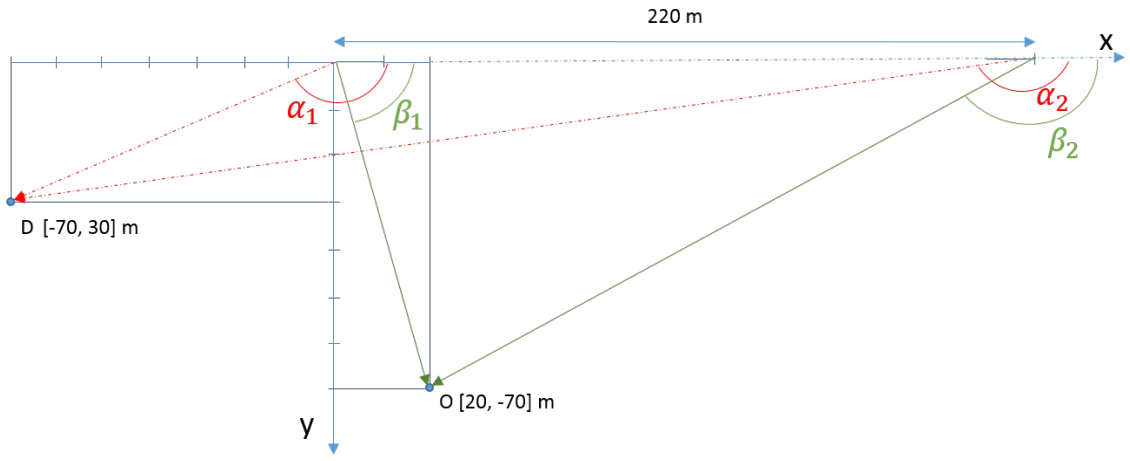

Figure 76: Theoretical Doppler Shift Estimation.

Table 15: Expected Doppler Shift

Expected Doppler Shift	**Firing Instant** $v = 643.23$ **m/s**	**Impact Instant** $v = 424.25$ **m/s**
Directional Station	-4.43 kHz $\alpha_1 = 156.80°$	-3.16 kHz $\alpha_2 = 173.75°$
Omnidirectional Station	1.32 kHz $\beta_1 = 74.05°$	-3.00 kHz $\beta_1 = 160.71°$

Before analyzing the CFO obtained during the firings, we have to characterize the δ_f parameter. Considering the SDR equipment available, we can expect a frequency instability of 2.5 ppm. In our experiences at 2250 MHz, the value we measured was δf =4.1 kHz, which is in accordance with the manufacturer's datasheet. Such a value of δf will completely mask a f_d value of 60 Hz. This was the expected for a car moving at 30 km/h as we assumed in the low speed experiments. However, for a supersonic projectile the situation will be different as the maximum expected value for f_d will be around 4 kHz for a projectile flying at 650 m/s as we already showed. In Fig. 77, we compare the theoretical expected Doppler shift with the measured value in the 2250 MHz firing.

In spite of the power loss anomaly detected in the path loss characterization, the results concerning the Doppler shift estimation show a great agreement with the theoretical expected values. After having compensated δf at the Directional Station (Fig .77(a)), the measured value follows the theoretical one during most of the flight. As we know, the performance of the CFO estimation algorithm depends on the SNR. It is not surprising then to observe an oscillating measured value during the last 40 ms of flight as this region correspond to the OFDM frames received at a SNR level around 10 dB.

Similar results can be found for the Doppler shift estimation at the omnidirectional station. In Fig. 77(b), we can see how in general the measured Doppler shift value follows the theoretical one. This time, two regions with a high deviation from the theoretical value can be observed. One at the beginning of the measurement up to 80 ms, the other one being from 325 ms to the end of the measurement. Taking a look at Fig. 75(b), we can see how both regions correspond to the noisy OFDM frames received at the omnidirectional station.

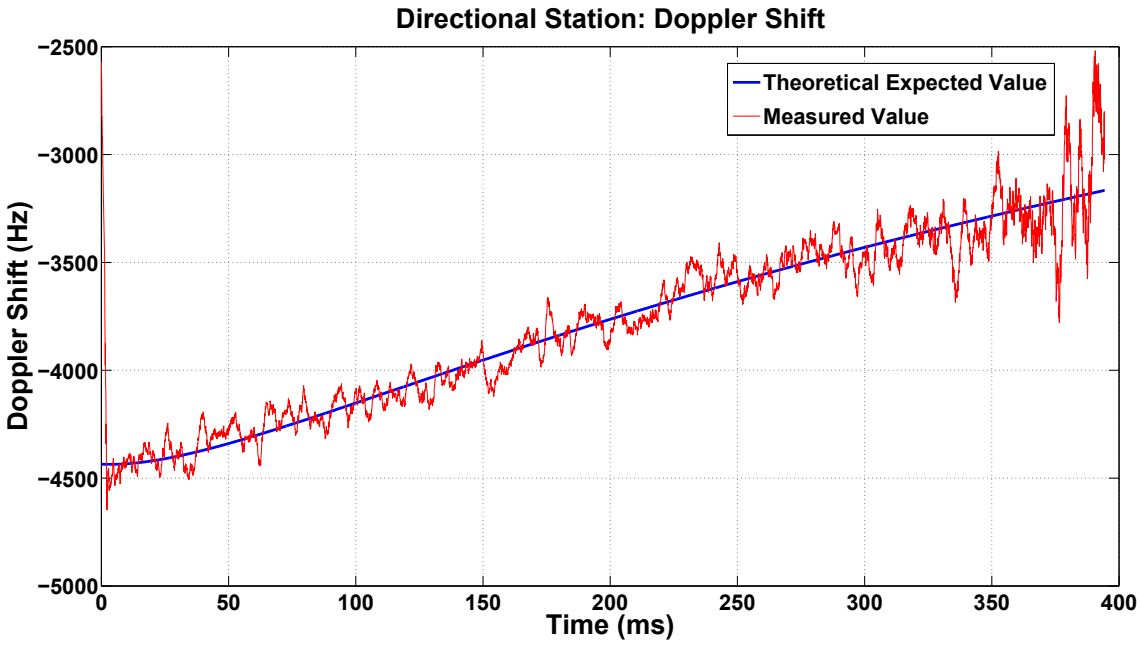

(a) Directional Station Doppler Shift.

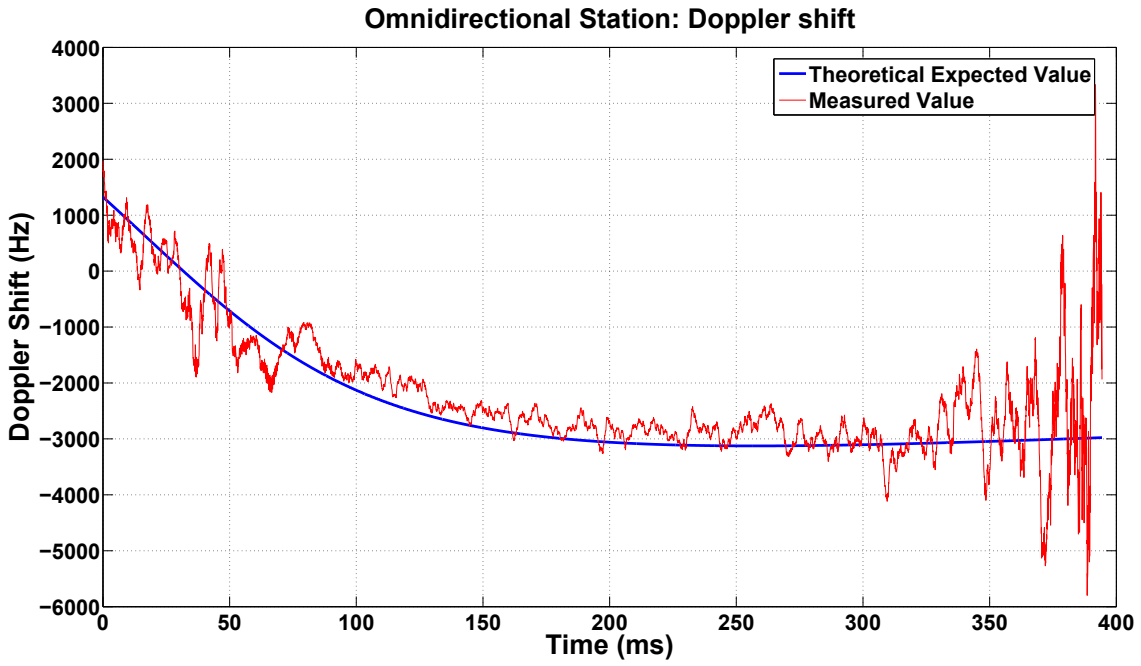

(b) Omnidirectional Station Doppler Shift

Figure 77: Doppler Shift Comparison: Theoretical Expected Value Vs Measured Value.

We can conclude the power loss anomaly did not affect the local oscillator of the Avnet's Picozed embedded in the prototype. Otherwise, neither the measured value δf nor the measured Doppler shift would have been in accordance with their expected values. As

a result, we can consider our CFO estimation algorithm as validated as it gave results matching the theoretical expected values. The high deviation regions correspond to OFDM frames received at a low SNR regime as it was predicted by the authors in [22].

5.5.2.2 Flight Performance of the CFR Estimation Algorithm

Once the Doppler shift behavior has been characterized, we can compensate its effect in the OFDM frames and continue with the CFR characterization of the channel.

In the case of the measurements concerning the 2250 MHz prototype, 7703 OFDM frames were emitted during the flight. As expected, the CFR estimation algorithm behaved differently at each one of the receiving stations as we can see in Fig. 78. In the figure, the invalid OFDM frames at each one of the receiving stations are marked in red. This representation allows us to have an insight into the error distribution in function of the SNR as we did for the low speed experiments.

The CFR estimator performance at the directional station can be found in Fig. 78(a). In this case, the 7703 frames were received at a SNR range between 5 and 28 dB. In spite of the power loss detected, the CFR estimator found only 326 OFDM frames invalid for channel estimation purposes, i.e. these invalid frames represent only 4.23 % of the measurement. Additionally, most of them are concentrated the really low SNR regime between 5 - 10 dB.

The same results are obtained in Fig. 78(b) at the omnidirectional station. Because of the worst SNR regime, the CFR estimation algorithm found 2878 frames invalid for channel estimation. Such value represents 37.36 % of the global measurement.

Regarding the good results obtained at the directional station in spite of the power loss detected, we conclude we can continue with our channel characterization. The origin for the high PER at the omnidirectional station, i.e. whether it comes from the low SNR regime of the measurement or it is caused by the multipath effect, is something we will discuss in the following sections.

A summary of the CFR estimator performance can be found in Tab. 16.

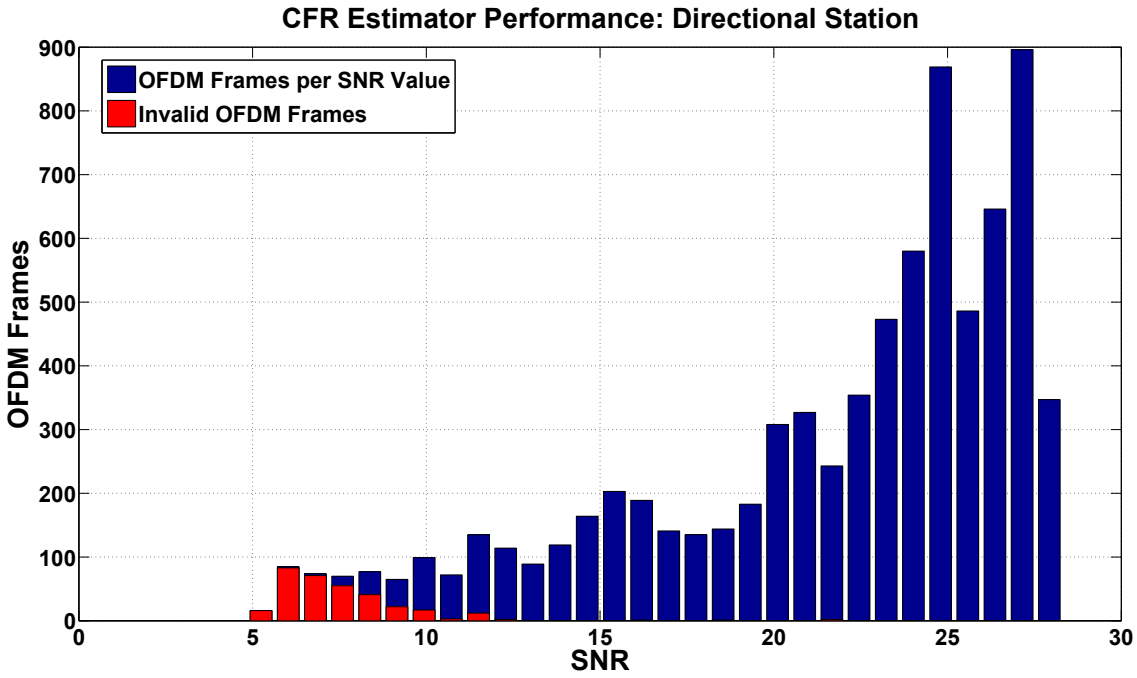

(a) Performance at the Directional Station.

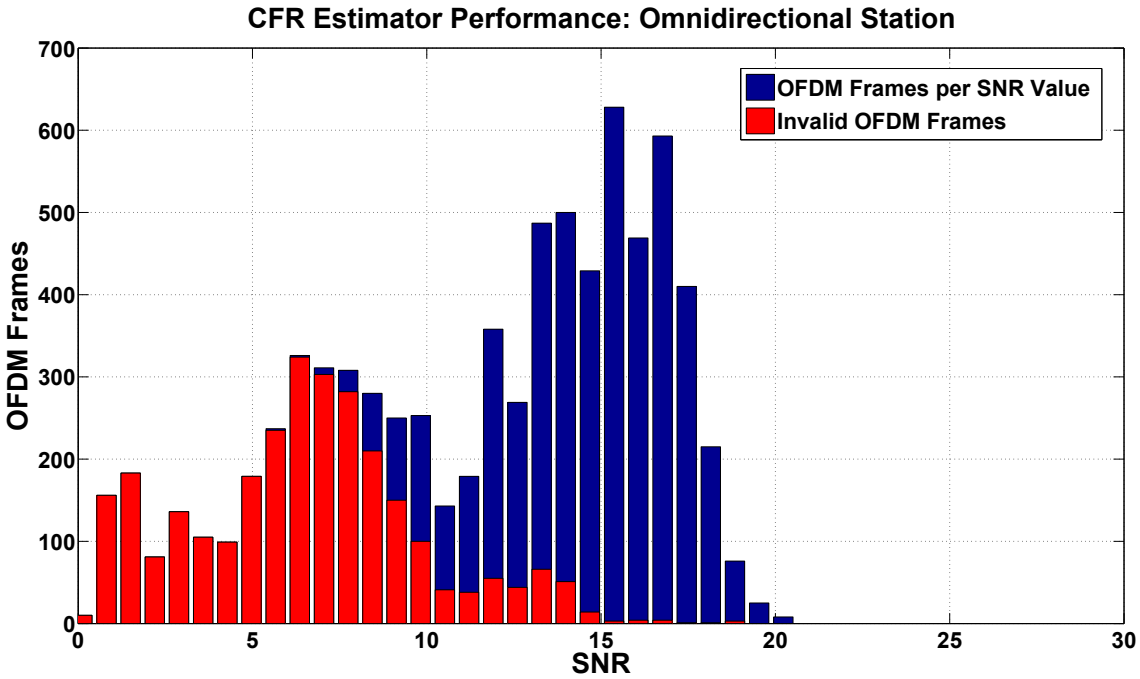

(b) Performance at the Omnidirectional Station.

Figure 78: High Speed CFR Estimator Performance.

Table 16: CFR Estimator Performance in High Speed Experiment.

	Total OFDM Frames	**Invalid Frames**	**SNR Range (dB)**
Directional Station	7703	326 (4.23 %)	5 - 28
Omnidirectional Station	7703	2878 (37.36 %)	0 - 20

5.5.3 Multipath Characterization & Power Delay Profile

The application of the multipath estimation algorithm proposed in section 3.2.2.4 allows us to obtain the CIR. In the following, this algorithm was applied to each OFDM frame considered as valid for channel estimation purposes.

An example of how this algorithm works can be found in Fig. 79. The CIR 150 ms after the shot of the projectile is shown for a period of time of 30 ms at both receiving stations. According to our CIR estimation algorithm and the OFDM frame rate emission, one CIR is obtained every 51.2 μs. Indeed, 585 CIRs are plotted in the time axis. The origin of the delay axis ($\tau = 0$ ns) corresponds to the LOS ray. Knowing the CP of our OFDM frames is 16 samples long, we represent up to $\tau = 15 \times 50 = 750$ ns with a resolution of 50 ns. According to our algorithm, the amplitude and phase evolution for 16 paths can be obtained.

As expected, the CIR behaves differently at each one of the stations. Both CIRs present a strong LOS path. However, while in the directional station the amplitude of the MPCs is barely observable their influence is higher in the case of the omnidirectional station. At this point, we can evaluate the impact of each multipath component at the receiver side. In order to perform this task, the MPCs will be evaluated in function of their power contribution.

In Fig. 80 - 81, we show the power contribution of the LOS path at both receiving stations with respect to the power of the received OFDM frame. In both cases, the blue line corresponds to the OFDM frame power. The red line, which correspond to the power contribution of the LOS path. It was computed as it appears in Eq. 92, where a_{LOS} represents the LOS path gain in each one of the CIRs obtained. Additionally, P_{OFDM} is the power of the emitted OFDM sensing signal.

$$P_{LOS}(dB) = 10log_{10}\left[a_{LOS}^2 P_{OFDM}\right] \tag{92}$$

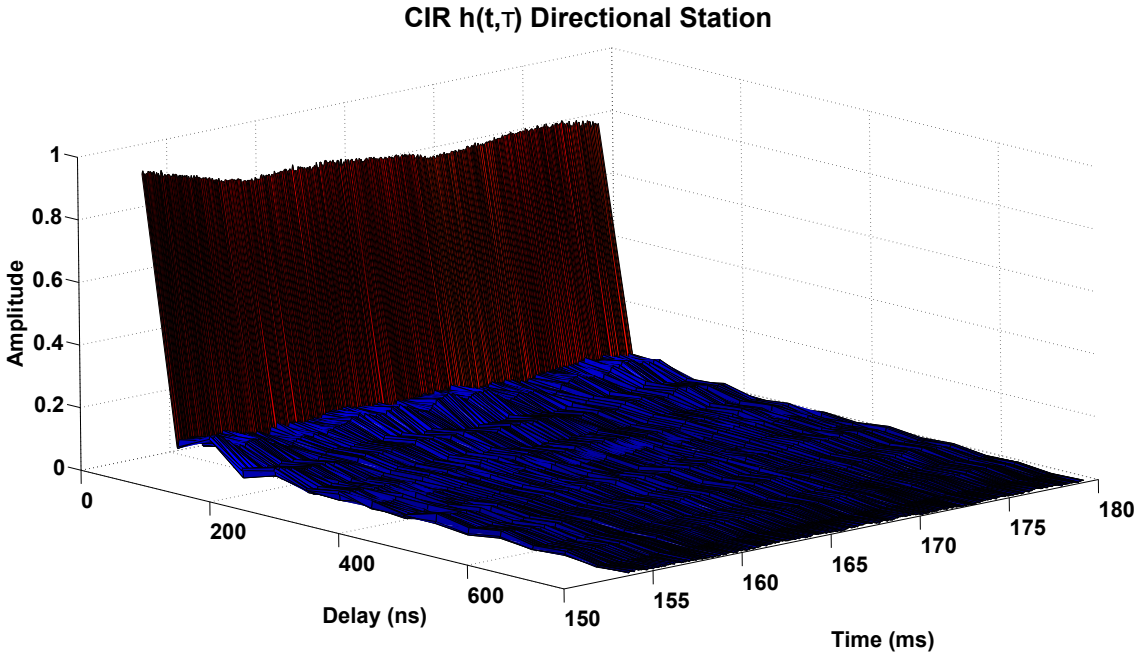

(a) Directional Station: CIR between 150 - 180 ms.

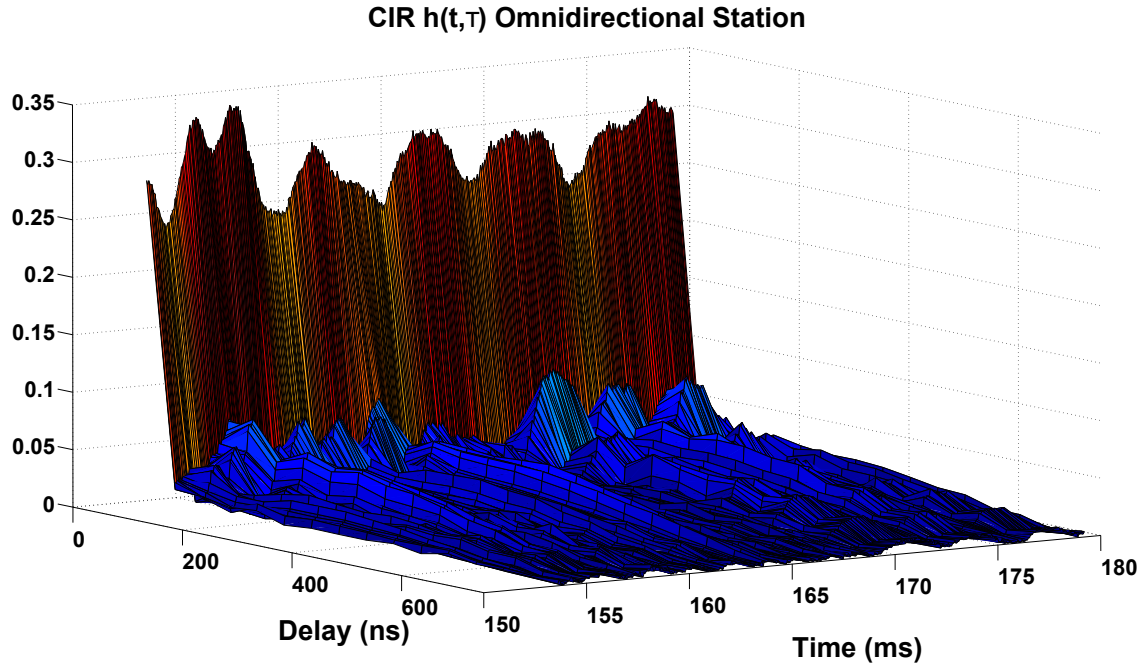

(b) Omnidirectional Station: CIR between 150 - 180 ms.

Figure 79: CIR $h(t, \tau)$ Estimation.

In Fig. 80(a), we compare the power contribution of the LOS path, which would correspond with the first tap of a TDL filter, with the power measured at the directional station. In the following analysis, only the power information from the OFDM valid frames will be considered. As we can see, it seems to be fair to assume the LOS condition. According to the figure, the global received power profile correspond to the received power profile of the LOS path.

In order to confirm the previous assumption, in Fig. 80(b) we show an histogram in which we can see how the power contribution of the LOS component is higher than 95% of the global power in the 100% of the OFDM analyzed frames. For that reason, the TDL filter which models the channel behavior at the directional station will be defined in terms of a 1-TDL (1 Tap Tapped Delay Line) filter [4].

The same previous reasoning can be applied in the case of the omnidirectional station. The power profile of the LOS path is showed in red in Fig. 81(a). Again, the received power profile is plotted in blue for comparison. As predicted by the CIR estimation, the presence of stronger MPCs has an impact on the lower power contribution of the LOS path. The decision on the number of taps required to model the channel at this station will be taken in function of the histogram in Fig. 81.

As it is shown in Fig. 81(b), in the case of the omnidirectional station the LOS path contributes with at least the 95% of received power in the 94.53% of the analyzed frames. Even this contribution has decreased with respect to the directional station because of the multipath effect, we will still model the channel at as a 1-TDL filter.

Through our experiments, we have determined the channel model can be seen as a 1-TDL filter at both stations. In the next section 5.6, the channel model will be finally specified.

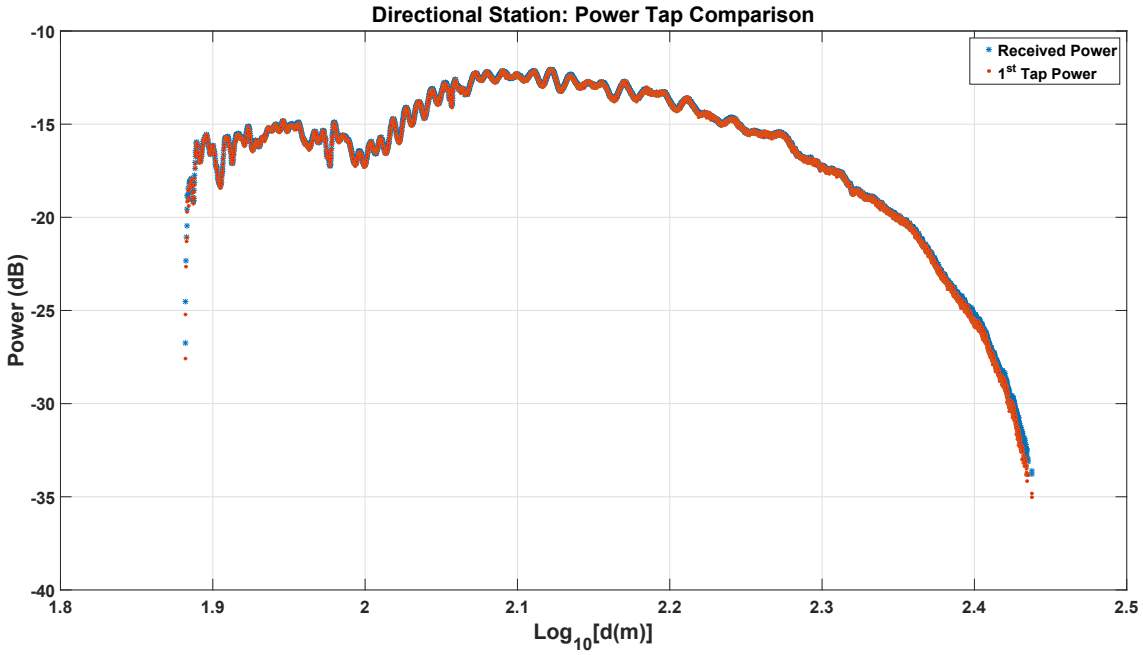

(a) Directional Station Power Evolution Comparison.

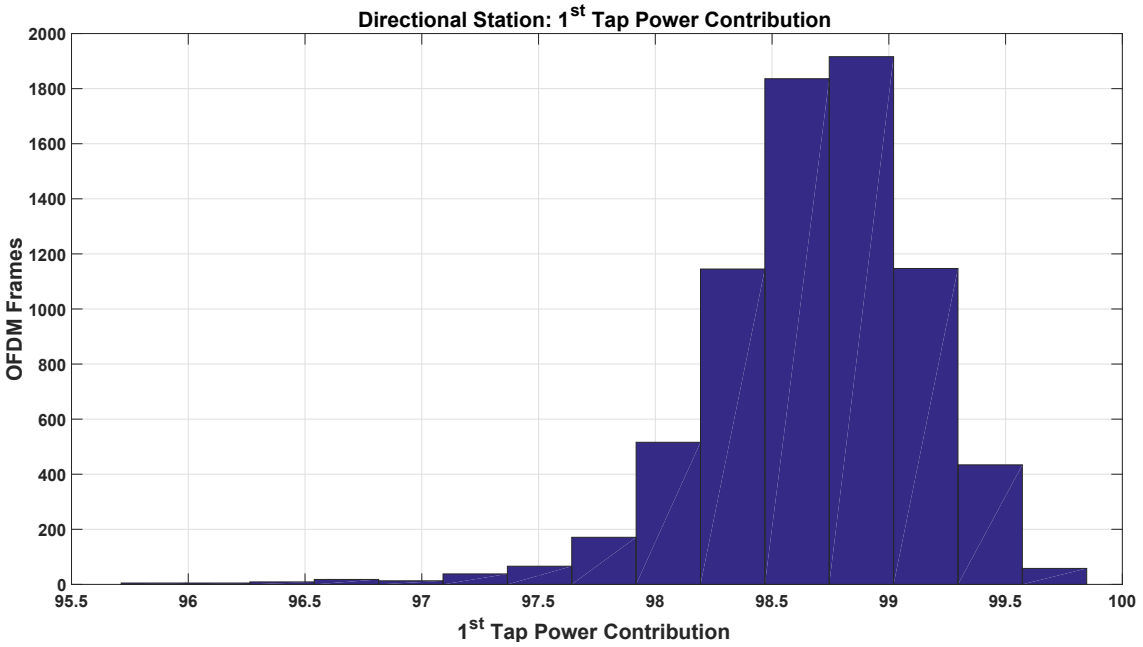

(b) Directional Station: LOS Relative Power Contribution.

Figure 80: Directional Station: LOS Power Contribution.

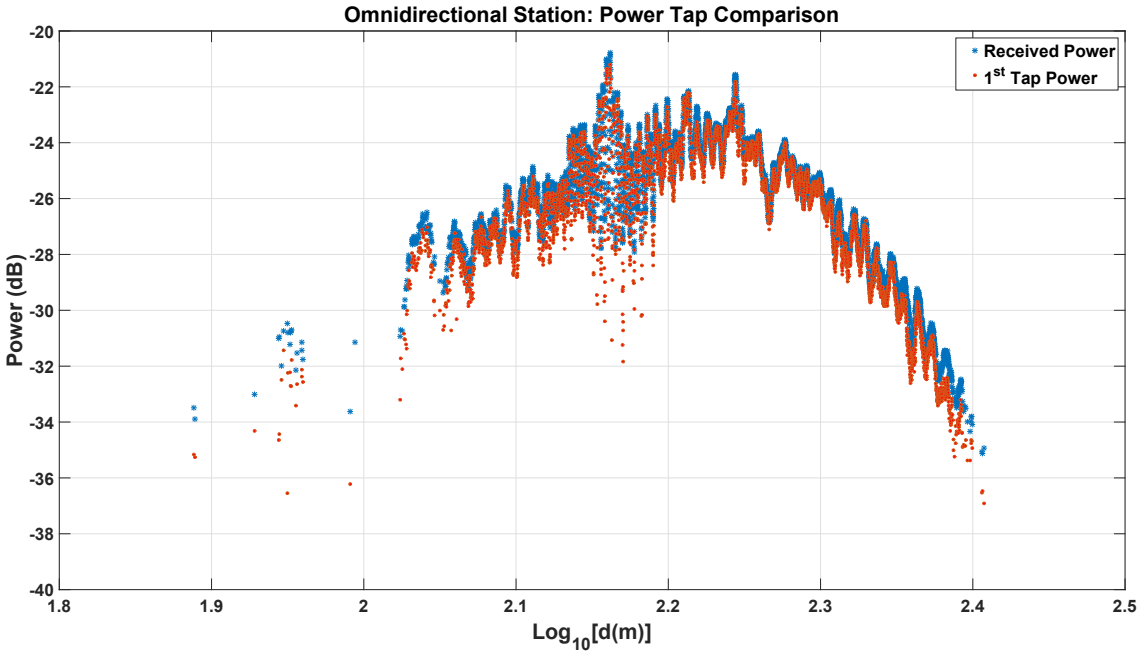

(a) Omnidirectional Station: Power Evolution Comparison.

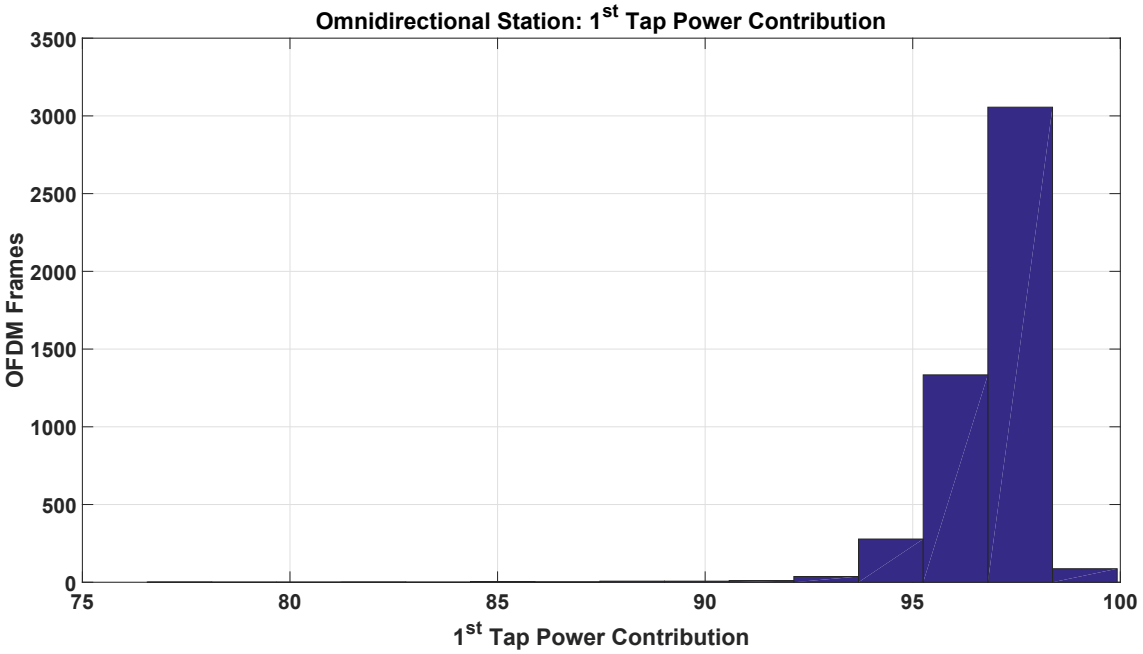

(b) Omnidirectional Station: LOS Relative Power Contribution

Figure 81: Omnidirectional Station: LOS Power Contribution.

5.6 The Channel Model

The channel model will be built in base of the experimental data we have measured. As we have stated in section 5.5.3, it will be modeled as a function of the LOS path.

- Path loss behavior: this parameter could not be obtained through the experiments with the prototype. However, through the failure analysis we found a value of 2.3. This is in accordance with the expected value for the studied propagation scenario, i.e. LOS situation with limited multipath influence. For that reason, this parameter will adopt the values between 2 - 3. Which is a compromise between the free space situation and the urban area in Tab. 18.

- Doppler spectrum: the Doppler spectrum was obtained in section 5.5.2. As we showed, the CFO estimation algorithm was able to track the Doppler shift of the LOS component at both stations. In this situation, where the multipath effect can be neglected, the power density will be concentrated in the LOS component. For simulation purposes, the Doppler spectrum will be composed of a sole peak with a frequency value obtained through Eq. 89 and the position of the receiving station.

- Multipath behavior: even though the channel will be modeled as a 1-TDL filter, we have to accept the limitation of the time resolution when characterizing the channel multipath behavior. No consistent MPCs with a propagation delay higher than 50 ns with respect to the LOS component were detected. However, we can observe in Fig. 80(a)-81(a) a certain grade of multipath influence which causes the oscillations in the received power profiles. It is assumed that the propagation delay for these components is lower than 50 ns with respect to the LOS component. For this reason, they cannot be characterized with our sampling rate of 20 MHz. Instead, they will be modeled statistically taking into account the envelope (magnitude) of the LOS component obtained through the CIR estimation algorithm. In Fig. 82, we show the histogram of the envelope's value at both stations and how it can be approximately modeled either with a Rician or a Weibull distribution. Rician distributions are commonly proposed

Table 17: MLE Distribution Fitting

Directional Station	**Rice Distribution (s | σ)**		**Weibull Distribution (a | b)**	
	0.18	0.04	0.21	5.08
Omnidirectional Station	0.06	0.02	0.07	3.86

for the characterization of the amplitude's envelope of the LOS component in TDL channel models. For example, in microcell channels [72], in satellite communications [3] or Vehicle - to - Vehicle applications [27]. As stated by Sagias in [89], the Weibull distribution has been utilized for characterizing experimental data in the field of wireless communications with a good agreement. Concretely, studies have been reported in indoor [10] and outdoor applications [45].

The Probability Density Function (PDF) of the Rice and Weibull distributions can be found in Eq. 93 - 94. As we can see, Rice PDF is defined in function of two parameters, i.e. s and σ. In our context, s^2 can be considered as the power of the LOS component, σ^2 being the power of the scattered components. The Ricean K factor is defined as $K = s^2/2\sigma^2$, i.e. the power ratio between the LOS path and the MPC as we defined in chapter 4. In Eq. 93, the $I_0(z)$ function represents the zero order modified Bessel function of the first kind. The following Tab. 17 shows the estimated parameter for each one of the distributions at both receiving stations, they were obtained after performing a Maximum Likelihood Estimation (MLE) with the MATLAB software.

$$PDF_{Rice}(x) = \frac{x}{\sigma^2} exp\left(\frac{-(x^2+s^2)}{2\sigma^2}\right) I_0\left(\frac{xs}{\sigma^2}\right) \tag{93}$$

$$PDF_{Weibull}(x) = \frac{b}{a}\left(\frac{x}{a}\right)^{b-1} e^{-(x/a)^b} \tag{94}$$

The global estimated K factor is 10.05 dB for the case of the directional station and 6.53 dB in the case of the omnidirectional station. This value is in accordance with the theory as the influence of the multipath effect in the directional station shall be lower than the one

in the omnidirectional case, i.e. the LOS path will have a bigger influence in the case of the directional station.

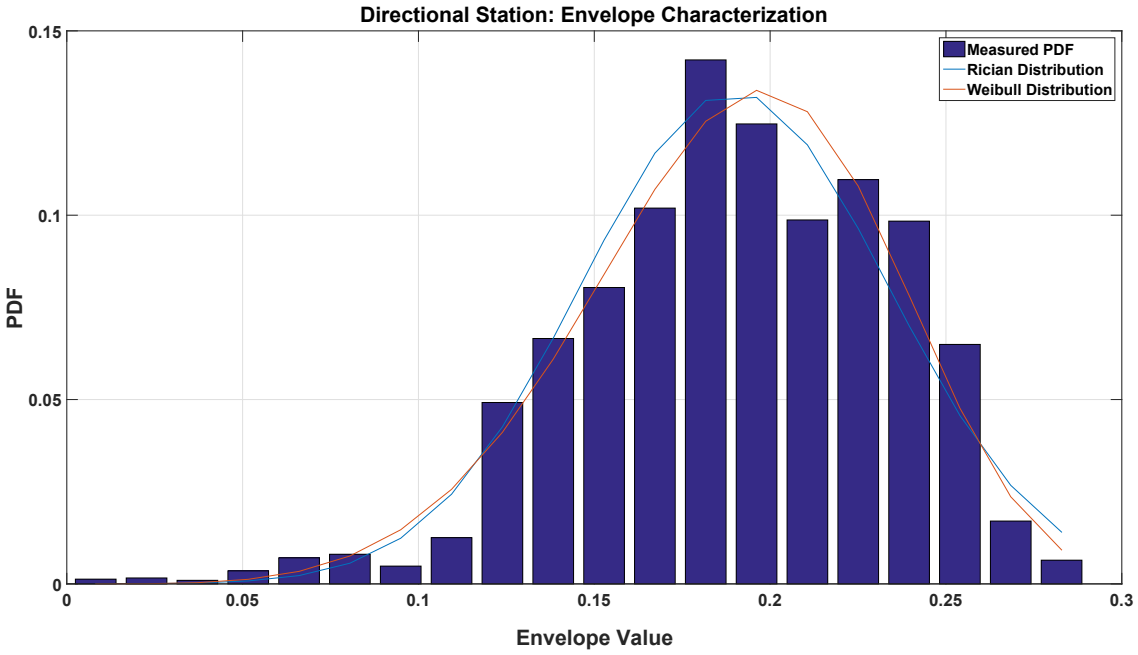

(a) Directional Station: Envelope Characterization.

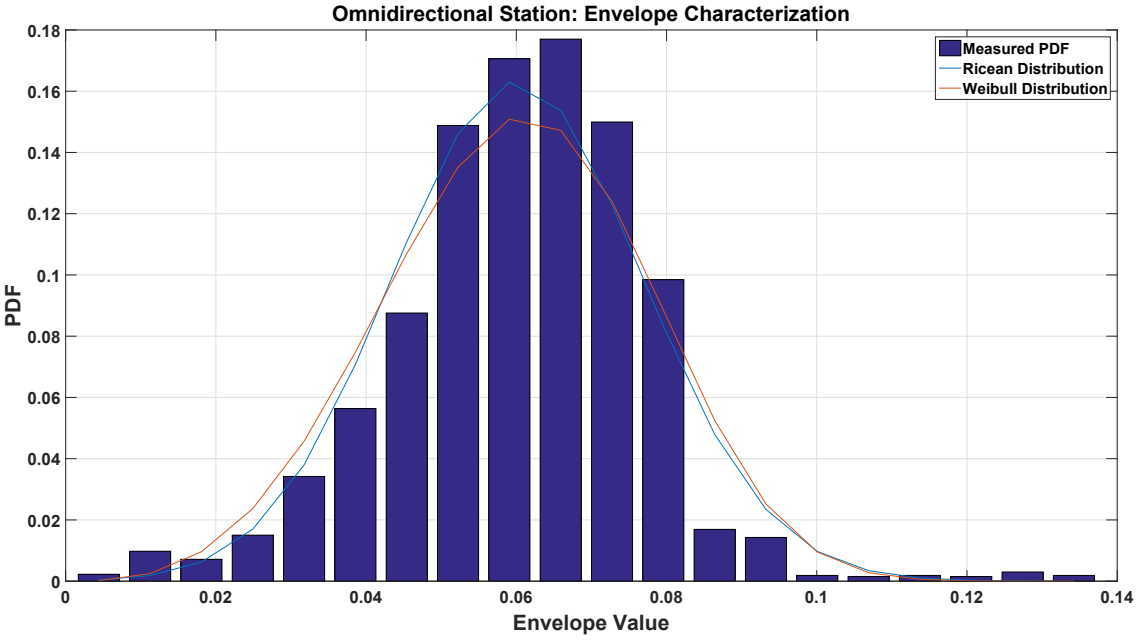

(b) Omnidirectional Station: Envelope Characterization.

Figure 82: LOS Envelope Characterization.

The CIR estimation algorithm allows us to observe the phase behavior of the LOS component at both receiving stations. Fig. 83(a) shows how the phase behavior of this component at the directional station is almost constant because of the low influence of the MPCs. In Fig. 83(b), the behavior is not as linear as in the previous case because of the higher influence of the MPCs in the omnidirectional antenna.

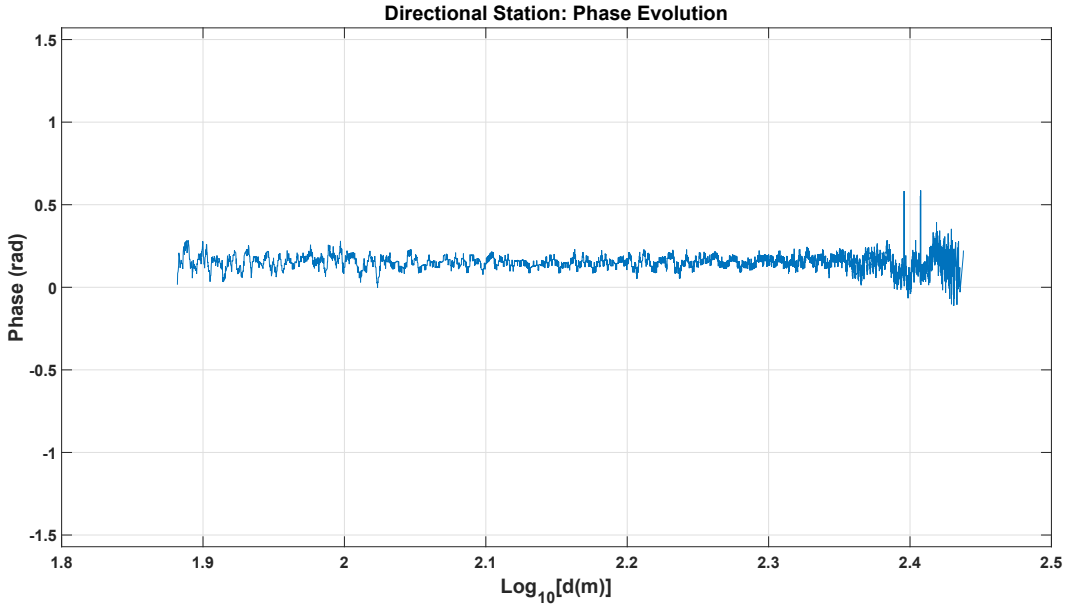

(a) Directional Station: Phase Characterization.

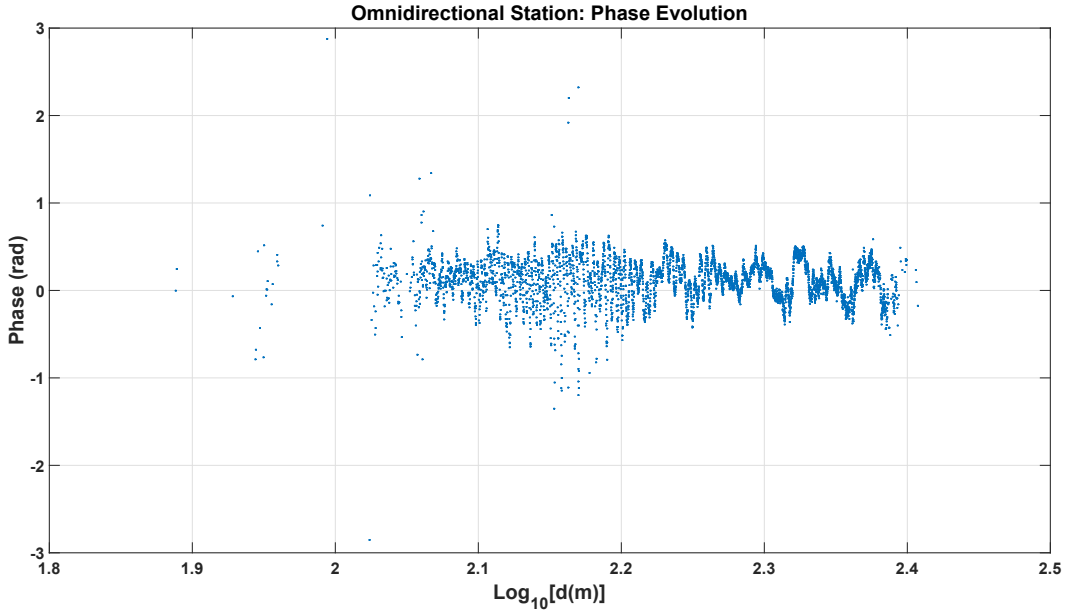

(b) Omnidirectional Station: Phase Characterization.

Figure 83: LOS Phase Characterization.

5.7 Towards an Embedded Wideband Digital Transceiver

In this chapter, we have demonstrated how the current off-the-shelf electronics can be embedded for projectile applications. At the same time, we achieved to establish a communication link between the projectile and the receiving station. Even though the experiments were performed in order to characterize the wideband channel, a vast part of the work will be used for the design of a wideband digital transceiver.

- Embeddability: in our testing we have employed an Avnet Picozed Board. In spite of the power failure we experienced, we were still able to make this device work in an hostile environment as a firing is. With further research, we can base the future hardware on the one employed in this experiment.

- Wideband Digital Transmission: ISL experiment field in Baldersheim represents an ideal case as far as multipath propagation is concerned. Moreover, when the transmission bandwidth increases with the data throughput, the channel has more chance to become frequency selective as we introduced in chapter 2 (the sampling rate increases and MPCs become detectable and degrade the transmission spectrum). This concept will have to be taken into account when deploying a new digital transmission system with higher sampling rate.

5.8 Conclusions

We started this chapter in section 5.1 with a brief revision of the telemetry systems employed at ISL. The need for high throughput transceivers has been increasing over the years. For that reason, there is a necessity in migrating from single carrier transmission techniques to more spectrum-efficient multicarrier ones. However, a wideband characterization of the channel has to be performed prior to the implementation of these systems.

We continued in section 5.2 by presenting the setup of the experiments in which we tested our channel sounding methodology. The experimentation process was structured in two different situations: in the first one, the methodology was partially tested in low speed scenarios. We sought here to test the path loss estimation technique and the CFR estimator. In the second set of experiments, a fully operational channel sounder prototype was tested in real firing conditions.

At this point, we were in conditions to define in section 5.3 how the measurements from the experiments will be treated.

The results out of the low speed experiments can be found in section 5.4. They were satisfactory enough to validate the path loss estimation algorithm and the CFR estimator, which is a crucial element in our methodology as the CIR is obtained after the CFR characterization.

The construction of the channel model for projectile applications started in section 5.5. As we did in the low speed experiments, firstly we performed a path loss estimation of the channel. The results were not satisfactory because of the system failure during the flight. For that reason, the path loss behavior had to be found in another experiment with a VNA. Nevertheless, the data recovered from one of the firings was considered to be exploitable.

In the next step, we evaluated the CFO estimation algorithm. In spite of the flight failure, the results were in accordance to those predicted in theory. This partially confirmed we could use the measured data to characterize the channel. Finally, the CFR estimator results totally confirmed this assumption. In general, it demonstrated to perform satisfactory if a minimum SNR of 10 dB can be assured during the measurement process, result which coincides with

the one in the low speed scenario where no system failure occurred.

After having obtained the CFR of the channel, we applied the multipath estimation algorithm in order to obtain the CIR. This allowed us to obtain the power delay profile. It was determined the channel could be modeled as a 1-TDL filter.

The chapter concluded in section 5.6 with the definition of the channel model. The future aspects to be considered in the conception of wideband digital transceivers were sketched in section 5.7. The final outcome of this chapter, which is the channel model, was defined on the basis of three parameters.

- The path loss exponent, obtained through the repetition of the received power profile.
- The Doppler spectrum, which was obtained taking into account the LOS assumption, the projectile's speed and the position of the receiving antennas.
- Finally, the statistical distribution for the tap's envelope was obtained after having removed the path loss effect from the measurements.

GENERAL CONCLUSION & OUTLOOK

The presented manuscript summarizes three years of study in the radio channel modeling applied to the field of instrumented projectiles. The document has been structured in five chapters, each one written with the objective of progressively introducing the reader into this specific topic.

The context of the thesis was introduced in chapter I. A brief introduction to the history of the wireless transmission systems was given. Nowadays, almost every electronic device is equipped with some kind of communication system. In the frame of applications for defense and security, the instrumentation of projectiles has been gaining in importance with the miniaturization of the electronics commercially available. Nevertheless, the instrumentation of projectiles is a demanding task which requires the use of high throughput telemetry and communication systems. At ISL, the STC group is in charge of the development of the embedded radio systems employed in instrumented projectiles. In such context, a joint initiative between ISL, XLIM laboratory from the University of Poitiers and DGA was established with the objective of improving the capabilities of the current communication systems. One of the first elements to consider in the conception of a radio equipment is the channel where it will be deployed. For this reason, the characterization of the radio channel has been the major concern of this thesis.

Before addressing the characterization of the radio channel, it was necessary to introduce the nomenclature required to follow this document in chapter II. Consequently, the chapter was divided in two parts. The first one was focused on the mathematical description of the channel properties. This lead to the definition of the channel impulse response and the Bello's functions. The second part of the chapter was centered on the description of some of the most popular channel sounding techniques. Regarding the particularities of this work (size, supersonic speed of the projectiles, etc.), we concluded we needed to develop our own channel sounding technique and the prototyping instrumentation.

Before starting the development of a channel sounder for projectile applications, we

presented the instruments and tools available at the beginning of the thesis in chapter III. Since the budged was a constraint to be taken into account, this allowed us to approach the problem in a realistic manner. The second part of this chapter was devoted to the conception of our channel sounding technique. The proposed sounding methodology is based on the OFDM transmission technique while the hardware chosen for its implementation was some of the latest SDR devices available on the market. A prototype was developed in order to perform channel sounding in flight conditions.

Before testing the prototype in flight conditions, a preliminary study of the propagation channel was performed in chapter IV. Globally, the chapter was structured in two parts: in the first one we studied the effect of the spinning and nutation on the received signal. It was determined that their effects could be excluded for channel modeling purposes. However, the simulations we performed in this chapter with the RaPSor ray propagation software allowed us to have a first insight into the key elements to characterize: the Doppler and multipath behavior of the channel. In the second part of the chapter, real data from a previous firing campaign at ISL was analyzed. We observed how the Doppler shift was in accordance to the one obtained by means of simulations.

In chapter V, we finally tested our wideband channel sounder prototype in real firing conditions. However, some of its functionalities were previously checked at low speed conditions. A firing campaign took place in September 2017 with the objective of obtaining a channel model for projectiles applications at ISL. A failure analysis had to be performed after having detected some anomalies in the measured data. In spite of that, we proved how the data could be used for channel modeling. Finally, the channel was modeled as a 1-TDL filter. It was constructed through the path loss properties of the channel, its CFR and an analysis of the PDP.

The contributions of this thesis were: the development of a channel sounding method based on the OFDM transmission technique, its implementation in an instrumented projectile and the characterization of the supersonic channel at the ISL firing facilities. Some questions are still open for further analysis in the coming years.

- Propagation Conditions: in this thesis, we have characterized open propagation scenarios with a limited impact of the multipath effect. The characterization of propagation scenarios in presence of strong MPCs, for example, in densely populated urban areas, remains an open subject.

- Improvement of our Methodology: during this thesis, most of the experiments have been carried out in LOS condition. The results from performing experiments in situations where this condition is not fulfilled will help improving the proposed algorithms in our methodology.

- Angle of Arrival: an interesting parameter to study is the angle of arrival from the impinging signals at the receiver side of the communication. This subject, which was not studied in this thesis, will allow to extract additional information from channel sounding. For example, it will allow to determine the geographic origin of the emitter and the type of the emission antenna.

- Time Resolution: in chapter V, the time resolution of the configuration used did not allow to completely model the multipath behavior of the channel. Instead, the MPCs were clustered in a single LOS path. The behavior of the envelope of the LOS component was characterized as a Ricean or a Weibull distribution. An open question is the improvement of the time resolution of the sounder. As a result, MPCs with delay propagation lower than 50 ns could be observed.

- This thesis pioneered the use of a wideband transmission system at ISL in projectile applications. In the coming years, the STC group will continue with the optimization of this transmission system as well as the reception mechanisms. As a result, demanding applications in terms of throughput can be implemented.

APPENDIX A

LIST OF PUBLICATIONS

Journals

- H. Boeglen, M. Milla, D. Schmoltzi, L. Bernard and R. Vauzelle, "Analysis of an experimental Doppler behaviour on a supersonic speed ground-projectile channel," in *IET Microwaves, Antennas and Propagation*, vol. 11, issue 12, p. 1702 –1707.

International Conferences

- M. Milla, H. Boeglen, L. Bernard, D. Schmoltzi and R. Vauzelle, "Analysis of the Doppler shift due to pendulation and static spinning for projectile antennas," *2016 IEEE 27th Annual International Symposium on Personal, Indoor, and Mobile Radio Communications (PIMRC)*, Valencia, 2016, pp. 1-6.

- M. Milla, H. Boeglen, L. Bernard, D. Schmoltzi and R. Vauzelle, "Experimental comparison of 4 OFDM channel estimation methods for V2V communications," *2017 IEEE 28th Annual International Symposium on Personal, Indoor, and Mobile Radio Communications (PIMRC)*, Montreal, QC, 2017, pp. 1-7.

- M. Milla, D. Schmoltzi, L. Bernard, H. Boeglen, and R. Vauzelle, "A Supersonic Projectile - Embedded OFDM Channel Sounder. First Validation Experimental Results", *2018 12th European Conference on Antennas and Propagation (EUCAP)*, London, UK, 2018, pp 1-6.

National Conferences

- M. Milla, H. Boeglen, L. Bernard, D. Schmoltzi and R. Vauzelle, "Un sondeur de canal embarqué pour la caractérisation d'un canal supersonique à 2.3 GHz", *20èmes Journées Nationales Micro-Ondes (JNM)*, Saint-Malo, France, 2017, pp. 1-4.

APPENDIX B

RÉSUMÉ

B.1 Introduction

L'utilisation des ondes électromagnétiques pour la transmission d'informations a favorisé l'avènement des communications sans fil au début du XXe siècle [60]. Cette étape a été l'une des percées technologiques majeures de l'histoire récente de l'humanité. Cependant, les limitations techniques de l'époque restreignaient leur utilisation aux gouvernements et aux entreprises privées disposant de suffisamment de puissance économique pour couvrir les coûts de déploiement et d'exploitation associés. À cet âge, des institutions telles que la célèbre British Broadcasting Corporation (BBC) et des institutions équivalentes dans d'autres pays ont commencé à être créées. L'accès du grand public à cette technologie a progressivement augmenté depuis le début des années 40 jusqu'à l'explosion des appareils mobiles sans fil au début des années 90 [40]. Au cours de ces années, nous sommes passés des systèmes primitifs "over-and-out" popularisés après la Seconde Guerre mondiale aux "smarphones" actuels. De nos jours, le nombre d'applications qui tirent parti de la technologie sans fil mobile est presque impossible à énumérer. Son utilisation a été généralisée dans presque toutes les applications technologiques. Dans le cadre des applications pour la défense et la sécurité, les communications sans fil avec des projectiles ou des missiles balistiques a été un domaine d'intérêt actif depuis la fin des années 50 [82]. Un des domaines de recherche connexe est le développement de projectiles instrumentés. Ce type de projectiles est généralement doté d'une charge utile non explosive. Au lieu de cela, un ensemble de capteurs est intégré dans le but de surveiller certains paramètres d'intérêt (température, attitude, position, etc.). D'une manière générale, un projectile est beaucoup plus petit qu'un missile balistique, ce qui constitue un problème pour l'espace disponible pour l'électronique embarquée. En raison de cette limitation, le développement de projectiles instrumentés n'a cessé de prendre de l'importance avec la capacité d'intégration de l'électronique analogique puis numérique disponible sur le

marché. Néanmoins, instrumenter un projectile reste une tâche exigeante qui nécessite de faire face à plusieurs contraintes. Nous pouvons les organiser en deux groupes: la capacité de survie électronique et les contraintes de télémesure. Effectivement, l'un des principaux défis consiste à protéger la charge utile des très fortes accélérations au moment du tir. Dans des tirs réels, on peut s'attendre à des forces g supérieures à 30 kG. Ces forces considérables peuvent détruire les composants électroniques si un durcissement approprié de cette électronique n'est pas réalisé [58]. Cependant, une fois que nous pouvons assurer le fonctionnement de l'électronique embarquée, nous pouvons concentrer notre attention sur les contraintes de télémesure. L'objectif de chaque système de télémesure est d'envoyer les données recueillies par les capteurs à la station réceptrice le plus efficacement possible. Habituellement, dans ce contexte, le temps de vol d'un projectile est de l'ordre de quelques minutes. Pour cette raison, l'utilisation d'émetteurs à haut débit est obligatoire [69]. Les progrès récents en matière de miniaturisation électronique, associés à la disponibilité de puces radio haute performance, permettent aujourd'hui la mise en place de liaisons de communication bidirectionnelles entre le projectile et la station terrestre. Dans le contexte des communications mobiles sans fil, il existe une variété d'éléments qui peuvent affecter les performances du système de communication. C'est la capacité de fournir des informations fiables entre les émetteurs-récepteurs. L'un de ces éléments est le canal, qui est le milieu où se produit la propagation de l'onde. Lorsqu'une onde électromagnétique se propage dans le canal, elle interagit avec la matière présente dans le scénario de propagation. En fait, il est possible d'établir une relation entre les ondes rayonnées et les ondes reçues. La caractérisation précise de cette relation est appelée modélisation de canal, c'est-à-dire qu'une abstraction du scénario de propagation est présentée sous la forme d'un modèle mathématique. Dans la littérature, on peut trouver des modèles de canaux pour une large gamme d'applications sans fil mobiles comme ceux déjà utilisés dans les communications téléphoniques [80, 81] ou de véhicule à véhicule (V2V) [4]. Cependant, les conditions de cette thèse seront légèrement différentes de celles habituellement utilisées dans les applications civiles. Certains des paramètres clés généralement pris en compte pour leur conception sont à plusieurs ordres de grandeur de ceux concernés par cette thèse. Par exemple, la vitesse entre les émetteurs-récepteurs peut atteindre 3 fois la vitesse

du son. Cette valeur est éloignée des quelques dizaines de kilomètres à l'heure habituels dans les applications V2V. Comme nous le verrons, certains paramètres du modèle de canal dépendront de la vitesse relative entre les émetteurs-récepteurs. L'un des principaux objectifs de cette thèse est d'optimiser les performances de communication dans le domaine des projectiles instrumentés. C'est pourquoi une grande partie des travaux sera consacrée à l'étude des conditions de propagation et à la conception d'un modèle de canal adapté à cet environnement particulier. En raison de la politique de confidentialité des applications militaires, la littérature disponible sur les projectiles instrumentés est limitée. En conséquence, nous devrons définir un ensemble de procédures d'analyse de données dans le domaine de la modélisation de canal. Pour cette raison, certains des algorithmes habituels utilisés dans la chaîne de communication doivent être adaptés. Dans une dernière étape, les bases de la conception d'un émetteur-récepteur numérique peuvent être proposées une fois le canal connu et une stratégie de communication définie. Compte tenu du contexte précédemment exposé, les contributions de cette thèse peuvent être résumées comme suit:

- Développement des outils et algorithmes nécessaires: la nouveauté de ce travail conduit à l'introduction d'une approche différente de la modélisation de canaux supersoniques.
- Conception d'un modèle de canal pour projectiles instrumentés supersoniques: connaître le canal de propagation est crucial dans l'optimisation d'un système de télémétrie, nous devons modéliser le canal afin de minimiser son impact sur les performances de la liaison radio.

Toutes ces contributions requièrent l'expertise de plusieurs institutions pour être réalisées avec succès. Dans notre cas, cette thèse a été soutenue par les trois institutions suivantes: le laboratoire XLIM, l'Institut de recherche franco-allemand de Saint-Louis (ISL) et la Direction générale de l'armement (DGA). Chacun a contribué différemment à la réalisation de nos objectifs: le rôle de XLIM et l'ISL a été d'ont assuré la supervision scientifique du projet. Le soutien financier a été fourni à la fois par l'ISL et la DGA. Les trois institutions ont fourni des installations d'essai et un soutien technique.

- XLIM: cette institution est un institut de recherche multidisciplinaire implanté sur plusieurs sites géographiques. La section XLIM de l'Université de Poitiers est celle impliquée dans cette thèse. XLIM regroupe plus de 440 personnes: professeurs, chercheurs du CNRS, ingénieurs, techniciens, post-doctorants, doctorants et personnels administratifs. Cette institution de recherche s'articule autour de trois centres d'activité: électronique, photonique et mathématiques - informatique et image. La branche impliquée dans cette thèse appartient à la section XLIM Smart System and Network.

- ISL: L'Institut franco-allemand de recherche de Saint-Louis est un institut de binational créé par la République fédérale d'Allemagne et la République française sur la base d'un traité signé en 1958. Le centre de recherche principal est situé à Saint-Louis, tandis que les expériences nécessitant l'utilisation d'explosifs ou de projectiles sont testées dans les installations d'essais de Baldersheim. Les deux sites sont situés en Alsace, en France. La mission principale d'ISL est la recherche fondamentale, les études scientifiques et le pré-développement de bases dans le domaine de la défense et de la sécurité. L'ISL a renforcé ses activités sur les questions de sécurité civile et les mesures de lutte contre le terrorisme rencontrées à la fois sur leterritoire national et lors d'opérations militaires à l'étranger. Cette thèse a été réalisée dans le groupe Sensors, Telemtry and Communications (STC) de la Division II.

- DGA: cette institution dépend du ministère français des Forces armées. Sa mission est de gérer l'équipement de l'armée française, de préparer technologiquement ses capacités et de promouvoir l'exportation d'armement fabriqué en France. Pour ces tâches, un budget d'environ 25 milliards d'euros a été alloué en 2016. Cette institution apporte un soutien financier à environ 130 programmes de doctorat chaque année.

La suite de ce document est organisée comme suit: au chapitre 2, nous présenterons les principaux concepts de canaux et la terminologie nécessaire à la compréhension de ce manuscrit. De plus, nous allons présenter certaines des techniques utilisées dans la conception de modèles de canal et expliquer la nécessité d'adapter le processus de sondage de canal à notre domaine. Le chapitre finira par montrer les contraintes et les exigences spécifiques qui

ont motivé une nouvelle approche dans la modélisation de canaux pour les applications de projectiles. Dans le chapitre 3, nous présenterons dans un premier temps tous les instruments et équipements disponibles au début de la thèse. Plus tard, avec l'utilisation de ces éléments, nous montrerons comment nous développons une méthode de sondage de canal adaptée aux exigences et aux contraintes expliquées au chapitre 2. Le matériel et les algorithmes utilisés seront détaillés de manière à permettre la reproduction de nos méthodes par d'autres groupes de recherche, avec l'objectif d'améliorer la méthodologie proposée. Le chapitre se terminera par la présentation du prototype conçu pour le sondage de canal. Les premiers résultats seront montrés au chapitre 4 en effectuant une étude préliminaire de l'environnement à modéliser. Nous devrons faire attention à plusieurs phénomènes liés à la dynamique de vol pouvant affecter le comportement du projectile. Concrètement, deux effets seront étudiés (rotation et pendulation) afin d'évaluer leur impact sur la performance de la communication. Ce chapitre jettera les bases de la caractérisation d'un canal à large bande au chapitre 5. La construction d'un modèle de canal pour les applications de projectiles sera finalement détaillée dans le chapitre 5. Dans ce chapitre, les données obtenues lors d'expériences à basse vitesse et de tirs réels (vitesse supersonique) seront analysées et utilisées pour développer un modèle de canal. Les concepts présentés au chapitre 2 concernant la définition d'un modèle de canal seront appliqués ici. De plus, nous montrerons l'utilisation complète de la méthodologie et du prototype conçu au chapitre 3. Le chapitre se terminera par la présentation du modèle de canal et une discussion sur l'avenir des émetteurs-récepteurs mis au point à l'ISL. Enfin, les conclusions et les travaux futurs seront détaillés à la fin de ce document.

B.2 Concepts de Canaux Radio-Mobiles (Sans Fil) et Sondage de Canal

Dans ce chapitre, nous présentons le principal sujet d'étude de cette thèse, à savoir le canal de propagation radio-mobile. Comme il est montré sur la figure 84, le canal peut être vu comme une abstraction de tout ce qui arrive à une onde depuis son émission jusqu'à sa réception.

Plusieurs phénomènes sont impliqués dans la propagation des ondes. Cependant, du point de vue du récepteur, le canal peut être vu comme un élément qui a la propriété de modifier les informations transmises. La caractérisation de la manière dont le canal affecte les signaux transmis est appelée modélisation de canal. Dans ce chapitre, nous présentons les principaux éléments à prendre en compte dans ce domaine.

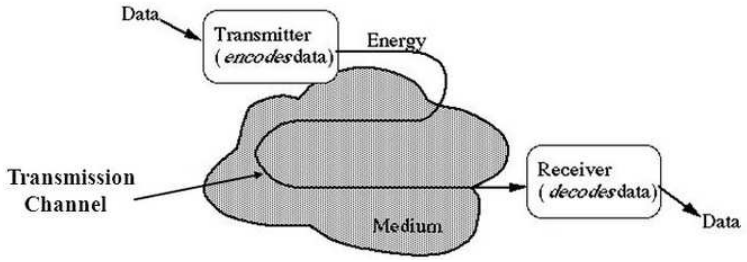

Figure 84: Schéma Simplifié d'un Système de Transmission.

Ce chapitre est structuré en trois sections: dans la première, le canal est traité du point de vue des effets physiques impliqués dans la propagation des ondes (atténuation, trajets multiples et effet Doppler).

Dans la deuxième partie, le canal est abordé du point de vue du traitement du signal. En conséquence, le canal est traité comme un système linéaire caractérisé par sa réponse impulsionnelle sur le canal (CIR). De plus, la commodité de considérer le canal comme un processus stochastique est discutée.

Enfin, une méthode empirique pour obtenir le CIR est présentée. Ce processus s'appelle le sondage de canal et consiste à étudier comment le canal modifie un signal de test connu. Une revue des techniques de sondage de canal les plus populaires est présentée. Malgré leur popularité et leur efficacité, les sondeurs de canal classiques ne peuvent être utilisés

pour atteindre les objectifs de cette thèse. Leur poids, leur taille et leur consommation d'énergie nous empêchent d'intégrer ce type de sondeurs dans des applications impliquant des projectiles. Cette contrainte conduit à la proposition d'un sondeur de canal adapté à nos besoins au chapitre 3.

B.2.1 Concepts de canaux radio-mobiles (sans fil)

Les trois phénomènes de propagation présentés dans la première section de ce chapitre sont les suivants:

Perte de propagation: ce phénomène explique la perte d'énergie des ondes lorsqu'elles se propagent à travers le milieu. Dans les systèmes de communication sans fil, la chaîne de communication a également un impact sur la puissance reçue. Cet effet est caractérisé par l'équation de Friis [40]:

$$\begin{aligned} 10log_{10}(P_r) &= 10log_{10}(P_t) \\ &\quad - 10\alpha log_{10}(d) \\ &\quad + 20log_{10}\left(\frac{\lambda}{4\pi}\right) \\ &\quad + 10log_{10}(G_t(\theta,\phi)G_r(\theta,\phi)(1-|\Gamma_t|^2)(1-|\Gamma_r|^2)\,|\hat{\rho}_r\cdot\hat{\rho}_t|^2) \\ P_r(dBW) &= P_t(dBW) - 10\alpha log_{10}(d) + C \end{aligned}$$

Où P_r est la puissance reçue, P_t est la puissance transmise, α est l'exposant d'affaiblissement par propagation, G_t est le gain de l'antenne d'émission et G_r le gain de l'antenne de réception, Γ_t est le coefficient de réflexion de l'antenne d'émission à la chaine d'émission et Γ_r le coefficient de réflexion de l'antenne de réception à la chaine de répcetion et $\hat{\rho}_{r,t}$ est le vecteur de polarisation des antennes.

Dans les communications radio-mobiles, l'exposant d'affaiblissement par propagation varie en fonction du scénario de propagation. Le tableau suivant montre les valeurs attendues dans certains scénarios de propagation courants [83].

Multi-trajet: lorsque l'onde se propage à travers le milieu, elle peut rencontrer des obstacles sur son chemin. À la suite de cette interaction, plusieurs répliques du signal sont reçues à des instants différents. C'est ce qu'on appelle l'effet multitrajet.

Table 18: Valeurs Usuelles d'Exposant d'Affaiblissement.

Environment	**Path Loss Exponent**
Free Spece	2
In building LOS	1.6 - 1.8
NLOS factories	2 - 3
NLOS buildings	4 - 6
Urban area	2.7 - 3.5
Shadowed urban area	3 - 5

Dans les communications radio, l'effet de propagation par trajets multiples est principalement responsable de la communication possible dans les liaisons sans visibilité directe NLOS (non-light-of-sight) [7]. Trois effets physiques différents entrent en jeu, comme le montre la figure 85 suivante:

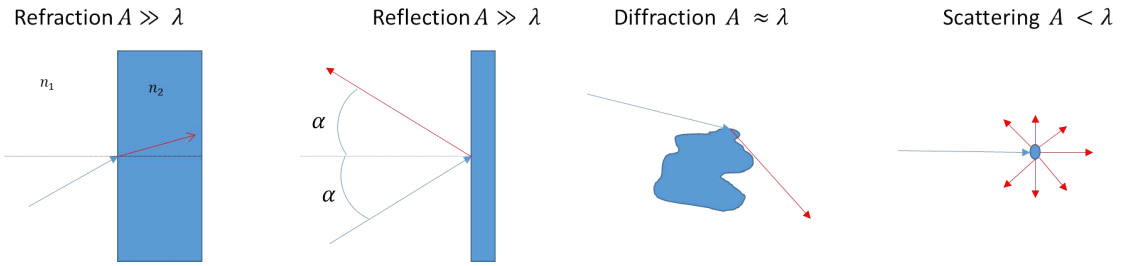

Figure 85: Réfraction, Diffraction et Diffusion.

- Réfraction: ce phénomène est le changement de la direction de propagation d'une onde lorsqu'elle passe d'un milieu à un autre avec des indices de réfraction différents. La réflexion est un cas particulier de réfraction où l'onde incidente retourne au premier milieu au lieu de pénétrer à travers le second.

- Diffraction: ce phénomène se produit lorsqu'une onde rencontre un obstacle, une ouverture ou une fente. La diffraction peut être expliquée par le principe de Huygens - Fresnel, qui s'applique lorsqu'une onde rencontre un obstacle dont la taille est de l'ordre de sa longueur d'onde.

- Diffusion: lorsqu'une onde électromagnétique se propage à travers le milieu, elle rencontre généralement des particules ou des inhomogénéités sur son trajet. Ce phénomène se produit quand l'onde rencontre un obstacle dont la taille est inférieure à sa longueur

d'onde.

Dans un scénario de trajets multiples, le signal reçu $y(t)$ est une somme des répliques atténuées et retardées du signal transmis $x(t)$, comme indiqué dans l'équation suivante:

$$y(t) = \sum_{i=1}^{N} A_i x(t - \tau_i)$$

Effet Doppler: l'effet Doppler est le changement de la fréquence observée lorsque des sources électromagnétiques mobiles sont impliquées. La fréquence Doppler ω_D est obtenue telle qu'elle apparaît dans l'équation:

$$\omega_D = \pm \frac{2\pi}{\lambda} ||\vec{v}|| \, cos(\alpha)$$

où λ est la longueur d'onde du signal, $\vec{v}$ est le vecteur vitesse et α est l'angle entre le vecteur d'onde et le vecteur position. En conséquence, notre signal reçu sera finalement la somme de répliques retardées, atténuées et affectées par l'effet Doppler. Pour cette raison, $y(t)$ peut être modifié comme le montre l'équation suivante:

$$y(t) = \sum_{i=1}^{N} A_i(t) x(t - \tau_i) e^{j\omega_{Di} t}$$

B.2.2 Le canal en tant que filtre

Dans la deuxième partie du chapitre, nous changeons le point de vue lors de la caractérisation du canal. Nous présentons comment le canal peut être étudié en tant que filtre. Dans ce cas, le comportement du canal est totalement déterminé par la réponse impulsionnelle du canal (CIR). Si le canal est traité comme un filtre, le signal reçu $y(t)$ peut être exprimé tel qu'il apparaît dans l'équation suivante:

$$y(t) = \int_{-\infty}^{\infty} x(t - \tau) h(t, t - \tau) d\tau$$

Dans le traitement du signal, il est parfois plus pratique de travailler dans le domaine fréquentiel plutôt que dans le domaine temporel. Dans le contexte des communications radio-mobiles, les fonctions de Bello sont employés à cette fin [14]. Il en existe quatre: la réponse

impulsionnelle variant dans le temps $h(t, \tau)$ (fonction utile pour obtenir le profil PDP du canal), la réponse impulsionnelle variant selon le décalage Doppler $s(\tau, f')$ (le spectre Doppler peut être obtenue par cette fonction), la fonction de transfert dépendante du temps $H(f, t)$ et la fonction de transfert dépendante du décalage Doppler $T(f, f')$. Nous pouvons voir comment elles sont liées les unes aux autres à travers les opérations de transformation de Fourier sur la figure 86:

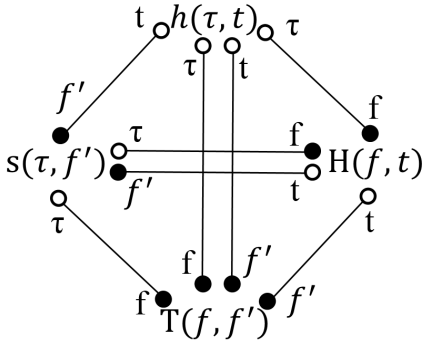

Figure 86: Fonctions de Bello.

Dans des scénarios de propagation réels, la nature aléatoire du canal transforme les fonctions de Bello en processus stochastiques. Dans la plupart des cas, dans les canaux de radio-mobile, ils sont considérés comme des processus de diffusion stationnaire non corrélée à sens large (WUSSUS). Habituellement, la condition WSSUS permet la représentation du canal sous la forme d'un filtre TDL (Tapped Delay Line) dans lequel les coefficients variant dans le temps sont modélisés sous forme de processus gaussiens colorés. On peut trouver des exemples de modèles basés sur un filtre TDL dans [23, 104, 55]. La forme générale d'un modèle TDL est illustrée à la figure 87.

À la fin de cette section, nous introduisons les concepts de bande étroite et de bande large. Ces concepts sont liés aux propriétés multitrajets et Doppler du canal.

B.2.3 Sondage de canal

Dans cette thèse, nous souhaitons caractériser de manière empirique le CIR au champ de tir de l'ISL. Pour cet objectif, le sondage de canal est la technique préférée. Les techniques de sondage de canal peuvent être structurées en techniques de sondage à bande étroite (exemple

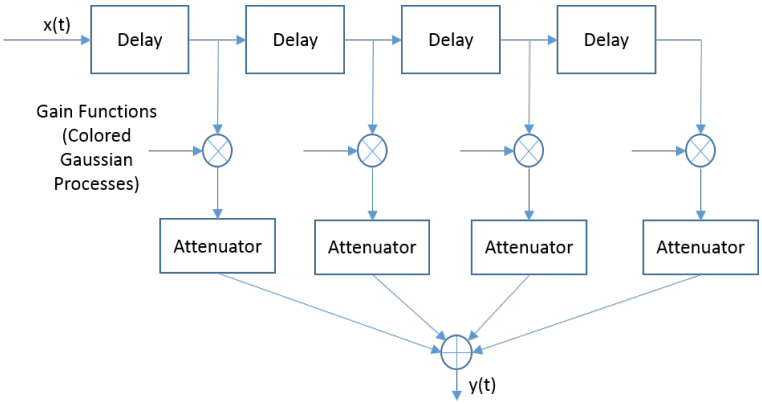

Figure 87: Modèle TDL.

dans [46]) ou en technique de sondage de canal à large bande [84, 54, 58, 34]. Comme une technique de sondage de canal à large bande est nécessaire en raison des exigences futures des systèmes RF développés par l'ISL, la facilité d'utilisation des sondeurs de canal cités a été évaluée. Nous avons constaté que nous devions créer notre propre technique de sondage de canal en raison de contraintes matérielles et logicielles. Le sondeur de canal doit répondre aux exigences suivantes:

- Vitesse: le sondeur de canal doit pouvoir produire suffisamment d'estimations CIR pour pouvoir caractériser un décalage Doppler de plusieurs kHz.
- Intégrabilité: le sondeur de canal doit être suffisamment petit pour pouvoir être testé dans des conditions réelles, c'est-à-dire embarqué et tiré dans un projectile.
- Fiabilité: le sondeur de canal devrait pouvoir résister à la forte accélération dans le canon lors du tir.
- Flexibilité: le sondeur de canal doit pouvoir être utilisé dans plusieurs environnements.

Dans le chapitre 3 ci-après, nous présenterons les instruments dont nous disposions au début de la thèse et comment ils contribueront à la réalisation de nos objectifs. La méthodologie de sondage de canal proposée sera également présentée, ainsi que son implémentation matérielle. Dans les chapitres suivants, le prototype développé sera utilisé pour construire un modèle de canal.

B.3 Instruments et Installations. Développement d'un Sondeur de Canal Embarqué

Après avoir présenté le sujet d'étude de cette thèse dans le chapitre précédent, celui-ci est structuré en deux parties: une dédiée à la présentation des instruments et des équipements disponibles au moment de commencer cette thèse alors que la deuxième partie est consacrée à l'introduction de notre méthodologie de sondage de canal.

B.3.1 Instruments et outils

Notre objectif étant d'aborder de manière réaliste la modélisation des canaux, un inventaire des ressources disponibles a été réalisé. Ceux-ci sont détaillés ci-dessous.

Nous disposons d'un simulateur de propagation de rayons, RaPSor, qui est un logiciel de propagation open source développé par le laboratoire XLIM. Il permet d'obtenir le CIR du canal au moyen de simulations pour un scénario défini par l'utilisateur.

Un banc de rotation permet de reproduire la rotation (roulis) d'un projectile en laboratoire. Il a été utilisé pour étudier l'impact de la rotation sur le signal reçu.

Des cartes de radio-logicielle (SDR) permettent à l'utilisateur de décrire un système radio au moyen d'un logiciel [35]. Dans cette thèse, le logiciel utilisé est GNU Radio [1]. Les équipements SDR disponibles au début de la thèse dans notre laboratoire et destinés à être utilisés avec GNU Radio sont les suivants: plusieurs unités d'équipements USRP (Universal Software Radio Peripheral) d'Ettus Research [52] et SOM PicoZed SDR 2x2 d'Avnet [9].

Nous disposons d'une antenne directive à gain élevé (NE5023 de Hyptra) et d'une antenne omnidirectionnelle (VERT2450 de Ettus Research), qui ont été utilisées pour les mesures au champ de tir de l'ISL.

Une chambre anéchoïque est disponible à l'ISL. Cette chambre de mesure nous permet d'obtenir le diagramme de rayonnement en champ lointain des antennes développées à l'ISL ou achetés et à caractériser, par le biais de mesures en champ proche.

Un analyseur de réseau vectoriel (VNA) ZVA40 de Rohde & Schwarz est disponible dans notre laboratoire. Il a été utilisé pour les premiers tests avec notre sondeur de canal.

Le Basic Finner (BF) est un projectile de référence bien connu, c'est-à-dire un projectile

aux dimensions définies et aux caractéristiques aérodynamiques bien déterminées. Il consiste en un cône de nez de 20° dans un corps cylindrique à 4 ailettes rectangulaires [36]. Dans cette thèse, nous avons utilisé les données de campagnes de tir précédentes à l'ISL dans le but d'étudier les propriétés du canal.

Le champ de tir extérieur de l'ISL est situé à Baldersheim, à une trentaine de kilomètres de Saint-Louis (Alsace, France). Sur cette installation, une ligne de tir de 235 m est disponible pour les tests de projectiles ainsi que l'équipement auxiliaire nécessaire pour effectuer notamment le suivi optique du projectile depuis le tir jusqu'à l'instant de l'impact.

B.3.2 Sondage du canal OFDM

Dans la deuxième partie du chapitre, nous décrivons notre méthodologie de sondage de canal. Nous proposons une méthode de sondage de canal basée sur la technique de transmission OFDM. Cette technique a déjà été utilisée dans d'autres sondeurs de canal [77, 49, 97, 108, 113, 93, 26, 107]. Un des apports de cette thèse a été d'adapter la méthodologie de sondage OFDM au matériel disponible en tenant compte du scénario de propagation (propriétés Doppler du canal, dues à des vitesses supersoniques).

Les principales caractéristiques du sondeur de canal proposé se trouvent dans le tableau suivant:

Table 19: Caractéristiques du Sondeur de Canal.

OFDM Channel Sounder	51200 ns 1024 samples		
Frame structure	1600 ns of silence 32 samples	8000 ns synchronization symbol 160 samples	40000 ns OFDM symbols 800 samples 80 samples/symbol 16 CP + 64 samples 10 OFDM symbols
Sampling Frequency	50 ns		
Multipath Resolution	15 m		
Carriers	64		
Carrier Spacing	312500 kHz		
Bandwidth	20 MHz (Total) / 16.25 MHz (Effective)		
Minimum Channel Sampling Frequency	20.53 kHz		

La méthode de sondage du canal OFDM que nous proposons est illustrée à la Fig. 88. Dans ce schéma de sondage, la difficulté réside principalement du côté du récepteur. Au

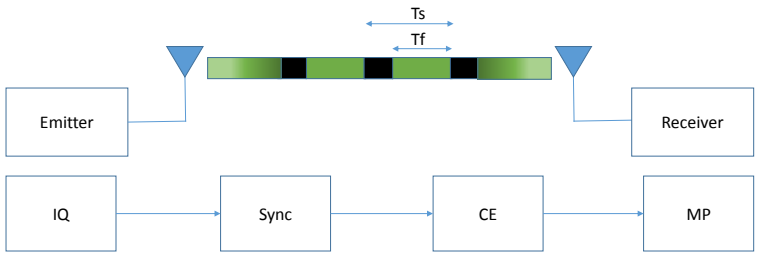

Figure 88: Méthode Proposé pour le Sondage de Canal OFDM.

contraire, le fonctionnement de l'émetteur est limité à l'émission continue d'une trame OFDM d'une durée de 51200 ns. Sur la figure 88, la période noire correspond aux échantillons silencieux. Nous allons décrire le fonctionnement du récepteur dans les sections suivantes. En guise d'introduction, ses étapes sont esquissées ici:

- IQ: à ce stade, les composantes en phase (I) et en quadrature (Q) du signal OFDM sont obtenues par un processus d'échantillonnage à $T_s = 50$ ns.

- Sync: la synchronisation de fréquence et de temps est effectuée ici afin d'éviter les interférences entre symboles (ISI) et les interférences entre porteuses (ICI). Notre algorithme de synchronisation peut être trouvé dans [22].

- CE: la réponse en fréquence de canal (CFR) du canal est trouvée dans cette étape. Nous avons utilisé la méthode décrite dans [49]. Afin de pouvoir extraire les propriétés de propagation des trajets multiples du canal, c'est-à-dire le CIR du système. Une vérification d'erreur de décision définitive est proposée dans le but de supprimer les trames OFDM reçues contenant des erreurs après le processus d'égalisation.

- MP: le CIR est obtenu à partir du CFR à ce stade. Nous proposons un algorithme d'estimation pour trajets multiples basé sur une optimisation par la méthode des moindres carrés en comparant le signal reçu avec celui théoriquement attendu.

Après avoir comparé les performances du sondeur avec le VNA dans un scénario de propagation réalisable en laboratoire, le prototype final est présenté; il est donné à la figure suivante:

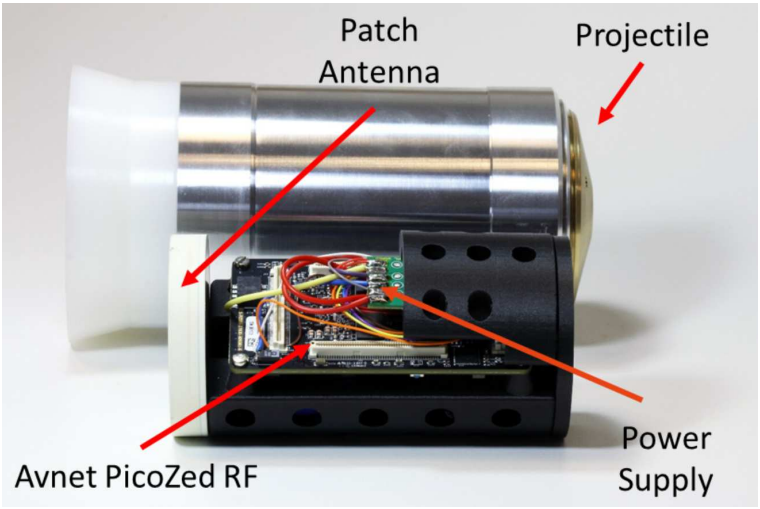

Figure 89: Prototype du Sondeur

Avant de tester le prototype lors d'un tir réel, il était nécessaire de procéder à une étude préliminaire des conditions de vol. Effectivement, une campagne de tir est coûteuse en termes de personnel et d'équipement utilisé. En outre, nous devons envisager la possibilité que le prototype soit détruit et que l'on ne puisse pas le réutiliser. Pour cette raison, au chapitre 4, nous réalisons une série d'études préalables afin d'avoir une idée approximative de ce que nous pouvons attendre lors de la campagne de tir.

B.4 Etudes Préliminaires du Canal de Propagation

Dans les applications projectiles, la mécanique du vol est un élément à prendre en compte pour une première approche de la modélisation de canal. Dans cette thèse, deux effets majeurs ont été pris en compte: le roulis et la pendulation. Leur impact sur la caractérisation de canal a été étudié différemment: la pendulation a été étudiée par le biais de simulations numériques alors que le roulis a été traité expérimentalement.

Dans la deuxième partie de ce chapitre, nous analysons les résultats de précédentes mesures effectuées à l'ISL afin de valider les simulations effectuées.

B.4.1 Roulis et pendulation

La gyro-stabilisation ou stabilisation par roulis est une technique utilisée en balistique afin de maintenir le projectile dans la bonne direction pour un vol efficace. Des projectiles stabilisés par empennage peuvent également présenter un roulis. Comme on peut le voir sur la Fig. 90, intégrée à un projectile en rotation, l'antenne (source d'ondes électromagnétiques) tourne également. Par conséquent, un décalage de fréquence (Doppler) du récepteur peut être mesuré en raison du changement d'aspect de la phase du diagramme de l'antenne vu depuis un repère extérieur (fixe).

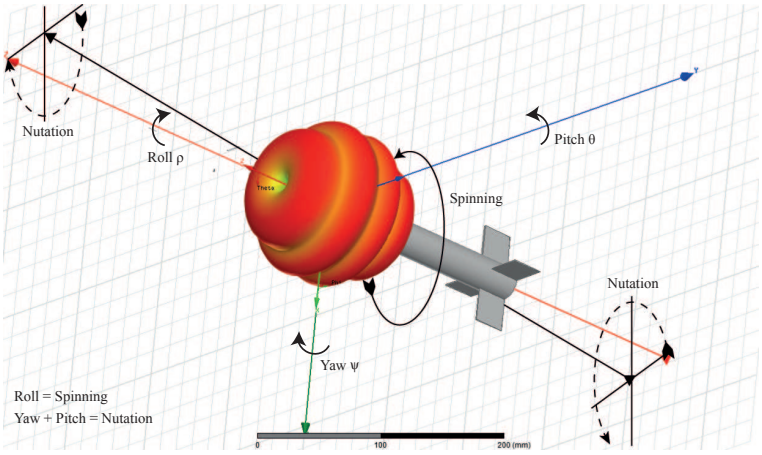

Figure 90: Pendulation et Roulis.

L'effet des dispositifs d'émission en rotation sur le signal reçu a été étudié dans plusieurs domaines [65, 60, 98]. Si des signaux polarisés circulairement sont impliqués, le décalage de

fréquence f_D provoqué par la rotation sera:

$$f_D = \pm f_r cos(\alpha)$$

où f_r est la fréquence de rotation et α l'angle d'incidence de l'onde au point d'observation. Une expérience a été réalisée avec le banc de rotation présenté au chapitre 3. La condition de roulis peut être reproduite avec une antenne présentant différentes configurations de rapport axial (AR) autour d'une fréquence de 1150 MHz. Dans la plupart des cas, le décalage mesuré est dans l'ordre de grandeur théoriquement attendu (jusqu'à 60 Hz). On peut en conclure que le décalage Doppler induit peut être négligé par rapport à la valeur de l'ordre de plusieurs kHz causée par la vitesse de vol du projectile.

Table 20: Valeurs du Décalage de Frequence dû à la Rotation.

Frequency (MHz)	Spinning Rate (Hz)	f_r (Hz)	Measured Shift (Hz)	Theoretical Shift (Hz)
1147 AR = 2.2 dB	0	340	0	0
	25	320	20	25
	50	313	27	50
1148 AR = 4.8 dB	0	348	0	0
	25	325.2	22.8	25
	50	298.4	49.6	50
1149 AR = 7.5 dB	0	305.4	0	0
	25	316.5	11.1	25
	50	347.1	41.6	50

Dans notre cas, la pendulation est un effet indésirable qui doit être réduit au minimum afin de ne pas affecter la trajectoire du projectile. Dans le mouvement de pendulation, le centre de pression de l'air et le centre de masse sont impliqués [67]. En vol, le centre de pression est légèrement avancé par rapport au centre de masse. La combinaison de cette configuration et de la rotation du projectile produira une petite rotation à la pointe du projectile. Ce phénomène peut également être observé à la Fig. 90.

Les conditions habituelles de pendulation ont été simulées pour le tir d'un projectile

émettant à une fréquence proche de 2,3 GHz, selon la norme IRIG106 [41]. L'objectif était d'étudier l'impact de la pendulation dans le spectre Doppler.

En ce qui concerne les résultats de la simulation sur la figure 91, nous pouvons conclure que l'effet de pendulation n'a pas d'impact significatif sur le récepteur (variations du décalage Doppler autour de 10 Hz). Pour cette raison, l'effet de pendulation sera exclu de la modélisation du canal.

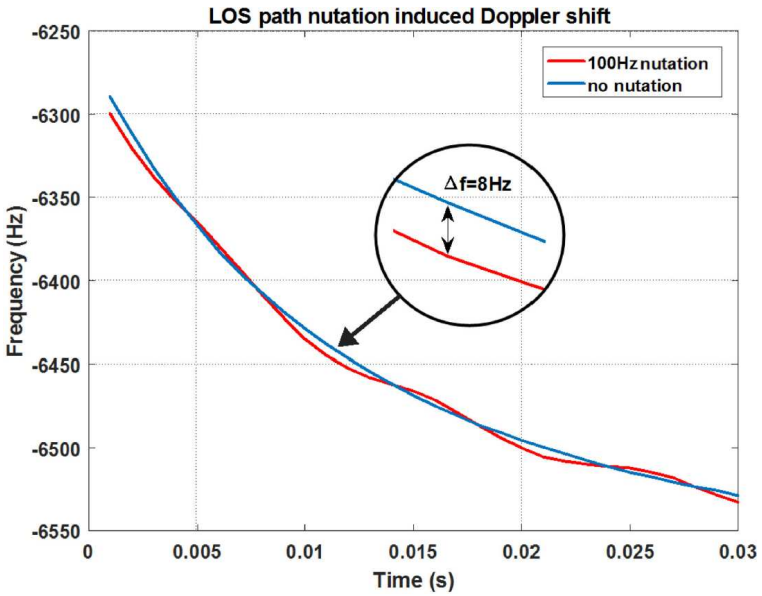

Figure 91: Impact de la Pendulation sur le Décalage Doppler.

B.4.2 Firing tests

Fin juillet 2015, le groupe STC a organisé une campagne de tir afin de valider la conception d'un émetteur numérique miniaturisé à faible débit utilisé dans les mesures d'attitude de projectile. Ces mesures ont été récupérées au début de cette thèse pour la caractérisation Doppler du canal radio.

Les simulations avec RaPSor ont également permis d'avoir un premier aperçu des propriétés Doppler du canal. Concrètement, une estimation du spectre Doppler pour le scénario de propagation du champ de tirs peut être obtenue. Ces simulations ont montré la prédominance du trajet LOS avec un décalage Doppler de l'ordre de - 6,5 kHz. L'analyse d'un précédent tir instrumenté a confirmé ce résultat issu de la simulation, comme le montre la

figure 92 suivante. Deux stations de réception ont été utilisées: une équipée d'une antenne directive, l'autre d'une antenne omnidirectionnelle. La position des deux stations de réception a été choisie en fonction de la position des campagnes de tir instrumentées précédentes.

L'analyse effectuée dans ce chapitre a servi d'étude préliminaire à ce que nous devrions observer dans le prochain chapitre 5. Certaines des clés pour la modélisation du canal ont été décrites. Concrètement, le décalage Doppler dû à la translation peut être bien déterminé. Cependant, le canal n'a pas été complètement caractérisé car le CIR n'a pas été obtenu. Dans le chapitre suivant, nous allons tester notre prototype de sondeur de canal pour effectuer une caractérisation complète du canal en large bande.

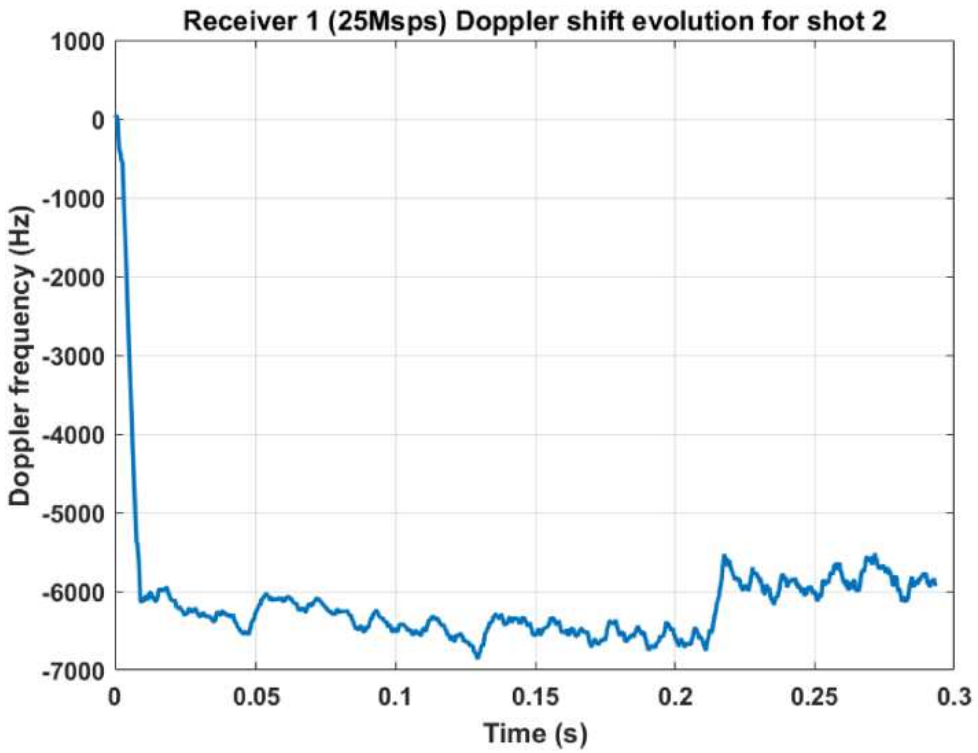

(a) Station Directive.

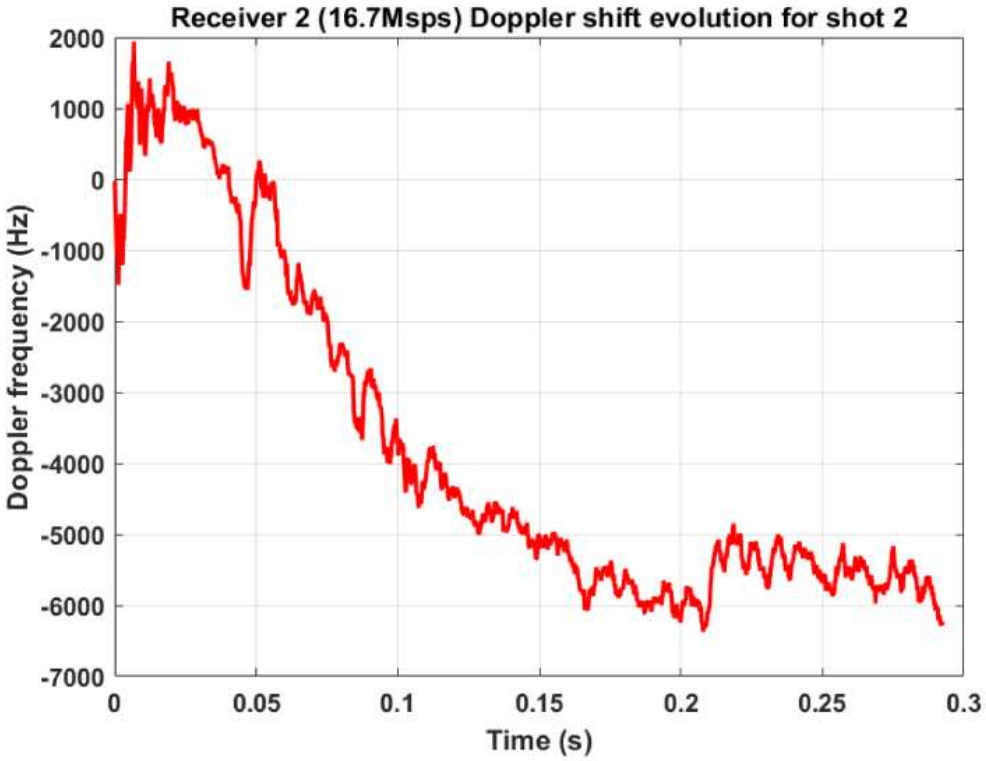

(b) Station Omnidirectionnelle.

Figure 92: Evolution du Décalage Doppler pour le Tir BF Numero 2.

B.5 Caractérisation Large Bande du Canal Radio. Définition d'un Modèle de Canal et Validation du Sondeur de Canal

Ce chapitre est consacré à la modélisation large bande du scénario de propagation à Baldersheim. La dernière génération de systèmes de communication à l'ISL a motivé la migration des systèmes de transmission à porteuse unique vers des systèmes à porteuses multiples. Avant de déployer un tel équipement, une caractérisation large bande du canal de propagation est nécessaire.

Dans ce chapitre, la méthodologie de sondeur de canal présentée au chapitre 3 a été testée dans un scénario à faible vitesse afin d'identifier les défaillances possibles avant une véritable campagne de tir à Baldersheim. Dans la deuxième partie du chapitre, le prototype du sondeur de canal est utilisé lors de tirs et le canal radio-mobile a été caractérisé.

B.5.1 Tests à basse vitesse

Deux séries d'expériences sont réalisées à l'aide de SDR montés sur deux voitures. Dans les deux expériences, la fréquence de travail est de 2,3 GHz. Le premier se déroule à proximité de l'université dePoitiers (Expérience I), et le second à la Cité de l'Automobile (Mulhouse) (Expérience II).

Le scénario de propagation de ces expériences est présenté à la Fig. 93. Dans cette expérience, l'exposant d'affaiblissement sur le trajet s'est révélé conforme aux valeurs théoriques attendues. Dans le même temps, la performance de l'estimateur CFR a été évaluée pour les deux expériences. Le tableau ci-dessous résume la performance de l'estimateur CFR dans l'expérience I. Dans le cas de l'expérience II, il est constaté que la totalité des trames OFDM reçues est valide pour l'estimation de canal, ce qui nous a permis de poursuivre la caractérisation du scénario de propagation à grande vitesse à Baldersheim.

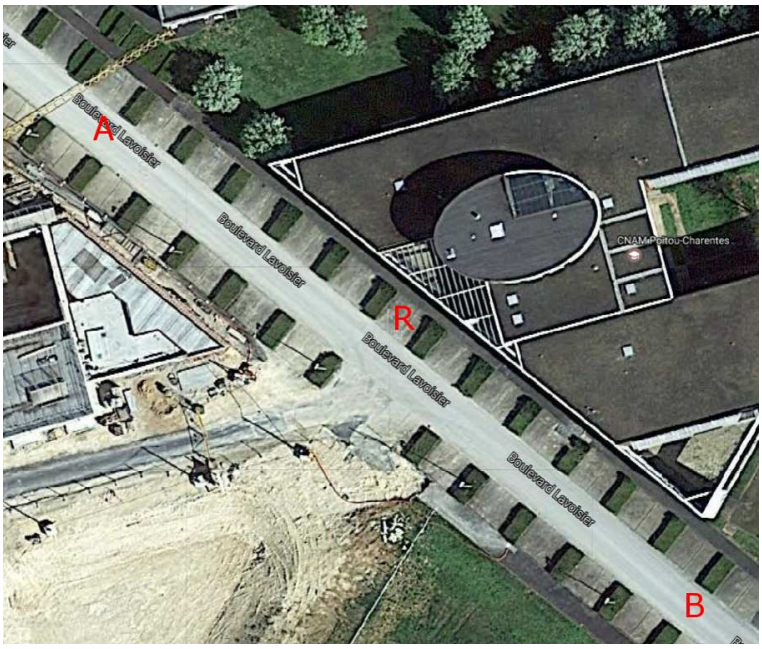

(a) Expérience I.

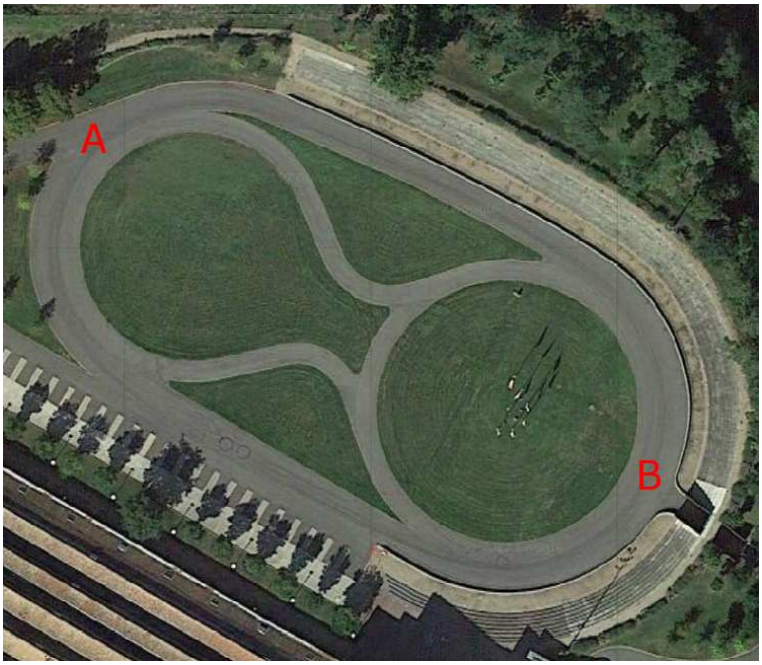

(b) Expérience II.

Figure 93: Configuration des Essais à Basse Vitesse.

Table 21: Résumé des Performances de l'Estimation de CFR lors de l'Expérience I.

	Total OFDM Frames	**Invalid Frames**	**SNR Range (dB)**
Case A - B	17126	689 (4.02 %)	15 - 46
Case B - A	10000	842 (8.42 %)	18 - 34

B.5.2 Scénario grande vitesse: caractérisation du canal à Baldersheim

La campagne de tir a eu lieu en septembre 2017 à Baldersheim. Quatre projectiles ont été tirés. La configuration des tirs peut être trouvée dans le tableau Tab. 22, et la configuration de l'expérience à la Fig. 94. Dans ce cas, deux stations de réception ont été utilisées: l'une équipée d'une antenne directive à gain élevé, la seconde d'une antenne omnidirectionnelle. La vitesse initiale de tir pour les projectiles tirés est d'environ Mach 2.

Table 22: Configuration des Tirs.

	Electronically Instrumented	**Frequency Band (MHz)**
Firing #1	no	-
Firing #2	yes	2205
Firing #3	no	-
Firing #4	yes	2250

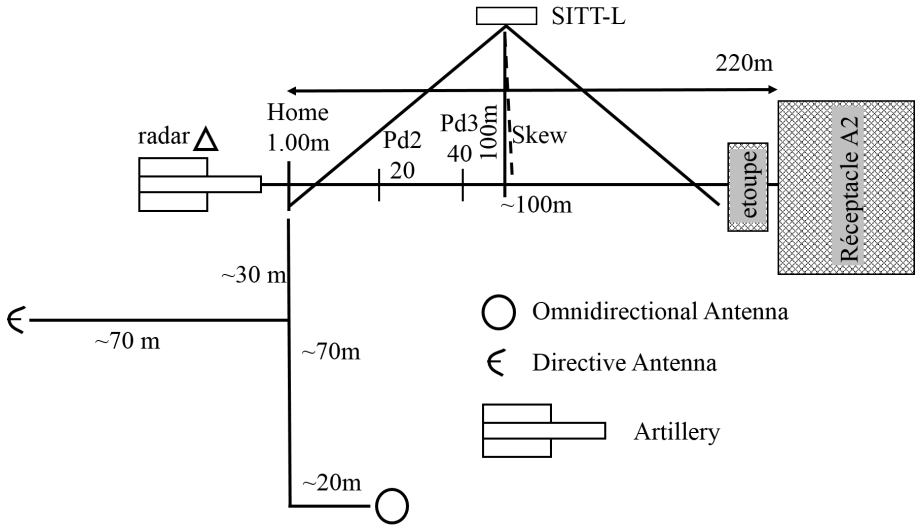

Figure 94: Configuration des Essais à Vitesse Supersonique.

Le canal est caractérisé selon le processus d'analyse des données suivant:

- La première tâche à effectuer consiste à isoler chacune des trames OFDM reçues afin de calculer le profil de puissance reçue et de fournir une estimation du rapport signal sur bruit SNR.

- La deuxième étape consiste à caractériser le comportement des pertes par propagation entre le dispositif émetteur et la station de réception (comportement à grande échelle du canal).

- La troisième étape consiste à appliquer l'estimateur CFR. La validité de la trame reçue est évaluée à des fins de sondage de canal. De plus, le comportement Doppler de la composante directe LOS peut être obtenu à ce stade.

- Après avoir obtenu le CFR, nous effectuons la caractérisation du CIR. À ce stade, le canal est complètement caractérisé. Les propriétés à petite échelle du canal sont obtenues.

Un algorithme d'estimation de pertes de propagation est proposé. Il est utilisé pour les deux stations de réception. Dans le tableau 23 suivant se trouvent les valeurs obtenues à la

station directionnelle. L'incohérence des valeurs données par rapport aux valeurs théoriques attendues (entre 2 et 3) est due à une défaillance matérielle lors du vol.

Table 23: Station Directive: Caractérisation des Pertes par Propagation.

Directional Station Path Loss Characterization	**OFDM Frames**	**Path Loss Exponent**	**Distance Covered**	**Flight Time**	**Regression Goodness**
First ROI	2099	2.14	57.97 m	107.47 ms	0.91
Second ROI	1600	5.51	39.98 m	81.92 ms	0.98
Third ROI	999	11.84	23.43 m	51.15 ms	0.99

Malgré les problèmes rencontrés lors de l'estimation de l'affaiblissement sur le trajet, nous poursuivons la caractérisation du canal. La prochaine étape réalisée est la caractérisation de la composante décalage Doppler du trajet direct LOS. Les résultats sont illustrés à la figure 95. Comme nous pouvons le constater, les résultats sont satisfaisants car les valeurs mesurées et les valeurs théoriques concordent.

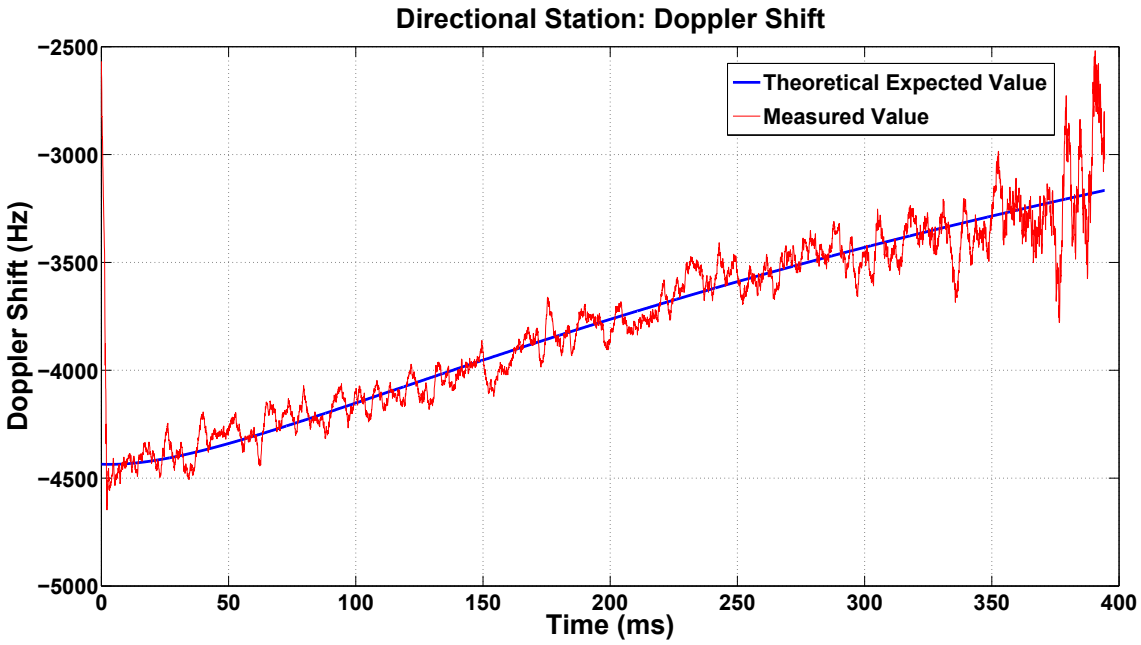

(a) Station Directive: Décalage Doppler.

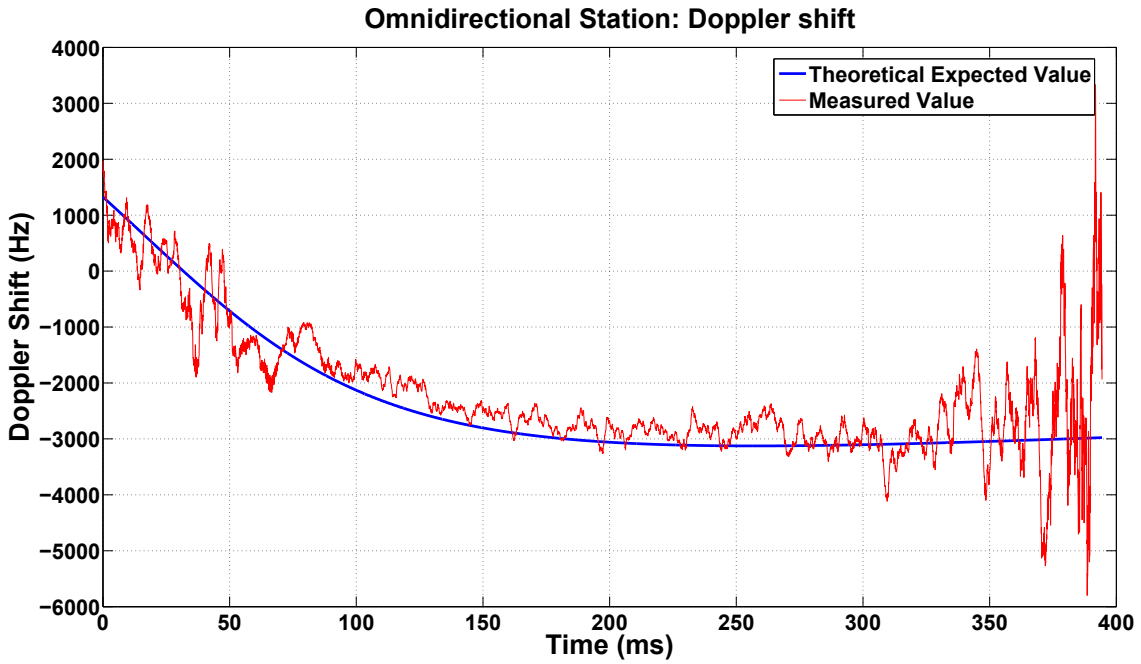

(b) Station Omnidirectionnelle: Décalage Doppler.

Figure 95: Comparaison de Décalage Doppler: Valeurs Théoriques Attendues et Valeurs Mesurées

Comme nous l'avons décrit dans notre processus d'analyse des données, nous poursuivons l'évaluation de la performance de l'algorithme d'estimation CFR. Dans le cas des mesures

concernant le prototype à 2250 MHz, 7703 trames OFDM ont été émises pendant le vol. Le tableau 24 présente un résumé des performances de l'estimateur CFR pour les deux stations de réception.

Table 24: Performance de l'Estimation de CFR pour l'Expérience à Vitesse Supersonique.

	Total OFDM Frames	**Invalid Frames**	**SNR Range (dB)**
Directional Station	7703	326 (4.23 %)	5 - 28
Omnidirectional Station	7703	2878 (37.36 %)	0 - 20

Les résultats de l'évaluation de l'algorithme d'estimation CFR permettent de poursuivre la caractérisation du canal. Nous appliquons notre algorithme d'estimation pour trajets multiples, qui nous permet d'établir quele canal peut être considéré comme un filtre 1-TDL en ce qui concerne l'évolution de la puissance du chemin LOS. Ce résultat peut être observé aux figures Fig. 96 - 97 ci-dessous.

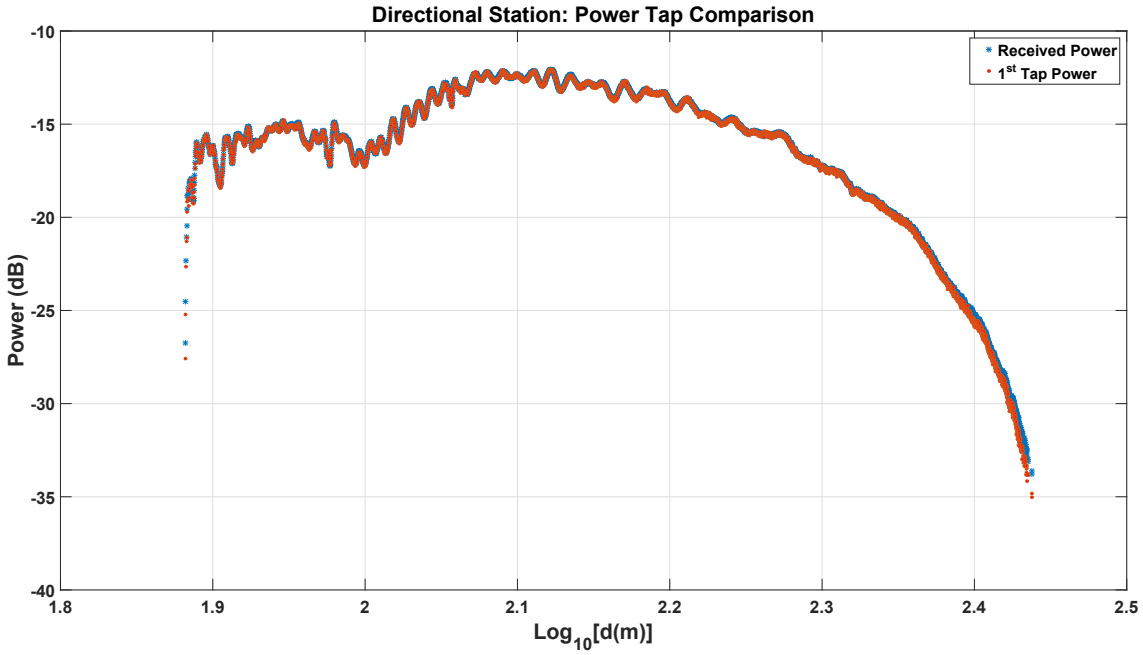

(a) Station Directive: Comparaison de l'Evolution de la Puissance.

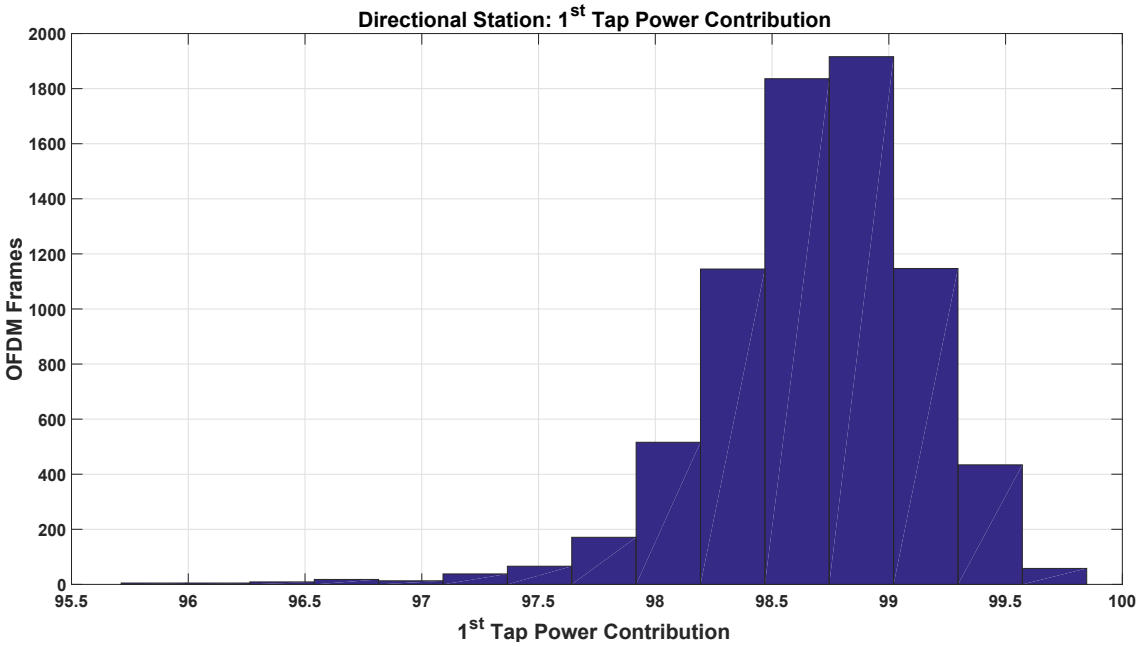

(b) Station Directive: Contribution de la Puissance Relative du Trajet LOS.

Figure 96: Station Directive: Contribution de la Puissance du Trajet LOS.

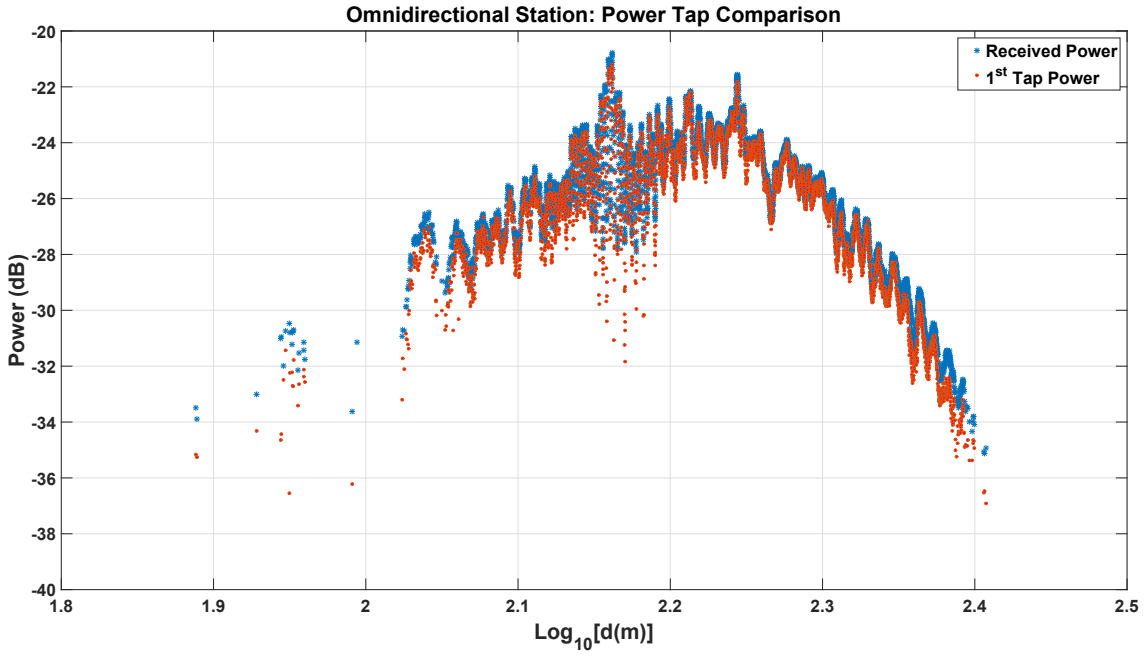

(a) Station Omnidirectionnelle: Comparaison de l'Evolution de la Puissance.

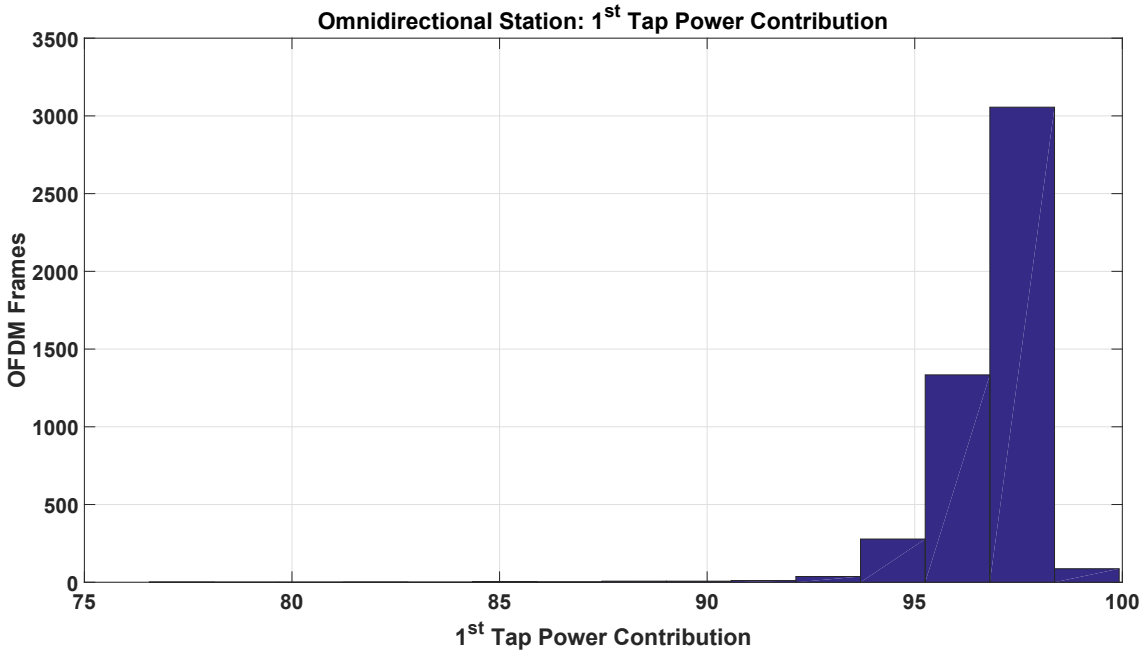

(b) Station Omnidirectionnelle: Contribution de la Puissance Relative du Trajet LOS.

Figure 97: Station Omnidirectionnelle: Contribution de la Puissance du Trajet LOS.

Enfin, selon l'étude de canal réalisée, il est possible définir le modèle de canal pour le scénario de propagation de Baldersheim. Il est modélisé en fonction du trajet direct LOS.

- Comportement de perte par propagation: ce paramètre ne peut pas être obtenu avec les

Table 25: Valeurs MLE.

Directional Station	**Rice Distribution (s | σ)**		**Weibull Distribution (a | b)**	
	0.18	0.04	0.21	5.08
Omnidirectional Station	0.06	0.02	0.07	3.86

données obtenues lors des expériences avec le prototype. Cependant, grâce à l'analyse des défaillances et des mesures complémentaires, une valeur de 2,3 est trouvée. Pour cette raison, la valeur de ce paramètre est par la suite considéré comprise entre 2 et 3. Il s'agit d'un compromis entre la situation d'espace libre et la zone urbaine.

- Spectre Doppler: l'algorithme d'estimation CFO permet de suivre le décalage Doppler de la composante LOS aux deux stations. Dans cette situation où l'effet de propagation par trajets multiples peut être négligé, la densité de puissance est concentrée dans la composante LOS. Pour les besoins de la simulation, le spectre Doppler est considéré composé d'un seul pic avec une valeur de fréquence obtenue à partir de la position du projectile et de la position de la station de réception.

- Comportement par trajets multiples: même si le canal est modélisé comme un filtre 1-TDL, nous devons accepter la limitation de la résolution temporelle lors de la caractérisation du comportement trajets multiples du canal. Aucun trajet multiple cohérent avec un temps de propagation supérieur à 50 ns par rapport à la composante LOS n'est détecté. Les propriétés à petite échelle du canal sont modélisées en tant que processus de Rice ou de Weibull. Leurs propriétés sont trouvées après avoir effectué une estimation de vraisemblance maximale (MLE) avec le logiciel MATLAB. Elles peuvent être trouvées dans le tableau Tab. 25.

B.6 Conclusion Générale et Perspectives

Ce manuscrit résume trois années d'étude de la modélisation du canal radio appliquée au domaine des projectiles instrumentés. Le document a été structuré en cinq chapitres, chacun rédigé dans le but d'introduire progressivement le lecteur à ce sujet spécifique.

Le contexte de la thèse a été présenté au chapitre I. Une brève introduction de l'histoire des systèmes de transmission sans fil a été donnée. De nos jours, presque tous les appareils électroniques sont équipés d'un système de communication sans fil. Dans le cadre des applications de défense et de sécurité, l'instrumentation de projectiles a pris de l'importance avec la miniaturisation de l'électronique disponible sur le marché. Néanmoins, l'instrumentation de projectiles est une tâche exigeante qui nécessite l'utilisation de systèmes de télémesure et de communication à haut débit. A l'ISL, le groupe STC est en charge du développement des systèmes radiofréquences (RF) embarqués utilisés dans les projectiles instrumentés. Dans ce contexte, une initiative conjointe entre l'ISL, le laboratoire XLIM de l'Université de Poitiers et la DGA a été mise sur pied dans le but d'améliorer les capacités des systèmes de communication actuels. L'un des premiers éléments à prendre en compte dans la conception d'un équipement RF est le canal sur lequel il sera déployé. Pour cette raison, la caractérisation du canal radio a été le cœur de cette thèse.

Avant d'aborder la caractérisation du canal radio, il était nécessaire d'introduire au chapitre II la nomenclature requise pour suivre ce document. Par conséquent, le chapitre a été divisé en deux parties. La première portait sur la description mathématique des propriétés du canal. Cela a conduit à la définition de la réponse impulsionnelle du canal et des fonctions de Bello. La deuxième partie du chapitre était centrée sur la description de certaines des techniques de sondage de canal les plus populaires. Concernant les particularités de ce travail (encombrement, vitesse supersonique des projectiles, etc.), nous avons conclu que nous devions développer notre propre technique de sondage de canal et l'instrumentation de prototype.

Avant de commencer le développement d'un sondeur de canal pour les applications de projectiles, nous avons présenté les instruments et outils disponibles au début de la thèse

au chapitre III. Comme le budget était une contrainte à prendre en compte (destruction quasi-systématique de l'électronique à l'impact), cela nous a permis d'aborder le problème de manière réaliste. La deuxième partie de ce chapitre a été consacrée à la conception de notre technique de sondage de canal. La méthodologie de sondage proposée est basée sur la technique de transmission OFDM, tandis que le matériel choisi pour sa mise en œuvre était parmi les derniers dispositifs SDR disponibles sur le marché. Un prototype a finalement été développé afin de réaliser le sondage de canal en conditions de vol.

Avant de tester le prototype en conditions de vol, une étude préliminaire du canal de propagation a été réalisée au chapitre IV. Globalement, le chapitre était structuré en deux parties: dans la première, nous étudions l'effet de la rotation et de la pendulation sur le signal reçu. Il a été déterminé que leurs effets pourraient être négligés pour la modélisation de canal. Cependant, les simulations que nous avons effectuées dans ce chapitre avec le logiciel de propagation de rayons RaPSor nous ont permis d'avoir un premier aperçu des éléments clés à caractériser: le comportement Doppler et les trajets multiples du canal. Dans la deuxième partie du chapitre, les données réelles d'une campagne de tir précédente de l'ISL ont été analysées. Nous avons observé comment le décalage Doppler était conforme à celui obtenu par la simulation.

Au chapitre V, nous avons finalement testé notre prototype de sondeur à canal large bande dans des conditions de tir réelles. Cependant, certaines de ses fonctionnalités avaient déjà été vérifiées à basse vitesse. Une campagne de tir a eu lieu en septembre 2017 à l'ISL dans le but d'obtenir les données nécessaire à la définition d'un modèle de canal pour les applications projectiles. Une analyse de défaillance a dû être effectuée après avoir détecté certaines anomalies dans les données reçues. Malgré cela, nous avons prouvé que ces données pouvaient être utilisées pour la modélisation de canal. Enfin, le canal a été modélisé comme un filtre 1-TDL. Il a été construit à partir des propriétés de pertes de trajet du canal, de sa réponse fréquentielle CFR et d'une analyse du PDP.

Les contributions de cette thèse ont été le développement d'une méthode de sondage de canal basée sur la technique de transmission OFDM, sa mise en œuvre dans un projectile instrumenté et la caractérisation du canal supersonique au champ de tir ISL. Certaines

questions doivent encore être analysées dans les années à venir, qui sont données ci-après.

- Conditions de propagation: dans cette thèse, nous avons caractérisé des scénarios de propagation ouverts avec un impact limité de l'effet de propagation par trajets multiples. La caractérisation de scénarios de propagation en présence de multi-trajets puissants, par exemple dans des zones urbaines densément peuplées, reste un sujet ouvert.

- Amélioration de notre méthodologie: au cours de cette thèse, la plupart des expériences ont été réalisées dans des conditions de visée directe (Line of Sight LOS, en anglais). Les résultats des expériences effectuées dans des situations où cette condition n'est pas remplie aideront à améliorer les algorithmes proposés dans notre méthodologie.

- Angle d'arrivée: un paramètre intéressant à étudier est l'angle d'arrivée des signaux en conflit du côté récepteur de la communication. Ce sujet, qui n'a pas été étudié dans cette thèse, permettra d'extraire des informations supplémentaires du sondage de canal. Par exemple, cela permettra de déterminer l'origine géographique de l'émetteur.

- Résolution temporelle: au chapitre V, la résolution temporelle de la configuration utilisée ne permettait pas de modéliser complètement le comportement de la propagation par trajets multiples du canal. Au lieu de cela, les composants multi-trajets étaient regroupés dans un seul chemin LOS. Le comportement de l'enveloppe de la composante LOS a été qualifié de distribution de Ricean ou de Weibull. Une question ouverte est l'amélioration de la résolution temporelle du sondeur. En conséquence, des composants multi-trajets avec une propagation de retard inférieure à 50 ns ont pu être observés

- Cette thèse est la première à utiliser un système de transmission à large bande à l'ISL dans des applications de projectiles. Dans les années à venir, le groupe STC poursuivra l'optimisation de ce système de transmission ainsi que des mécanismes de réception. Ainsi, des applications exigeantes en termes de débit pourront être mises en œuvre.

REFERENCES

[1] "Gnuradio. the free & open software radio ecosystem." https://www.gnuradio.org/. Accessed: 2018-08-31.

[2] *Telemetry Standards*. AD-a375 340, Range commanders council white sands missile range nm telemetry Group, 2000.

[3] Abdi, A., Lau, W. C., Alouini, M. ., and Kaveh, M., "A new simple model for land mobile satellite channels: first- and second-order statistics," *IEEE Transactions on Wireless Communications*, vol. 2, pp. 519–528, May 2003.

[4] Acosta-Marum, G. and Ingram, M. A., "Six time- and frequency-selective empirical channel models for vehicular wireless lans," in *2007 IEEE 66th Vehicular Technology Conference*, pp. 2134–2138, Sept 2007.

[5] Akki, A. S. and Haber, F., "A statistical model of mobile-to-mobile land communication channel," *IEEE Transactions on Vehicular Technology*, vol. 35, pp. 2–7, Feb 1986.

[6] Ambardar, A., *Analog and Digital Signal Processing*. Brooks/Cole Publishing Company, 1999.

[7] Andersen, J. B., Rappaport, T. S., and Yoshida, S., "Propagation measurements and models for wireless communications channels," *IEEE Communications Magazine*, vol. 33, pp. 42–49, Jan 1995.

[8] Anderson, J. D. and Mashhoon, B., "Pioneer anomaly and the helicity-rotation coupling," *Physics Letters A*, vol. 315, no. 3–4, pp. 199 – 202, 2003.

[9] AVNET, "Avnet. research further," 2018. https://www.avnet.com/.

[10] Babich, F. and Lombardi, G., "Statistical analysis and characterization of the indoor propagation channel," *IEEE Transactions on Communications*, vol. 48, pp. 455–464, March 2000.

[11] Bajwa, A. S. and Parsons, J. D., "Small-area characterisation of uhf urban and suburban mobile radio propagation," *IEE Proceedings F - Communications, Radar and Signal Processing*, vol. 129, pp. 102–109, April 1982.

[12] Balanis, C. A., *Antenna Theory: Analysis and Design*. Wiley-Interscience, 2005.

[13] Bartlett, M., *An Introduction to Stochastic Processes: With Special Reference to Methods and Applications*. Cambridge University Press, 1978.

[14] Bello, P., "Characterization of randomly time-variant linear channels," *IEEE Transactions on Communications Systems*, vol. 11, pp. 360–393, December 1963.

[15] Bello, P., "Aeronautical channel characterization," *IEEE Transactions on Communications*, vol. 21, pp. 548–563, May 1973.

[16] Bernard, L., "Design of the monopole antenna for ISL's guided supersonic projectile," in *2008 IEEE Antennas and Propagation Society International Symposium*, pp. 1–4, July 2008.

[17] Bernard, L., "Small-size circularly polarized patch antenna with an opening for a video grenade," *IEEE Antennas and Wireless Propagation Letters*, pp. 681–684, 2008.

[18] Bernard, L., Adam, R., Schmoltzi, D., Thomas, C., Kreitz, J., and Schneider, A., "Instrumentation of the basic finner reference projectile for attitude measurements at supersonic velocities," *IEEE Aerospace and Electronic Systems Magazine*, vol. 31, pp. 32–40, February 2016.

[19] Berner, C. and Rondot, F., "Soft recovery of on-board instrumented projectiles," in *International Symposium om Ballistics*, pp. 404–409, August 2004.

[20] Boyer, L., "Carrier-phase wrap-up caused by rotating a global positioning system antenna and its effect on measurements," Master's thesis, Ohio University, 1999.

[21] Cacopardi, S., Frescura, F., Gatti, F., and Reali, G., "Channel estimation and tracking of an indoor orthogonal multicarrier ds-cdma system using measured channel delay profiles," in *Proceedings of Vehicular Technology Conference - VTC*, vol. 3, pp. 1559–1563 vol.3, April 1996.

[22] Canet, M. J., Almenar, V., Marin-Roig, J., and Valls, J., "Time synchronization for the ieee 802.11a/g wlan standard," in *2007 IEEE 18th International Symposium on Personal, Indoor and Mobile Radio Communications*, pp. 1–5, Sept 2007.

[23] Cassioli, D., Win, M. Z., and Molisch, A. F., "The ultra-wide bandwidth indoor channel: from statistical model to simulations," *IEEE Journal on Selected Areas in Communications*, vol. 20, pp. 1247–1257, Aug 2002.

[24] Chang, R. W., "Synthesis of band-limited orthogonal signals for multichannel data transmission," *The Bell System Technical Journal*, vol. 45, pp. 1775–1796, Dec 1966.

[25] Chang, R. W., "Orthogonal frequency multiplex data transmission system," Jan 1970.

[26] Chen, J., Daneshrad, B., and Zhu, W., "Mimo performance evaluation for airborne wireless communication systems," in *2011 - MILCOM 2011 Military Communications Conference*, pp. 1827–1832, Nov 2011.

[27] Cheng, X., Wang, C., Ai, B., and Aggoune, H., "Envelope level crossing rate and average fade duration of nonisotropic vehicle-to-vehicle ricean fading channels," *IEEE Transactions on Intelligent Transportation Systems*, vol. 15, pp. 62–72, Feb 2014.

[28] Cho, Y. S., Kim, J., Yang, W. Y., and Kang, C. G., *MIMO-OFDM Wireless Communications with MATLAB*. Wiley Publishing, 2010.

[29] Ciccognani, W., Durantini, A., and Cassioli, D., "Time domain propagation measurements of the uwb indoor channel using pn-sequence in the fcc-compliant band

3.6-6 ghz," *IEEE Transactions on Antennas and Propagation*, vol. 53, pp. 1542–1549, April 2005.

[30] Cid, E. L., Sanchez, M. G., and Alejos, A. V., "High speed transmission at 60 ghz for 5g communications," in *2015 IEEE International Symposium on Antennas and Propagation USNC/URSI National Radio Science Meeting*, pp. 1007–1008, July 2015.

[31] Cimini, L., "Analysis and simulation of a digital mobile channel using orthogonal frequency division multiplexing," *IEEE Transactions on Communications*, vol. 33, pp. 665–675, Jul 1985.

[32] Clarke, R. H., "A statistical theory of mobile-radio reception," *The Bell System Technical Journal*, vol. 47, pp. 957–1000, July 1968.

[33] Cooper, G. R. and Costello, M., "Trajectory prediction of spin-stabilized projectiles with a liquid payload," *Journal of Spacecraft and Rockets*, vol. 48, no. 4, pp. 664–670, 2011.

[34] Cox, D., "Delay doppler characteristics of multipath propagation at 910 mhz in a suburban mobile radio environment," *IEEE Transactions on Antennas and Propagation*, vol. 20, pp. 625–635, September 1972.

[35] Dillinger, M., Madani, K., and Alonistioti, N., *Software Defined Radio: Architectures, Systems and Functions*. Wiley Series in Software Radio, Wiley, 2005.

[36] Dupuis, A., "Aeroballistic range tests of the basic finner reference projectile at supersonic velocities," tech. rep., Aeroballistic range tests of the basic finner reference projectile at supersonic velocities.

[37] Elsaadany, A. and Wen-jun, Y., "Accurate trajectory prediction for typical artillery projectile," in *Proceedings of the 33rd Chinese Control Conference*, pp. 6368–6374, July 2014.

[38] "Radio broadcasting systems; digital audio broadcasting (dab) to mobile, portable and fixed receivers," standard, ETSI, Sophia Antipolis, France, 2006.

[39] Fernandez, J. A., Borries, K., Cheng, L., Kumar, B. V. K. V., Stancil, D. D., and Bai, F., "Performance of the 802.11p physical layer in vehicle-to-vehicle environments," *IEEE Transactions on Vehicular Technology*, vol. 61, pp. 3–14, Jan 2012.

[40] Friis, H. T., "A note on a simple transmission formula," *Proceedings of the IRE*, vol. 34, pp. 254–256, May 1946.

[41] Glass, M., "Irig 106 chapter 10 standardizes mil-std-1553b data recording," in *2007 IEEE/AIAA 26th Digital Avionics Systems Conference*, pp. 2.B.5–1–2.B.5–9, Oct 2007.

[42] Gnemmi, P., Changey, S., Roussel, E., Meder, K., Rey, C., Grandvallet, B., Chauffaut, C., Bernard, L., Schertzer, S., Wey, P., and others, "Conception et réalisation d'un démonstrateur pour un système hybride projectile/drone miniature-état des travaux après 20 mois,"

[43] Goodman, D. J., "Trends in cellular and cordless communications," *IEEE Communications Magazine*, vol. 29, pp. 31–40, June 1991.

[44] Guan, K., Ai, B., Peng, B., He, D., Lin, X., Wang, L., Zhong, Z., and Kürner, T., "Scenario modules, ray-tracing simulations and analysis of millimetre wave and terahertz channels for smart rail mobility," *IET Microwaves, Antennas Propagation*, vol. 12, no. 4, pp. 501–508, 2018.

[45] Healey, A., Bianchi, C. H., and Sivaprasad, K., "Wideband outdoor channel sounding at 2.4 ghz," in *2000 IEEE-APS Conference on Antennas and Propagation for Wireless Communications (Cat. No.00EX380)*, pp. 95–98, Nov 2000.

[46] Hervas, M., Alsina-Pagès, R., Orga, F., Pijoan, J., Badia, D., and Altadill, D., "Narrowband and wideband channel sounding of an antarctica to spain ionospheric radio link," vol. 7, 06 2015.

[47] Hoeher, P., "A statistical discrete-time model for the wssus multipath channel," *IEEE Transactions on Vehicular Technology*, vol. 41, pp. 461–468, Nov 1992.

[48] Hogg, D. C., "Fun with the friis free-space transmission formula," *IEEE Antennas and Propagation Magazine*, vol. 35, pp. 33–35, Aug 1993.

[49] Hwang, J. K., Lin, K.-H., Chiu, Y.-L., and Li, J.-D., "An ofdm-based multipath channel sounding method with fractional delays resolution," in *2010 IEEE International Conference on Wireless Information Technology and Systems*, pp. 1–4, Aug 2010.

[50] Hwang, T., Yang, C., Wu, G., Li, S., and Li, G. Y., "Ofdm and its wireless applications: A survey," *IEEE Transactions on Vehicular Technology*, vol. 58, pp. 1673–1694, May 2009.

[51] Iglesias, D. R. and Sánchez, M. G., "Wideband channel characterization for low-elevation satellites in l-band," *IEEE Transactions on Antennas and Propagation*, vol. 61, pp. 2231–2240, April 2013.

[52] Instruments, N., "Ettus research. a national instrument brand," 2017. https://www.ettus.com/.

[53] Johnson, G., *The Ten Most Beautiful Experiments*. Vintage Books, 2009.

[54] Kivinen, J., Korhonen, T. O., Aikio, P., Gruber, R., Vainikainen, P., and Haggman, S. G., "Wideband radio channel measurement system at 2 ghz," *IEEE Transactions on Instrumentation and Measurement*, vol. 48, pp. 39–44, Feb 1999.

[55] Kivinen, J., Zhao, X., and Vainikainen, P., "Empirical characterization of wideband indoor radio channel at 5.3 ghz," *IEEE Transactions on Antennas and Propagation*, vol. 49, pp. 1192–1203, Aug 2001.

[56] Kwon, H., Kim, M., and Liang, J., "Evaluation of multi-path resolution for millimeter wave channel sounding system," in *2015 International Conference on Information and Communication Technology Convergence (ICTC)*, pp. 1034–1036, Oct 2015.

[57] Le Henanff, M., "Etude du canal de propagation pur des communications avec des projectiles ou des systèmes volants," Master's thesis, Ecole Polytechnique de l'Université de Nantes. Institut Franco-Allemand de Saint-Louis. Laboratoire XLIM-SIC, France, 2014.

[58] LE NAOUR, A., GOUBET, O., Moy, C., and Leray, P., "Spread spectrum channel sounder implementation with usrp platforms," *SUPELEC/IETR, Cesson-Sévigné Cedex, France*, 2013.

[59] Lee, J. H., Choi, J. S., and Kim, S. C., "Cell coverage analysis of 28 ghz millimeter wave in urban microcell environment using 3-d ray tracing," *IEEE Transactions on Antennas and Propagation*, vol. 66, pp. 1479–1487, March 2018.

[60] Lees, M. L., "The effect of rotating antennas and signal polarization on doppler shift," *IEEE Transactions on Aerospace and Electronic Systems*, no. 5, pp. 903–905, 1975.

[61] Leonor, N. R., Sánchez, M. G., Fernandes, T. R., and Caldeirinha, R. F. S., "A 2d ray-tracing based model for wave propagation through forests at micro- and millimeter wave frequencies," *IEEE Access*, vol. 6, pp. 32097–32108, 2018.

[62] Lodge1, D. and Dilkes, A., "Use of an instrumented 120mm projectile for obtaining in-bore gun dynamics data," in *10th U.S. Army Gun Dynamics Symposium Proceedings*, 2000.

[63] Lucki, M., Jares, P., and Kozlowska, E., "Modeling of the multi-carrier modulation benefits for data transmission," in *2010 12th International Conference on Transparent Optical Networks*, pp. 1–4, June 2010.

[64] Marconi, F. G., "Marconi and the invention of wireless communications," in *Proceedings of 1995 SBMO/IEEE MTT-S International Microwave and Optoelectronics Conference*, vol. 1, pp. 5–, July 1995.

[65] Marini, J. W., "The effect of satellite spin on two-way doppler rangerate measurements," *IEEE Transactions on Aerospace and Electronic Systems*, vol. AES-7, pp. 316–320, March 1971.

[66] Mashhoon, B., "Modification of the doppler effect due to the helicity–rotation coupling," *Physics Letters A*, vol. 306, no. 2–3, pp. 66 – 72, 2002.

[67] McCoy, R., *Modern Exterior Ballistics: The Launch and Flight Dynamics of Symmetric Projectiles*. Schiffer military history, Schiffer Publishing, Limited, 2012.

[68] Merhav, T., Savuskan, V., and Nemirovsky, Y., "Gun muzzle flash detection using cmos sensors," in *2013 IEEE International Conference on Microwaves, Communications, Antennas and Electronic Systems (COMCAS 2013)*, pp. 1–4, Oct 2013.

[69] Minn, H., Zeng, M., and Bhargava, V. K., "On timing offset estimation for ofdm systems," *IEEE Communications Letters*, vol. 4, pp. 242–244, July 2000.

[70] Minn, H., Bhargava, V. K., and Letaief, K. B., "A robust timing and frequency synchronization for ofdm systems," *IEEE Transactions on Wireless Communications*, vol. 2, pp. 822–839, July 2003.

[71] Moose, P. H., "A technique for orthogonal frequency division multiplexing frequency offset correction," *IEEE Transactions on Communications*, vol. 42, pp. 2908–2914, Oct 1994.

[72] Muammar, R. H., "The effects of ricean fading channel on microcellular mobile radio systems," in *IEEE Conference on Military Communications*, pp. 786–790 vol.2, Sept 1990.

[73] Muller, P. C., Bukowski, E. F., Katulka, G. L., and Peregino, P., "Flight test and recovery of gun-launched instrumented projectiles using high-g lt;newline/ gt;onboard recording techniques," *IEEE Transactions on Magnetics*, vol. 43, pp. 388–390, Jan 2007.

[74] Mutagi, R. N., "Pseudo noise sequences for engineers," *Electronics Communication Engineering Journal*, vol. 8, pp. 79–87, April 1996.

[75] Neul, A., Hagenauer, J., Papke, W., Dolainsky, F., and Edbauer, F., "Propagation measurements for the aeronautical satellite channel," in *37th IEEE Vehicular Technology Conference*, vol. 37, pp. 90–97, June 1987.

[76] O'Hara, B. and Petrick, A., *The IEEE 802.11 Handbook: A Designer's Companion*. Standards Information Network IEEE Press, 1999.

[77] Oliveira, T. R., Finamore, W. A., and Ribeiro, M. V., "A sounding method based on ofdm modulation for plc channel measurement," in *2013 IEEE 17th International Symposium on Power Line Communications and Its Applications*, pp. 185–190, March 2013.

[78] Park, B., Cheon, H., Kang, C., and Hong, D., "A novel timing estimation method for ofdm systems," *IEEE Communications Letters*, vol. 7, pp. 239–241, May 2003.

[79] Parsons, J. D. and Bajwa, A. S., "Wideband characterisation of fading mobile radio channels," *IEE Proceedings Communications, Radar and Signal Processing*, vol. 129, pp. 95–101, April 1982.

[80] Parsons, J. D., Demery, D. A., and Turkmani, A. M. D., "Sounding techniques for wideband mobile radio channels: a review," *IEE Proceedings I - Communications, Speech and Vision*, vol. 138, pp. 437–446, Oct 1991.

[81] Phillips, C., Sicker, D., and Grunwald, D., "A survey of wireless path loss prediction and coverage mapping methods," *IEEE Communications Surveys Tutorials*, vol. 15, pp. 255–270, First 2013.

[82] Ptzold, M., *Mobile Radio Channels*. Wiley Publishing, 2nd ed., 2012.

[83] Rappaport, R. S., *Wireless commnunications: Principles and Practice*. Prentice Hall PTR, 1996.

[84] Rappaport, T. S., "Characterization of uhf multipath radio channels in factory buildings," *IEEE Transactions on Antennas and Propagation*, vol. 37, pp. 1058–1069, Aug 1989.

[85] Rappaport, T. S., MacCartney, G. R., Samimi, M. K., and Sun, S., "Wideband millimeter-wave propagation measurements and channel models for future wireless communication system design," *IEEE Transactions on Communications*, vol. 63, pp. 3029–3056, Sept 2015.

[86] Rappaport, T. S., Sun, S., Mayzus, R., Zhao, H., Azar, Y., Wang, K., Wong, G. N., Schulz, J. K., Samimi, M., and Gutierrez, F., "Millimeter wave mobile communications for 5g cellular: It will work!," *IEEE Access*, vol. 1, pp. 335–349, 2013.

[87] Rauch, L. L., "Ballistic missile telemetry," *IRE Transactions on Telemetry and Remote Control*, vol. TRC-3, pp. 2–5, May 1957.

[88] "Attenuation by atmospheric gases," standard, International Telecommunication Union, Geneva, CH, February 2012.

[89] Sagias, N. C. and Karagiannidis, G. K., "Gaussian class multivariate weibull distributions: theory and applications in fading channels," *IEEE Transactions on Information Theory*, vol. 51, pp. 3608–3619, Oct 2005.

[90] Saleh, A. A. M. and Valenzuela, R., "A statistical model for indoor multipath propagation," *IEEE Journal on Selected Areas in Communications*, vol. 5, pp. 128–137, February 1987.

[91] Sarkar, T. K., Ji, Z., Kim, K., Medouri, A., and Salazar-Palma, M., "A survey of various propagation models for mobile communication," *IEEE Antennas and Propagation Magazine*, vol. 45, pp. 51–82, June 2003.

[92] Schmidl, T. M. and Cox, D. C., "Robust frequency and timing synchronization for ofdm," *IEEE Transactions on Communications*, vol. 45, pp. 1613–1621, Dec 1997.

[93] Schneckenburger, N., Jost, T., Shutin, D., Walter, M., Thiasiriphet, T., Schnell, M., and Fiebig, U., "Measurement of the l-band air-to-ground channel for positioning applications," *IEEE Transactions on Aerospace and Electronic Systems*, vol. 52, pp. 2281–2297, October 2016.

[94] Speth, M., Daecke, D., and Meyr, H., "Minimum overhead burst synchronization for ofdm based broadband transmission," in *IEEE GLOBECOM 1998 (Cat. NO. 98CH36250)*, vol. 5, pp. 2777–2782 vol.5, Nov 1998.

[95] Stüber, G. L., *Principles of Mobile Communication (2Nd Ed.)*. Norwell, MA, USA: Kluwer Academic Publishers, 2001.

[96] Sykora, J., "Tapped delay line model of linear randomly time-variant wssus channel," *Electronics Letters*, vol. 36, pp. 1656–1657, Sept 2000.

[97] Talebi, F. and Pratt, T., "Channel sounding and parameter estimation for a wideband correlation-based mimo model," *IEEE Transactions on Vehicular Technology*, vol. 65, pp. 499–508, Feb 2016.

[98] Tetewsky, A. K. and Mullen, F. E., "Carrier phase wrap-up by rotating gps antennas," *Proceedings of the 52nd Annual Meeting of The institute of Navigation*, pp. 21–28, June 1996.

[99] International Telecommunication Union, "ITU-R recommendation P.525.3: Calculation of free-space attenuation," tech. rep., ITU, 2016.

[100] Tomita, S., Miyake, Y., Kashiwamura, I., Komatsu, K., Tran, N. H., Oguma, H., Izuka, N., Kameda, S., Takagi, T., and Tsubouchi, K., "Hybrid single-carrier and multi-carrier system: Improving uplink throughput with optimally switching modulation," in *21st Annual IEEE International Symposium on Personal, Indoor and Mobile Radio Communications*, pp. 2438–2443, Sept 2010.

[101] Toth, V. T. and Turyshev, S. G., "Finding the source of the pioneer anomaly," *IEEE Spectrum*, vol. 49, pp. 38–62, December 2012.

[102] van de Beek, J. J., Edfors, O., Sandell, M., Wilson, S. K., and Borjesson, P. O., "On channel estimation in ofdm systems," in *1995 IEEE 45th Vehicular Technology Conference. Countdown to the Wireless Twenty-First Century*, vol. 2, pp. 815–819 vol.2, Jul 1995.

[103] van de Beek, J. J., Sandell, M., and Borjesson, P. O., "Ml estimation of time and frequency offset in ofdm systems," *IEEE Transactions on Signal Processing*, vol. 45, pp. 1800–1805, Jul 1997.

[104] Watterson, C., Juroshek, J., and Bensema, W., "Experimental confirmation of an hf channel model," *IEEE Transactions on Communication Technology*, vol. 18, pp. 792–803, December 1970.

[105] Weinstein, S. and Ebert, P., "Data transmission by frequency-division multiplexing using the discrete fourier transform," *IEEE Transactions on Communication Technology*, vol. 19, pp. 628–634, October 1971.

[106] Yang, B., Letaief, K. B., Cheng, R. S., and Cao, Z., "Timing recovery for ofdm transmission," *IEEE Journal on Selected Areas in Communications*, vol. 18, pp. 2278–2291, Nov 2000.

[107] Yanmaz, E., Kuschnig, R., and Bettstetter, C., "Channel measurements over 802.11a-based uav-to-ground links," in *2011 IEEE GLOBECOM Workshops (GC Wkshps)*, pp. 1280–1284, Dec 2011.

[108] Yeh, C., Lai, C., Tseng, M. ., and Li, H., "An ofdm-based channel sounder system," in *2009 IEEE Antennas and Propagation Society International Symposium*, pp. 1–4, June 2009.

[109] Zemen, T. and Mecklenbrauker, C. F., "Time-variant channel estimation using discrete prolate spheroidal sequences," *IEEE Transactions on Signal Processing*, vol. 53, pp. 3597–3607, Sept 2005.

[110] Zhao, X., Li, Y., Coulibaly, B. M., Guan, L., and Liu, S., "Performance evaluation of a new tapped-delay-line model for indoor mimo channels," in *9th International Conference on Communications and Networking in China*, pp. 416–421, Aug 2014.

[111] Zhao, X., Kolmonen, V., Geng, S., and Vainikainen, P., "Tapped delay line channel models for indoor mimo radio channels at 5 ghz," in *34th European Microwave Conference, 2004.*, vol. 3, pp. 1261–1264, Oct 2004.

[112] Zhao, Z., Cheng, X., Wen, M., Yang, L., and Jiao, B., "Constructed data pilot-assisted channel estimators for mobile environments," *IEEE Transactions on Intelligent Transportation Systems*, vol. 16, pp. 947–957, April 2015.

[113] Zhou, T., Tao, C., Salous, S., Liu, L., and Tan, Z., "Channel sounding for high-speed railway communication systems," *IEEE Communications Magazine*, vol. 53, pp. 70–77, October 2015.